Magnetic Fluid Flow Phenomena in DC and Rotating Magnetic Fields

by

Scott E. Rhodes

Submitted to the Department of Electrical Engineering and Computer Science in partial fulfillment of the requirements for the degree of

Master of Science in Electrical Engineering and Computer Science

at the

MASSACHUSETTS INSTITUTE OF TECHNOLOGY

Feb. 2004

Author .....
Department of Electrical Engineering and Computer Science
Feb. 9, 2004

Certified by .....
Markus Zahn
Professor of Electrical Engineering and Computer Science
Thesis Supervisor

Accepted by .....
Arthur C. Smith
Chairman, Departmental Committee on Graduate Students

Magnetic Fluid Flow Phenomena in DC and Rotating Magnetic Fields

by

Scott E. Rhodes

Submitted to the Department of Electrical Engineering and Computer Science on Feb. 9, 2004, in partial fulfillment of the requirements for the degree of Master of Science in Electrical Engineering and Computer Science

Abstract

An investigation of magnetic fluid experiments and analysis is presented in three parts: a study of magnetic field induced torques in magnetorheological fluids, a characterization and quantitative measurement of properties relating to the transition of a ferrofluid drop from a continuous phase into a discrete phase and also into a spiral flow, and a study of magnetic field induced ferrofluid flow reversals.

The torque exerted on a spindle filled with magnetorheological fluid (MR fluid) and placed inside a uniform rotating magnetic field is measured with varying rotating magnetic field amplitude and frequency, total fluid volume, and MR fluid volume ratio. When compared to similar ferrofluid torque measurements where the torque increased with rotating magnetic field frequency, the torque frequency dependence of the MR fluid decreases with increasing magnetic field frequency. A simple analysis determines the dependence of the magnetic body torque on particle size to describe the different behavior between the ferrofluid and MR fluid.

When a fluorocarbon based ferrofluid is contained between two glass plates separated by a small gap (Hele-Shaw cell) and excited by an applied uniform rotating magnetic field first and then a DC axial magnetic field, a phase like transition occurs that transforms the ferrofluid drop from a continuous phase to a discrete phase. Considering the dominant energy in the configuration to be contributed from the magnetostatic energy of the DC magnetic field and interfacial surface energy, a calculus of minimization of free energy is performed to determine the number of smaller ferrofluid drops that will result from the transition and the threshold axial magnetic field for the transition to occur. When the order of the applied magnetic fields is reversed, the DC axial magnetic field is applied first causing the ferrofluid droplet to form the labyrinth instability. The rotating magnetic field is then applied creating a spiral formation. Experiments are conducted for varying Hele-Shaw cell separation gap, and rotating magnetic field amplitude and frequency. Measurements were consistent with our model.

A cylindrical vessel is filled with a water-based ferrofluid and excited by a uniform rotating magnetic field that induces a counter-rotating circular flow in the vessel. A

DC axial magnetic field is slowly raised to change the curvature of the fluid surface and results in a change in the ferrofluid flow direction to co-rotating with the applied magnetic field. Measurements are taken of the threshold axial magnetic field that results in the change of flow direction for varying rotating magnetic field direction, amplitude, and frequency. An analysis is included that describes the change in flow direction due to surface curvature.

Thesis Supervisor: Markus Zahn
Title: Professor of Electrical Engineering and Computer Science

AKNOWLEDGEMENTS

I would like to thank my thesis advisor, Dr. Markus Zahn, for being an excellent mentor. He always had the time to share his time, knowledge, and experience and has helped me to become a better engineer. I would also like to thank Wayne Ryan, our lab technician. His creations and thoughts have played a key role in every experiment presented in this thesis.

I would like to thank Juan Perez, Shihab Elborai, Xiaowei He, Tommy Franklin, Willie Sanchez and the other members of our laboratory group for always welcoming discussions about our work in progress. Each person named above has saved me from spending countless hours headed down the wrong path.

Thanks also goes to Dr. Jeffrey Lang for supplying me with two micro-motors (both of which I destroyed), and Dr. Caroline Ross for letting me use her Vibrating Sample Magnetometer.

We appreciate Ferrofluidics Corp. (now FerroTec Corp.) for supplying the ferrofluids and Lord Corp. for suppling the magnetorheological fluid.

On a personal level, thank you to my father for never losing hope. At my lowest point in life, you picked me up and taught me the importance of honesty, integrity, and diligence. It is from these qualities that I have made it where I am today. Thanks should also be passed to my mother for always listening to me gripe about life as a graduate student. Your love is the only part of my life that has been constant and invariant.

This research was supported by the U.S. National Science Foundation Grant # CTS-0084070.

Contents

List of Figures

List of Tables

Chapter 1

Introduction

Magnetic fluids may be divided into two different categories: ferrofluids containing up to 10% magnetic particles by volume with diameter of approximately 10 nm, and magnetorheological fluids containing up to 80% magnetic particles by volume with diameter of 10 μm and larger. This thesis examines experiments performed on ferrofluids and magnetorheological fluids.

1.1 Magnetic Fluids

The background information on magnetic fluids given in this section is explained in more detail in "Ferrofluids, Magnetically Controllable Fluids and Their Applications" [20].

1.1.1 Ferrofluids

Ferrofluids are stable colloidal dispersions of single domain nano-sized particles of ferro- and ferrimagnetic particles in a carrier liquid. Theoretically, it should be possible to disperse magnetic nanoparticles in any carrier fluid enabling one to tailor the constraints of viscosity, surface tension, temperature, and stability to the application in mind.

When a ferrofluid is subjected to a magnetic and/or gravitational field, the mag-

netic particle diameter must be approximately 10 nm in order that the colloidal suspension remain stable. When the particles are this small, they possess only a single magnetic domain. Thus a strong magnetostatic attraction exists between individual particles which could lead to sedimentation and agglomeration of the magnetic particles unless the magnetic particles are also given a means for repulsive interactions. Therefore, the magnetic particles are coated with a surfactant (surface active material) to produce a repulsive force between neighboring particles. Brownian motion also helps to keep the magnetic particles evenly distributed throughout the carrier fluid.

1.1.2 Magnetorheological Fluids

All magnetic fluids exhibit magnetorheological effects; however, magnetorheological fluids (MR fluids) are confined to those that exhibit very strong effects only. MR fluids usually contain micron-sized particles of ferromagnetic materials. In contrast to the nano-sized particles in ferrofluids, the much larger particles are magnetically polydomain. If a material does not retain a remanent magnetization after being excited by an external applied magnetic field, the material is said to be soft. Then, without an applied magnetic field, the net magnetization of each particle is approximately zero and magnetic interactions between particles is minimal. However, after the application of even modest external magnetic fields (40 kA/m), the magnetic moment of the polydomain particles become aligned attaining large magnetic moments resulting in strong magnetic interaction between particles leading to chaining. The MR fluid changes from a low viscous liquid state to a very viscous "solid like" state. They are classified as being "smart" fluids because the viscosity may be carefully controlled by the amplitude of the applied magnetic field.

The most commonly used material for the magnetic particles is carbonyl iron, and MR fluids are typically 70% magnetic particles by weight. When the particles are placed in a carrier fluid with a low specific gravity (silicone oil), gravitational settling can occur. Brownian motion does not play the same role as it does in the case of ferrofluids because the particles are much larger. In many applications, the MR fluid

is located in a large shear force environment, which can render the fluid homogeneous in a short time. In applications where the forces are not large enough to mix the MR fluid, thixotropic agents can be added to the fluid that creates a network of particles that at low shear rates forms a loose structure that adds some rigidity to the fluid. This structure is destroyed and reformed upon subsequent application and removal of a shearing force.

1.2 Applications

Magnetic fluid applications span a wide array of industries and show future promise for new technologies as advancements are made.

Ferrofluids were introduced in the mid-1960s, discovered during the search to find a method to convert heat to work with no mechanical parts. However, many other uses were soon conceived from the ability to control the fluid with a magnetic force field. Present applications include novel zero-leakage rotary shaft seals used in computer hard drives, vacuum feedthroughs for semiconductor manufacturing, and pressure seals for compressors and blowers. Liquid cooled loudspeakers use the ferrofluid to conduct heat away from the speaker coils, lowering the speaker temperature and increasing the maximum power the coil can withstand and hence increasing the output of the speaker. By using the high effective specific gravity demonstrated by a pool of ferrofluid excited by a non-uniform magnetic field, sink-float separation systems have been developed to separate scrap metals such as titanium, aluminum, and zinc. By magnetically guiding the ferrofluid to produce printed characters on a substrate, the future may use magnetic fluid ink for inexpensive, high speed, silent printing [16].

The magnetically controlled metallic thrombosis of intracranial aneurysms has been using magnetic fluids in medicine since the 1960s. Current research in the biomedical field is separated into two main categories; magnetic drug delivery systems, and radiofrequency induced hyperthermia. Developments have recently been made in the preparation of magnetite/maghemite powders, the only magnetic materials accepted for medical applications [15]. Traditional application of chemotherapy,

releases the drug to a relatively non-specific location, almost always resulting in toxicity to normal tissues. By attaching the chemotherapeutic agents to ferrofluids and concentrating the drug in the precise location of the tumor through the use of an external magnetic field, one can greatly reduce the toxicity in surrounding normal tissues [4]. Advancements have been made preparing high toxicity magnetic particles for entering human beings by coating the particles with low toxicity, biocompatiable and biodegradable poly-lactide-co-glycolide (PLGA) [19]. Heating effects may also be achieved in AC magnetic fields by remagnetization losses (Néel losses) or energy dissipation through particle rotation in the carrier fluid (Brownian losses). Since malignant cells are much more sensitive to heat than healthy cells, hyperthermia is an established technique in clinical oncology. Radiofrequency induced ferrofluid hyperthermia together with chemotherapy and radiation have proven to be an effective therapeutic solution to cancer treatment [13, 14].

Lord Corporation has developed many applications for magnetorheological fluids. An automotive primary suspension incorporates MR fluid to provide real time optimization of suspension characteristics to improve the ride and handling and has been equipped on several winning race cars. MR fluid is being used in the construction of buildings and bridges by utilizing a damping system with MR fluid dampers, protecting the structure from earthquakes and windstorms. An artificial knee damper using MR fluid allows above-the-knee amputees to walk up and down stairs and inclines much easier than before [5].

Ferrofluids and MR fluids make perfect candidates for use in magnetic field based microelectromechanical (MEMS) technology because of their nano-sized and micron-sized particles. Magnetic field based MEMS technology offers advantages over analogous electric field based devices. Magnetic field systems have no limitations analogous to electric breakdown in dielectrics, and in general, magnetic forces are much larger than electric forces on such small scales because of the limitations due to electric breakdown. Researchers have proposed a system that can isolate individual particles and set each particle in a circulatory motion by subsequent application of a rotating magnetic field resulting in a rotary nanomotor that can be operated as a synchronous

machine [8].

1.3 Scope of Thesis

Chapter 2 provides measurements and theory of the torque exerted on a stationary spindle filled with magnetorheological fluid in a uniform rotating field. The torque is examined with changing rotating magnetic field amplitude and frequency, total fluid volume, and MR fluid volume ratio. The spindle is enclosed such that no top free surface exists and surface effects may be neglected. The experiments show a different trend for torque frequency dependence then did the ferrofluids under similar experimental parameters. An analysis is included to determine the relationship of the body torque density on the magnetic particle size in a magnetic liquid excited by a uniform rotating magnetic field. This analysis is used to explain the difference in torque frequency dependence between the two fluids.

Chapter 3 is focused on a fluid instability that transforms a ferrofluid drop from a continuous phase into a discrete phase. Measurements are taken to measure the number of smaller droplets that result from the single larger droplet, the threshold axial magnetic field that results in the transition occurring, and the surface area of the ferrofluid drop as it grows under increasing DC axial magnetic field excitation. These measurements are taken with varying Hele-Shaw cell separation gap, rotating magnetic field amplitude and frequency. By considering the total energy of the configuration to be the sum of the magnetostatic energy and the interfacial surface energy, a calculus of minimization is performed on the total energy to relate the number of smaller ferrofluid drops and the threshold axial magnetic field to the experiment parameters. Experiments are also conducted on spiral flows in a Hele-Shaw cell, by reversing the order of application of the magnetic fields. The trends are examined for changing Hele-Shaw cell separation gap, and rotating magnetic field amplitude and frequency.

Chapter 4 provides a summary of measurements and theory to explain magnetic field induced flow reversals in water-based ferrofluids excited by simultaneous applied

in-plane rotating and DC axial magnetic fields. The rotating magnetic field causes the ferrofluid contained in a cylindrical vessel to flow in the direction opposite to the applied field. A subsequent DC axial magnetic field is added to change the curvature of the free top surface from being concave, to flat, to convex. When the surface of the ferrofluid becomes convex, the direction of ferrofluid reverses and rotates in the direction of the rotating field. Measurements are taken of the threshold DC axial magnetic field that results in the reversal of ferrofluid flow direction for varying rotating magnetic field direction, amplitude, and frequency. An analysis is given to explain the dependence of rotational direction on ferrofluid surface curvature.

Chapter 5 is a discussion of the results obtained in this thesis.

Chapter 2

Magnetorheological Fluid Torque Measurements

Various mixtures of magnetorheological fluid (MR fluid) and non-magnetic Shell Diala A transformer oil have been placed inside of 5mL, 10mL, 20mL, and 60mL sized volumes to measure the torque exerted on them when placed inside a uniform rotating magnetic field. The volume is completely enclosed such that no free top surface exists. The torque exerted on these volumes has been measured as a function of magnetic field amplitude, frequency, total fluid volume, and MR fluid volume ratio in the experiments of this chapter. The various MR fluid volume ratios are 25%, 50%, and 100% MR fluid, the remaining fluid being non-magnetic transformer oil. Each MR fluid mixture fills a cylindrical spindle without a free top surface, and the torque induced by a uniform rotating magnetic field is measured. The MR fluid torque measurements are compared to similar torque measurements taken for a water-based ferrofluid to show opposite torque frequency dependencies between the two different fluids.

By relating the net magnetization of the fluid to the applied magnetic field through the magnetic relaxation equation, the body torque density is calculated in terms of the applied magnetic field. This is done to help explain the difference in torque frequency dependencies between the ferrofluid and magnetorheological fluid.

2.1 Procedure and Fluid Properties

Magnetorheological fluid is a concentrated suspension of large magnetic particles in a carrier fluid whose rheological properties vary with the application of a magnetic field.

In a uniform rotating magnetic field, the magnetization, $\mathbf{M}$, of each particle tries to align its magnetic moment with the applied field, $\mathbf{H}$. However, because of the viscosity of the carrier fluid, the magnetic moment lags behind the applied field causing a torque density on the particle, $\mathbf{\Gamma} = \mu_o(\mathbf{M} \times \mathbf{H})$, where $\mu_o = 4\pi \times 10^{-7}$ H/m is the permeability of free space.

2.1.1 Mass Density Measurements

The mass density of each fluid was measured by weighing the amount of fluid in each of the 5mL, 10mL, 20mL, and 60mL Becton Dickinson plastic syringes. Each syringe was weighed on a Denver Instrument Company Model S-11C digital scale without any fluid and again when filled with fluid to determine the mass of the fluid. This mass was divided by its corresponding volume for each syringe, and the average of these densities is reported for each fluid. The mass density of the transformer oil is 0.88 grams/cm^3, and the results of the MR fluid mixtures are shown in Table 2.1.

2.1.2 Viscosity Measurements

The viscosity of each fluid was measured with the Brookfield DV-I Viscometer without a magnetic field applied. The Brookfield suggested procedure was followed and will be briefly described. A 600mL beaker was filled to 500mL with fluid and placed under the viscometer. The Brookfield S61 calibrated stainless steel spindle with the guard-leg was attached to the viscometer and lowered into the fluid. The spindle rotation speed was increased until a torque reading of at least 10% of the full scale value (67.3μNm) was measured. Any viscosity reading with a torque under 10% is deemed inaccurate by Brookfield and is not considered. The spindle rotation speed is varied across the allowed speeds of the Brookfield viscometer to determine the

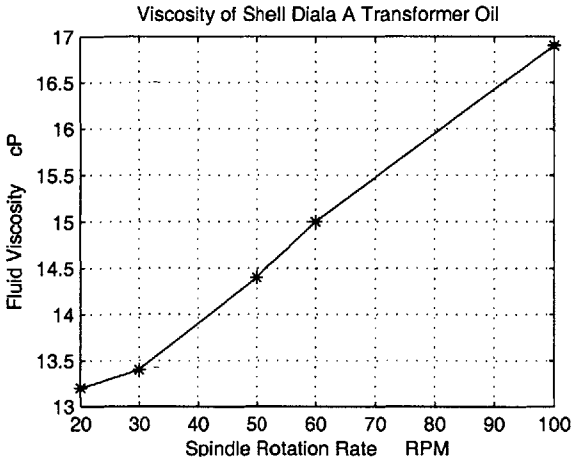

Figure 2-1: A plot of the measured viscosity of pure Shell Diala A transformer oil vs. spindle rotation rate at room temperature.

viscosity. The viscosity of the transformer oil is shown in Figure 2-1. The viscosity of the pure MR fluid was beyond the maximum torque capability (67.3 μNm) of the Brookfield viscometer for the entire range of spindle rotation speeds; therefore, no viscosity data was obtained for this fluid. The viscosity of the 50% MR fluid and 50% transformer oil by volume mixture and of the 25% MR fluid and 75% transformer oil by volume mixture is plotted as a function of spindle rotation speed and is displayed in Figures 2-2(a) and (b) respectively. These viscosity plots demonstrate that each of the MR fluid mixtures are non-Newtonian fluids, or the viscosity is dependent on the shear rate and decreases at higher shear rates, also known as shear thinning.

2.1.3 Magnetization Measurements

The magnetization data is obtained using the standard operating procedure for the Vibrating Sample Magnetometer (VSM, ADE Technologies model 880 Digital Measurement System). A plot was obtained for each concentration of MR fluid; pure MR fluid, 50% MR fluid, and 25% MR fluid and is shown in Figure 2-3. The measured values of the saturation magnetization and magnetic susceptibility are listed in Table 2.1.

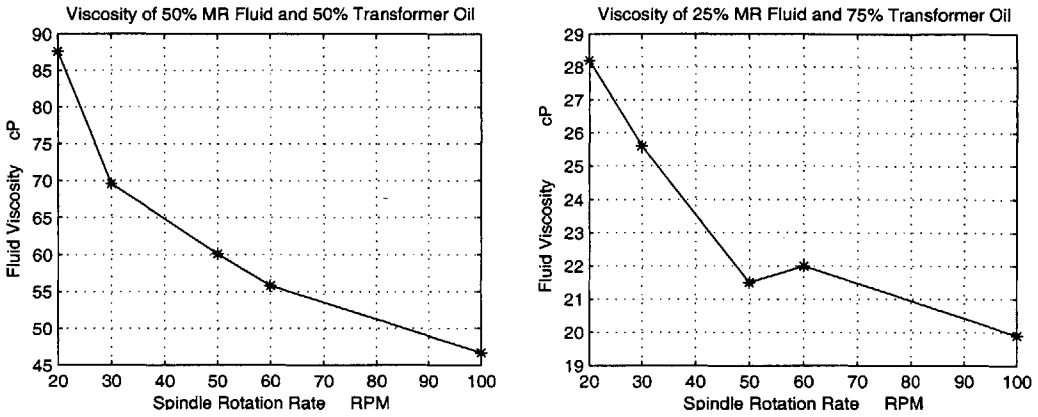

(a) 50% MR Fluid (b) 25% MR Fluid

Figure 2-2: A plot of the measured viscosity at room temperature of the (a) 50% MR fluid and 50% transformer oil by volume mixture and (b) 25% MR fluid and 75% transformer oil by volume mixture vs. spindle rotation speed.

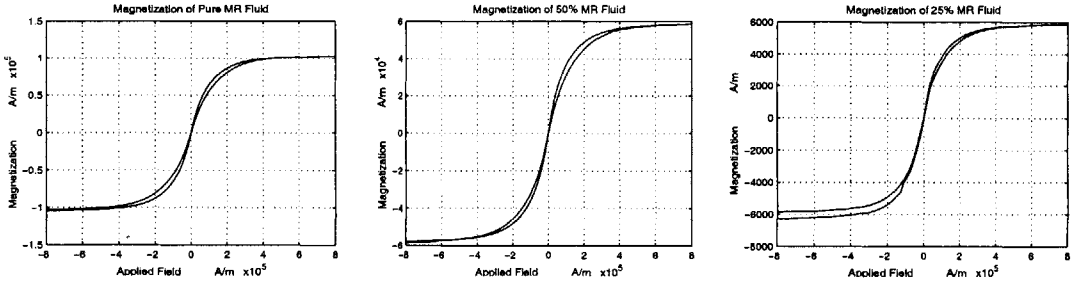

(a) Pure MR Fluid (b) 50% MR Fluid (c) 25% MR Fluid

Figure 2-3: A plot of the measured magnetization vs. the applied magnetic field at room temperature of the (a) pure MR fluid, (b) 50% MR fluid, and (c) 25% MR fluid.

Table 2.1: Summary of the MR fluid properties.

	MR Fluid	50% MR Fluid	25% MR Fluid
Mass Density	1.68 g/cm^3	1.16 g/cm^3	0.99 g/cm^3
Viscosity		46-88 cP	20-28 cP
Saturation Magnetization	1x10^5 A/m	6x10^4 A/m	6x10^3 A/m
Magnetic Susceptibility	0.74	0.43	0.05

Because the 50% MR fluid has half the magnetic material as the pure MR fluid, the saturation magnetization is expected to be approximately half the value for the pure MR fluid. The measurements show that this is approximately true. Similarly, the saturation magnetization of the 25% MR fluid should be approximately a quarter of the magnetization of the pure MR fluid. However, the measurements show the magnetization is approximately 1/17 the value of the pure MR fluid. This is believed to be caused by the small density of magnetic particles not allowing the particles to chain together.

2.1.4 Torque Measurements

The magnetic field induced torque was measured by using the Brookfield viscometer as a torque meter with the MR fluid mixtures placed inside a uniform rotating magnetic field.

The uniform rotating magnetic field was created by exciting a 2 pole motor stator winding with balanced 3 phase AC currents with the frequency ranging from 5 to 500 Hz as described in Appendix A. Each of the MR fluid mixtures are placed inside a 5mL, 10mL, 20mL, and 60mL Becton Dickinson syringe. The syringe's plunger has been modified to attach to the Brookfield Viscometer as a spindle as shown in Fig. 2-4. The syringe is then lowered into the motor stator winding to begin taking torque measurements. The plastic syringes are non-conducting; therefore, the eddy currents induced are negligible so that the torque measured is only due to the MR fluid.

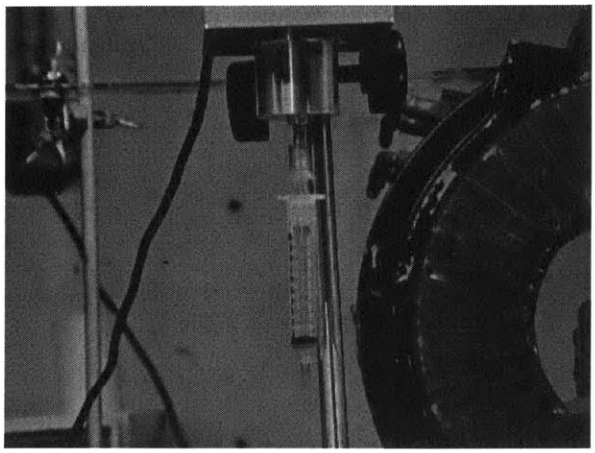

Figure 2-4: An illustration of the modified syringe's plunger that attaches to the Brookfield viscometer.

2.2 Torque Measurements

For all torque measurements the magnetic field is rotating clockwise, and the Brookfield viscometer measures the torque exerted on a stationary spindle in the clockwise direction. The maximum torque that can be measured by the Brookfield viscometer is 67.3 μNm. In all cases, the viscous shear stress on the spindle due to magnetic field induced flow is co-rotating with the field, increasing the torque as magnetic field amplitude is increased.

The torque data is plotted as a function of magnetic field amplitude and frequency.

2.2.1 Torque vs. Magnetic Field Amplitude

The measured torque is plotted vs. magnetic field amplitude for the following MR fluid volume ratio fluids; pure MR fluid, 50% MR fluid, and 25% MR fluid. The magnetic field frequency ranges from 5 Hz to 500 Hz for the following experiments.

For the 50% and 25% MR fluid mixtures, as soon as the fluid is placed inside of the rotating magnetic field, the clear transformer oil would separate from the mixture and collect at the top of the syringe. All of the MR fluid would collect at the bottom of the syringe. The MR fluid mixtures would only separate after long periods of time

from gravitational settling without an applied magnetic field. A normalization of the data is presented in Section 2.2.3 and shows that the torque scales with the MR fluid volume fraction.

Pure MR Fluid

The pure MR fluid is placed inside of the 5mL, 10mL, 20mL, and 60mL syringes for torque readings as described in Section 2.1.4.

The torque exerted on a 5mL syringe filled with pure MR fluid and placed in a uniform rotating magnetic field is plotted in Figure 2-5 as a function of magnetic field amplitude at different frequencies. The torque exerted does not significantly change over the rotating magnetic field frequency range covered in these experiments. Instead, the torque increases with magnetic field amplitude in essentially the same manner for all measured frequencies. Even at magnetic field strengths as large as 180 Gauss (rms), the torque meter has not reached its full scale value at 67.3 μNm.

The torque exerted on the 10mL syringe filled with pure MR fluid and placed inside a clockwise rotating magnetic field is shown in Figure 2-6. The torque increases as the magnetic field amplitude increases and measurably spreads with frequency at amplitudes above 72 Gauss (rms). Noting from the plot that the full scale value of the torque meter is reached at approximately 127 Gauss (rms), we see that the rate at which the torque climbs with increasing rotating magnetic field amplitude has increased when compared to the 5mL graph in Figure 2-5. For a given magnetic field strength the total measured torque for the 10 mL sample is about double the total measured torque for the 5 mL sample in Fig 2-5.

The torque exerted on a 20mL and 60mL syringe filled with pure MR fluid is shown in Figures 2-7 and 2-8 respectively. The torque increases as the magnetic field amplitudes increase and spreads with frequency above 63 Gauss (rms) for the 20mL syringe, and above 36 Gauss (rms) for the 60mL syringe. The magnetic field amplitude range covered for these volumes is decreased because of the torque limitations of the torque meter. The 60mL torque data's dependence on frequency may be due to the weight of the spindle exceeding the Brookfield 5 ounce (141.7 grams) limit. The

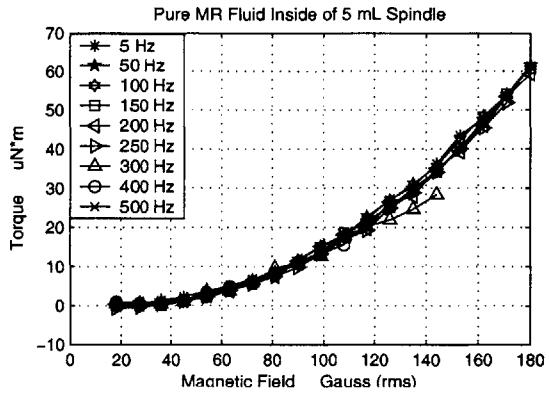

Figure 2-5: Torque measurements for pure MR fluid inside of a 5mL spindle are plotted vs. magnetic field amplitude for various magnetic field frequencies. The torque is relatively independent of magnetic field frequency.

spindle filled with fluid weighed 143.7 grams.

As the spindle volume of fluid stressed by the magnetic field increases, the torque reaches the full scale maximum value of the torque meter at lower fields. This indicates that the torque exerted on the spindle increases with the amount of magnetic material inside of the spindle.

50% MR Fluid Mixture

The 50% MR fluid and 50% Shell Diala A transformer oil by volume mixture is placed inside of the 5mL, 10mL, 20mL, and 60mL syringes for torque readings as described in Section 1.1.3. Each set of torque measurements are plotted versus the rotating magnetic field amplitude for various rotating magnetic field frequencies.

In Figure 2-9, the torque exerted on the 50% MR fluid mixture inside of the 5mL spindle is plotted vs. the magnetic field amplitude. The syringe experiences a much larger torque when stressed at 5 Hz. All of the higher frequencies essentially follow the same torque curve. At 180 Gauss (rms) and 5 Hz excitation, the torque on the 5mL spindle climbs to more than twice the value reached for higher frequencies tested from 50 Hz to 500 Hz.

Torque measurements for the 50% MR fluid mixture inside of the 10mL spindle

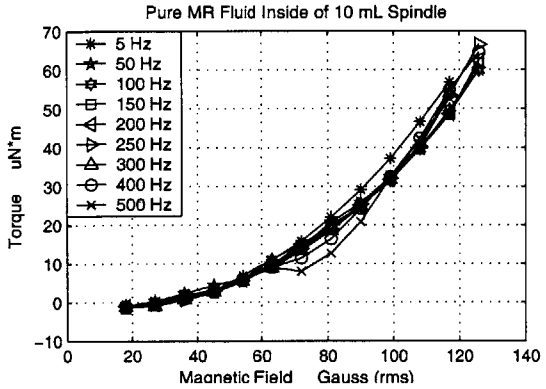

Figure 2-6: Torque measurements for pure MR fluid inside of a 10mL spindle are plotted vs. magnetic field amplitude for various magnetic field frequencies. The torque begins to show frequency dependence at magnetic field strengths above 72 Gauss (rms).

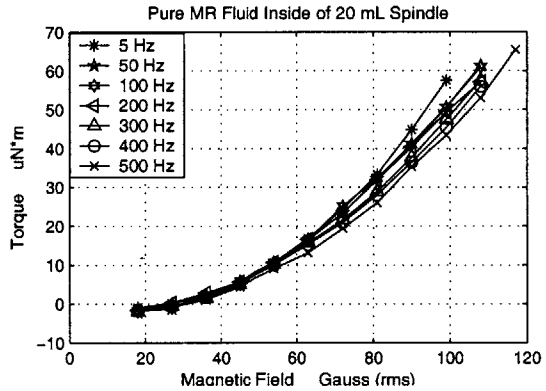

Figure 2-7: Torque measurements for pure MR fluid inside of a 20mL spindle are plotted vs. magnetic field amplitude for various magnetic field frequencies. The torque increases as magnetic field strength is increased; however the torque slightly drops with increasing frequency.

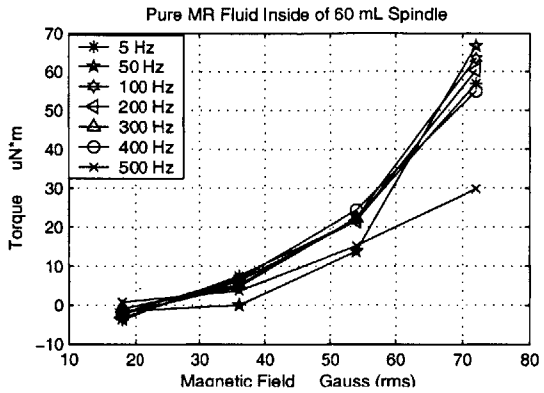

Figure 2-8: Torque measurements for pure MR fluid inside of a 60mL spindle are plotted vs. magnetic field amplitude for various magnetic field frequencies. The unclear response to frequency changes is likely caused by the spindle weight of 5.13 ounces, exceeding the Brookfield viscometer's 5 ounce maximum.

is plotted as a function of magnetic field amplitude in Figure 2-10. As the magnetic field increases, the torque exerted on the spindle increases; however, it now becomes clear that the torque does indeed decrease as the frequency is increased. A very clear distinction between frequencies can be seen at field amplitudes above 35 Gauss (rms).

The torque exerted on the 20mL spindle when filled with the 50% MR fluid mixture is plotted vs. the magnetic field amplitude in Figure 2-11. The torque increases as the magnetic field amplitude increases; however, the torque decreases as the frequency is increased. The distinction between different frequencies can be seen at field strengths above 50 Gauss (rms). Some torque measurements were not possible due to the maximum torque capability of the Brookfield viscometer. For this reason measurements stopped at 145 Gauss (rms).

In Figure 2-12, a plot is displayed of the torque measurements for the 50% MR fluid mixture inside of the 60mL spindle. The torque increases as the magnetic field amplitude increases; however, the torque decreases as the frequency is increased. While this data still exhibits the same characteristics as the smaller volumes, the decreasing torque with increasing frequency is stronger than in the smaller volumes.

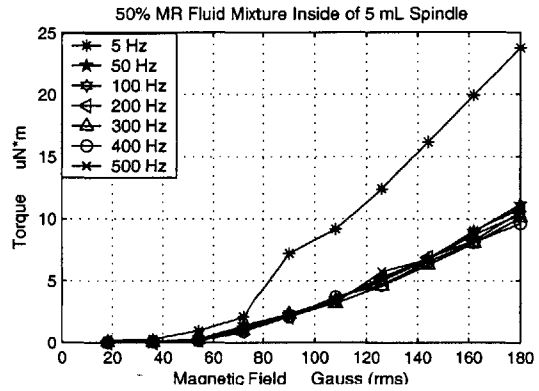

Figure 2-9: Torque measurements for the 50% MR fluid and 50% transformer oil by volume mixture in a 5mL spindle are plotted vs. magnetic field amplitude for various magnetic field frequencies. The torque at 5 Hz is greatly larger than the torque generated at higher magnetic field frequencies.

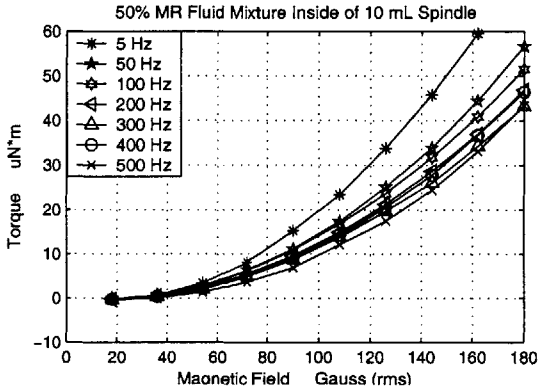

Figure 2-10: Torque measurements for the 50% MR fluid and 50% transformer oil by volume mixture inside of a 10mL spindle are plotted vs. magnetic field amplitude for various magnetic field frequencies. The torque measurably decreases with increasing frequency at magnetic field strengths above 54 Gauss (rms).

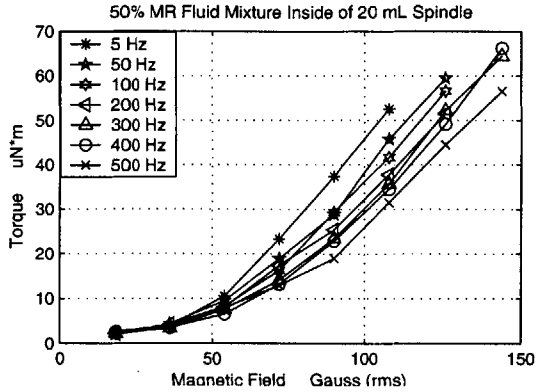

Figure 2-11: Torque measurements for the 50% MR fluid and 50% transformer oil by volume mixture inside of a 20mL spindle are plotted vs. magnetic field amplitude for various magnetic field frequencies. The torque measurably decreases with increasing frequency at magnetic field strengths above 54 Gauss (rms).

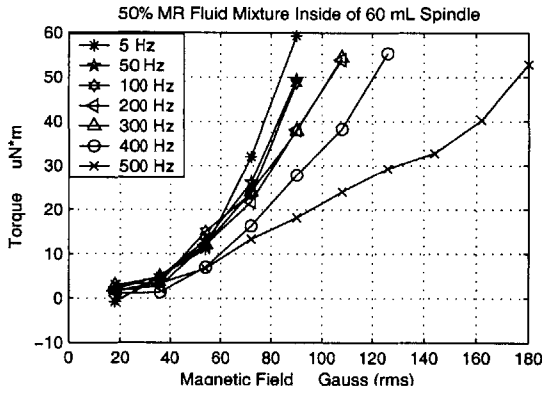

Figure 2-12: Torque measurements for the 50% MR fluid and 50% transformer oil by volume mixture inside of a 60mL spindle are plotted vs. magnetic field amplitude for various magnetic field frequencies. The torque at 500 Hz is greatly less than the torque generated at lower rotating magnetic field frequencies.

25% MR Fluid Mixture

The 25% MR fluid and 75% transformer oil by volume mixture is placed inside of the 5mL, 10mL, and 20mL spindles for torque measurements as described in the procedure. Each set of torque measurements has been plotted versus the magnetic field amplitude.

Torque measurements for the 25% MR fluid inside of the 5mL spindle are plotted as a function of magnetic field amplitude in Figure 2-13 for various magnetic field frequencies. As the magnetic field increases, the torque exerted on the spindle increases; however, the torque decreases for increases in frequency. The torque readings in this plot appear to be erratic and are caused by the very small torques generated. Brookfield suggests that torque measurements under 7 μNm are inaccurate; this is believed to be the cause for the erratic pattern.

Torque measurements for the 25% MR fluid inside of the 10mL spindle are plotted as a function of magnetic field amplitude in Figure 2-14 for various magnetic field frequencies. The torque increases as the magnetic field amplitude increases; however, it decreases as the frequency is increased. Once again, the 5 Hz excitation generated much larger torques than the higher frequency excitation. At 180 Gauss (rms), the torque at 5 Hz is approximately 80% larger than the torque at other frequencies in the range of 50 to 500 Hz.

Torque measurements for the 25% MR fluid mixture inside of the 20mL spindle are plotted as a function of magnetic field amplitude in Figure 2-15 for various magnetic field frequencies. The torque increases as the magnetic field amplitude increases; however, the torque continues to show a consistent decrease with increasing frequency. As before, the 5 Hz excitation causes much larger torques.

2.2.2 Torque vs. Magnetic Field Frequency

This section will look at the same torque data as in the previous section, but now the data will be plotted vs. the rotating magnetic field frequency. By changing the data representation in this manner, it is easier to visualize the rate of decrease in torque as

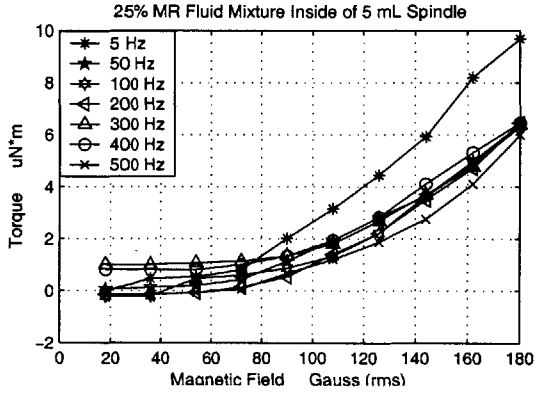

Figure 2-13: Torque measurements for the 25% MR fluid and 75% transformer oil by volume mixture inside of a 5mL spindle are plotted vs. magnetic field amplitude. Because the measured torque is less than 10% of the 67.3 μNm maximum, these results are deemed inaccurate by Brookfield.

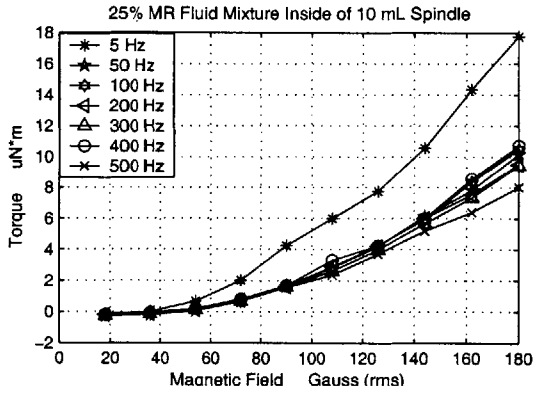

Figure 2-14: Torque measurements for the 25% MR fluid and 75% transformer oil by volume mixture inside of a 10mL spindle are plotted vs. magnetic field amplitude. The torque at 5 Hz is greatly larger than the torques generated at higher rotating magnetic field frequencies.

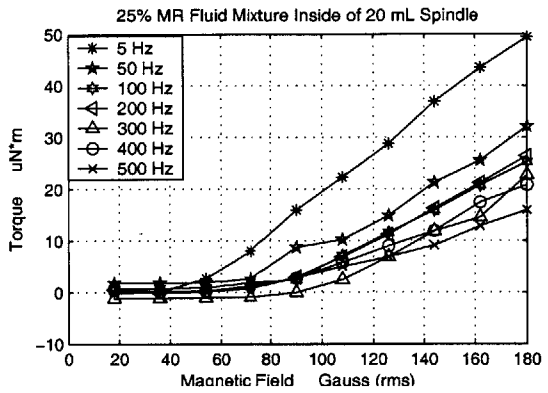

Figure 2-15: Torque measurements for the 25% MR fluid and 75% transformer oil by volume mixture inside of a 20mL spindle are plotted vs. magnetic field amplitude. Once again, excitations at 5 Hz induce much larger torques than higher magnetic field frequencies.

the magnetic field frequency is increased. The magnetic field amplitude ranges from 0 to 180 Gauss (rms). The torque measurements for some of the MR fluid mixtures were not able to cover this entire amplitude range because the torque would reach its maximum reading before measurements at the upper bound were reached.

Pure MR Fluid

The torque measurements for the pure MR fluid inside of the 5mL, 10mL, 20mL, and 60mL syringes are now plotted vs. the magnetic field frequency for various magnetic field amplitudes.

The torque exerted on the 5mL syringe is plotted in Figure 2-16. The nonlinear response to increased magnetic field amplitude is seen by the unequal spacing between torque curves that differ in magnetic field strength in increments of 18 Gauss (rms). However, the torques appear to be approximately constant over the frequency range covered in these experiments.

The torque exerted on the 10mL syringe is plotted in Figure 2-17. Most of the torque curves appear to be constant over the entire frequency range. However, the 72 and 90 Gauss (rms) curves experience slight decreases in slope for frequencies above 300 Hz.

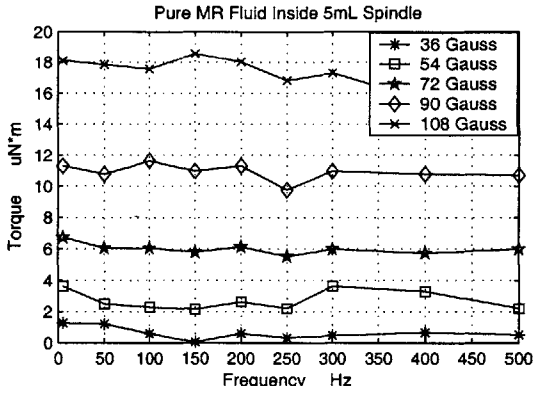

Figure 2-16: Torque measurements for the pure MR fluid inside of a 5mL spindle are plotted vs. magnetic field frequency for various magnetic field amplitudes. The torque is primarily constant for each magnetic field amplitude over the frequency range 5 - 500 Hz.

The torque exerted on the 20mL syringe is plotted in Figure 2-18. The 36 and 54 Gauss (rms) torque curves appear to be constant over the entire frequency range; however, the torque curves above 54 Gauss (rms) all have a slight negative slope.

The torque exerted on the 60mL syringe is plotted in Figure 2-19. This plot shows no consistent pattern for the torque measured over the prescribed frequency range. This erratic behavior is believed to be caused by the spindle exceeding the 5 ounce weight limit of the torque meter, and it should not be considered accurate.

50% MR Fluid Mixture

The torque measurements for the 50% MR fluid and 50% transformer oil mixture are plotted in this section for 5mL, 10mL, 20mL, and 60mL volumes excited by a uniform rotating magnetic field.

The torque exerted on the 5mL syringe is plotted in Figure 2-20. There is a very sharp decrease in torque from 5 Hz to 50 Hz for field strengths larger than 108 Gauss (rms). The torque then appears to be constant for all frequencies above 50 Hz.

The torque exerted on the 10mL syringe is plotted in Figure 2-21. Torque curves at magnetic field strengths above 108 Gauss (rms) experience a slight decrease in torque with increasing frequency. While there is a larger drop in torque between

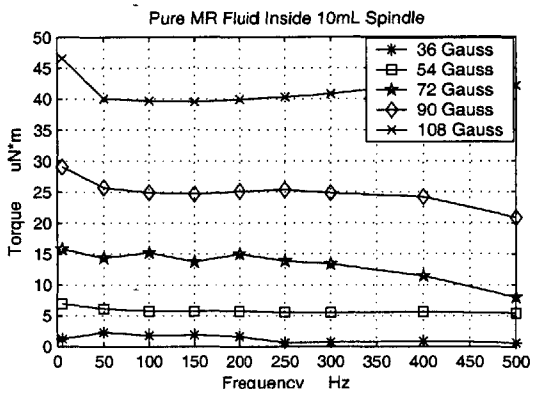

Figure 2-17: Torque measurements for the pure MR fluid inside of a 10mL spindle are plotted vs. magnetic field frequency. The torque at 72 and 90 Gauss (rms) experience a slight decrease in torque with increasing magnetic field frequency above 300 Hz.

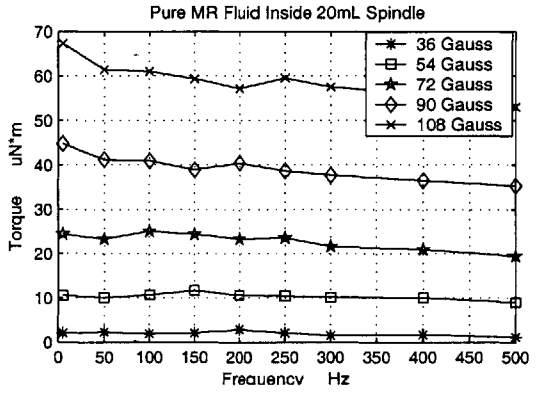

Figure 2-18: Torque measurements for the pure MR fluid inside of a 20mL spindle are plotted vs. magnetic field frequency. The slight negative slope indicates the torque decreasing as the frequency increases.

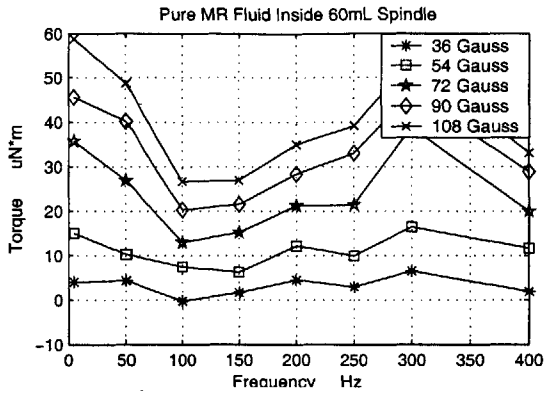

Figure 2-19: Torque measurements for the pure MR fluid inside of a 60mL spindle are plotted vs. magnetic field frequency. The erratic response is believed to be caused by the increased weight of the spindle beyond the maximum weight limit of 5 ounces.

5 and 50 Hz than other frequency intervals, this drop is not as dramatic as that demonstrated by the 5mL data.

The torque exerted on the 20mL syringe is plotted in Figure 2-22. The negative slope can now be seen on the 72 Gauss (rms) curve. Measurements at 180 Gauss (rms) could not be shown because the torques produced exceeded the limits of the torque meter.

The torque exerted on the 60mL syringe is plotted below in Figure 2-23. The torque generated at 144 Gauss (rms) drops approximately 30% over the range from 5 to 500 Hz. The erratic behavior does not appear in this data set, thus it appears that the increased weight of the spindle does not effect the torque measurements as it has before.

25% MR Fluid Mixture

The torque measurements for the 25% MR fluid and 75% transformer oil mixture are plotted in this section for the 5mL, 10mL, and 20mL volumes excited by a uniform rotating magnetic field.

The torque exerted on the 5mL syringe is plotted in Figure 2-24. Besides the initial drop between 5 and 50 Hz, the torque appears to remain constant for frequencies up

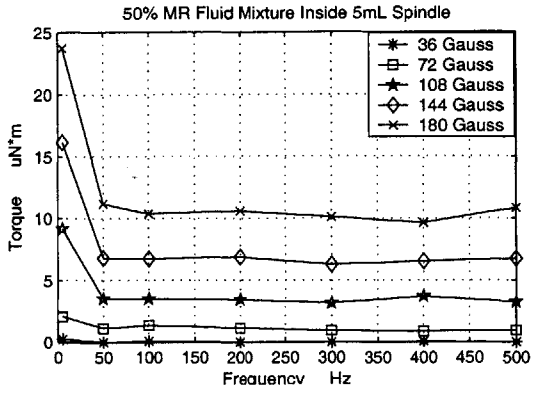

Figure 2-20: Torque measurements for the 50% MR fluid and 50% transformer oil inside of a 5mL spindle are plotted vs. magnetic field frequency. A sharp decrease in torque is experienced between field frequencies of 5 and 50 Hz. However, the torque is primarily constant for frequencies above 50 Hz.

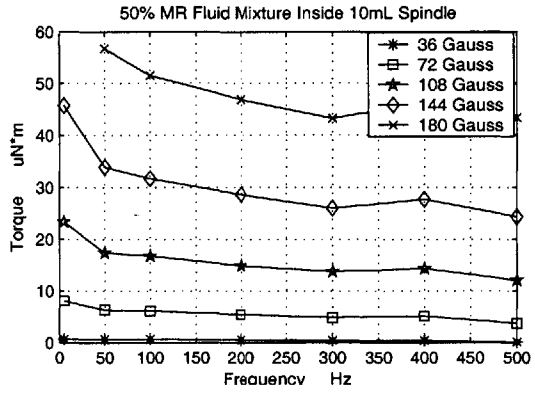

Figure 2-21: Torque measurements for the 50% MR fluid and 50% transformer oil inside of a 10mL spindle are plotted vs. magnetic field frequency. The torques generated clearly decrease as rotating magnetic field frequency is increased.

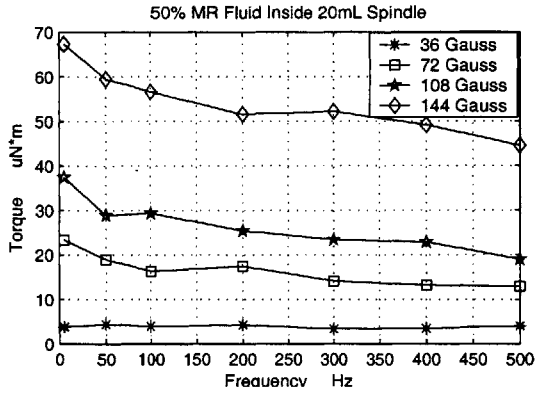

Figure 2-22: Torque measurements for the 50% MR fluid and 50% transformer oil inside of a 20mL spindle are plotted vs. magnetic field frequency. The consistent but negative slope indicates the torque decreasing as the frequency increases.

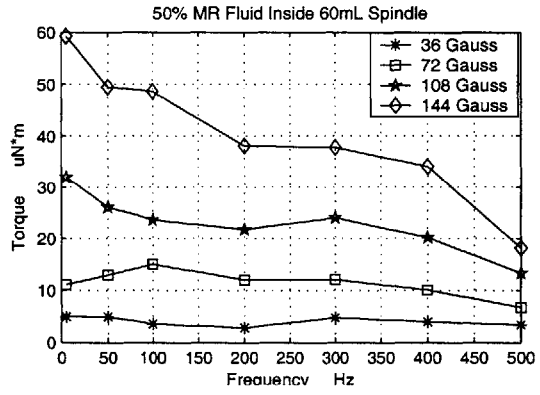

Figure 2-23: Torque measurements for the 50% MR fluid and 50% transformer oil by volume mixture inside of a 60mL spindle are plotted vs. magnetic field frequency. The torque at 144 Gauss (rms) experiences a much sharper decrease than has been seen previously.

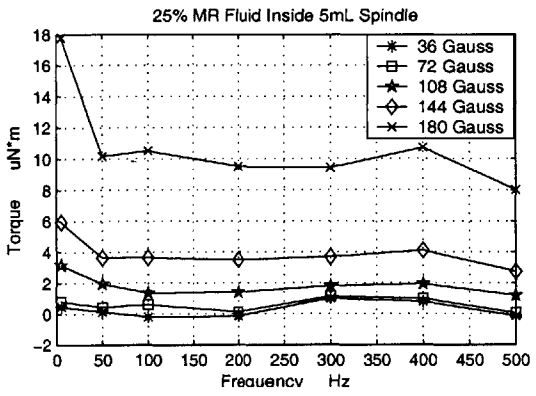

Figure 2-24: Torque measurements for the 25% MR fluid and 75% transformer oil inside of a 5mL spindle are plotted vs. magnetic field frequency. A sharp decrease in torque is experienced between 5 and 50 Hz. For frequencies larger than 50 Hz, the torque induced is essentially constant.

to 400 Hz. Then each of the curves at fixed magnetic field strengths exhibit a slight decrease in torque between 400 and 500 Hz.

The torque exerted on the 10mL syringe is plotted in Figure 2-25. The torque exerted at 180 Gauss (rms) appears to follow the same pattern as the 5mL data, while all the other field strengths produced larger torques for the larger volume of MR fluid mixture.

The torque exerted on the 20mL syringe is plotted in Figure 2-26. The measured torque curves decrease quickly from the 5 to 100 Hz measurements, before they level off and start to decrease at a consistent slight negative slope.

2.2.3 Normalization of MR Fluid Torque Measurements with MR Fluid Volume Ratio

Next, all of the 10mL torque data from the diluted MR fluid mixtures will be normalized with the MR fluid volume ratio to scale with the pure MR fluid. For example, the 50% MR fluid mixture contains half as much magnetic material as the pure MR fluid. Therefore, the 50% MR fluid mixture torque data will be multiplied by two to compare with the pure MR fluid torque results.

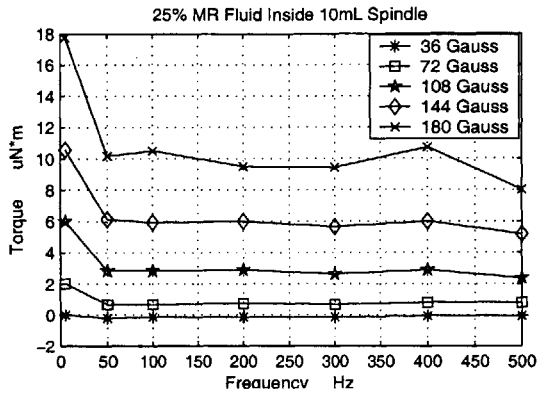

Figure 2-25: Torque measurements for the 25% MR fluid and 75% transformer oil inside of a 10mL spindle are plotted vs. magnetic field frequency. A sharp decrease in torque is experienced between 5 and 50 Hz. For frequencies larger than 50 Hz, the torque is essentially constant.

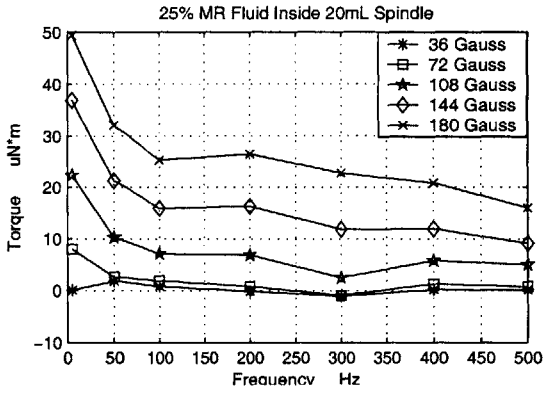

Figure 2-26: Torque measurements for the 25% MR fluid and 75% transformer oil inside of a 20mL spindle are plotted vs. magnetic field frequency. The consistent but negative slope indicates the torque decreasing as the frequency increases.

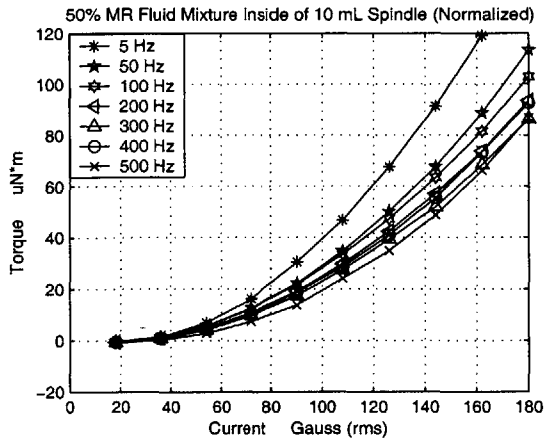

Figure 2-27: Torque measurements for the 50% MR fluid mixture in a 10 mL spindle is normalized with the MR fluid volume ratio and plotted versus the rotating magnetic field amplitude. This data correlates well with the pure MR fluid in Figure 2-6, as the torque is approximately equal at the same rotating magnetic field amplitude.

The normalized torque measurements are presented for the 50% and 25% MR fluid mixtures in Figures 2-27 and 2-28 respectively. The 50% MR fluid mixture when normalized by a factor of two makes a good fit to the pure MR fluid torque measurements. The two data sets agree to within approximately 10%. The 25% MR fluid mixture is normalized to the pure MR fluid by multiplying by a factor of four. However, the fit between the normalized 25% MR fluid mixture and pure MR fluid is not as close. The torque for the normalized 25% MR fluid mixture falls to about 30% of the value obtained with the pure MR fluid. This can be attributed to the fact that the magnetization of the 25% MR fluid shown in Figure 2-3 (c) saturates at approximately 1/17 the value of the pure MR fluid. Thus, in Figure 2-28, where the measured torque of the 25% MR fluid has been multiplied by 4 to scale with the torque measurements of the pure MR fluid in Figure 2-6, the normalized torque is still about a factor of 4 smaller than the pure MR fluid, and thus about 1/16 in absolute torque values, consistent with the 1/17 ratio of saturation magnetization measurements.

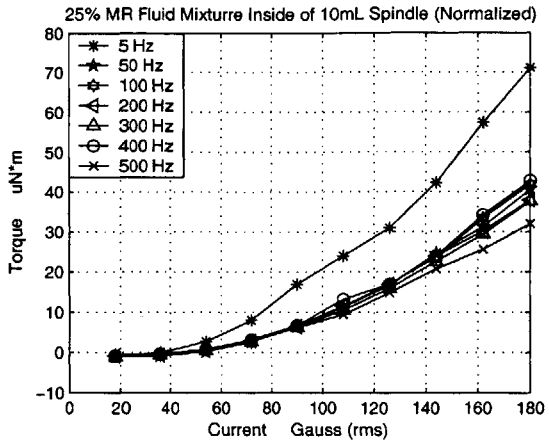

Figure 2-28: Torque measurements for the 25% MR fluid mixture is normalized with the MR fluid volume ratio and plotted versus the rotating magnetic field amplitude. This data does not correlate well with Figure 2-6, as the normalized torque is approximately 30% of the value measured for the pure MR fluid.

2.2.4 Comparison to Similar Ferrofluid Torque Measurements

The following ferrofluid torque data was obtained by the exact same procedure as the MR fluid torque measurements of this chapter. The only change made in the experiment is the substitution of a water based ferrofluid for the MR fluid mixture in the cylindrical spindle. The torque measurements are then obtained as described in Section 1.1.3. This ferrofluid data was collected by Chinnawat Surussavadee and Xiaowei He.

The torque measurements for a 10mL spindle filled with a water-based ferrofluid and plotted versus magnetic field amplitude and frequency are shown in Figures 1.26 and 1.27 respectively. It can be seen from these plots that the torque at a fixed magnetic field strength is increased for increasing frequency. For each fixed magnetic field strength, the torque increases to approximately twice its final value for increases in frequency from 100 to 500 Hz.

This ferrofluid data has been included to display the distinction between the ferrofluid's and the MR fluid's torque frequency dependencies. While the torque de-

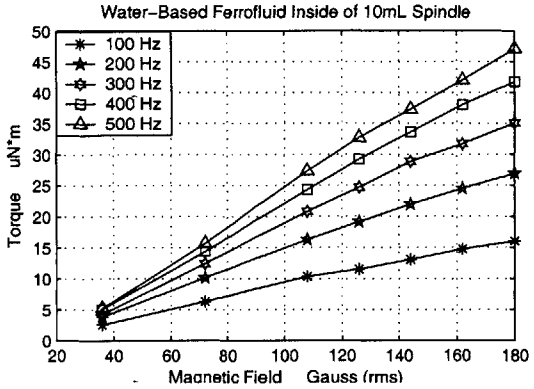

Figure 2-29: Torque measurements for a water-based ferrofluid inside of a 10mL spindle are plotted vs. the rotating magnetic field amplitude. The torque clearly increases with magnetic field frequency.

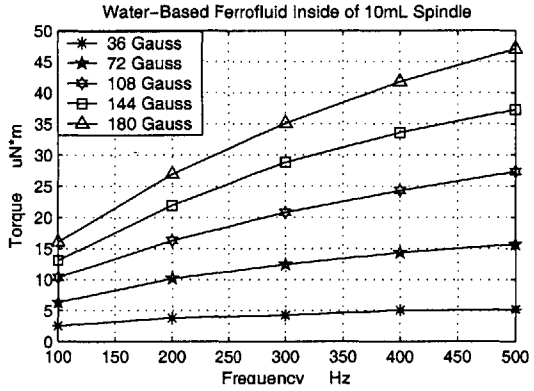

Figure 2-30: Torque measurements for a water-based ferrofluid inside of a 10mL spindle are plotted vs. the rotating magnetic field frequency. The torque clearly increases with magnetic field frequency.

creases as the frequency increases for all of the different MR fluid concentrations, the torque increases with frequency for the ferrofluid. This difference will be examined in the next section.

2.3 Theoretical Analysis

Previous researchers have calculated the body torque density acting on a planar magnetic fluid layer and magnetically stressed by a spatially uniform traveling wave magnetic field along the length of the layer [9, 12, 10, 11]. A similar analysis is presented for a cylindrical magnetic fluid layer and magnetically stressed by a uniform rotating magnetic field. The analysis is performed by carrying out the same calculations as was done for the planar layer, but now for a cylinder of magnetic fluid.

2.3.1 The Fluid Magnetization

The net magnetization of a magnetic fluid is $\mathbf{M} = N\mathbf{m}$, where $\mathbf{M}$ is the net magnetization of the magnetic fluid, $\mathbf{m}$ is the magnetic dipole moment of each magnetic fluid particle, and N is equal to the number of magnetic dipoles per unit volume. In the absence of an applied magnetic field, the magnetic moment of each particle is randomly oriented due to thermal agitation, resulting in a zero net magnetization of the fluid. In the presence of an applied magnetic field, the magnetic moment of each particle tends to align with the applied field. However, when $\mathbf{H}$ is rotating, the viscosity of the carrier fluid causes the magnetic moment of each particle, $\mathbf{m}$, to lag behind the magnetic field. This is shown pictorially in Figure 2-31. With $\mathbf{M}$ and $\mathbf{H}$ not collinear, there is a resulting body torque density acting on the fluid described by $\boldsymbol{\Gamma} = \mu_o(\mathbf{M} \times \mathbf{H})$. It is this body torque density that we wish to calculate.

The time it takes for a magnetic moment $\mathbf{M}$ to spatially reorient with an applied magnetic field, $\mathbf{H}$, is called the magnetic relaxation time constant, τ. The magnetization constitutive law for an incompressible magnetic fluid traveling at velocity $\mathbf{v}$

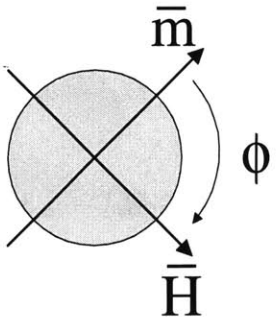

Figure 2-31: The viscosity of the carrier fluid causes the magnetic moment to lag behind a rotating applied magnetic field.

and particle spin at angular velocity $\boldsymbol{\omega}$, is

$$\frac{\partial \mathbf{M}}{\partial t} + (\mathbf{v} \cdot \nabla)\mathbf{M} - \boldsymbol{\omega} \times \mathbf{M} + \frac{1}{\tau}(\mathbf{M} - \chi_o \mathbf{H}) = 0 \tag{2.1}$$

where χ_o is the effective magnetic susceptibility. In general, χ_o can be magnetic field dependent, however, it may be taken as being constant for magnetic fields well below the saturation magnetization of the fluid. For the cylindrical spindle experiments of this chapter, $\mathbf{v}$ may only be ϕ directed, and $\boldsymbol{\omega}$ may only be z directed

$$\mathbf{v} = v_\phi \mathbf{i}_\phi, \qquad \boldsymbol{\omega} = \omega_z \mathbf{i}_z. \tag{2.2}$$

By applying a uniform rotating magnetic field, we may assume that $\mathbf{H}$ and $\mathbf{M}$ will take the following form,

$$\mathbf{H} = H_r(r, \phi, t)\mathbf{i}_r + H_\phi(r, \phi, t)\mathbf{i}_\phi, \tag{2.3}$$

$$\mathbf{M} = M_r(r, \phi, t)\mathbf{i}_r + M_\phi(r, \phi, t)\mathbf{i}_\phi. \tag{2.4}$$

Substituting Eq. 2.3 and Eq. 2.4 into Eq. 2.1, yields an equation relating the

components of **M** to the components of **H**. These relations are

$$\frac{\partial M_r}{\partial t} + \frac{v_\phi}{r}(\frac{\partial M_r}{\partial \phi} - M_\phi) + \omega_z M_\phi + \frac{M_r}{\tau} = \frac{\chi_o}{\tau} H_r \tag{2.5}$$

$$\frac{\partial M_\phi}{\partial t} + \frac{v_\phi}{r}(\frac{\partial M_\phi}{\partial \phi} + M_r) - \omega_z M_r + \frac{M_\phi}{\tau} = \frac{\chi_o}{\tau} H_\phi. \tag{2.6}$$

By assuming that **H** and **M** are uniformly rotating in the ϕ direction in the sinusoidal steady state, we may convert the above partial differential equations into simpler algebraic equations. Under these conditions, **H** and **M** take the form,

$$\mathbf{H} = \Re\{[\hat{H}_r(r)\mathbf{i}_r + \hat{H}_\phi(r)\mathbf{i}_\phi]e^{j(\Omega t - \phi)}\}, \tag{2.7}$$

$$\mathbf{M} = \Re\{[\hat{M}_r(r)\mathbf{i}_r + \hat{M}_\phi(r)\mathbf{i}_\phi]e^{j(\Omega t - \phi)}\}, \tag{2.8}$$

where Ω is the radian frequency of the sinusoidally varying magnetic fields. The "hat" character denotes a complex amplitude which only depends on r for the present case. Therefore, the r dependence will be considered implicit for the remainder of this section since all complex amplitude quantities are only r dependent.

Now making the sinusoidal steady state substitutions into Eqs. 2.5 and 2.6 yields the algebraic relations between the magnetic field and the fluid magnetization.

$$[\frac{1}{\tau} + j(\Omega - \frac{v_\phi}{r})]\hat{M}_r + [\omega_z - \frac{v_\phi}{r}]\hat{M}_\phi = \frac{\chi_o}{\tau}\hat{H}_r \tag{2.9}$$

$$[\frac{v_\phi}{r} - \omega_z]\hat{M}_r + [\frac{1}{\tau} + j(\Omega - \frac{v_\phi}{r})]\hat{M}_\phi = \frac{\chi_o}{\tau}\hat{H}_\phi \tag{2.10}$$

We may now solve for the components of the fluid net magnetization as

$$\hat{M}_r = \frac{\chi_o\{[1 + j(\Omega\tau - \frac{\tau v_\phi}{r})]\hat{H}_r + (\frac{\tau v_\phi}{r} - \omega_z\tau)\hat{H}_\phi\}}{[\omega_z\tau - \frac{\tau v_\phi}{r}]^2 + [1 + j(\Omega\tau - \frac{\tau v_\phi}{r})]^2} \tag{2.11}$$

$$\hat{M}_\phi = \frac{\chi_o\{[1 + j(\Omega\tau - \frac{\tau v_\phi}{r})]\hat{H}_\phi + (\omega_z\tau - \frac{\tau v_\phi}{r})\hat{H}_r\}}{[\omega_z\tau - \frac{\tau v_\phi}{r}]^2 + [1 + j(\Omega\tau - \frac{\tau v_\phi}{r})]^2}. \tag{2.12}$$

2.3.2 Magnetic Body Torque Density

When $\mathbf{H}$ and $\mathbf{M}$ are not collinear, there is a resulting magnetic body torque density given by $\mathbf{\Gamma} = \mu_o(\mathbf{M} \times \mathbf{H})$ acting on the magnetic fluid. Because $\mathbf{H}$ and $\mathbf{M}$ only have components in the $\mathbf{i}_r$ and $\mathbf{i}_\phi$ directions, the resulting body torque is only $\mathbf{i}_z$ directed, and is given by,

$$\Gamma_z = \mu_o(M_r H_\phi - M_\phi H_r). \tag{2.13}$$

It will be convenient to express each quantity in a dimensionless form that will be indicated with tildes. Time will be normalized to the magnetic relaxation time constant τ, space is normalized to the cylinder of radius R, and magnetic field quantities are normalized to an arbitrary magnetic field strength H_o.

$$\tilde{\mathbf{H}} = \frac{\hat{\mathbf{H}}}{H_o}, \qquad \tilde{\mathbf{M}} = \frac{\hat{\mathbf{M}}}{H_o}, \qquad \tilde{\mathbf{\Gamma}} = \frac{\mathbf{\Gamma}}{\mu_o H_o^2} \tag{2.14}$$

$$\tilde{\Omega} = \Omega\tau, \qquad \tilde{\mathbf{v}} = \frac{\tau}{R}\mathbf{v}, \qquad \tilde{\boldsymbol{\omega}} = \boldsymbol{\omega}\tau \tag{2.15}$$

Using Eq. 2.14 and Eq. 2.13 and taking the time average of the torque yields,

$$< \tilde{\Gamma}_z >= \frac{1}{2}\Re\{\tilde{M}_r \tilde{H}_\phi^* - \tilde{M}_\phi \tilde{H}_r^*\} \tag{2.16}$$

where the * character denotes the complex conjugate. Now using the normalized quantities together with Eqs. 2.11 and 2.12, we may now express the magnetic body torque density in terms of the applied field as

$$\begin{aligned} < \tilde{\Gamma}_z > = \frac{\chi_o}{2}\Big\{ & (\tilde{v_\phi} - \tilde{\omega_z})[(\tilde{\omega_z} - \tilde{v_\phi})^2 - (\tilde{\Omega} - \tilde{v_\phi})^2 + 1](|\tilde{H}_r|^2 + |\tilde{H}_\phi|^2) \\ & + \Re\{[\tilde{\omega_z}^2 + 2\tilde{v_\phi}^2 + \tilde{\Omega}^2 - 2\tilde{v_\phi}(\tilde{\omega_z} + \tilde{\Omega}) + 1 \\ & + j(\tilde{\Omega} - \tilde{v_\phi}) \cdot (\tilde{\omega_z}^2 - \tilde{\Omega}^2 - 1 + 2\tilde{v_\phi}(\tilde{\Omega} - \tilde{\omega_z}))][\tilde{H}_r \tilde{H}_\phi^* - \tilde{H}_r^* \tilde{H}_\phi]\}\Big\} \\ & \overline{(\tilde{\omega_z}^2 + 2\tilde{v_\phi}(\tilde{\Omega} - \tilde{\omega_z}) - \tilde{\Omega}^2 + 1)^2 + 4(\tilde{\Omega}^2 + \tilde{v_\phi}^2 - 2\tilde{\Omega}\tilde{v_\phi})} \end{aligned} \tag{2.17}$$

The order of $\tilde{\Omega}$ in the numerator is 3, and in the denominator is 4; therefore, as $\tilde{\Omega}$ becomes large, the magnetic body torque density is proportional to $\frac{\tilde{\Omega}^3}{\tilde{\Omega}^4} = \frac{1}{\tilde{\Omega}}$.

This shows that the measured torque for magnetic fluid will increase with frequency up to a breakpoint frequency, $\Omega_b \sim \frac{1}{\tau}$. Above Ω_b, the torque decreases with frequency. For 10 nm diameter ferrofluid particles, $\tau \sim 10^{-6} - 10^{-5}$ seconds (Brownian relaxation time) [16], such that Ω_b, is much larger than the range of our experimental apparatus, $f_b = \frac{\Omega_b}{2\pi} \sim 16 - 160$kHz [2].

The magnetic relaxation time constant, τ, increases with particle volume and thus with the cube of the particle diameter. The MR fluid particles are typically about 10μm in diameter, or 10^3 times larger than the ferrofluid particles. Therefore, the magnetic relaxation time constant increases by about a factor of 10^9, so that Ω_b decreases by a factor of about 10^9 corresponding to $f_b \sim 10^{-5} - 10^{-4}$ Hz for the MR fluid. Thus in our ferrofluid experiment, we were operating below Ω_b, so that torque increased with frequency. With our MR fluid torque experiments, we were operating greatly above Ω_b where the torque decreases with frequency. This is the likely qualitative explanation for the different measured torque variation with frequency between the ferrofluid and the MR fluid mixtures.

2.4 Discussion

The MR fluid mixtures generate a significant torque on a stationary spindle when excited by a uniform rotating magnetic field. This demonstrates that the magnetization vector lags the rotating magnetic field in the MR fluid. These torques are also due only to volumetric effects, because the top of the spindle is enclosed such that no free top surface exists.

The generated torques are in the same direction as the rotating magnetic field for both ferrofluids and MR fluids. As the rotating magnetic field amplitude is increased, the torque generated also increased. However, the torque decreases for increasing magnetic field frequency in MR fluids and increased with magnetic field frequency for ferrofluids [1]. This is a clear distinction between the dependence of the torque on frequency for the MR fluid mixtures and the ferrofluids.

By calculating the dependence of the magnetic torque density on the applied

magnetic field frequency, the different torque frequency dependence between the two fluids becomes evident. There is a critical magnetic field frequency $f_b \sim \frac{1}{2\pi\tau}$, such that the torque will decrease with frequency when measurements are taken above f_b (MR fluids), and increase with frequency when measurements are taken below f_b (ferrofluids). This critical magnetic field strength depends on the magnetic relaxation time constant τ which is proportional to the particle volume. Therefore, by this qualitative model, this distinction between the ferrofluids and the MR fluids is primarily due to the different particle sizes in each of the fluids.

Chapter 3

Spiral Flows and Phase Transitions of Ferrofluid Drops

When a fluorocarbon based ferrofluid drop is excited by simultaneously applied uniform rotating and DC axial magnetic fields, a phase like transition occurs. The ferrofluid drop is contained inside of a Hele-Shaw cell, two glass plates separated by a thin gap. The ferrofluid is surrounded with a 50% isopropyl alcohol/ 50% deionized water mixture to prevent the ferrofluid from wetting the glass plates. The rotating magnetic field sets the single ferrofluid drop in motion, co-rotating with the applied magnetic field. An axial DC magnetic field is then added to the configuration that at a critical value causes the ferrofluid drop to expand until the transition occurs. The transition consists of a single large rotating ferrofluid drop morphing into many smaller rotating ferrofluid drops. This instability was first observed by Cory Lorenz in the summer of 2002 at The Laboratory for Electromagnetic and Electronic Systems, MIT [3]. If the application of the magnetic fields are reversed, spirals are formed. The application of the DC axial magnetic field causes a labyrinth pattern, and subsequent application of rotating magnetic field causes the legs of the labyrinth to curl upon themselves from viscous shear forming the spirals.

A preliminary minimum free-energy analysis will be outlined that will model the phase transition. By considering the evolution of the ferrofluid drop to be idealized as a transition into N smaller drops, a calculus of minimization can be performed on

the total energy of the configuration to determine N, the number of smaller ferrofluid drops, and the critical DC axial magnetic field strength for the transition to occur.

Experiments are conducted to show the evolution of the ferrofluid drop as the DC axial magnetic field strength is increased, for fixed Hele-Shaw cell separation gap, and rotating magnetic field amplitude and frequency. Because this instability is very sensitive to experiment parameters, the parameters involved will only cover a small range. Three different Hele-Shaw cell separation gap distances are used: 0.9 mm, 1.15 mm, and 1.40 mm. The rotating magnetic field amplitudes range from 17.1 to 96.9 Gauss (rms), and the frequency ranges covered are from 20 to 40 Hz. The DC axial magnetic field is ranged from 0 to 335 Gauss [21, 22].

3.1 Introduction

A typical transition is shown in Figure 3-1. From this figure, we can see that the surface area of the ferrofluid drop increases with increasing axial magnetic field strength up to a threshold magnetic field strength, H_t. When the axial magnetic field reaches H_t, the ferrofluid drop morphs into many smaller ferrofluid drops surrounded by a ferrofluid ring that encompasses the smaller ferrofluid drops. In general, this ring may form "fingers" as shown in Figure 3-1 (f). These fingers always curl in the direction of the applied rotating magnetic field. For large in-plane rotating magnetic field strengths these "fingers" may form spirals.

These phase transitions do not always result in the interior of the single large ferrofluid drop morphing into smaller ferrofluid drops. For low in-plane rotating magnetic field strengths, the transition results in most of the ferrofluid creating the "fingers" around the exterior of the drop, leaving little fluid to morph when the axial magnetic field rises above the threshold, H_t. Examples of this behavior is shown in Figure 3-2.

For large rotating magnetic field strengths, the phase transition becomes unstable, resulting in stochastic behavior. At times the ferrofluid drop may tear apart into a mass of smaller spinning ferrofluid shapes, and other times, the interior of the

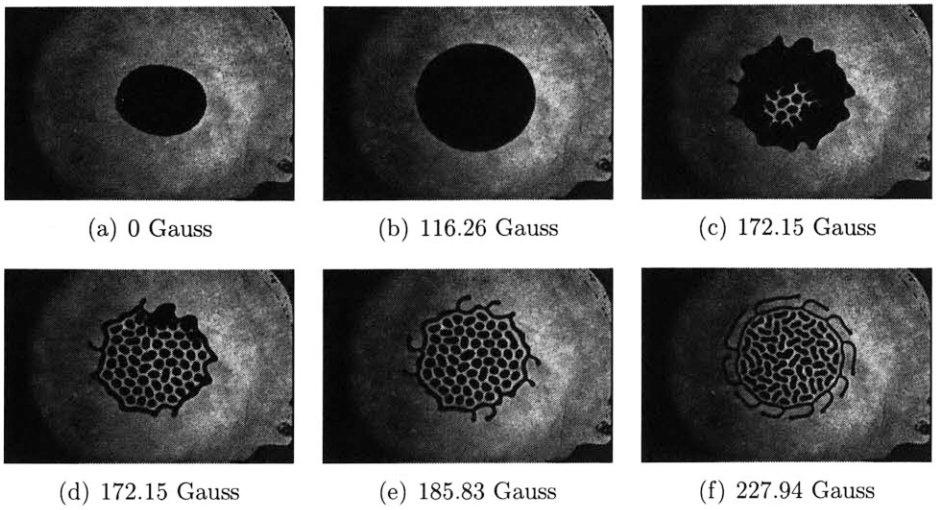

(a) 0 Gauss (b) 116.26 Gauss (c) 172.15 Gauss

(d) 172.15 Gauss (e) 185.83 Gauss (f) 227.94 Gauss

Figure 3-1: An example of a typical ferrofluid phase transition is shown above. The Hele-Shaw cell separation gap is 1.15 mm, and the ferrofluid volume is 200 μl. The in-plane clockwise rotating magnetic field amplitude is fixed at 39.9 Gauss (rms), and the frequency is fixed at 25 Hz. The DC axial magnetic field is slowly increased and is labeled on each picture above.

ferrofluid will morph into a series of spirals. Examples of this behavior can be seen in Figure 3-3.

3.2 Theoretical Analysis

A minimum energy analysis, like that used in modeling ferrofluid labyrinth phenomena [18], is performed to model the transition of the ferrofluid droplet into many smaller droplets. The idealized energy minimization model of the transition considers the ferrofluid drop to be a large cylinder of radius R and height t that breaks up into N smaller cylinders of radius r and height t. This is shown schematically in Figure 3-4. We assume that the drops are spaced far enough apart that they are not magnetically interacting.

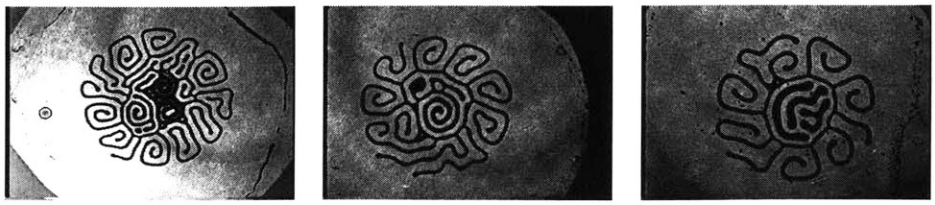

(a) 0.9 mm Gap, 25 Hz, 39.9 Gauss (rms), 231 Gauss DC

(b) 1.15 mm Gap, 20 Hz, 24.7 Gauss (rms), 166 Gauss DC

(c) 1.4 mm Gap, 30 Hz, 17.1 Gauss (rms), 179 Gauss DC

Figure 3-2: Typical transitions are presented at small clockwise rotating magnetic field strengths with 200 μl of ferrofluid. When the rotating magnetic field amplitude is small, the ferrofluid drop does not morph into smaller drops, but grows longer "fingers" and morphs into ferrofluid lines and spirals.

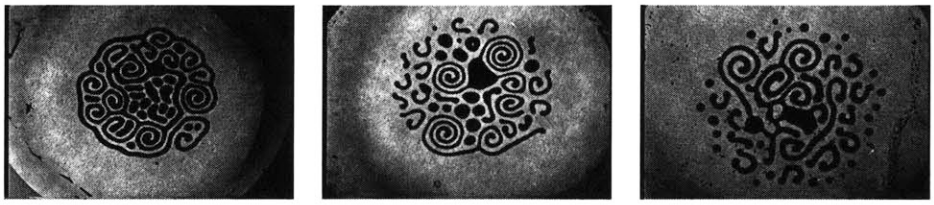

(a) 0.9 mm Gap, 25 Hz, 96.9 Gauss (rms), 227 Gauss DC

(b) 1.15 mm Gap, 35 Hz, 39.9 Gauss (rms), 160 Gauss DC

(c) 1.4 mm Gap, 40 Hz, 32.3 Gauss (rms), 172 Gauss DC

Figure 3-3: Typical transitions are presented for large clockwise rotating magnetic field strengths with 200 μl of ferrofluid. When the rotating magnetic field amplitude is high, the ferrofluid drop does not morph into smaller drops, but it becomes unstable and morphs into many smaller objects as shown above.

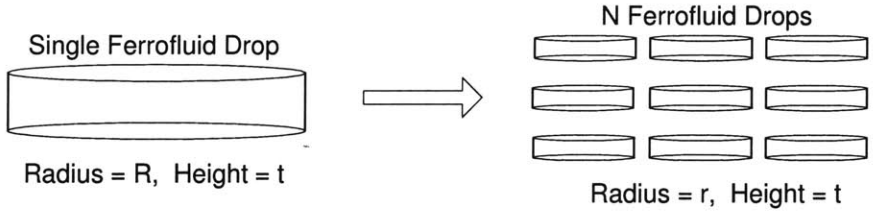

Figure 3-4: Schematic of the ferrofluid drop transitioning from a continuous phase to a discrete phase.

3.2.1 Demagnetization Theory

At low magnetic fields, the magnetization $\mathbf{M}$ of a ferrofluid is proportional to the applied magnetic field $\mathbf{H}$ inside the ferrofluid, $\mathbf{M} = \chi\mathbf{H}$. The constant of proportionality is known as the magnetic susceptibility of the material and is denoted by χ. When $\mathbf{M}$ is linear with $\mathbf{H}$ through the constant χ, we may conclude that $\mathbf{M}$ and $\mathbf{H}$ have no divergence, or

$$\nabla \cdot \mathbf{B} = \nabla \cdot \mu_0(1+\chi)\mathbf{H} = \nabla \cdot \mathbf{H} = \nabla \cdot \mathbf{M} = 0. \tag{3.1}$$

However, the magnetic field inside the ferrofluid differs from the applied magnetic field outside of the material $\mathbf{H_0}$ by the demagnetization field $\mathbf{H_d}$. Thus,

$$\mathbf{H} = \mathbf{H_0} + \mathbf{H_d} = \mathbf{H_0} - D\mathbf{M}. \tag{3.2}$$

Eq. 3.2 is strictly true for ellipsoid shapes where D is constant so that H is uniform inside the ferrofluid. Special cases of ellipsoid shapes include spheres, prolate and oblate spheroids, and infinitely long cylinders and planes. For non-ellipsoidal shapes, we will take Eq. 3.2 as an approximation, recognizing that the "field inside" non-ellipsoidal shapes is spatially dependent.

The demagnetization field results from an effective magnetic surface charge induced on the surface of the magnetic material. Noting that D is given by $\mathbf{H_d} = -D\mathbf{M}$, we can find D by solving for the demagnetization field in terms of the magnetization for a magnetized cylinder of ferrofluid. When the radius of the ferrofluid drop is much larger than the height, as was the case in our experiments, the droplet may be approximated by an oblate spheroid. With this approximation, we can assume that the magnetization is essentially uniform within the bulk of the material and thus has no divergence. Therefore, $\mathbf{H_d}$ results solely from the effective magnetic surface charge σ_m present on the faces of the cylinder of ferrofluid. This surface charge is then given by,

$$\sigma_m = -\mathbf{n} \cdot (\mu_0\mathbf{M}) = \pm\mu_0 M \tag{3.3}$$

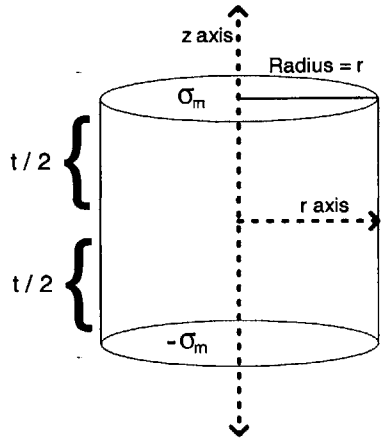

Figure 3-5: Schematic of the magnetic field inducing an effective magnetic surface charge of $\sigma_m = \pm\mu_0 M$ on the top and bottom faces of the ferrofluid cylinder.

where the plus sign refers to the upper face, the minus sign refers to the lower face of the cylinder, and M is the amplitude of $\mathbf{M}$ when $\mathbf{M}$ is normal to the ferrofluid interface. Because no current density exists in the region of the ferrofluid, Ampere's Law reduces to $\nabla \times \mathbf{H_d} = 0$. Because the curl of the demagnetization field is zero, we will represent this field as the negative gradient of a magnetic scalar potential ψ, or $\mathbf{H_d} = -\nabla\psi$. Therefore, by making an analogy to electrostatics, we may solve for the magnetic potential along the $r = 0$ symmetry line by using the superposition integral and noting that $-\frac{1}{2} < \frac{z}{t} < \frac{1}{2}$ when examining regions inside the fluid cylinder. Thus the magnetic potential for a drop of radius r is,

$$\begin{aligned}\psi &= \frac{1}{4\pi\mu_0}\int_0^{2\pi}\int_0^{r}\sigma_m\left[\frac{1}{\sqrt{r'^2+(z-\frac{t}{2})^2}}-\frac{1}{\sqrt{r'^2+(z+\frac{t}{2})^2}}\right]r'dr'd\theta \\ &= \frac{Mt}{2}\left(\sqrt{\left(\frac{r}{t}\right)^2+\left(\frac{z}{t}-\frac{1}{2}\right)^2}-\sqrt{\left(\frac{r}{t}\right)^2+\left(\frac{z}{t}+\frac{1}{2}\right)^2}+\frac{2z}{t}\right). \qquad (3.4)\end{aligned}$$

Now we solve for the demagnetization field by $\mathbf{H_d} = -\nabla\psi$, where the minus sign is present to make the field lines point from high to low magnetic potential. Therefore

the demagnetization field along the $r = 0$ symmetry line is,

$$\mathbf{H_d} = -\frac{\partial \psi}{\partial z}\mathbf{i_z} = -\frac{M}{2}\left(\frac{\frac{z}{t}-\frac{1}{2}}{\sqrt{\left(\frac{r}{t}\right)^2+\left(\frac{z}{t}-\frac{1}{2}\right)^2}} - \frac{\frac{z}{t}+\frac{1}{2}}{\sqrt{\left(\frac{r}{t}\right)^2+\left(\frac{z}{t}+\frac{1}{2}\right)^2}} + 2\right)\mathbf{i_z} \tag{3.5}$$

The demagnetization field is approximated as being uniform within the fluid drop with the value it takes at $z = 0$,

$$\mathbf{H_d} \approx \mathbf{H_d}(z=0) = M\left(\frac{1}{2\sqrt{\left(\frac{r}{t}\right)^2+\left(\frac{1}{2}\right)^2}} - 1\right) \tag{3.6}$$

Now that we have solved for the demagnetization field in terms of the magnetization of the fluid drop, we may use the fact that $\mathbf{H_d} = -D\mathbf{M}$ to solve for the demagnetization coefficient,

$$D = 1 - \frac{1}{\sqrt{\left(\frac{2r}{t}\right)^2+1}} \tag{3.7}$$

As a check, we examine the limits as $r \to \infty$ and $t \to \infty$. As $r \to \infty$, $D = 1$ which is the demagnetization coefficient for a planar layer of infinite extent in a magnetic field applied parallel to the normal. As $t \to \infty$, we obtain $D = 0$, which is the demagnetization coefficient for an infinitely long cylinder in an axial magnetic field.

3.2.2 Minimization of Energy

By considering the total energy in the ferrofluid configuration to be composed of only interfacial energy U_S and the magnetic energy U_M as in Eq. 3.8, a minimization of energy is performed to determine the number N of smaller ferrofluid cylinders that result for different experiment conditions.

$$U_T = U_S + U_M \tag{3.8}$$

The interfacial energy is the energy stored in the geometrical configuration of the fluid drop that holds the drop together, and it is given by Eq. 3.9 for N ferrofluid

cylinders, each of radius r where γ is the interfacial surface tension.

$$U_S = 2\pi N r t \gamma \tag{3.9}$$

Also, the magnetization energy stored in N ferrofluid cylinders is given in Eq. 3.10,

$$U_M = -\frac{\mu_0}{2}\int_V \mathbf{M}\cdot\mathbf{H_0} dV = -\frac{\mu_0}{2}\frac{N\pi r^2 t\chi H_0^2}{1+\chi D} \tag{3.10}$$

where V is the volume of the N ferrofluid cylinders [6].

By idealizing the ferrofluid to be a single cylinder of radius R that breaks into N smaller cylinders of radius r, conservation of mass requires that the volume of ferrofluid be the same before and after the transition, or

$$\pi R^2 t = N\pi r^2 t \qquad \Rightarrow \qquad R = \sqrt{N} r \tag{3.11}$$

Substituting Eq. 3.11 into Eqs. 3.9 and 3.10 yields expressions for the interfacial and magnetization energy in terms of the radius of the original single large cylinder with radius R.

$$U_S = 2\pi R t \gamma \sqrt{N} \tag{3.12}$$

$$U_M = -\frac{\mu_0}{2}\frac{\pi R^2 t\chi H_0^2}{1+\chi D} \tag{3.13}$$

Using Eqs. 3.7 and 3.11, D in Eq. 3.13 is given by,

$$D = 1 - \frac{1}{\sqrt{\frac{1}{N}\left(\frac{2R}{t}\right)^2 + 1}}. \tag{3.14}$$

Thus, the total energy U_T stored in the configuration is the sum of the interfacial and magnetization energies; therefore, with D as in Eq. 3.14, U_T can be expressed as

$$U_T = U_S + U_M = 2\pi R t\gamma\sqrt{N} - \frac{\frac{\mu_0}{2}\pi R^2 t\chi H_0^2}{1+\chi\left(1-\frac{1}{\sqrt{\frac{1}{N}\left(\frac{2R}{t}\right)^2+1}}\right)}. \tag{3.15}$$

This can be expressed in terms of non-dimensionalized quantities,

$$\hat{U}_T = \sqrt{N} - \frac{\frac{1}{2}\hat{R}\chi N_B}{1+\chi\left(1-\frac{1}{\sqrt{\frac{1}{N}\left(\frac{2R}{t}\right)^2+1}}\right)} \tag{3.16}$$

where we have defined the non-dimensional energy $\hat{U}_T$, the non-dimensional radius $\hat{R}$, and the magnetic bond number N_B as,

$$\hat{U}_T = \frac{U_T}{2\pi R t\gamma} \qquad N_B = \frac{\mu_0 H_0^2 t}{2\gamma} \qquad \hat{R} = \frac{R}{t}. \tag{3.17}$$

By finding the value of N such that the energy of the system is minimized, we can determine the number of smaller drops that will result from one larger drop. This minimization of the total energy is shown in Eq. 3.18,

$$\frac{\partial \hat{U}_T}{\partial N} = \frac{1}{2}\left[\frac{1}{\sqrt{N}} - \frac{\chi^2\hat{R}^3 N_B}{4N^2\left(\frac{\hat{R}^2}{N}+\frac{1}{4}\right)^{\frac{3}{2}}\left(1+\chi\left(1-\frac{1}{\sqrt{\frac{(2\hat{R})^2}{N}+1}}\right)\right)^2}\right] = 0 \tag{3.18}$$

Then the magnetic bond number at equilibrium is,

$$N_B = 4\left(1+\frac{N}{4\hat{R}^2}\right)^{\frac{3}{2}}\left(\frac{1}{\chi}+1-\frac{1}{\sqrt{\frac{(2\hat{R})^2}{N}+1}}\right)^2 \tag{3.19}$$

Figure 3-6 plots N_B versus N for various values of $\hat{R}$ and with $\chi \approx 3$ as the measured value of the magnetic susceptibility for the flourocarbon ferrofluid [23]. This plot illustrates that there exist a minimum value of the magnetic bond number N_B^{min}, beneath which no solution exists for any value of N. The general expression for N located at N_B^{min} is found by performing a calculus of minimization on N_B and is

$$N = \frac{2\hat{R}^2}{3(1+2\chi)}\left(\chi^2-6\chi-3+(1+\chi)\sqrt{\chi^2+18\chi+9}\right). \tag{3.20}$$

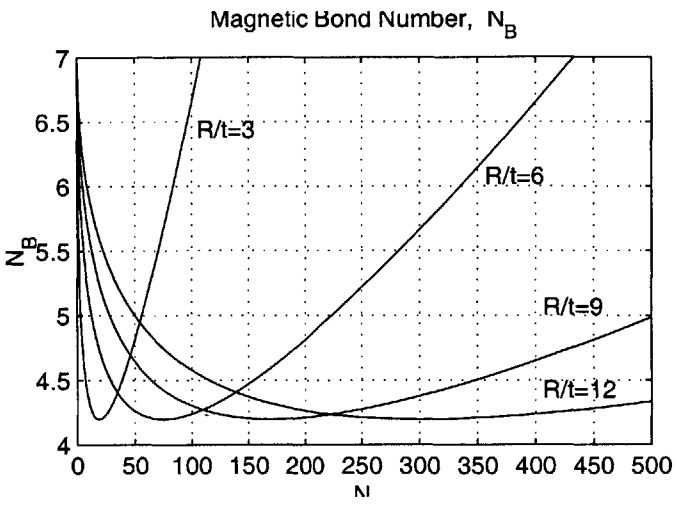

Figure 3-6: A plot of the magnetic bond number N_B versus the number of smaller ferrofluid droplets N for various values of R/t. $\chi \approx 3$

By placing this expression in Eq. 3.19, N_B^{min} may be expressed in terms of χ alone as

$$N_B^{min} = 4\left(1+\frac{1}{\chi}-\frac{2\chi\sqrt{2}}{5\chi^2+18\chi+9+3(1+\chi)\sqrt{\chi^2+18\chi+9}}\right)^2 \cdot \left(\frac{\chi^2+6\chi+3+(1+\chi)\sqrt{\chi^2+18\chi+9}}{6(1+2\chi)}\right)^{3/2}. \quad (3.21)$$

By placing this expression in Eq. 3.17, the threshold axial magnetic field B_t for the transition to occur may be expressed in terms of χ, t, and γ. A plot of N versus $\hat{R}$ for various values of χ is given in Figure 3-7, and a plot of B_t versus χ for various values of t is given in Figure 3-8.

3.3 Results

Experiments were conducted to determine the number of smaller ferrofluid drops N that result from the single larger ferrofluid drop, the threshold axial magnetic field strength, H_t, for the transition to occur, and the surface area of each ferrofluid cylindrical droplet as the DC axial magnetic field is raised. These experiments were

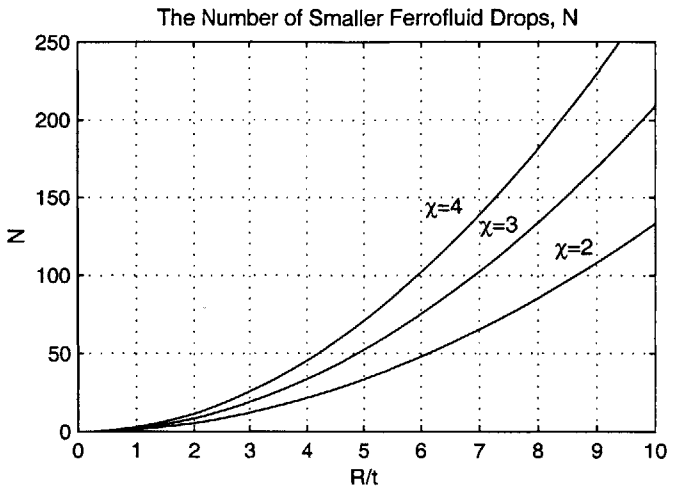

Figure 3-7: A plot of the number of smaller ferrofluid droplets N that result from the transition versus $\hat{R}$ for various values of χ.

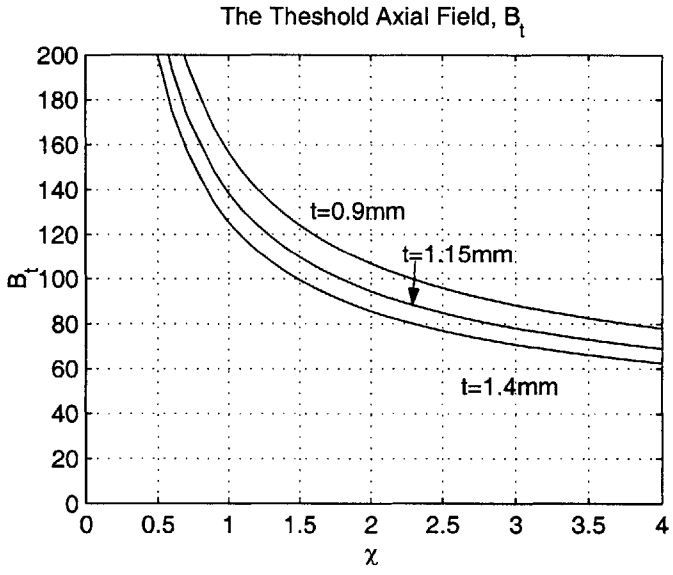

Figure 3-8: A plot of the threshold axial magnetic field B_t that results in the transition occurring versus the magnetic susceptibility χ for various values of t.

conducted for various in-plane rotating magnetic field strengths and frequencies. The Hele-Shaw cell separation gaps used in these experiments were 0.9 mm, 1.15 mm, and 1.4 mm. The rotating field frequency covers from 20 to 40 Hz in 5 Hz increments, and the rotating field strength ranges from 17.1 to 96.9 Gauss (rms) in 3.8 Gauss (rms) increments, corresponding to 0.1 ampere (rms) balanced current changes in the stator winding that produces the rotating magnetic field. Each experiment does not cover this entire range of rotating magnetic field frequencies and amplitudes, but only the range in which the transition occurs. The experiments would start being recorded when the transition would exhibit those characteristics of low rotating magnetic field strengths shown in Figure 3-2, and stop being recorded when the transition resembled those characteristics of large rotating magnetic field strengths shown in Figure 3-3.

For these experiments, the rotating Hele-Shaw cell separation gap, and magnetic field frequency and amplitude are fixed. The DC axial magnetic field is then increased until the transition occurs will being recorded in Labview as it changes in time. The experiment is recorded using a Panasonic KR222 analog video camara. During the analysis of the data, the value of the DC axial magnetic field at any specific point in time must be known. In order to synchronize the video recording and Labview, the video camera was set to start recording, and an object was placed over the camera lense. At the exact time that the run button is pushed in Labview to start recording the DC axial magnetic field, the object is removed from in front of the camera lense. This way the reference to the beginning of the experiment for both recording devices are synchronized. The labview program may be found in Appendix C.

3.3.1 N and H_t

In this section, the measured number of smaller ferrofluid drops N, that result from the transition and the threshold axial magnetic field H_t, that causes the transition are plotted versus the experiment parameters. However, as described in Section 3.1, the experiment is very sensitive to the parameters. Therefore, some of the transitions that occurred did not produce distinguishable smaller drops as the example in Figure 3-1 did. Thus, the data collected for N, only shows the experiments in which the

drop morphed into a countable number of smaller drops.

In almost all cases, the data shows that N increases with the rotating magnetic field amplitude and frequency, and decreases as the Hele-Shaw cell separation gap gets larger. The slope or rate of increase with respect to the rotating magnetic field strength dramatically increases as the separation gap is made smaller.

In Fig. 3-9, N is plotted versus the rotating magnetic field amplitude for various rotating magnetic field frequencies in a Hele-Shaw cell with a separation gap of 0.9 mm. The slope of each curve increases as the frequency is increased, meaning that changes in the applied rotating magnetic field strength by $\triangle H_r$ will result in a change in the number of droplets produced, $\triangle N$, that is larger at higher magnetic field frequencies.

In Fig. 3-11, N is plotted versus the rotating magnetic field amplitude for various rotating magnetic field frequencies for phase transitions that will occur in a Hele-Shaw cell with separation gap of 1.15 mm. The number of smaller droplets produced at a given rotating magnetic field strength clearly increases as the magnetic field frequency is increased. For the data obtained at 25 Hz, only one of the transitions resulted in a countable number of smaller ferrofluid droplets and is represented by the single * at approximately 40 Gauss (rms). Similarly, the data obtained at 35 Hz only produced two transitions with a countable number of droplets.

In Fig. 3-13, N is plotted versus the rotating magnetic field amplitude for various rotating magnetic field frequencies for phase transitions that will occur in a Hele-Shaw cell with separation gap of 1.4 mm. Only two frequencies produced a countable number of smaller ferrofluid droplets, 25 and 30 Hz. The transitions that occurred at other frequencies produced separate ferrofluid lines similar to the labyrinth instability; therefore, no data is reported for N at the other frequencies.

When compared to the calculated values for N in Figure 3-7, all of the measured values for N from the experiments fall below those calculated.

The plots for the threshold DC axial magnetic field strength shows a somewhat stochastic behavior. For the separation gap of 0.9 mm in Fig. 3-10, no trend is distinguishable. It appears as though the transition will occur at some random mag-

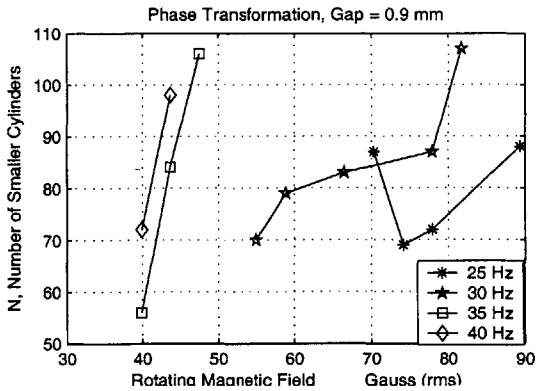

Figure 3-9: The measured number of smaller ferrofluid drops N that result from a single larger ferrofluid drop in a Hele-Shaw cell with a separation gap of t=0.9 mm is plotted versus the clockwise rotating magnetic field for various rotating magnetic field frequencies. The ferrofluid volume is 200 μl resulting in the radius of the large drop being R=8.40 mm. The DC axial magnetic field when the transition occurs is shown in Figure 3-10.

netic field strength within a bounded region. The separation gap of 1.15 mm in Fig. 3-12 still exhibits a very random pattern, but the plots all increase with the rotating magnetic field strength. For the separation gap of 1.4 mm in Fig. 3-14, the plots are much less stochastic. They are approximately constant over the range of rotating magnetic field strengths, but increase with the rotating magnetic field frequency. The measured value of the threshold axial magnetic fields for the experiments performed in this section is consistently larger than that calculated in Figure 3-8.

The discrepancy between measured and calculated values of N and B_t are attributed to the use of the assumption that the magnetization of the ferrofluid is linear with the applied field. Rather, the magnetization follows the Langevin relation for paramagnetic behavior. This would cause the magnetization M to be smaller than when a linear relationship is assumed.

3.3.2 Surface Area

The following summarizes and plots the surface area of ferrofluid drops as they evolve under an increasing applied DC axial magnetic field. As the DC axial field increases,

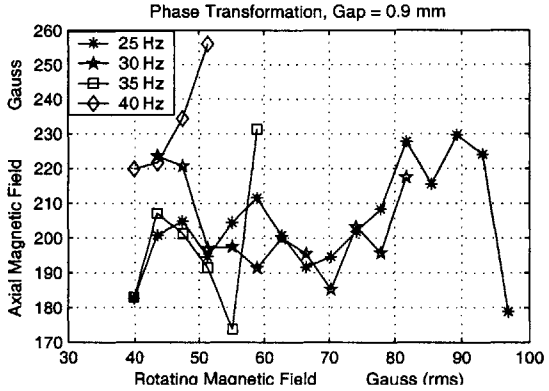

Figure 3-10: The measured threshold DC axial magnetic field strength $B_t = \mu_o H_t$ that results in the transition occurring in a Hele-Shaw cell with a separation gap of t=0.9 mm is plotted versus the clockwise rotating magnetic field for various rotating magnetic field frequencies. The ferrofluid volume is 200 μl resulting in the radius of the large drop being R=8.40 mm. The number of smaller ferrofluid droplets formed from the transition is shown in Figure 3-9.

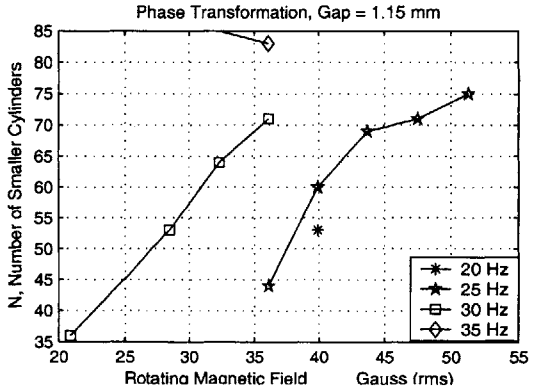

Figure 3-11: The measured number of smaller ferrofluid drops N that result from a single larger ferrofluid drop in a Hele-Shaw cell with a separation gap of t=1.15 mm is plotted versus the clockwise rotating magnetic field for various rotating magnetic field frequencies. The ferrofluid volume is 200 μl resulting in the radius of the large drop being R=7.45 mm. The DC axial magnetic field when the transition occurs is shown in Figure 3-12.

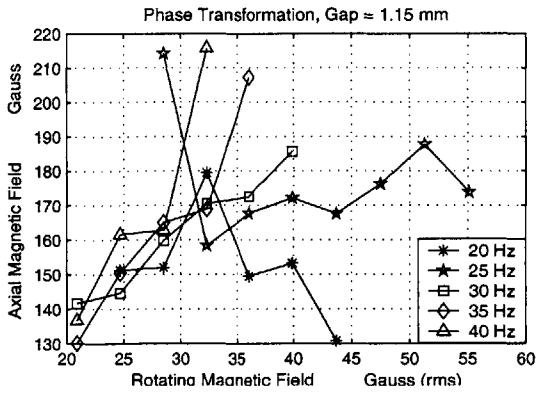

Figure 3-12: The measured threshold DC axial magnetic field strength $B_t = \mu_o H_t$ that results in the transition occurring in a Hele-Shaw cell with a separation gap of t=1.15 mm is plotted versus the clockwise rotating magnetic field for various rotating magnetic field frequencies. The ferrofluid volume is 200 μl resulting in the radius of the large drop being R=7.45 mm. The number of smaller ferrofluid droplets formed from the transition is shown in Figure 3-11.

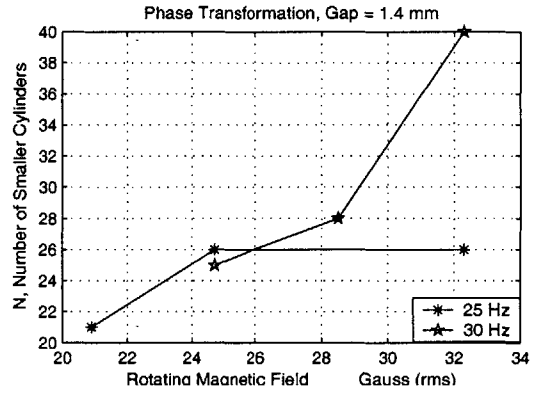

Figure 3-13: The measured number of smaller ferrofluid drops N that result from a single larger ferrofluid drop in a Hele-Shaw cell with a separation gap of t=1.4 mm is plotted versus the clockwise rotating magnetic field for various rotating magnetic field frequencies. The ferrofluid volume is 200 μl resulting in the radius of the large drop being R=6.74 mm. The DC axial magnetic field when the transition occurs is shown in Figure 3-14.

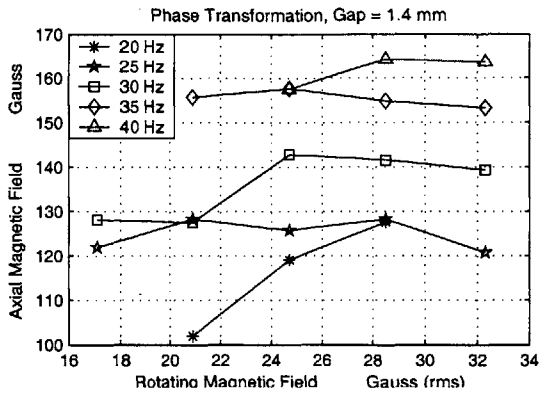

Figure 3-14: The measured threshold DC axial magnetic field strength $B_t = \mu_o H_t$ that results in the transition occurring in a Hele-Shaw cell with a separation gap of t=1.4 mm is plotted versus the clockwise rotating magnetic field for various rotating magnetic field frequencies. The ferrofluid volume is 200 μl resulting in the radius of the large drop being R=6.74 mm. The DC axial magnetic field when the transition occurs is shown in Figure 3-13.

the surface area of the ferrofluid drop grows until "cilia-like" features form as in Figure 3-1. After these features form the ferrofluid drop stops growing because the transition has already occurred, but a thin layer of ferrofluid remains covering the top surface. Then the thin layer abruptly peels away leaving the smaller ferrofluid droplets visable from above. The surface area was measured from the initial application of the DC axial magnetic field until the ferrofluid drop formed the "cilia-like" features. The surface area measurements are normalized with the initial surface area at 0 Gauss applied DC axial magnetic field when presented in this section.

The surface area was measured by analyzing each still frame picture in Adobe Photoshop. By increasing the contrast to 100%, the ferrofluid droplet was made to be completely black while all other areas of the photo were made to be completely white. Then, by invoking the histogram command, the percentage of black pixels in the photo can be found. Letting the value at 0 Gauss DC (no applied axial field) be our reference, the evolution of the ferrofluid drop as the axial DC field as increased is determined.

0.9 mm Gap

For all of the experiments conducted with a Hele-Shaw cell separation gap of 0.9 mm, the surface area grows at approximately the same rate with increasing DC axial magnetic field strength for each of the rotating magnetic field amplitudes.

In Fig. 3-15, the normalized surface area for the evolution of the ferrofluid drop, prior to the phase transition excited by a rotating magnetic field at frequency 25 Hz, is plotted versus the applied DC axial magnetic field for various rotating magnetic field amplitudes. The end-state of the transition for each rotating field amplitude is shown in Fig. 3-16. The surface area grows at approximately the same rate for all of the various rotating magnetic field amplitudes, but the normalized surface area measurements at lower rotating field strengths level off at lower DC axial fields. The surface area of the fluid drop stops increasing just before the transition occurs, signified in this plot by the slope of curve decreasing to approximately zero or the highest DC axial magnetic field at which a value is recorded for the surface area. The normalized surface area climbs to approximately 1.6 at 39.9 Gauss (rms) with DC axial magnetic field $\approx$ 106 Gauss and 2.2 at 96.9 Gauss (rms) with DC axial magnetic field $\approx$ 160 Gauss.

In Fig. 3-17, the normalized surface area for the evolution of the ferrofluid drop excited at 30 Hz is plotted versus the DC axial magnetic field for various rotating magnetic field amplitudes with the end-state of each transition shown in Figure 3-18. The range of rotating magnetic field amplitudes at which the transition occurs is narrower than the experiment at 25 Hz in Figures 3-15 and 3-16. The surface area grows to about 1.7 at 43.7 Gauss (rms) with the DC axial magnetic field $\approx$ 135 Gauss and approximately 2.25 at 81.7 Gauss (rms) with the DC axial magnetic field $\approx$ 160 Gauss.

In Fig. 3-19, the normalized surface area for the evolution of the ferrofluid drop excited at 35 Hz is plotted versus the DC axial magnetic field for various rotating magnetic field amplitudes with the end-state of each transition shown in Figure 3-20. The normalized surface area of the lowest rotating magnetic field amplitude of 39.9

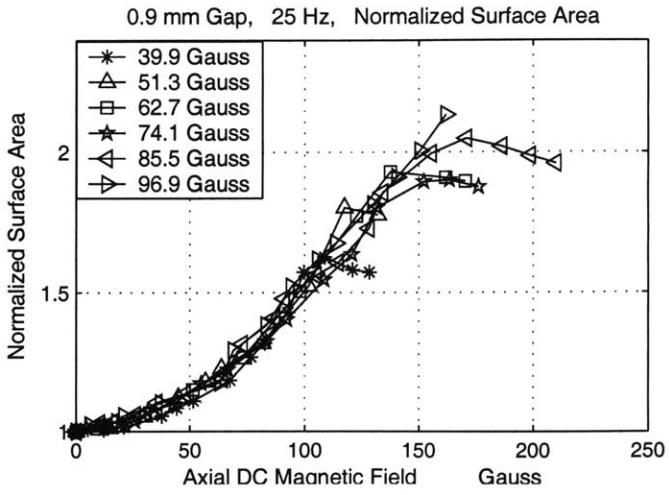

Figure 3-15: A plot of the normalized surface area of the 200 μl ferrofluid droplet of radius R=8.40 mm as it expands under an increasing DC axial magnetic field for various rotating magnetic field rms amplitudes and the rotating field frequency fixed at 25 Hz.

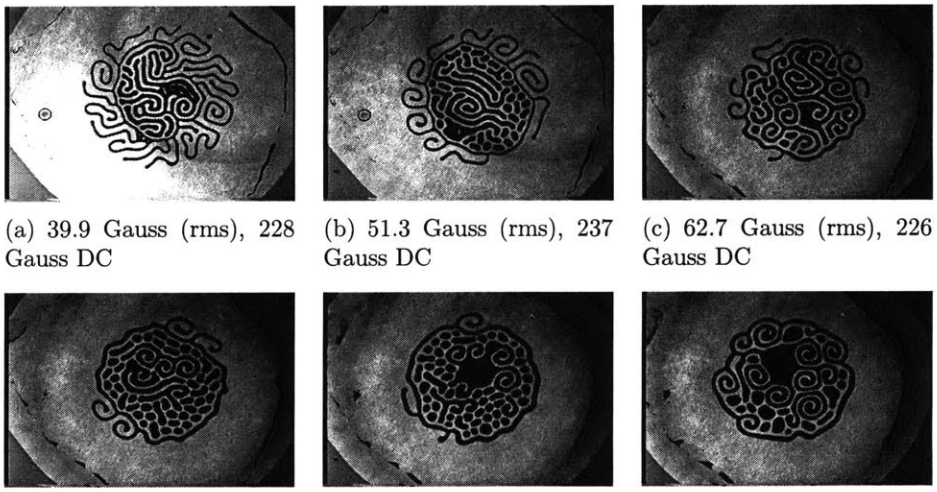

(a) 39.9 Gauss (rms), 228 Gauss DC

(b) 51.3 Gauss (rms), 237 Gauss DC

(c) 62.7 Gauss (rms), 226 Gauss DC

(d) 74.1 Gauss (rms), 223 Gauss DC

(e) 85.5 Gauss (rms), 240 Gauss DC

(f) 96.9 Gauss (rms), 220 Gauss DC

Figure 3-16: Pictures of the end result of the 25 Hz transition that occurs for each curve in Fig. 3-15.

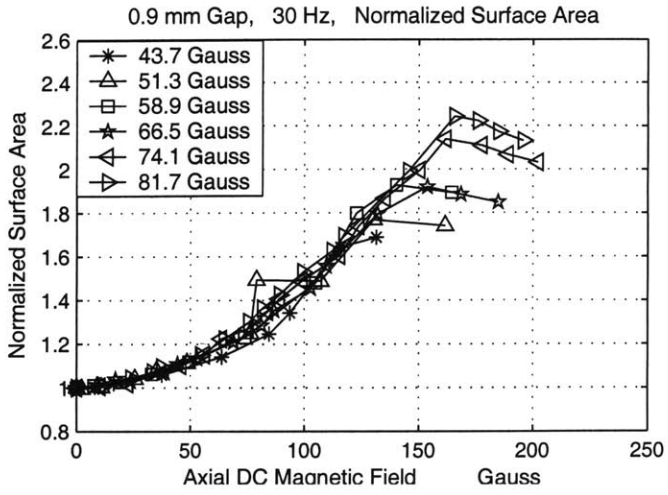

Figure 3-17: A plot of the normalized surface area of the 200 μl ferrofluid droplet of radius R= 8.40 mm as it expands under increasing DC axial magnetic field for various rotating magnetic field rms amplitudes and the rotating field frequency fixed at 30 Hz.

(a) 43.7 Gauss (rms), 239 Gauss DC

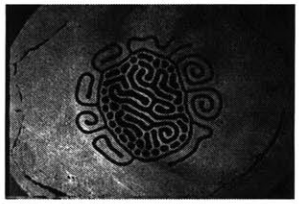

(b) 51.3 Gauss (rms), 245 Gauss DC

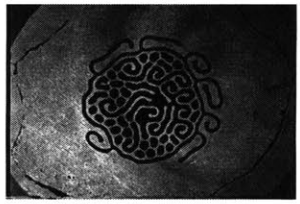

(c) 58.9 Gauss (rms), 227 Gauss DC

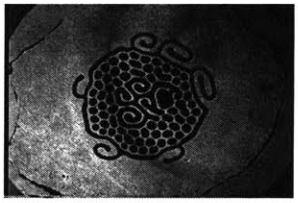

(d) 66.5 Gauss (rms), 234 Gauss DC

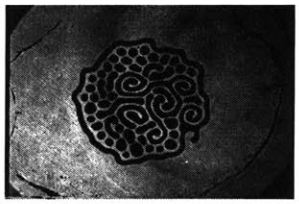

(e) 74.1 Gauss (rms), 230 Gauss DC

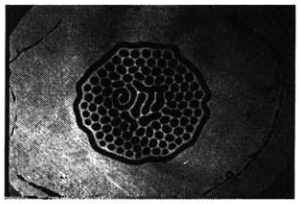

(f) 81.7 Gauss (rms), 225 Gauss DC

Figure 3-18: Pictures of the end result of the 30 Hz transition that occurs for each curve in Fig. 3-17.

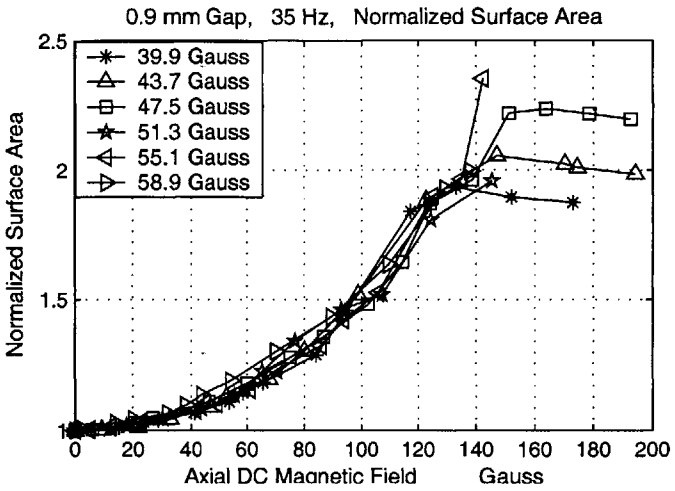

Figure 3-19: A plot of the normalized surface area of the 200 μl ferrofluid droplet of radius $R = 8.40$ mm as it expands under increasing DC axial magnetic field for various rotating magnetic field rms amplitudes and the rotating field frequency fixed at 35 Hz.

Gauss (rms) is approximately 1.85 at a DC axial magnetic field of $\approx$ 135 Gauss. This is larger than the measured surface area at 25 and 30 Hz. The largest the normalized surface area grows to is approximately 2.3 at 55.1 Gauss (rms) with the DC axial magnetic field $\approx$ 140 Gauss.

In Fig. 3-21, the normalized surface area of the ferrofluid drop excited at 40 Hz is plotted versus the DC axial magnetic field for various rotating magnetic field amplitudes with the end state of each transition shown in Figure 3-22. The transition only occurs for rotating magnetic field amplitudes in the range of 39.9 to 51.3 Gauss (rms). At 40 Hz, the surface area grows to a minimum of 1.75 at the largest rotating field amplitude of 51.3 Gauss (rms) with the DC axial magnetic field $\approx$ 138 Gauss. The surface area grows to a maximum of 2.3 at 43.7 Gauss (rms) with the DC axial magnetic field $\approx$ 150 Gauss. This is reversed from the same experiments performed at lower rotating field frequencies. In all other cases, the surface area would climb to a minimum at the smallest rotating magnetic field amplitude and would climb to a maximum at the largest rotating magnetic field amplitude.

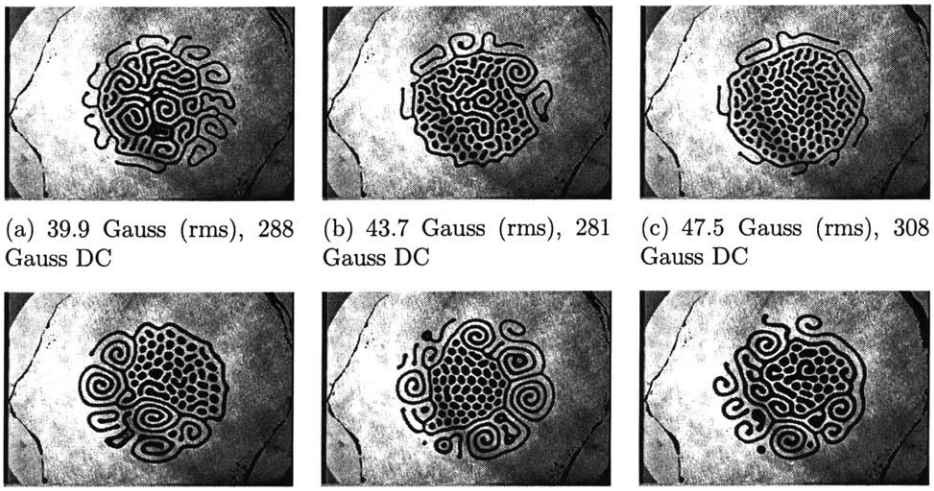

(a) 39.9 Gauss (rms), 288 Gauss DC

(b) 43.7 Gauss (rms), 281 Gauss DC

(c) 47.5 Gauss (rms), 308 Gauss DC

(d) 51.3 Gauss (rms), 257 Gauss DC

(e) 55.1 Gauss (rms), 288 Gauss DC

(f) 58.9 Gauss (rms), 241 Gauss DC

Figure 3-20: Pictures of the end result of the 35 Hz transition that occurs for each curve in Fig. 3-19.

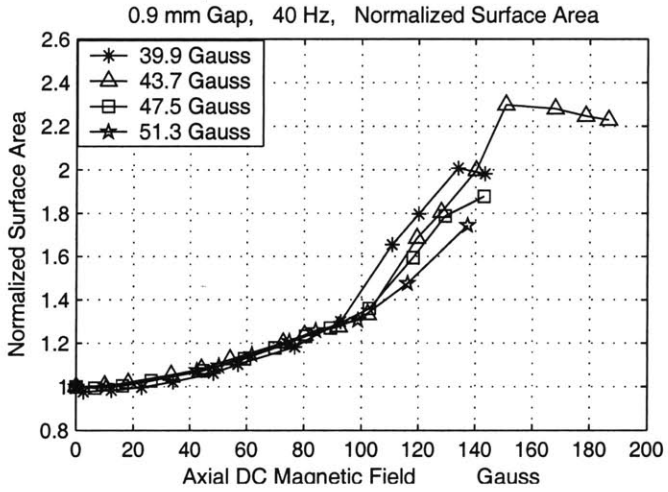

Figure 3-21: A plot of the normalized surface area of the 200 μl ferrofluid droplet of radius $R = 8.40$ mm as it expands under increasing DC axial magnetic field for various rotating magnetic field rms amplitudes and the rotating field frequency fixed at 40 Hz.

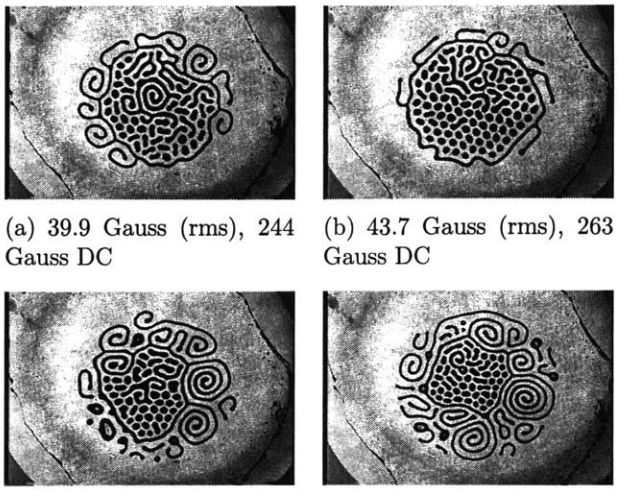

(a) 39.9 Gauss (rms), 244 Gauss DC

(b) 43.7 Gauss (rms), 263 Gauss DC

(c) 47.5 Gauss (rms), 285 Gauss DC

(d) 51.3 Gauss (rms), 330 Gauss DC

Figure 3-22: Pictures of the end result of the 40 Hz transition that occurs for each curve in Fig. 3-21.

1.15 mm Gap

When the separation gap is increased to 1.15 mm, the measured normalized surface area begins to spread with the rotating magnetic field amplitude. In the experiments conducted with the Hele-Shaw cell separation gap of 1.15 mm, the transition occurs over a range of magnetic field strengths that is smaller than when the separation gap was 0.9 mm.

In Fig. 3-23, the normalized surface area of the ferrofluid drop excited at 20 Hz is plotted versus the DC axial magnetic field for various rotating magnetic field amplitudes with the end-state of each transition shown in Figure 3-24. The normalized surface area is minimum at approximately 1.4 when excited at a rotating field strength of 24.7 Gauss (rms) with the DC axial magnetic field $\approx$ 121 Gauss and is maximum at approximately 1.95 when excited at a rotating field strength of 43.7 Gauss (rms) with the DC axial magnetic field $\approx$ 130 Gauss. The normalized surface area when the transition occurs grows to larger values at higher rotating magnetic field amplitudes.

In Fig. 3-25, the normalized surface area of the ferrofluid drop excited at 25 Hz is plotted versus the DC axial magnetic field for various rotating magnetic field am-

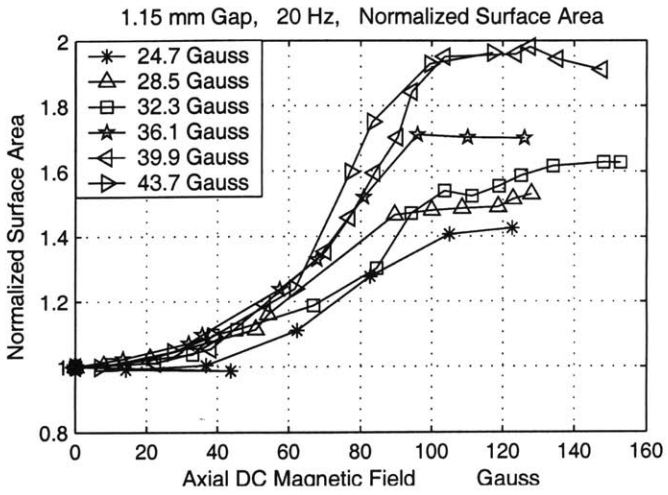

Figure 3-23: A plot of the normalized surface area of the 200 μl ferrofluid droplet with radius $R = 7.45$ mm as it expands under increasing DC axial magnetic field for various rotating magnetic field rms amplitudes and the rotating field frequency fixed at 20 Hz.

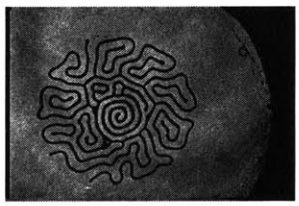

(a) 24.7 Gauss (rms), 214 Gauss DC

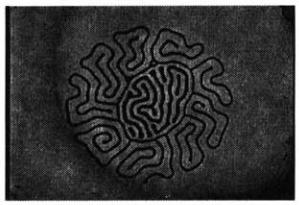

(b) 28.5 Gauss (rms), 244 Gauss DC

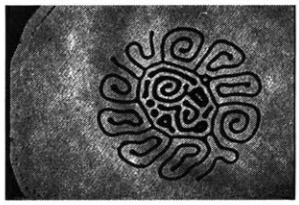

(c) 32.3 Gauss (rms), 204 Gauss DC

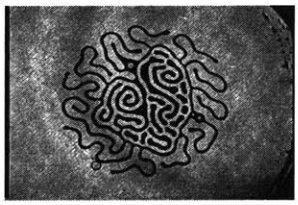

(d) 36.1 Gauss (rms), 245 Gauss DC

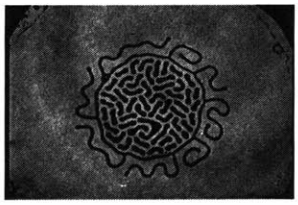

(e) 39.9 Gauss (rms), 227 Gauss DC

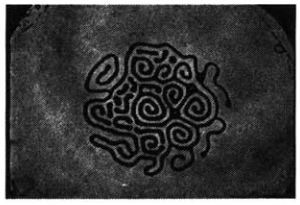

(f) 43.7 Gauss (rms), 229 Gauss DC

Figure 3-24: Pictures of the end result of the 20 Hz transition that occurs for each curve in Fig. 3-23.

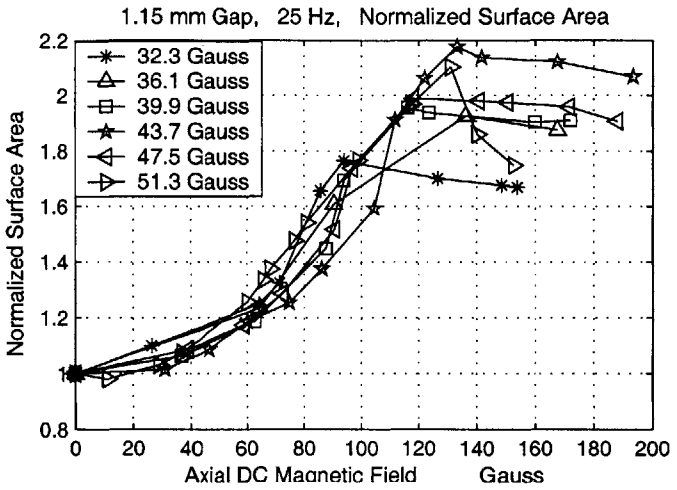

Figure 3-25: A plot of the normalized surface area of the 200 μl ferrofluid droplet with radius $R = 7.45$ mm as it expands under increasing DC axial magnetic field for various rotating magnetic field rms amplitudes and the rotating field frequency fixed at 25 Hz.

plitudes with the end-state of each transition shown in Figure 3-26. The minimum normalized surface area before the transition occurs is approximately 1.75 at 32.3 Gauss (rms) with DC axial magnetic field $\approx$ 95 Gauss, and the maximum is approximately 2.2 at 43.7 Gauss (rms) with the DC axial magnetic field $\approx$ 135 Gauss. The maximum does not occur at the largest rotating magnetic field strength of 51.3 Gauss (rms), although it climbs to a value of 2.1.

In Fig. 3-27, the normalized surface area of the ferrofluid drop excited at 30 Hz is plotted versus the DC axial magnetic field for various rotating magnetic field amplitudes with the end-state of each transition shown in Figure 3-28. The range of rotating magnetic field amplitudes at which the transition will occur is smaller than the range of rotating field amplitudes for the experiments performed at 20 and 25 Hz. The normalized surface area of the transition at the lowest rotating field amplitude of 20.9 Gauss (rms) grows the quickest but levels off at the lowest value of 1.8 when the DC axial magnetic field is $\approx$ 90 Gauss. All of the transitions with the rotating field amplitude in the range of 28.5 - 39.9 Gauss (rms) level at the same value of 2.2 when the DC axial magnetic field is $\approx$ 120 Gauss.

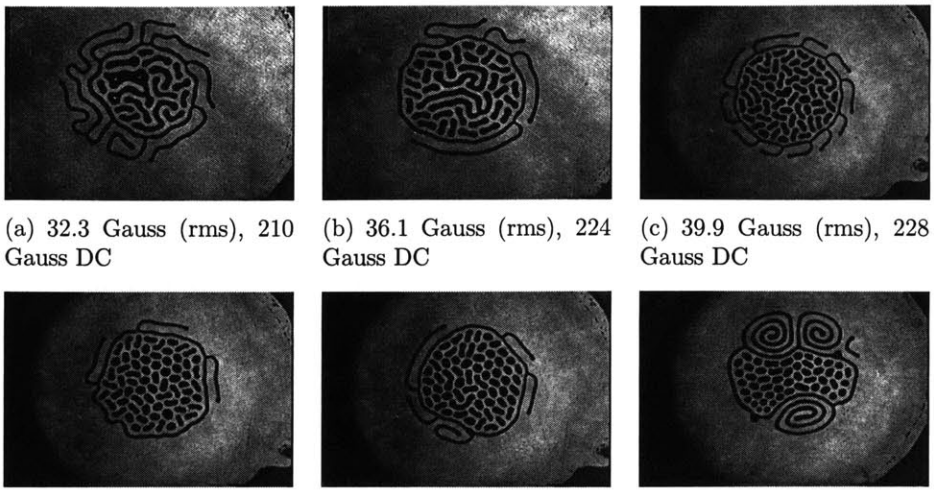

(a) 32.3 Gauss (rms), 210 Gauss DC

(b) 36.1 Gauss (rms), 224 Gauss DC

(c) 39.9 Gauss (rms), 228 Gauss DC

(d) 43.7 Gauss (rms), 229 Gauss DC

(e) 47.5 Gauss (rms), 237 Gauss DC

(f) 51.3 Gauss (rms), 227 Gauss DC

Figure 3-26: Pictures of the end result of the 25 Hz transition that occurs for each curve in Fig. 3-25.

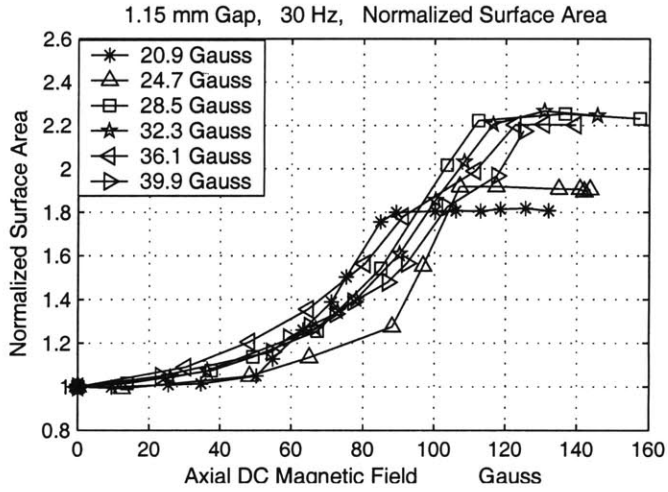

Figure 3-27: A plot of the normalized surface area of the 200 μl ferrofluid droplet with radius $R = 7.45$ mm as it expands under increasing DC axial magnetic field for various rotating magnetic field rms amplitudes and the rotating field frequency fixed at 30 Hz.

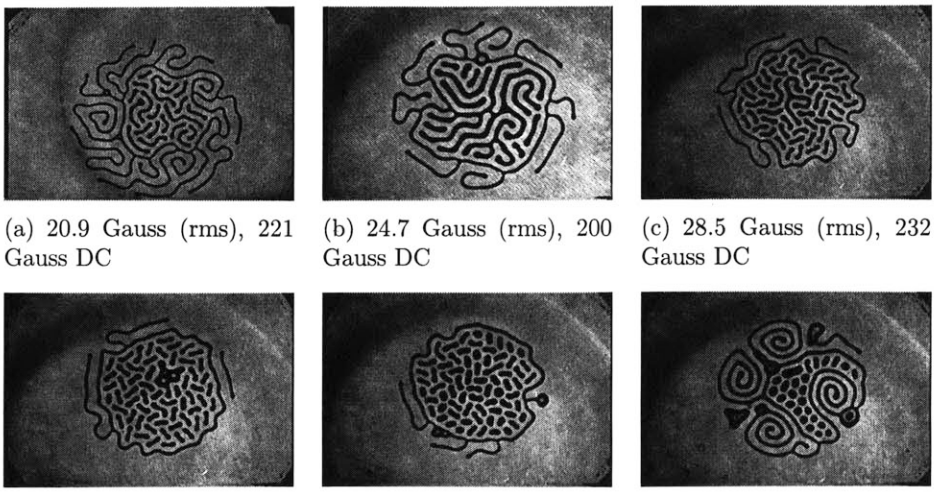

(a) 20.9 Gauss (rms), 221 Gauss DC

(b) 24.7 Gauss (rms), 200 Gauss DC

(c) 28.5 Gauss (rms), 232 Gauss DC

(d) 32.3 Gauss (rms), 231 Gauss DC

(e) 36.1 Gauss (rms), 243 Gauss DC

(f) 39.9 Gauss (rms), 238 Gauss DC

Figure 3-28: Pictures of the end result of the 30 Hz transition that occurs for each curve in Fig. 3-27.

In Fig. 3-29, the normalized surface area of the ferrofluid drop excited at 35 Hz is plotted versus the DC axial magnetic field for various rotating magnetic field amplitudes with the end-state of each transition shown in Figure 3-30. The value of the normalized surface area at the time of the transition is spread out much more than the experiments at lower rotating field frequencies. The normalized surface area before the transition has a minimum of 1.6 at 20.9 Gauss (rms) when the DC axial magnetic field is $\approx$ 80 Gauss and a maximum of 2.55 at 32.3 Gauss (rms) when the DC axial magnetic field is $\approx$ 110 Gauss. The experiments at 36.1 and 39.9 Gauss did not become larger because the ferrofluid droplet became unstable and tore apart similar to the examples given in Fig. 3-3.

In Fig. 3-31, the normalized surface area of the ferrofluid drop excited at 40 Hz is plotted versus the DC axial magnetic field for various rotating magnetic field amplitudes with the end-state of each transition shown in Figure 3-32. The normalized surface area of the transition that occurs when the rotating magnetic field is fixed at 20.9 Gauss (rms) climbs faster and to a larger value of 2.25 than the transitions at higher rotating magnetic field amplitudes. This occurs when the DC axial magnetic

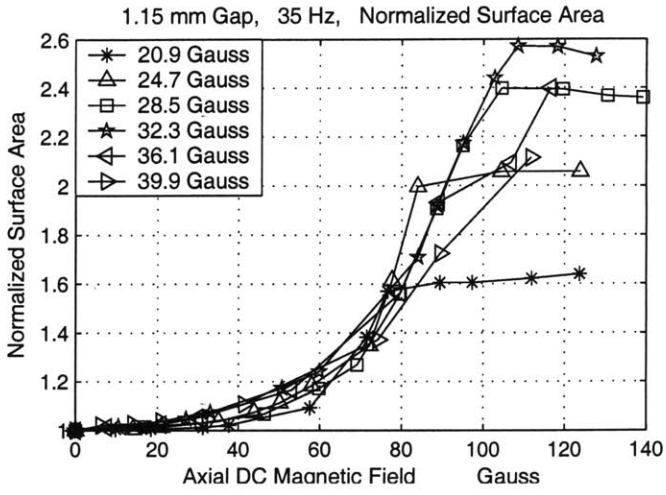

Figure 3-29: A plot of the normalized surface area of the 200 μl ferrofluid droplet with radius $R = 7.45$ mm as it expands under increasing DC axial magnetic field for various rotating magnetic field rms amplitudes and the rotating field frequency fixed at 35 Hz.

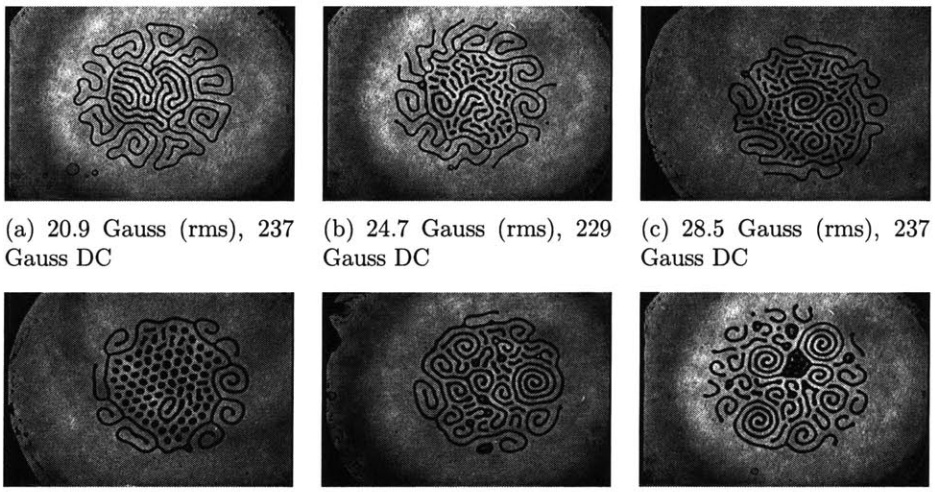

(a) 20.9 Gauss (rms), 237 Gauss DC

(b) 24.7 Gauss (rms), 229 Gauss DC

(c) 28.5 Gauss (rms), 237 Gauss DC

(d) 32.3 Gauss (rms), 203 Gauss DC

(e) 36.1 Gauss (rms), 243 Gauss DC

(f) 39.9 Gauss (rms), 217 Gauss DC

Figure 3-30: Pictures of the end result of the 35 Hz transition that occurs for each curve in Fig. 3-29.

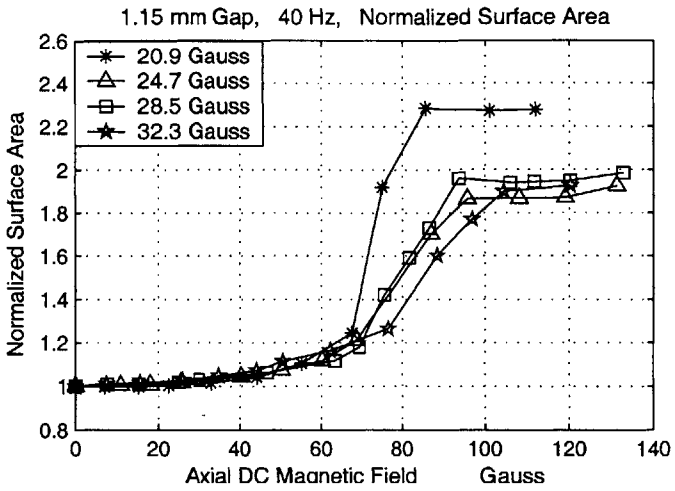

Figure 3-31: A plot of the normalized surface area of the 200 μl ferrofluid droplet with radius $R = 7.45$ mm as it expands under increasing DC axial magnetic field for various rotating magnetic field rms amplitudes and the rotating field frequency fixed at 40 Hz.

field is $\approx$ 85 Gauss. The transitions at higher field strengths all level off at approximately 1.9 surface area ratio when the DC axial magnetic field is $\approx$ 100 Gauss.

1.4 mm Gap

The transitions for the Hele-Shaw cell separation gap of 1.4 mm occur over a much smaller range of rotating magnetic field amplitudes than the smaller separation gaps. This is because the radius of the ferrofluid droplet is decreased as the separation gap becomes larger, resulting in the ferrofluid droplet becoming less stable under increasing DC axial magnetic field conditions.

In Fig. 3-33, the normalized surface area of the ferrofluid drop excited at 20 Hz is plotted versus the DC axial magnetic field for various rotating magnetic field strengths with the end-state of each transition shown in Figure 3-34. The ferrofluid droplet grew to its largest value when the rotating magnetic field is at 20.9 Gauss (rms) and again at 28.5 Gauss (rms), the smallest and largest rotating magnetic fields tested respectively. The minimum normalized surface area of approximately 1.62 results from the rotating magnetic field amplitude of 24.7 Gauss (rms), or the

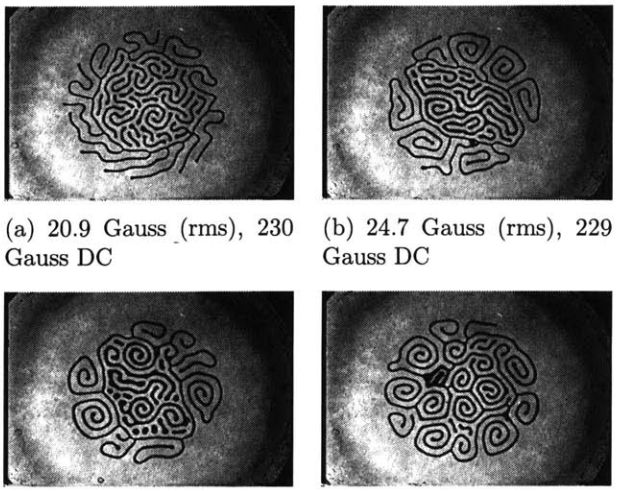

(a) 20.9 Gauss (rms), 230 Gauss DC

(b) 24.7 Gauss (rms), 229 Gauss DC

(c) 28.5 Gauss (rms), 209 Gauss DC

(d) 32.3 Gauss (rms), 194 Gauss DC

Figure 3-32: Pictures of the end result of the 40 Hz transition that occurs for each curve in Fig. 3-31.

middle value in the range tested, when the DC axial magnetic field is $\approx$ 75 Gauss.

In Fig. 3-35, the normalized surface area of the ferrofluid drop excited at 25 Hz is plotted versus the DC axial magnetic field for various rotating magnetic field strengths with the end-state of each transition shown in Figure 3-36. The range of rotating magnetic fields has been extended to include 17.1 Gauss (rms). The normalized surface area falls in the region between 2 at 24.7 Gauss (rms) when the DC axial magnetic field is $\approx$ 100 Gauss and 1.8 at 20.9 Gauss (rms) when the DC axial magnetic field is $\approx$ 85 Gauss.

In Fig. 3-37, the normalized surface area of the ferrofluid drop excited at 30 Hz is plotted versus the DC axial magnetic field for various rotating magnetic field strengths with the end-state for each transition shown in Figure 3-38. The normalized surface area climbs to a minimum of 1.25 at 17.1 Gauss (rms) when the DC axial magnetic field is $\approx$ 95 Gauss, which is significantly lower than the surface area of any of the transitions thus far. The maximum surface area is approximately 2 at 32.3 Gauss (rms) when the DC axial magnetic field is $\approx$ 115 Gauss.

In Fig. 3-39, the normalized surface area of the ferrofluid drop excited at 35 Hz is

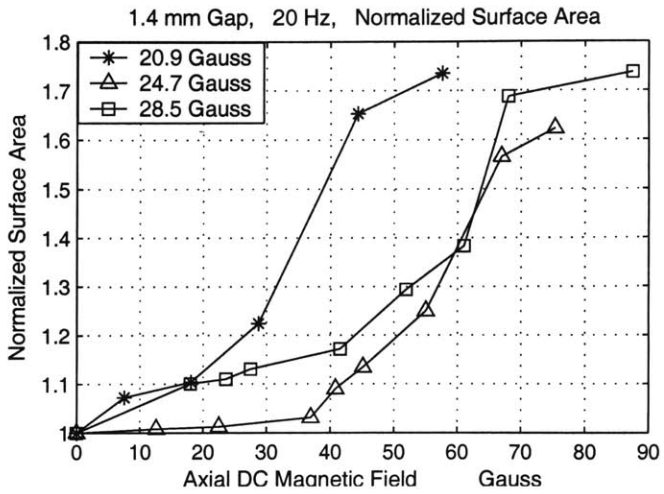

Figure 3-33: A plot of the normalized surface area of the 200 μl ferrofluid droplet with radius $R = 6.74$ mm as it expands under increasing DC axial magnetic field for various rotating magnetic field rms amplitudes and the rotating field frequency fixed at 20 Hz.

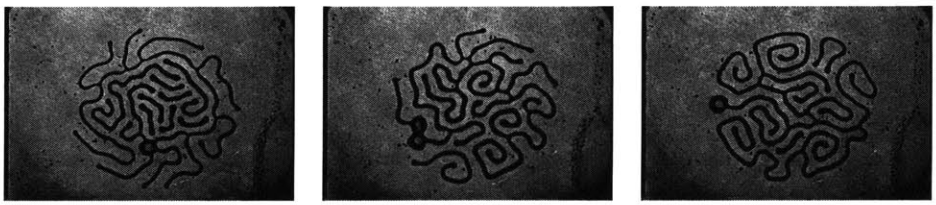

(a) 20.9 Gauss (rms), 97 Gauss DC

(b) 24.7 Gauss (rms), 187 Gauss DC

(c) 28.5 Gauss (rms), 218 Gauss DC

Figure 3-34: Pictures of the end result of the 20 Hz transition that occurs for each curve in Fig. 3-33.

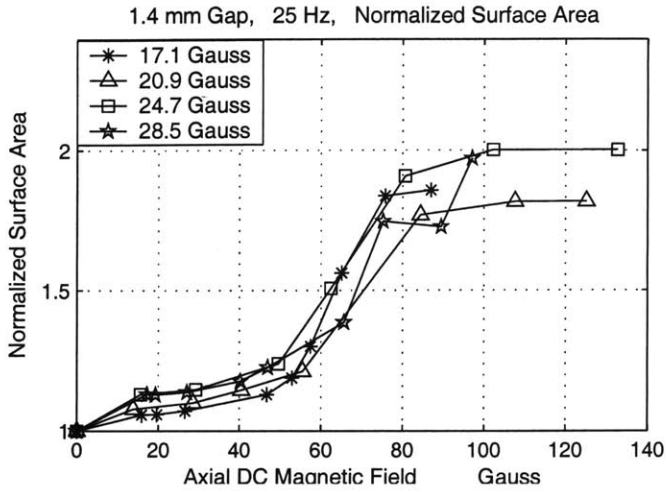

Figure 3-35: A plot of the normalized surface area of the 200 μl ferrofluid droplet with radius $R = 6.74$ mm as it expands under increasing DC axial magnetic field for various rotating magnetic field rms amplitudes and the rotating field frequency fixed at 25 Hz.

(a) 17.1 Gauss (rms), 159 Gauss DC

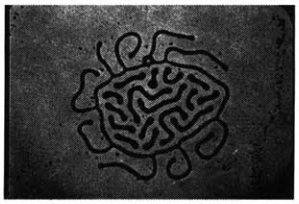

(b) 20.9 Gauss (rms), 196 Gauss DC

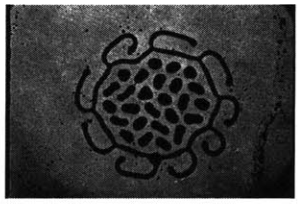

(c) 24.7 Gauss (rms), 166 Gauss DC

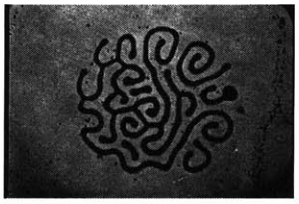

(d) 28.5 Gauss (rms), 168 Gauss DC

Figure 3-36: Pictures of the end result of the 25 Hz transition that occurs for each curve in Fig. 3-35.

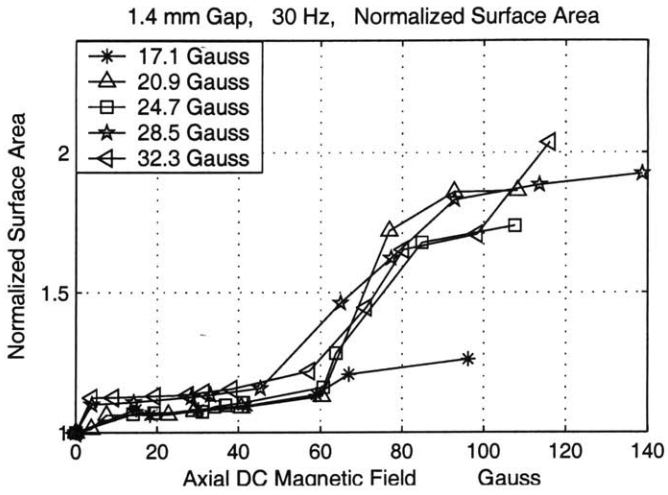

Figure 3-37: A plot of the normalized surface area of the 200 μl ferrofluid droplet with radius $R = 6.74$ mm as it expands under increasing DC axial magnetic field for various rotating magnetic field rms amplitudes and the rotating field frequency fixed at 30 Hz.

(a) 17.1 Gauss (rms), 207 Gauss DC

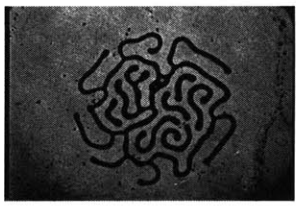

(b) 20.9 Gauss (rms), 157 Gauss DC

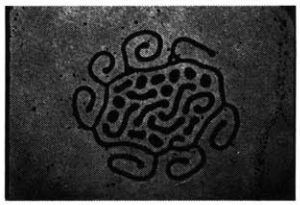

(c) 24.7 Gauss (rms), 168 Gauss DC

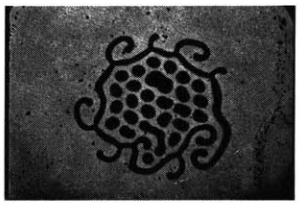

(d) 28.5 Gauss (rms), 150 Gauss DC

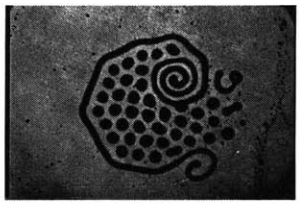

(e) 32.3 Gauss (rms), 163 Gauss DC

Figure 3-38: Pictures of the end result of the 30 Hz transition that occurs for each curve in Fig. 3-37.

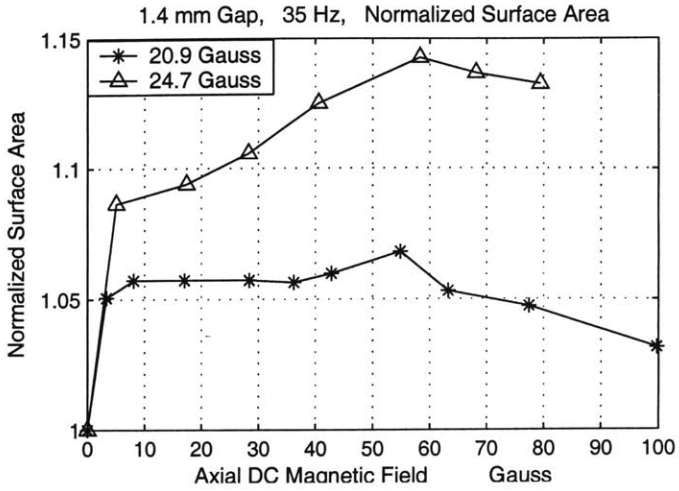

Figure 3-39: A plot of the normalized surface area of the 200 μl ferrofluid droplet with radius $R = 6.74$ mm as it expands under increasing DC axial magnetic field for various rotating magnetic field rms amplitudes and the rotating field frequency fixed at 35 Hz.

plotted versus the DC axial magnetic field for various rotating magnetic field strengths with the end-state of each transition shown in Figure 3-40. Only two rotating field strengths resulted in the transition occurring. The surface area of the ferrofluid droplet excited at 20.9 Gauss (rms) only grew to approximately 5% from the initial area to right before the transition occurred. Similarly at 24.7 Gauss (rms), the surface area only grew by approximately 14%.

(a) 20.9 Gauss (rms), 171 Gauss DC

(b) 24.7 Gauss (rms), 168 Gauss DC

Figure 3-40: Pictures of the end result of the 35 Hz transition that occurs for each curve in Fig. 3-39.

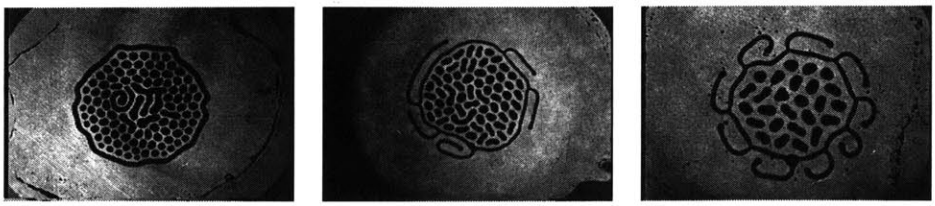

(a) 0.9 mm gap, 30 Hz, 81.7 Gauss (rms), 225 Gauss DC, N $\approx$ 108

(b) 1.15 mm gap, 25 Hz, 47.5 Gauss (rms), 237 Gauss DC, N $\approx$ 71

(c) 1.4 mm gap, 25 Hz, 24.7 Gauss (rms), 166 Gauss DC, N $\approx$ 26

Figure 3-41: Pictures of the end state of phase transitions showing a reduction in the number of smaller droplets with increasing Hele-Shaw cell separation gap.

3.4 Analysis of Data

The dependence of the phase transitions and spiral flows on experiment parameters is analyzed in this section. The experiment parameters discussed are Hele-Shaw cell separation gap, and rotating magnetic field amplitude and frequency.

3.4.1 Phase Transitions

Hele-Shaw Cell Separation Gap

As the Hele-Shaw cell separation gap increases, the ferrofluid drop grows more quickly with increasing axial magnetic field strength as demonstrated by the surface area plots of the previous section. The smaller number of ferrofluid drops, N, decreases as the Hele-Shaw cell gap increases demonstrating that the drops must be larger for the larger separation gaps. Examples are shown in Figure 3-41. The threshold axial magnetic field, $B_t = \mu_o H_t$, also decreases as the gap size is enlarged. All of these trends are consistent with the model predictions outlined in Section 3.2.2.

Rotating Magnetic Field Frequency

Only a small window of rotating field frequencies result in the transition occurring. For the experiments in this chapter with ferrofluid volume being 200 μl and Hele-Shaw cell separation gaps ranging anywhere between 0.9-1.4 mm, this window is between

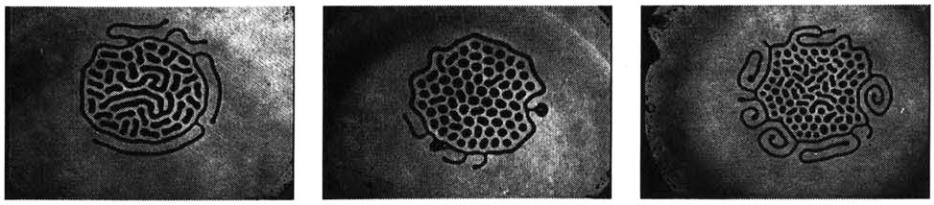

(a) 1.15 mm gap, 25 Hz, 36.1 Gauss (rms), 224 Gauss DC, N $\approx$ 44

(b) 1.15 mm gap, 30 Hz, 36.1 Gauss (rms), 213 Gauss DC, N $\approx$ 71

(c) 1.15 mm gap, 35 Hz, 36.1 Gauss (rms), 208 Gauss DC, N $\approx$ 83

Figure 3-42: Pictures of the end state of phase transitions showing an increase in the number of smaller droplets with increasing rotating magnetic field frequency.

20-40 Hz. Increases in rotating field frequency lower the window of magnetic field amplitudes that result in the transition to occur as shown in Section 3.3.1. With all other parameters equivalent, the number of smaller ferrofluid droplets increases with frequency as shown in Figure 3-42.

Rotating Magnetic Field Amplitude

Only a small window of rotating magnetic field amplitudes result in the transition occurring. This window is much smaller for larger Hele-Shaw cell separation gaps. When the amplitude of the rotating field is close to the lower limit of the window, the rotating field is not strong enough to hold the drop together under an increasing DC axial field, and the drop forms "fingers" similar to the labyrinth instability. This is illustrated by example in Figure 3-2. When the rotating field amplitude is close to the upper limit of the window, the rotating field is too strong and allows the increasing axial magnetic field to tear the ferrofluid drop apart. This is illustrated by example in Figure 3-3.

3.4.2 Spiral Flows

When the application of the magnetic fields are reversed, the ferrofluid droplet forms a spiral-like structure. First the droplet is excited with the DC axial magnetic field forcing the droplet to form the labyrinth instability. Then the in-plane uniform ro-

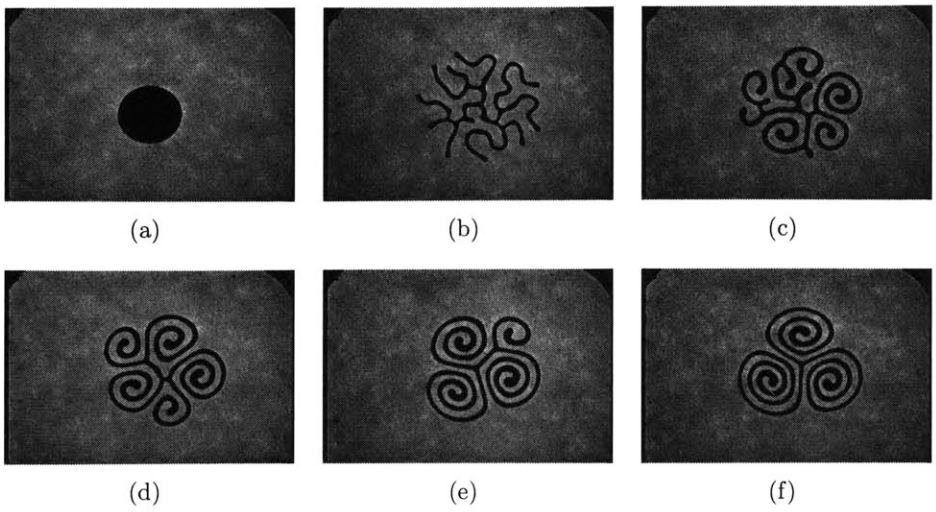

Figure 3-43: Spiral pattern formed when (a) a 100 μl ferrofluid droplet in a 1.1 mm Hele-Shaw cell is stressed by a 155 Gauss uniform DC axial magnetic field to form the labyrinth in (b) and then a uniform clockwise rotating magnetic field of 47.5 Gauss rms at frequency of 25 Hz is applied to create spiral flow (c)-(f).

tating magnetic field is turned on and forces each leg of the labyrinth to then curl in upon itself forming the spiral configuration. The smooth spirals form from viscous shear as the rotating magnetic field causes co-flow (same direction as the rotating field) on the outside surface which return on the inside surfaces. This flow causes the spiral to curl in towards the middle in the same direction as the rotating magnetic field.

An example of this spiral structure can be seen in Figure 3-43. When the ferrofluid drop contains only 100 μl of ferrofluid, the droplet forms a clover of spirals. More legs may be added to the spiral by adding more ferrofluid inside of the Hele-Shaw cell. This is shown in Figure 3-44 with 200 μl of ferrofluid.

Like the phase transition, the spiral only forms for specific windows of rotating magnetic field amplitude and frequency. At the lower extreme of the window for rotating magnetic field amplitude, the rotating field is not strong enough to cause the legs to curl in on themselves and the drop stays in a labyrinth. For large rotating field strengths (upper limit of window), the spiral can not stay together as a single

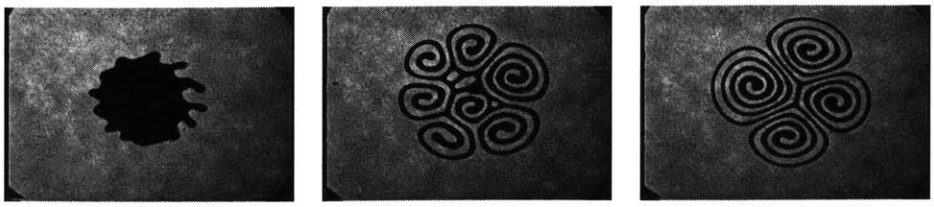

(a) (b) (c)

Figure 3-44: Spiral pattern formed when (a) a 200 μl ferrofluid droplet in a 1.1 mm Hele-Shaw cell is stressed by a 150 Gauss uniform DC axial magnetic field to form the labyrinth and then a uniform clockwise rotating magnetic field of 38 Gauss rms at frequency of 25 Hz is applied to create spiral flow (b,c). More fluid in the Hele-Shaw cell results in more legs on the spiral.

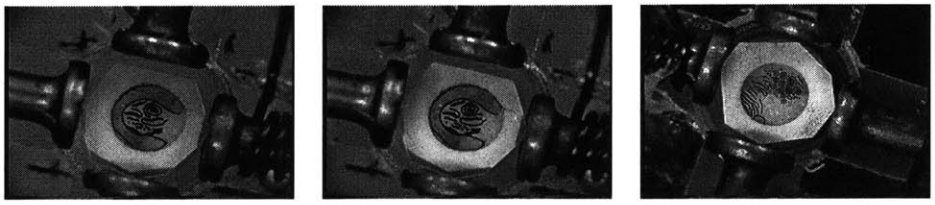

(a) (b) (c)

Figure 3-45: Spiral patterns formed when a ferrofluid droplet in a 0.1 mm gap Hele-Shaw cell is stressed by a uniform DC axial magnetic field to form the labyrinth and then a uniform clockwise rotating magnetic field is applied. These experiments were exploratory, thus the value of the magnetic fields were not recorded.

spiral due to the large force from the rotating field. Thus, the spiral breaks into many smaller spirals. Therefore, larger volumes of ferrofluid require the rotating magnetic field to be smaller for the single spiral. As the rotating field frequency is raised, the ferrofluid spiral lines become closer together. This is because the ferrofluid flow velocity along the edge is now increased, causing the bending to become more profound. The ferrofluid lines may be brought closer together by decreasing the Hele-Shaw cell gap separation. This is shown in Figure 3-45 for a Hele-Shaw cell with the separation gap size $\approx$ 0.1 mm.

3.5 Discussion

Experiments were performed on ferrofluid drops contained in Hele-Shaw cells of 0.9-1.4 mm gaps, corresponding to R/t ranging from 9.34-4.82. Figure 3-7 shows that as R/t increases (Hele-Shaw separation gap decreases and radius increases), the number of smaller ferrofluid droplets increases which is consistent with the experiments. Figure 3-8 shows the threshold axial magnetic field B_t decreases as the separation gap is widened. This is also consistent with the experiments. In our experiments the measured values of N range from 56-107 for the 0.9mm separation gap, 36-85 for the 1.15mm separation gap, and 21-40 for the 1.4mm gap. These values are slightly lower than the calculated values shown in Figure 3-7. The measured values of B_t range from 173-256 Gauss for the 0.9mm separation gap, 131-238 Gauss for the 1.15mm separation gap, and 70-164 Gauss for the 1.4mm separation gap. These values are higher than the calculated values in Figure 3-8. The difference in experimental and theoretical results can be attributed to the assumption of a linear magnetization relationship; however, the ferrofluid follows the Langevin relationship for paramagnetic behavior which has a smaller M for the same applied H than the linear model.

The value of N increases with rotating field amplitude at a fixed rotating field frequency. Increases in rotating field frequency only lower the window of rotating field amplitudes such that the transition will occur. The smaller Hele-Shaw cell separation gap sizes had the transitions occur at larger rotating field amplitudes.

Chapter 4

Magnetic Field Induced Ferrofluid Flow Reversals

The fluid surface of a cylindrical vessel filled with ferrofluid and placed in a uniform rotating magnetic field will rotate. Previous researchers have cited flow reversals in ferrofluids excited by uniform rotating magnetic fields as the magnetic field and amplitude is changed. Rosensweig shows that this flow in a uniform rotating magnetic field can be attributed to the change in curvature of the free top surface due to magnetic surface forces [17]. By examining the sign of the shear stress component of the stress tensor, he shows that the fluid rotates counter to the applied field rotational direction when the surface is concave, the rotation ceases for a flat surface, and rotates in the same direction as the applied field for a convex surface. He verifies these results with experimental data.

Others have found that ferrofluid flow reversals have occurred when the applied rotating magnetic field is raised above some critical value [7]. They have shown this to be true for spatially non-uniform and uniform rotating magnetic fields. This value of critical magnetic field strength is shown to be dependent upon the concentration of suspended magnetic particles, and the viscosity of the carrier fluid.

The experiments of this chapter have a vessel filled with ferrofluid and excited by an in-plane uniform rotating magnetic field. The fluid surface is placed at different heights within the motor stator winding to examine the surface behavior due to

Table 4.1: Summary of the fluid properties for MSG W11 waterbased ferrofluid.

	MSG W11 Waterbased Ferrofluid
Mass Density	1.204 g/cm^3
Saturation Magnetization	187.3 Gauss
Magnetic Susceptibility	0.669

fringing field effects. Tracer particles are added to the surface to determine the rotational flow direction, and then a larger particle is added to determine the direction a floating particle will spin. Then, the cylindrical vessel is placed in the center of the motor and a DC axial magnetic field is added to the configuration to alter the curvature of the free top surface. By noting the DC axial magnetic field strength for which the ferrofluid begins the transition from rotating against the applied field to rotating with the applied field, the magnetic field strength that results in a flat surface curvature will be determined. This measurement is noted for both a clockwise and counterclockwise rotating magnetic field, and is examined for varying rotational magnetic field amplitudes and frequencies.

A brief discussion of Rosensweig's theory will also be presented.

4.1 Procedure

The MSG W11 waterbased ferrofluid is used for all of the experiments in this chapter. A summary of the measured properties of this fluid is given in Table 4.1 [23].

4.1.1 Fringing Field Effects

A petri dish with diameter of 7.8 cm and depth of 1.25 cm is filled with ferrofluid and placed inside of a 2 pole motor stator winding with the fluid surface placed at three different levels: the top, middle and bottom of the motor. The surface has tracer particles to determine the rotational direction of the fluid surface. The tracer particles used were simple chalk dust because of its availability and floatability on the surface of the fluid. The motor is excited at 60 Hz and 152 Gauss (rms) for each

of the fluid surface locations inside the motor, and the experiments are performed for both a clockwise and counterclockwise rotating magnetic field. The fluid surface rotational direction is noted for each of the cases described and a floating sphere is placed on the surface to determine the direction of rotation experienced by a floating object.

4.1.2 Ferrofluid Flow Reversal

A 400 mL beaker is filled with 50 mL of water based ferrofluid and placed inside an in-plane spatially uniform rotating magnetic field by placing in the center of two pole motor stator winding. The rotating field sets the ferrofluid in motion by causing rotation in the direction opposite to the applied rotating field. By adding a DC axial magnetic field to control the curvature of the free top fluid surface, the direction of rotation can be reversed to flow in the same direction as the applied rotating field. At some critical DC axial magnetic field strength, the curvature of the ferrofluid surface becomes flattened, resulting in the rotation of the fluid to cease. Field strengths below this value cause the fluid to rotate counter to the applied field, while field strengths above this value cause the fluid to rotate with the applied field. For these experiments, this critical DC axial magnetic field strength will be measured for both clockwise and counterclockwise rotating magnetic fields with variations in rotating magnetic field amplitude and frequency.

The rotating magnetic field is created as described in Appendix A.

Because the ferrofluid is an opaque liquid with a mirror like surface, the direction of fluid rotation is not easy to determine by examination with the naked eye. Therefore, tracer particles were added to the surface of the ferrofluid to enable a clear determination of flow direction. The tracer particles used were sawdust because of its small particle size, ability to float on water, and its general availability.

Fixing the rotating magnetic field strength and frequency, the tracer particles would then be set in motion, flowing counter to the direction of the applied field. By then slowly raising the DC axial magnetic field strength, the tracer particles would then stop before beginning to flow in the direction of the applied field. It is the

value of this DC axial magnetic field strength that these experiments are trying to measure. However, because of some non-uniformities in the flow direction of the fluid, it was hard to pin-point exactly when the rotation stopped; therefore, upper and lower bounds of magnetic field values were recorded when the condition of flow reversal is not clear. The magnetic field that results in a zero velocity flow is taken as being the value of the magnetic field in the middle of this range. This was done for increasing DC axial magnetic field strength resulting in a flow changing from counter-flow to co-flow with the magnetic field rotation direction, and also again for decreasing axial magnetic field strength resulting in the flow changing from co-flow to counter-flow.

4.2 Results

4.2.1 Fringing Field Effects

The surface behavior of a water based ferrofluid placed inside of a 2 pole motor stator winding is presented. These experiments examine the flow direction with respect to the applied field and the spin direction of a plastic sphere floating on top of the ferrofluid surface.

A petri dish is filled with a water based ferrofluid and placed inside of the motor stator winding with the fluid surface parallel to the top, middle, and then bottom of the motor stator winding. The top and bottom of the motor are used to examine the effects of the fringing fields compared to the behavior of the fluid when in the center of the motor where the field is most uniform. The surface has tracer particles of chalk to determine the direction of rotation, and a floating plastic sphere is placed on the surface to determine the direction of $\boldsymbol{\omega}$, the body angular velocity, and $\mathbf{V}_\theta$, the flow velocity around the center of the vessel. This is shown pictorially in Figure 4-1.

The surface behavior for an applied clockwise rotating magnetic field is summarized in Table 4.2. An interesting observation is that when the fluid surface level is at the middle and bottom of the motor, the inner region of fluid rotates in the clockwise direction, but a particle floating on top of the surface rotates in the counterclockwise

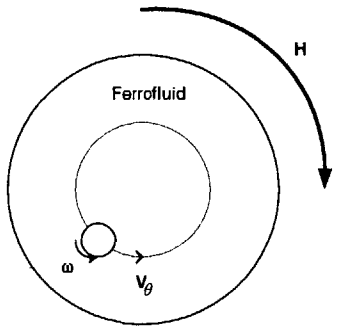

Figure 4-1: A pictorial representation of the petri dish filled with ferrofluid and put in a clockwise rotating magnetic field with no DC axial magnetic field is shown. A floating plastic sphere is shown to both rotate counterclockwise around its axis with angular velocity $\boldsymbol{\omega}$ and translate in a counterclockwise direction around the center of the dish with velocity $\mathbf{V}_\theta$.

Table 4.2: Summary of the surface behavior experiments for a clockwise rotating magnetic field.

Position in Motor	Inner Fluid Flow Direction	Outer Fluid Flow Direction	Particle Rotation Direction	Particle Translational Direction
Top	CCW	CCW	CCW	None
Middle	CW	CCW	CCW	CW
Bottom	CW	CW	CCW	CW

direction.

The surface behavior for an applied counterclockwise rotating magnetic field is summarized in Table 4.3. Once again, particle spin is opposite to fluid flow as when the fluid surface rotates counterclockwise, a particle floating on top of the surface rotates clockwise.

Just as expected, the two tables are complements of each other. When the direction of the applied magnetic field is reversed, every entry in the table also reverses.

4.2.2 Flow Reversal

Next, the measurements for the critical axial DC magnetic field strength that results in reversal of flow direction in a cylindrical vessel filled with a water based ferrofluid

Table 4.3: Summary of the surface behavior experiments for a counterclockwise rotating magnetic field.

Position in Motor	Inner Fluid Flow Direction	Outer Fluid Flow Direction	Particle Rotation Direction	Particle Translational Direction
Top	CW	CW	CW	None
Middle	CCW	CW	CW	CCW
Bottom	CCW	CCW	CW	CCW

and excited by a uniform rotating magnetic field will be studied as a function of the rotating magnetic field frequency and amplitude. Measurements are shown for increasing DC axial magnetic fields changing the flow direction from counter-flow to co-flow, and for decreasing DC axial magnetic fields changing the flow direction from co-flow to counter-flow. Measurements are taken for clockwise and counterclockwise rotating fields with the rotating field frequency ranging from 50 to 400 Hz and the rotating field amplitude ranging from 40 to 180 Gauss (rms). The DC axial magnetic field ranges from 0 to 260 Gauss.

For all of the clockwise rotating magnetic field measurements, the ferrofluid rotates counterclockwise at low axial magnetic fields and rotates clockwise for high axial magnetic fields. However, during the transition in rotation direction, the outer region would change direction first and then the inner fluid region follows. For all of the counterclockwise rotating magnetic field measurements, the ferrofluid rotates clockwise at low DC axial magnetic fields and rotates counterclockwise for high DC axial magnetic fields. However, during the reversal of fluid rotational direction the inner fluid region changes direction first and then the outer fluid region follows. Therefore, there is a clear distinction between how the flow evolves for the two different cases.

Clockwise Rotating Magnetic Field

In Figures 4-2 and 4-3, the critical DC axial magnetic field strength that results in the reversal of ferrofluid flow direction is studied as a function of the clockwise rotating magnetic field frequency and amplitude respectively. These measurements are for increasing DC axial magnetic fields resulting in the ferrofluid changing rotation

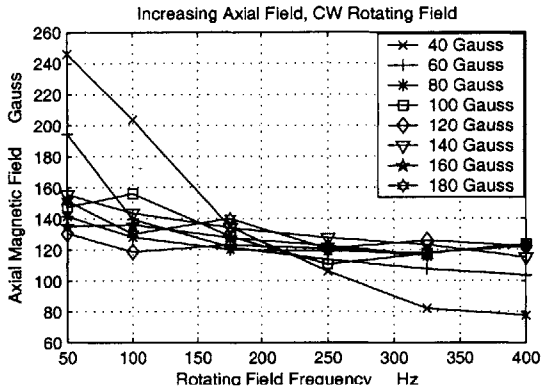

Figure 4-2: Measurement of the critical DC axial magnetic field strength that results in the rotation of the ferrofluid to cease is plotted versus the rotating magnetic field frequency for various clockwise rotating magnetic field rms amplitudes. These measurements are for an increasing DC axial magnetic field, and the fluid surface is located in the center of the motor.

direction from counter-flow (counter-clockwise) to co-flow (clockwise) with respect to the clockwise rotating magnetic field.

In Figures 4-4 and 4-5, the critical DC axial magnetic field that results in the reversal of ferrofluid flow direction is studied as a function of the clockwise rotating magnetic field frequency and amplitude respectively. These measurements are for decreasing axial magnetic fields resulting in the ferrofluid flow direction changing from co-flow (clockwise) to counter-flow (counterclockwise).

Counterclockwise Rotating Magnetic Field

In Figures 4-6 and 4-7, the critical axial magnetic field that results in the reversal of ferrofluid flow direction is plotted versus the counterclockwise rotating magnetic field frequency and amplitude respectively. These measurements are for increasing axial magnetic fields resulting in the ferrofluid changing rotation direction from co-flow (counterclockwise) to counter-flow (clockwise) with respect to the counterclockwise rotating magnetic field.

In Figures 4-8 and 4-9, the critical axial magnetic field that results in the reversal of ferrofluid flow direction is plotted versus the rotating magnetic field frequency and

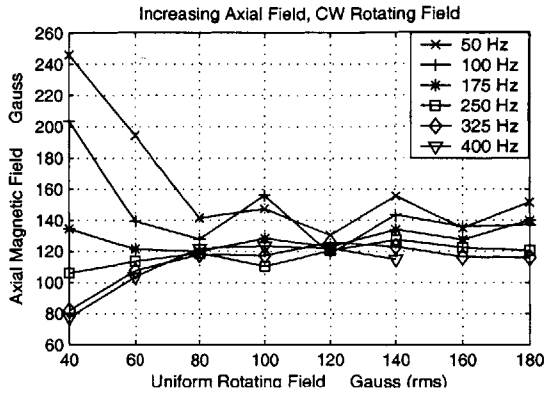

Figure 4-3: Replot of measurements shown in Fig. 4-2 of the critical DC axial magnetic field strength that results in the rotation of the ferrofluid to cease versus the clockwise rotating magnetic field rms amplitude for various rotating magnetic field frequencies. These measurements are for an increasing DC axial magnetic field, and the fluid surface is located in the center of the motor.

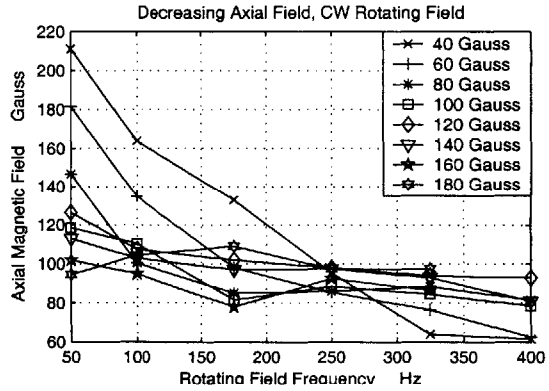

Figure 4-4: Measurement of the critical DC axial magnetic field strength that results in the rotation of the ferrofluid to cease is plotted versus the clockwise rotating magnetic field frequency for various clockwise rotating magnetic field rms amplitudes. These measurements are for a decreasing axial magnetic field, and the fluid surface is located in the center of the motor.

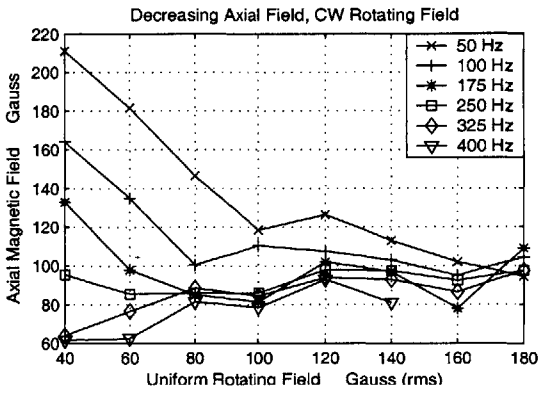

Figure 4-5: Replot of measurements shown in Fig. 4-4 of the critical DC axial magnetic field strength that results in the rotation of the ferrofluid to cease versus the clockwise rotating magnetic field rms amplitude for various rotating magnetic field frequencies. These measurements are for a decreasing DC axial magnetic field, and the fluid surface is located in the center of the motor.

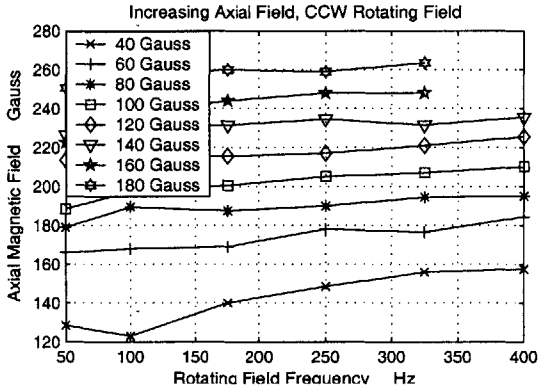

Figure 4-6: Measurement of the critical DC axial magnetic field strength that results in the rotation of the ferrofluid to cease is plotted versus the counterclockwise rotating magnetic field frequency for various counterclockwise rotating magnetic field rms amplitudes. These measurements are for an increasing DC axial magnetic field, and the fluid surface is located in the center of the motor.

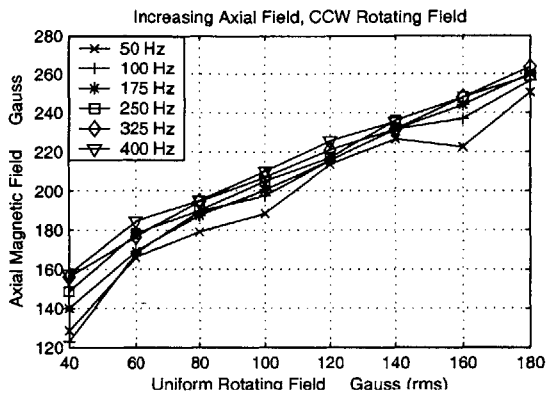

Figure 4-7: Replot of measurements shown in Fig. 4-6 of the critical DC axial magnetic field strength that results in the rotation of the ferrofluid to cease versus the counterclockwise rotating magnetic field rms amplitude for various counterclockwise rotating magnetic field frequencies. These measurements are for an increasing DC axial magnetic field, and the fluid surface is located in the center of the motor.

amplitude respectively. These measurements are for decreasing DC axial magnetic fields resulting in the ferrofluid changing rotation direction from counterclockwise (co-flow) to clockwise (counter-flow) with respect to the applied counterclockwise rotating magnetic field.

4.2.3 Summary of Results

A summary is presented in Table 4.4 that presents all of the flow reversal data for fixed rotating field amplitude, H_r, and rotating field frequency f. This table lists the DC axial field H_{DC} such that the ferrofluid flow direction reverses averaged over the increasing/decreasing axial field measurements and the CW/CCW rotating field directions.

4.3 Theoretical Analysis

Rosensweig analyzes the reversal in ferrofluid flow in a cylindrical vessel excited by a uniform rotating magnetic field by calculating the change in shear stress at the fluid surface with changing fluid surface curvature [16, 17]. A summary of his analysis is

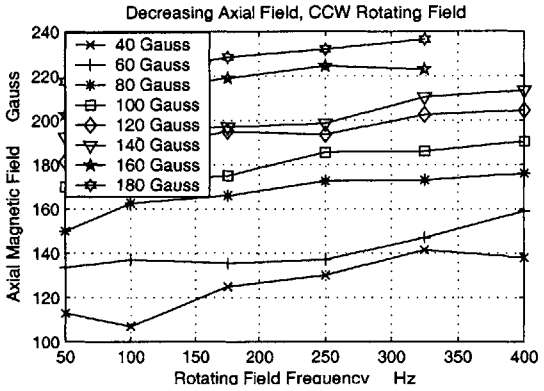

Figure 4-8: Measurement of the critical DC axial magnetic field strength that results in the rotation of the ferrofluid to cease is plotted versus the counterclockwise rotating magnetic field frequency for various counterclockwise rotating magnetic field rms amplitudes. These measurements are for a decreasing axial magnetic field, and the fluid surface is located in the center of the motor.

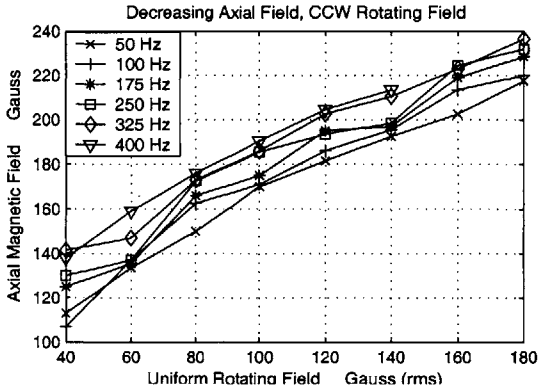

Figure 4-9: Replot of measurements shown in Fig. 4-8 of the critical DC axial magnetic field strength that results in the rotation of the ferrofluid to cease versus the counterclockwise rotating magnetic field rms amplitude for various counterclockwise rotating magnetic field frequencies. These measurements are for a decreasing DC axial magnetic field, and the fluid surface is located in the center of the motor.

Table 4.4: Summary of conditions for waterbased ferrofluid flow reversals.

H_r (Gauss rms)	f (Hz)	H_{DC} (Gauss)	H_r (Gauss rms)	f (Hz)	H_{DC} (Gauss)
40	50	175	120	50	163
	100	149		100	157
	175	133		175	159
	250	120		250	157
	325	111		325	161
	400	108		400	161
60	50	169	140	50	172
	100	145		100	168
	175	131		175	165
	250	129		250	165
	325	127		325	165
	400	127		400	161
80	50	154	160	50	166
	100	145		100	170
	175	140		175	167
	250	142		250	172
	325	144		325	169
	400	144			
100	50	156	180	50	179
	100	159		100	178
	175	146		175	184
	250	147		250	177
	325	149		325	178
	400	151			

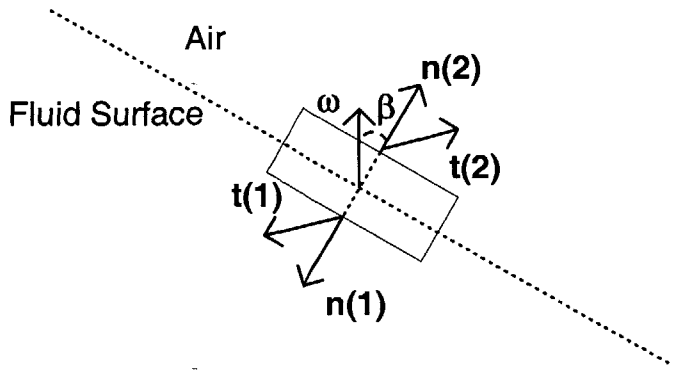

Figure 4-10: Pictorial representation of the stresses exerted on an arbitrary fluid surface element. The particle rotating rate $\boldsymbol{\omega}$, is always oriented vertically; however, the normal $\mathbf{n}$ may have an arbitrary direction such that the angle β satisfies $-\frac{\pi}{2} < \beta < \frac{\pi}{2}$. This corresponds to the surface changing from convex to concave.

described below.

From thermodynamic considerations, the total viscous, spin, and Maxwell stress tensor $\mathbf{T}$ can be expressed in general by,

$$\mathbf{T} = -p\mathbf{I} + \lambda(\nabla \cdot \mathbf{v})\mathbf{I} + \eta[\nabla\mathbf{v} + (\nabla\mathbf{v})^T] + \zeta\boldsymbol{\epsilon} \cdot (\boldsymbol{\Omega} - 2\boldsymbol{\omega}) - \frac{1}{2}\mu_0 H^2\mathbf{I} + \mathbf{BH}. \quad (4.1)$$

In this equation p is the pressure, $\mathbf{I}$ is the unit dyadic tensor, λ is the bulk or second coefficient of viscosity, $\mathbf{v}$ is the velocity vector, η is the ordinary or first coefficient of viscosity, ζ is the rotational viscosity, $\boldsymbol{\epsilon}$ is the polyadic alternator tensor, $\boldsymbol{\Omega} = \nabla \times \mathbf{v}$ is the vorticity, $\boldsymbol{\omega}$ is the fluid spin velocity, $\mathbf{H}$ is the applied magnetic field, $\mathbf{B} = \mu_0(\mathbf{H} + \mathbf{M})$ is the magnetic induction, and $\mathbf{M}$ is the magnetization or magnetic moment per unit volume.

By considering the fluid initially at rest, or $\mathbf{v} = 0$, the stress vector $\mathbf{t}$ acting on an arbitrary surface element oriented with a unit normal $\mathbf{n}$ and shown in Figure 4-10, is given by $\mathbf{t} = \mathbf{n} \cdot \mathbf{T}$.

$$\mathbf{t} = -\frac{1}{2}\mu_0 H^2\mathbf{n} + 2\zeta\mathbf{n} \times \boldsymbol{\omega} + B_n\mathbf{H} \quad (4.2)$$

The normal and tangential components of $\mathbf{t}$ are,

$$t_n = \mathbf{n} \cdot \mathbf{t} = -\frac{1}{2}\mu_0 H^2 + B_n H_n, \tag{4.3}$$

$$t_t = \mathbf{n} \times \mathbf{t} = 2\zeta\boldsymbol{\omega}\sin\beta + B_n H_t, \tag{4.4}$$

where β is the angle between the spin velocity $\boldsymbol{\omega}$ and the fluid surface normal $\mathbf{n}$ defined in Figure 4-10, where $\boldsymbol{\omega}$ is taken as being oriented vertically because the rotating magnetic field keeps the magnetic particles rotating in the horizontal plane. Applying these relationships to the surface straddling element in Figure 4-10 yields the difference in applied stress across the interface. Letting brackets [ ] denote the difference of its argument across the interface, then $[t_n] = -\frac{1}{2}\mu_0 M_n^2$, where we use the magnetic boundary conditions at the interface $[H_t] = 0$ and $[B_n] = 0$. The difference in tangential stress across the interface is given as,

$$[t_t] = -2\zeta\boldsymbol{\omega}\sin\beta \tag{4.5}$$

Examining this result yields the flow direction for a given fluid surface orientation. When $\beta = 0$, the surface is flat and the driving stress vanishes; therefore, the surface will not rotate under rotating field conditions. When the surface is concave, $\beta > 0$ and the surface counter-rotates to the applied magnetic field. When the surface is convex, $\beta < 0$ and the surface co-rotates with the applied magnetic field.

4.4 Discussion

By placing the surface of a cylindrical vessel filled with ferrofluid at the top, middle, and bottom of a motor stator winding, it is evident that the flow direction at the surface depends on the placement in the motor. Therefore, the fringing fields have a significant effect on the ferrofluid flow.

Placing the vessel of ferrofluid in the center of the motor stator winding and exciting with simultaneous applied rotating and DC axial magnetic fields, the direction

of rotation can be changed by raising the DC axial field above some threshold that results in the fluid surface curvature becoming convex. Measurements are taken of the threshold axial magnetic field for varying rotating magnetic field direction, amplitude, and frequency. These experiments measure the value of the DC axial magnetic field that results in the ferrofluid surface curvature being flat.

An analysis is also included to explain the reversal in flow direction due to a change in fluid surface curvature.

Chapter 5

Concluding Remarks

This work has focused on three major magnetic fluid experiments: measurement of magnetic field induced torques on a cylindrical spindle filled with MR fluid and excited by a uniform rotating magnetic field, a characterization of spiral flows and continuous-to-discrete phase transitions of ferrofluid drops contained in Hele-Shaw cells and excited with simultaneous applied rotating and DC axial magnetic fields, and measurement of the threshold DC axial magnetic field that results in ferrofluid flow direction reversing in a cylindrical vessel filled with ferrofluid and excited by simultaneous applied rotating and DC axial magnetic fields.

The MR fluid mixtures generate a significant torque on a stationary spindle when excited by a uniform rotating magnetic field. The generated torques are in the same direction as the rotating magnetic field for both ferrofluids and MR fluids. As the rotating magnetic field amplitude is increased, the torque generated also increased. However, the torque decreases for increasing magnetic field frequency in MR fluids and increased with magnetic field frequency for ferrofluids. By calculating the dependence of the magnetic body torque density on the applied magnetic field frequency, the different torque frequency dependence between the two fluids becomes evident. There is a critical magnetic field frequency $f_b \sim \frac{1}{2\pi\tau}$, such that the torque will decrease with frequency when measurements are taken above f_b (MR fluids), and increase with frequency when measurements are taken below f_b (ferrofluids). This critical magnetic field strength depends on the magnetic relaxation time constant τ which

is proportional to the particle volume. Therefore, by this qualitative model, this distinction between the ferrofluids and the MR fluids is primarily due to the different particle sizes in each of the fluids.

Experiments conducted on continuous-to-discrete phase transitions of ferrofluid drops aimed to measure the number of smaller ferrofluid drops that result from the transition, the threshold DC axial magnetic field needed for the transition to occur, and the surface area of the ferrofluid drop as it evolves under increasing DC axial fields. A minimum free-energy analysis is included to calculate the number of smaller ferrofluid drops, and the threshold axial field. Comparing the calculated results to the measured results shows that calculated results are of the same order of magnitude as the measured results. Differences can be attributed to the use of a linear magnetization relationship instead of the Langevin relationship for paramagnetic behavior and the neglect of the rotating field in the magnetic field energy. Use of this linear relationship yields values for the magnetization that are larger than the true value, as the ferrofluid approaches magnetic saturation.

Magnetic field induced ferrofluid flow reversals are examined in the last section. An analysis is included to show that the flow rotational direction depends on the fluid surface curvature. Concave surfaces exhibit counter-flow, flat surfaces have no flow, and convex surfaces exhibit co-flow with the rotating magnetic field. The direction of rotational flow in a cylindrical vessel filled with a water-based ferrofluid and excited by a uniform rotating magnetic field is shown to be dependent on the location of the fluid surface inside of the motor. Therefore, we place a vessel of ferrofluid in a rotating field and control the fluid surface curvature with the application of a DC axial magnetic field. When the field rises above some threshold value, the surface changes from being concave to convex resulting in the direction of fluid rotation reversing. Measurements are plotted of the threshold axial magnetic field for varying rotating magnetic field direction, amplitude and frequency.

Appendix A

Creating A Uniform Rotating Magnetic Field

The uniform rotating magnetic field is created with a Y connected three phase 2 pole motor stator winding. An ideal 2 pole machine would create a spatially uniform rotating magnetic field when balanced three phase current is supplied to its windings. However, because of the fringing fields at the top and bottom ends of the motor winding and in the region near the slots in the magnetic core, the magnetic field is not exactly uniform. However, the magnetic field is very uniform in the central region far from the top and bottom and far from the outer radius near the slots in the iron core. Each ampere (rms) produces 38 Gauss (rms) rotating field.

A.1 Three Phase Source

The motor requires three phase current to create a rotating magnetic field. This requires the current in each winding to be a sinusoid of the same amplitude, but 120 degrees out of phase. However, a two channel amplifier was used in the following manner with one phase grounded. A schematic of the motor windings is shown in Figure A-1. Each winding is assumed to be identical, therefore $Z_A = Z_B = Z_C = Z$. We aim to show that $V_B = V_A e^{\pm j\frac{\pi}{3}}$ will achieve three phase balanced currents in the three windings that create clockwise or counterclockwise rotating magnetic fields.

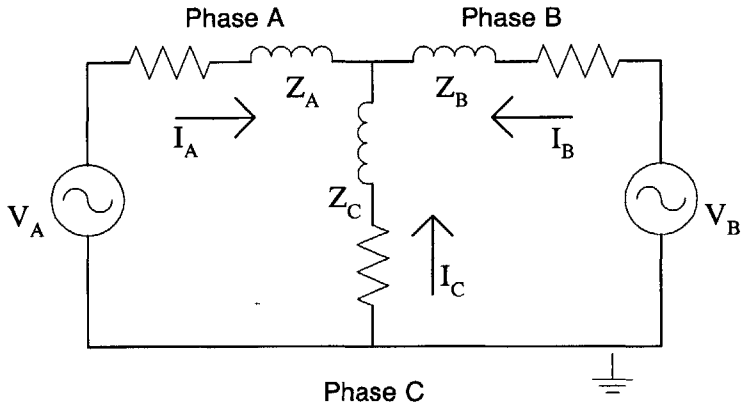

Figure A-1: Schematic of the motor windings connected to a two channel source where $V_B = V_A e^{\pm j\frac{\pi}{3}}$.

First, calculation of the currents in terms of the voltages V_A and V_B yields,

$$\begin{aligned} I_A &= \frac{1}{3Z}(2V_A - V_B) = \frac{V_A}{\sqrt{3}Z} e^{\mp j\frac{\pi}{6}} \\ I_B &= \frac{1}{3Z}(2V_B - V_A) = \frac{V_A}{\sqrt{3}Z} e^{\pm j\frac{\pi}{2}} \\ I_C &= \frac{-1}{3Z}(V_A + V_B) = \frac{V_A}{\sqrt{3}Z} e^{\pm j\frac{7\pi}{6}} \end{aligned} \tag{A.1}$$

Each current has the same amplitude but a $\frac{2\pi}{3}$ phase difference, hence the creation of balanced three phase currents in the motor stator winding.

Two Model 75 WaveTek Arbitrary Waveform Generators were synchronized to produce two identical sine waves, 60 degrees out of phase. Both signals were amplified by the AE Techron 5050 Linear Amplifier and connected to two of the windings on the 2 pole motor. The third motor winding (C) is connected directly to ground. This arrangement creates balanced three phase currents with $120° = \frac{2\pi}{3}(radians)$ phase differences which creates clockwise or counterclockwise rotating magnetic fields by choosing a phase difference of $60°$ (clockwise) or $-60°$ (counterclockwise) for the input voltages. The direction of rotation is determined by placing a compass needle in a low frequency rotating field. Each winding's current amplitude is monitored with a Fluke 45 Dual Display Multimeter connected in series with the winding. Each

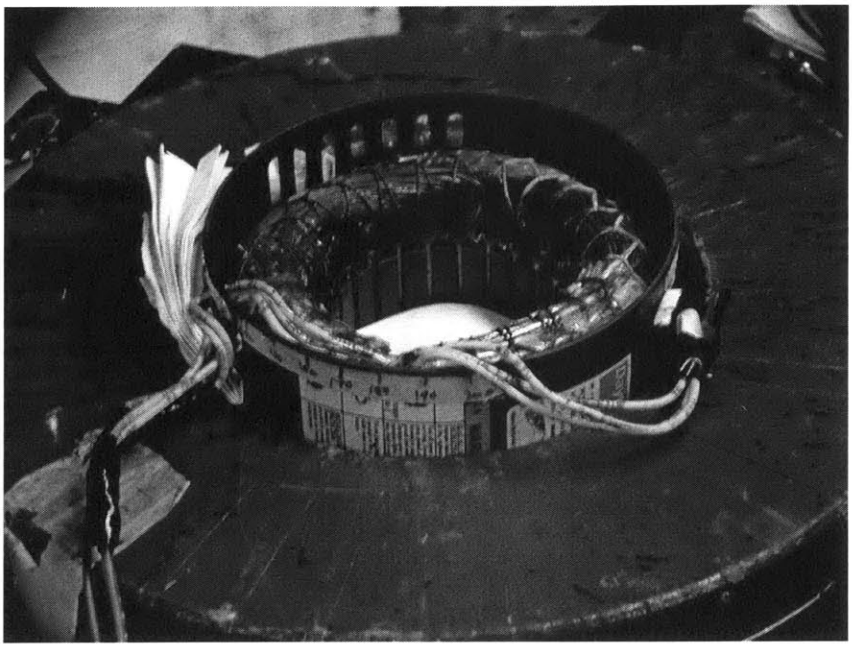

Figure A-2: A picture of the motor stator winding inside of the DC magnetic toroid winding.

ampere (rms) of current increases the magnetic field by 38 Gauss (rms). A picture of the motor inside of the DC magnetic toroid is shown in Figure A-2. The inside diameter of the motor core is 116 mm, and the height of the motor core is 65 mm.

Appendix B

Video Digitization

The experiments performed in Chapter 3 were recorded on an analog video camera (Panasonic KR222) and then digitized using MGI VidoeWave software. A description of the process in digitizing the video is presented.

The Sony TRV900 digital video camera could not be used in these experiments because the camera had to be positioned very close to the magnets to focus onto the Hele-Shaw cell. This put the camera so close to the magnets that the image was distorted. The Panasonic analog camera could be placed further away from the magnets and still focus on the experiment. In addition, the VHS video cassette used with the Panasonic camera, was external in a Panasonic Omnivision Model PV-V4521 VCR, which could be placed far from the magnets to avoid image distortion or erasure. The Sony video camera used mini DV cassettes inside the camera, within reach of the magnetic field that could cause erasure.

When digitizing the analog video, the video cassette tape must be loaded into the VCR, and the RCA video output of the VCR need be connected to the Dazzle input device. Next, open the VideoWave software. To capture the video, the capture environment must be set by pushing the capture button shown in Figure B-1. Once in the capture environment, start playing the cassette tape in the VCR. When you would like to start capturing the video, click the "Video and Audio" button to start the recording process. When you would like to stop capturing the video, click the "Stop" button. This will show the captured video in the "Video Display" region.

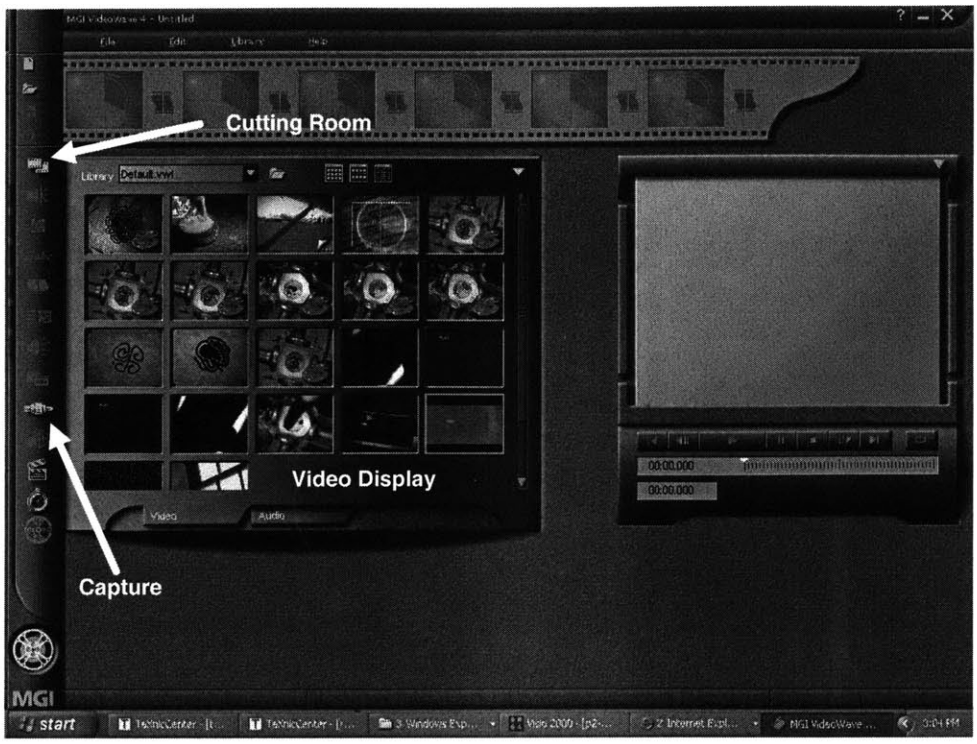

Figure B-1: Picture demonstrating the location of features in the MGI VideoWave software.

To pull still frame pictures from the video, one must enter the "Cutting Room" environment by pushing the button shown in Figure B-1. Once in the "Cutting Room", double click the video in the "Video Display" that you would like to take the still frames from. This will show the video in the on-screen TV environment. Set the position marker to the location in the video that you would like to take a picture of, and then click the image button. This will bring the typical windows explorer dialog box asking where to put the extracted image on the hard disk. Select the directory and give the file a name, then select OK.

Appendix C

Monitoring the DC Axial Magnetic Field In Labview

Labview was used to record the DC axial magnetic field in real time for the phase transition experiments. The current entering the electromagnetic is converted to a voltage using the Tektronix TM502A current probe, and voltage output of the current probe is monitored by Labview. Labview would display a plot of the current in time, and output the measurements into a spreadsheet format for analysis. The graphical Labview program is shown in Figure C-1.

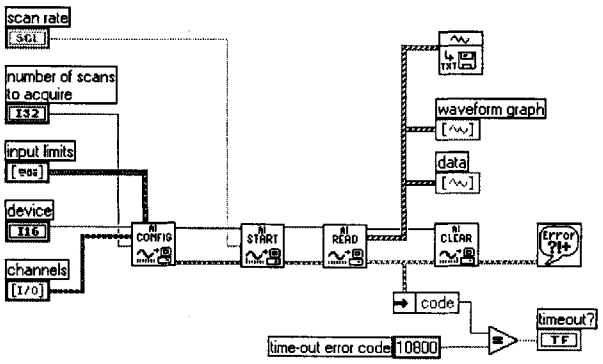

Figure C-1: Illustration of the Labview program used to monitor the DC axial magnetic field used in the phase transition experiments.

Appendix D

Phase Transition Data

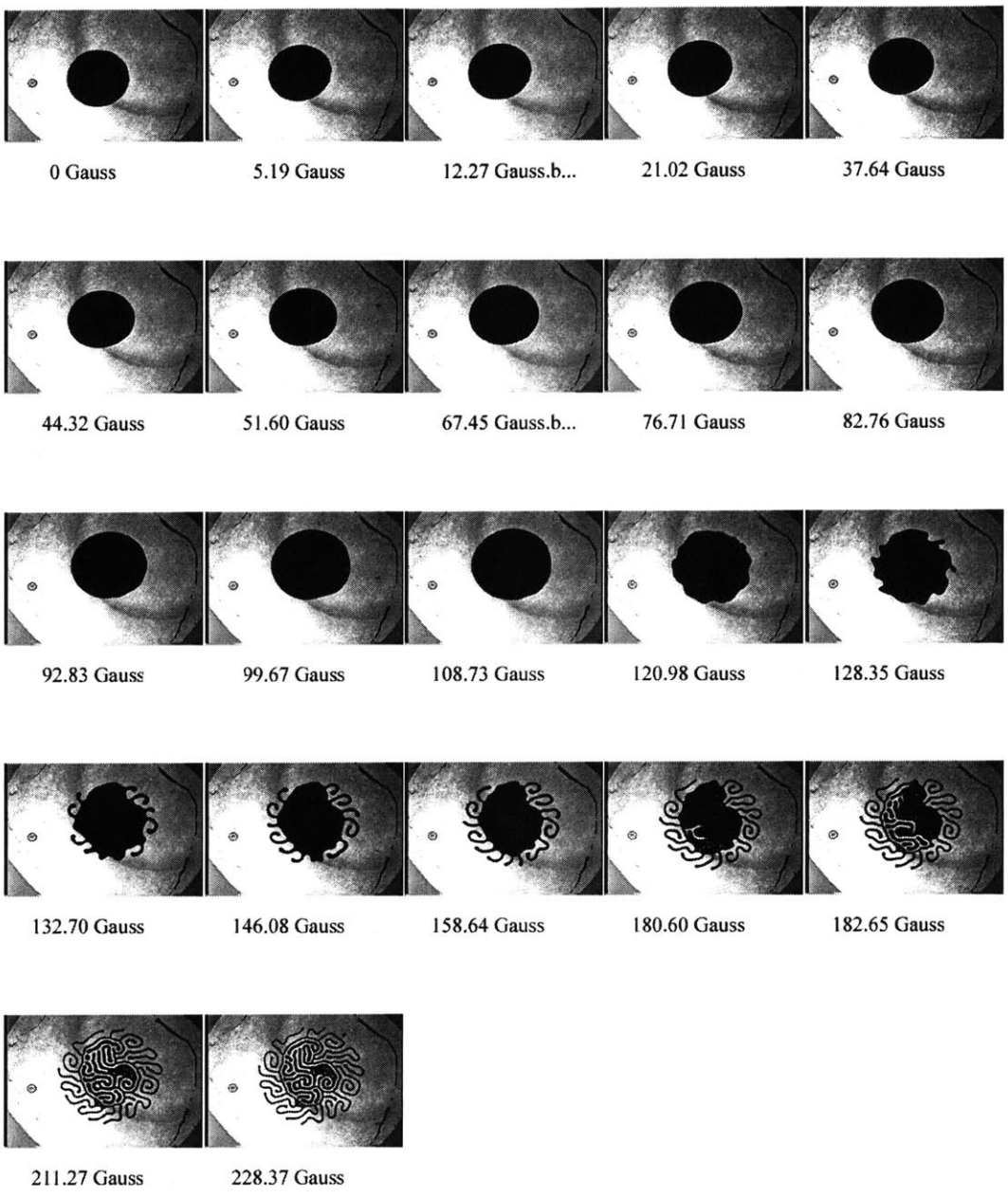

Figure D-1: Sequence 1: 200 μl, 0.9 mm, 25 Hz, 39.9 Gauss (rms)

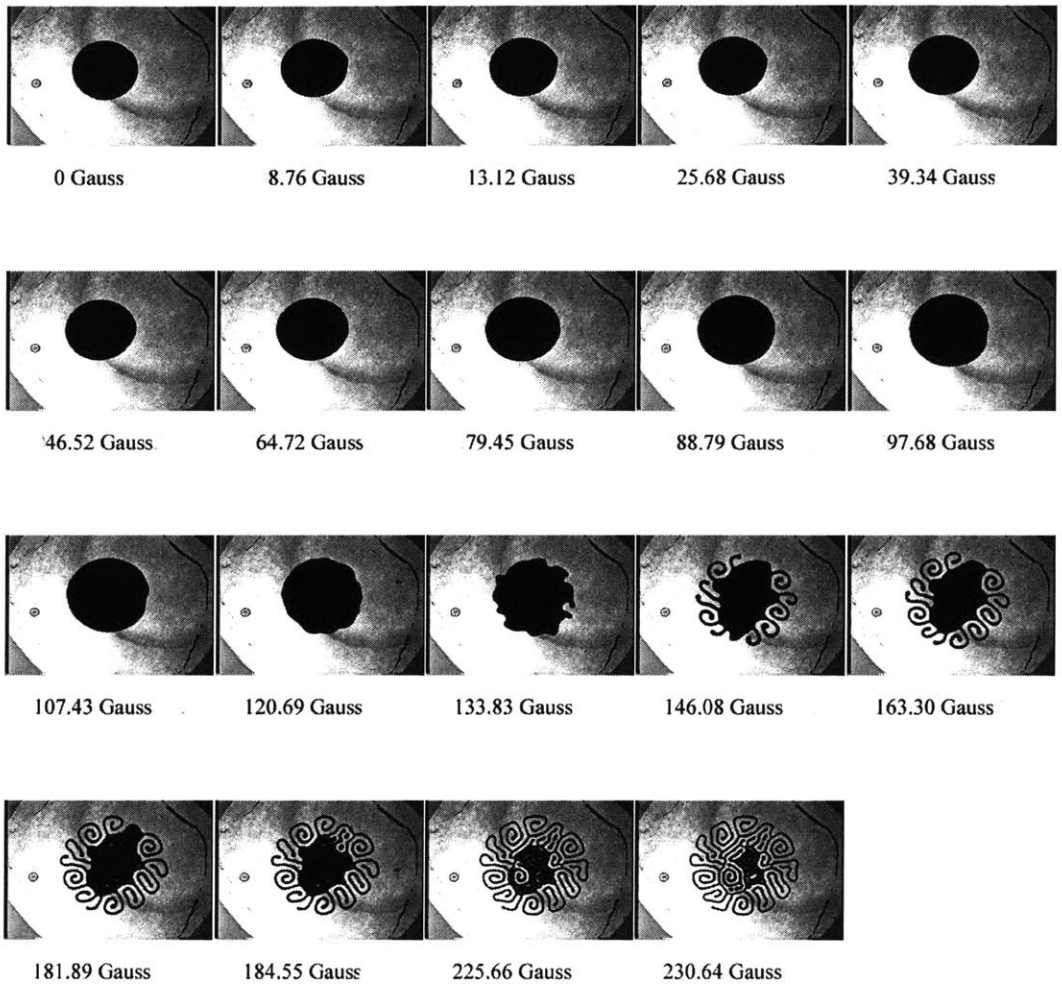

Figure D-2: Sequence 2: 200 μl, 0.9 mm, 25 Hz, 39.9 Gauss (rms)

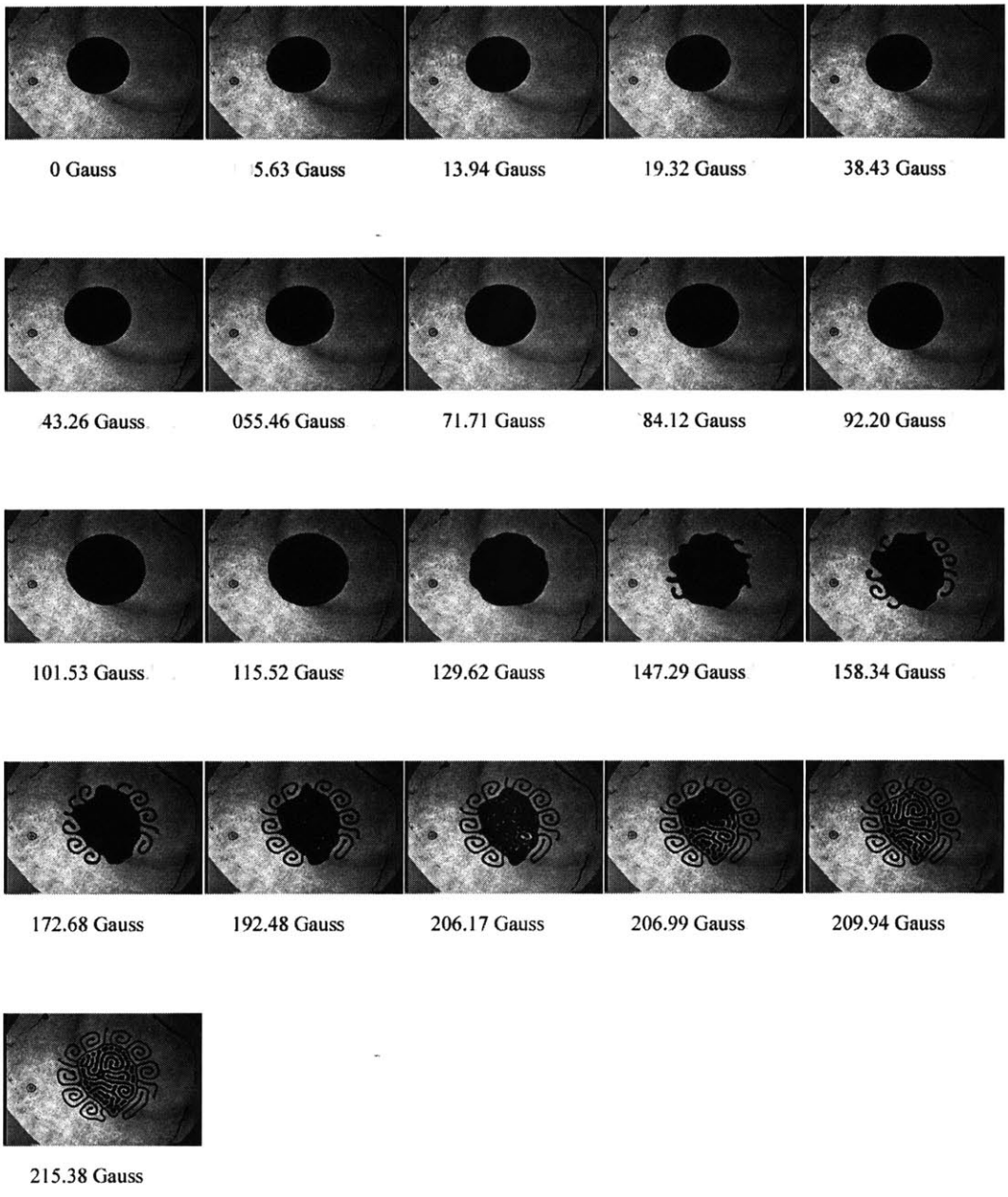

Figure D-3: Sequence 1: 200 μl, 0.9 mm, 25 Hz, 43.7 Gauss (rms)

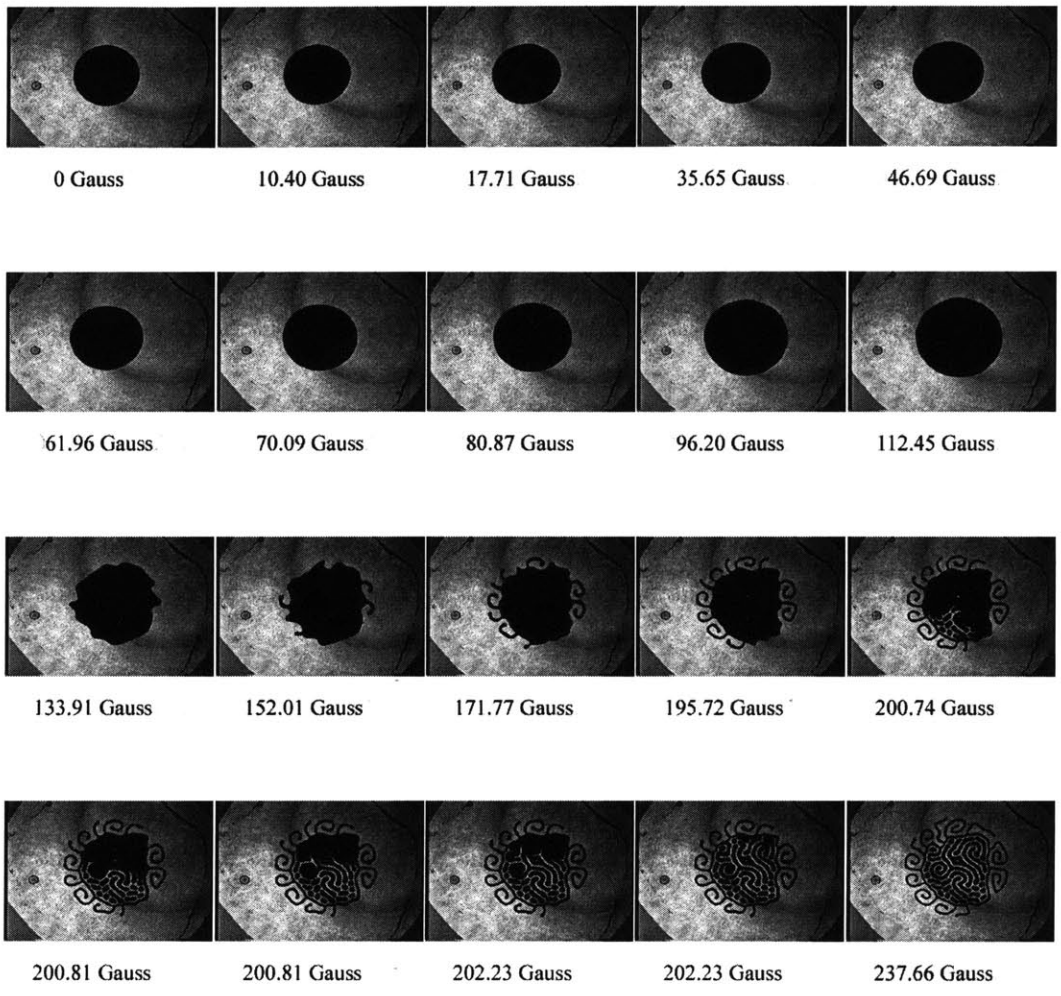

Figure D-4: Sequence 2: 200 μl, 0.9 mm, 25 Hz, 43.7 Gauss (rms)

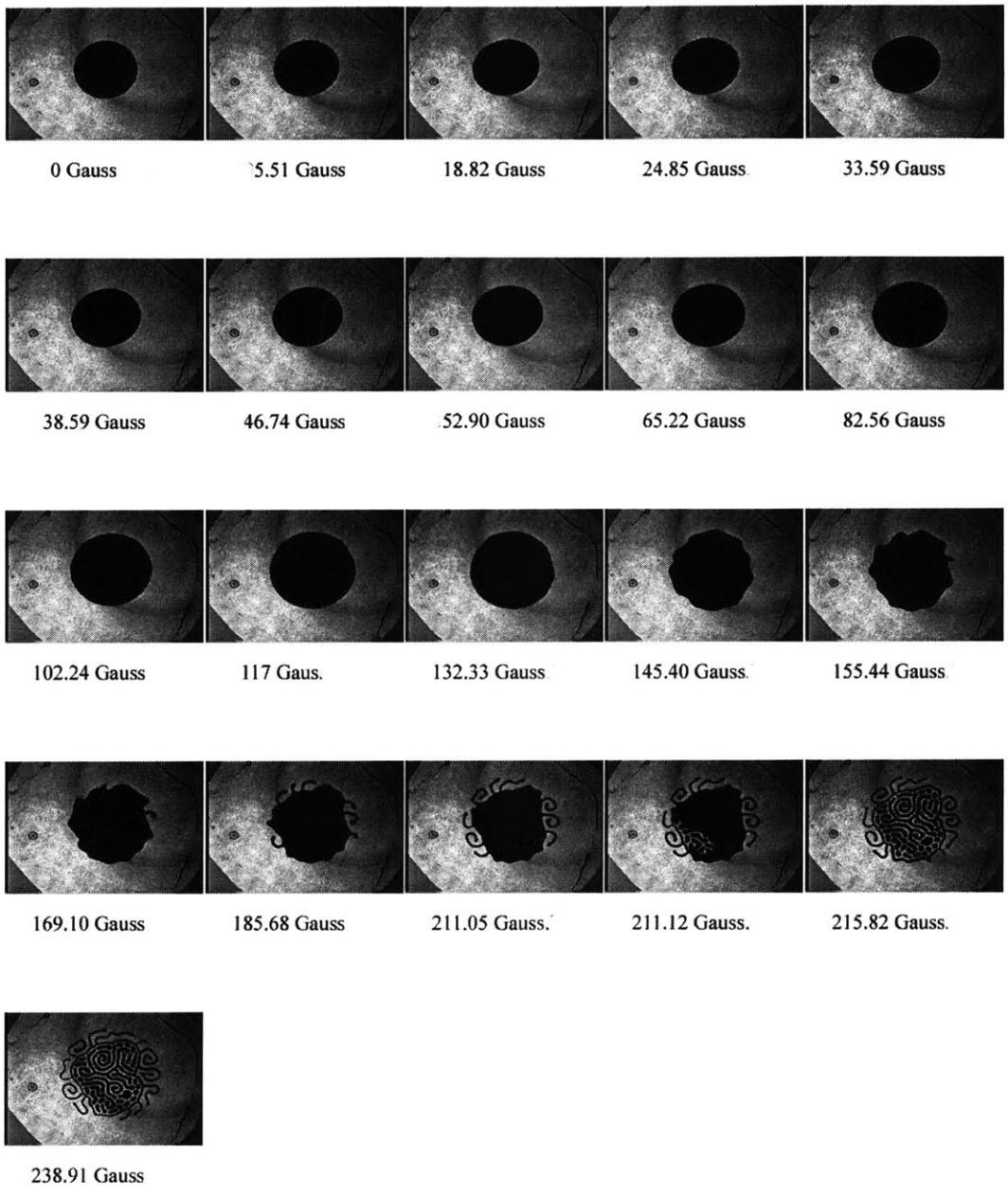

Figure D-5: Sequence 1: 200 μl, 0.9 mm, 25 Hz, 47.5 Gauss (rms)

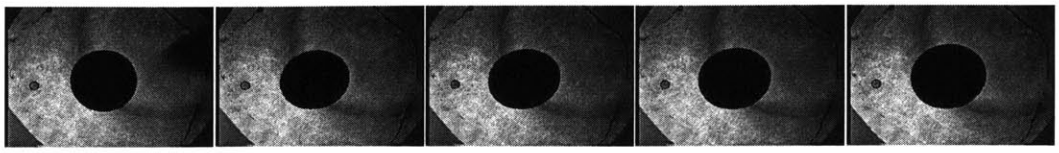

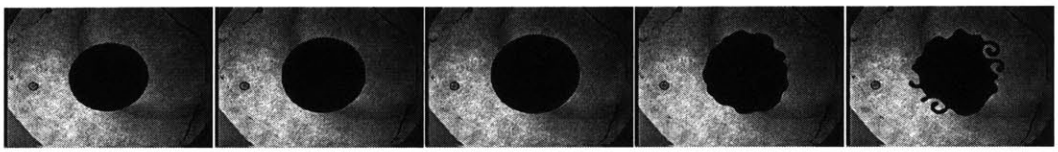

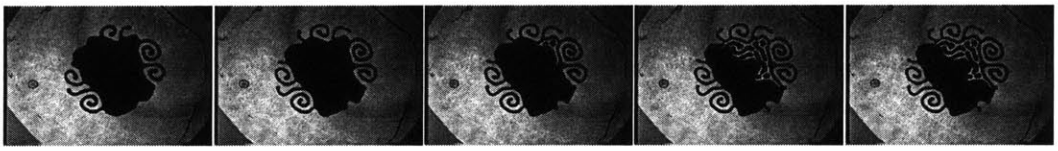

Figure D-6: Sequence 2: 200 μl, 0.9 mm, 25 Hz, 47.5 Gauss (rms)

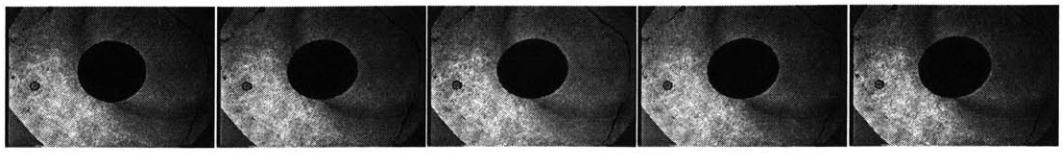

0 Gauss 10.03 Gauss 14.66 Gauss 20.04 Gauss 29.81 Gauss

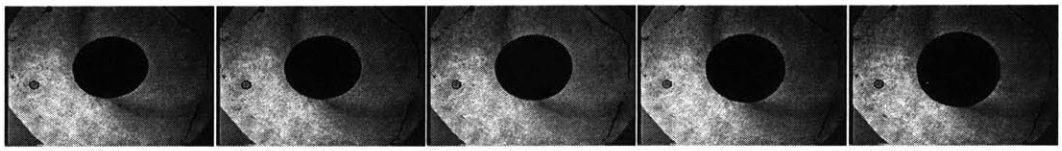

45.10 Gauss 56.79 Gauss 63.77 Gauss. 81.61 Gauss 101.74 Gauss

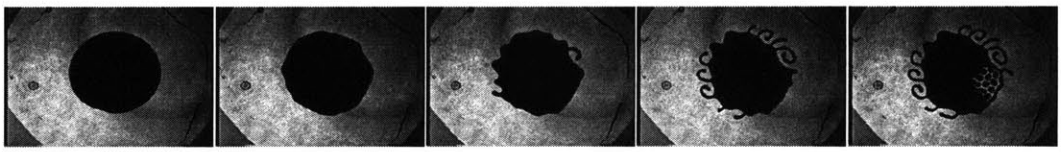

117.36 Gauss 132.03 Gauss 159.18 Gauss 186.52 Gauss 194.67 Gauss.

199.39 Gauss 232.90 Gauss 237.17 Gauss.

Figure D-7: Sequence 1: 200 μl, 0.9 mm, 25 Hz, 51.3 Gauss (rms)

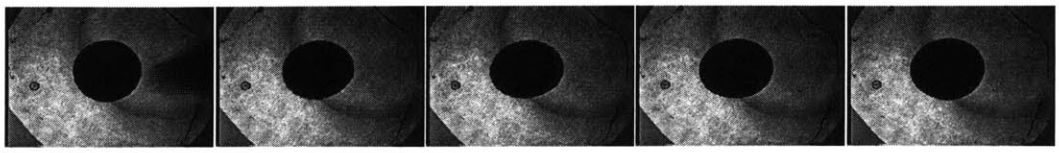

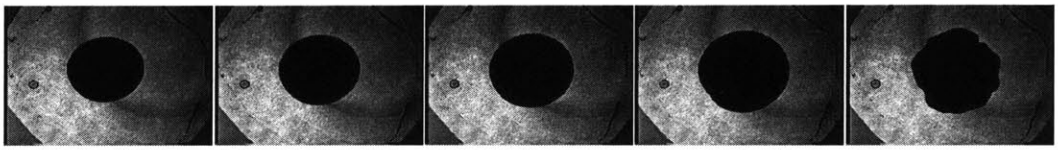

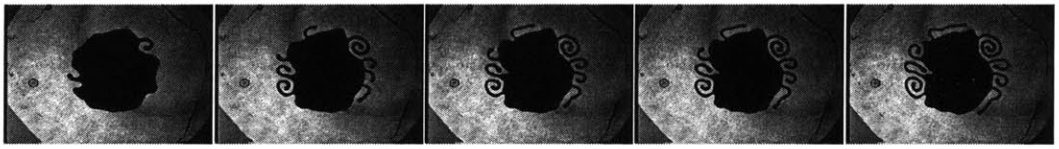

Figure D-8: Sequence 2: 200 μl, 0.9 mm, 25 Hz, 51.3 Gauss (rms)

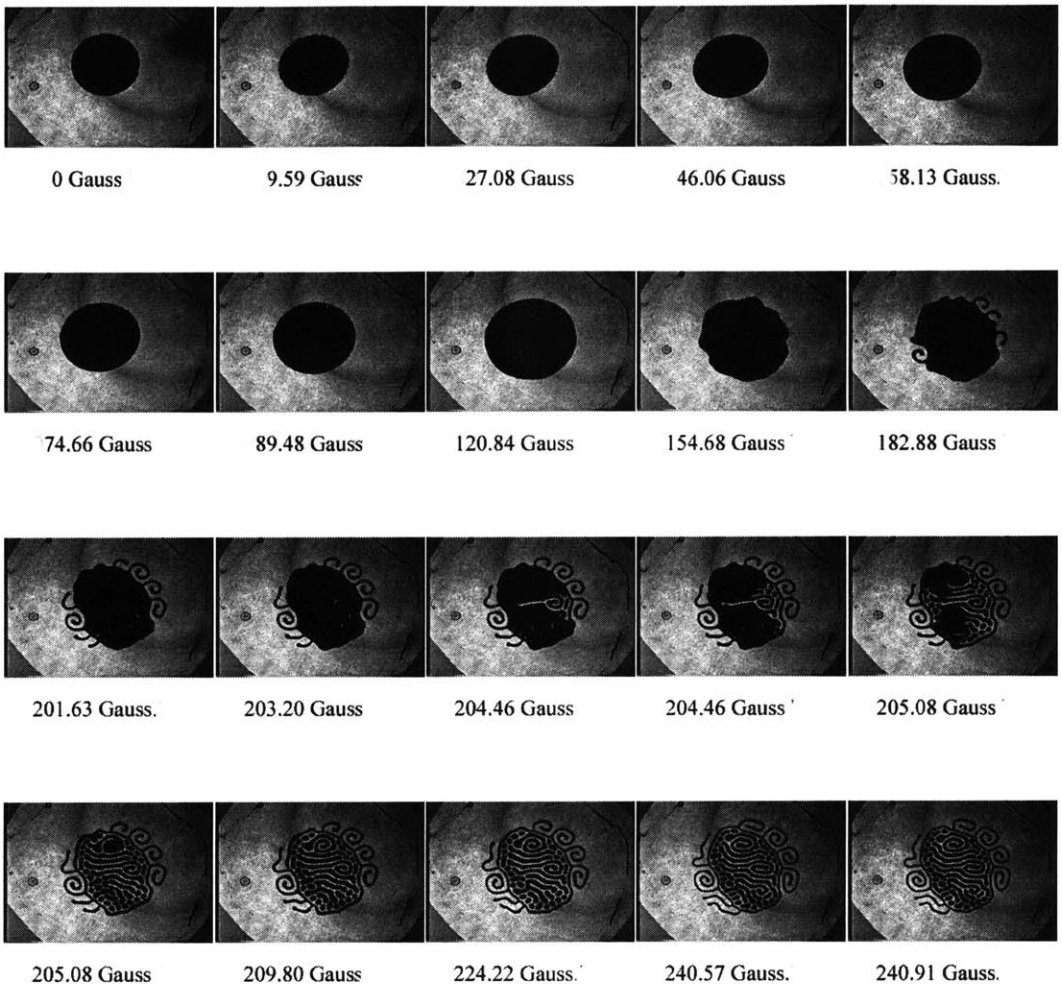

Figure D-9: Sequence 1: 200 μl, 0.9 mm, 25 Hz, 55.1 Gauss (rms)

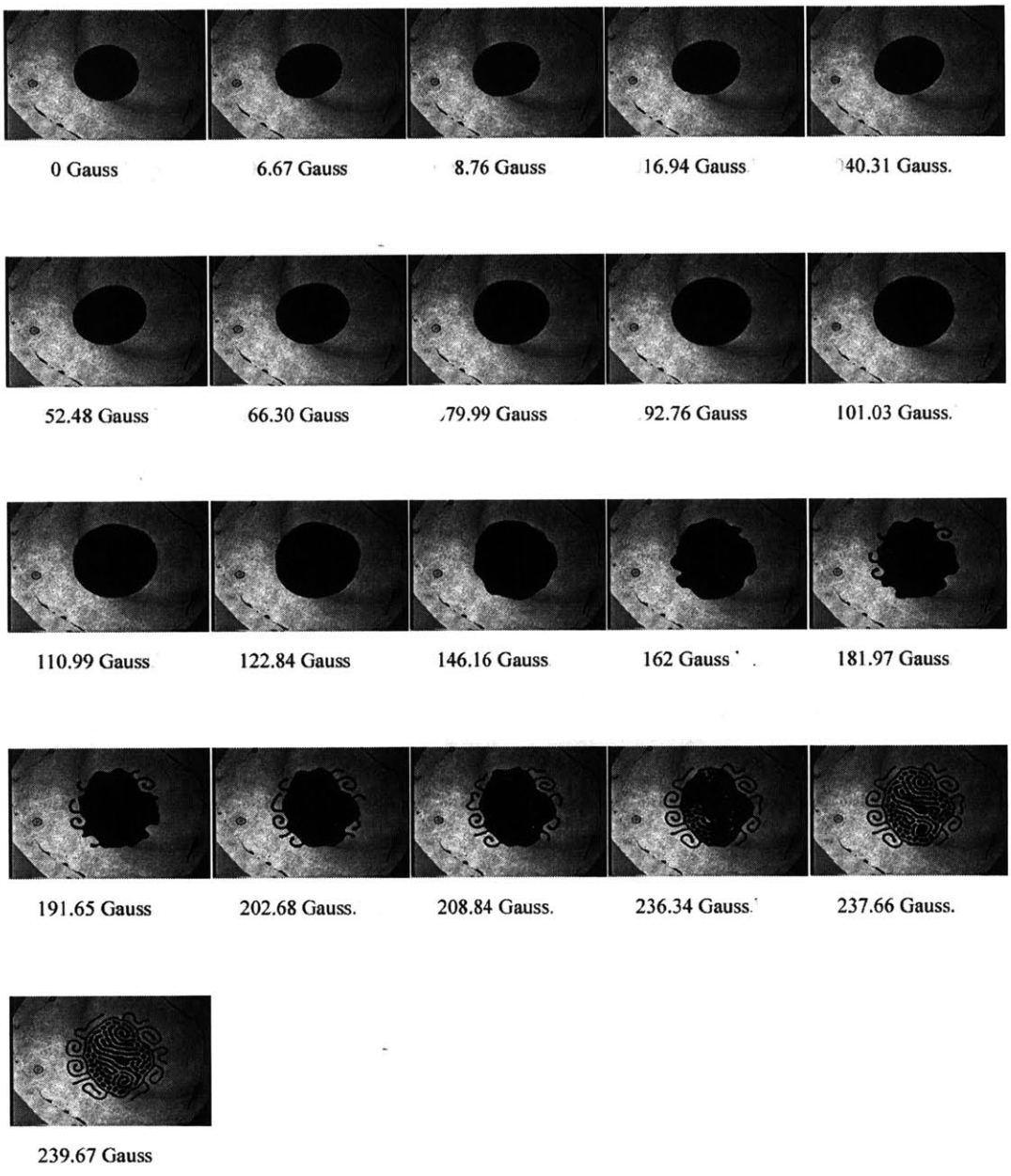

Figure D-10: Sequence 2: 200 μl, 0.9 mm, 25 Hz, 55.1 Gauss (rms)

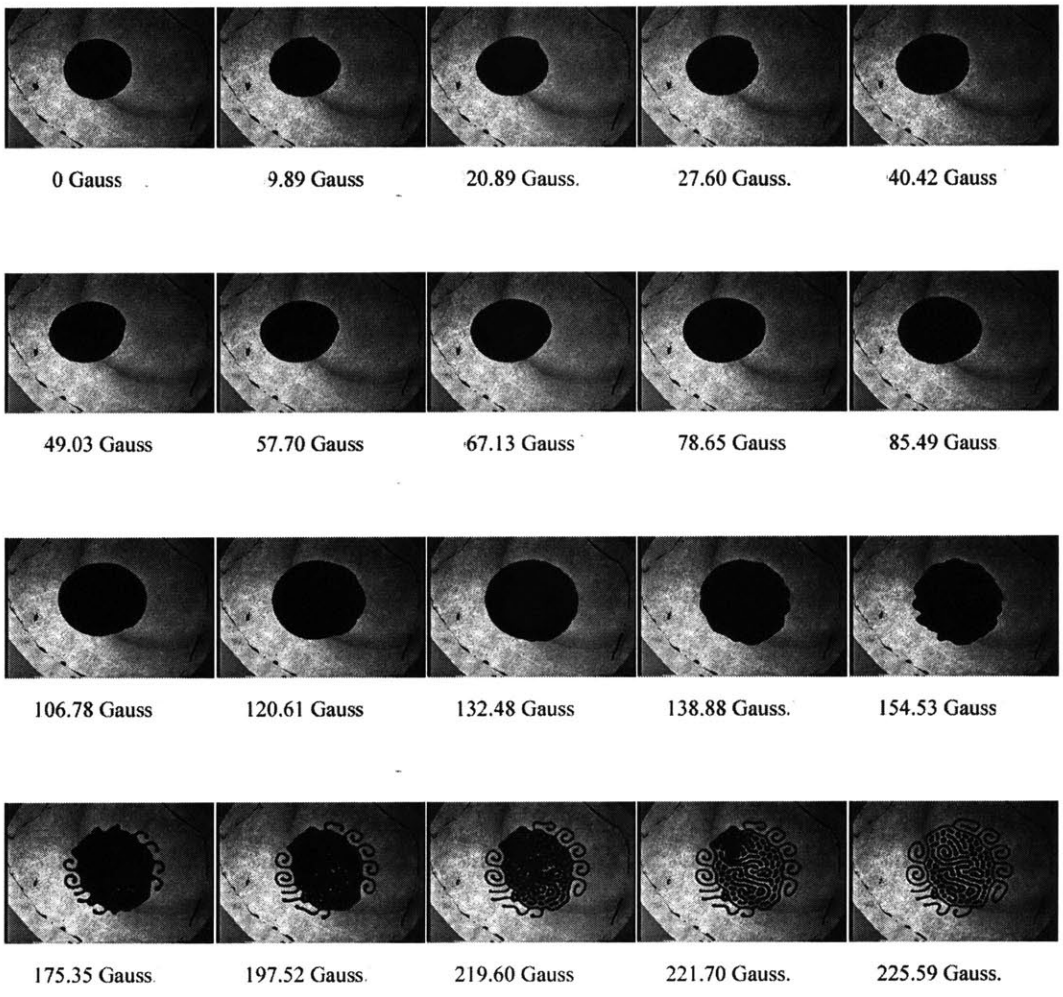

Figure D-11: Sequence 1: 200 μl, 0.9 mm, 25 Hz, 58.9 Gauss (rms)

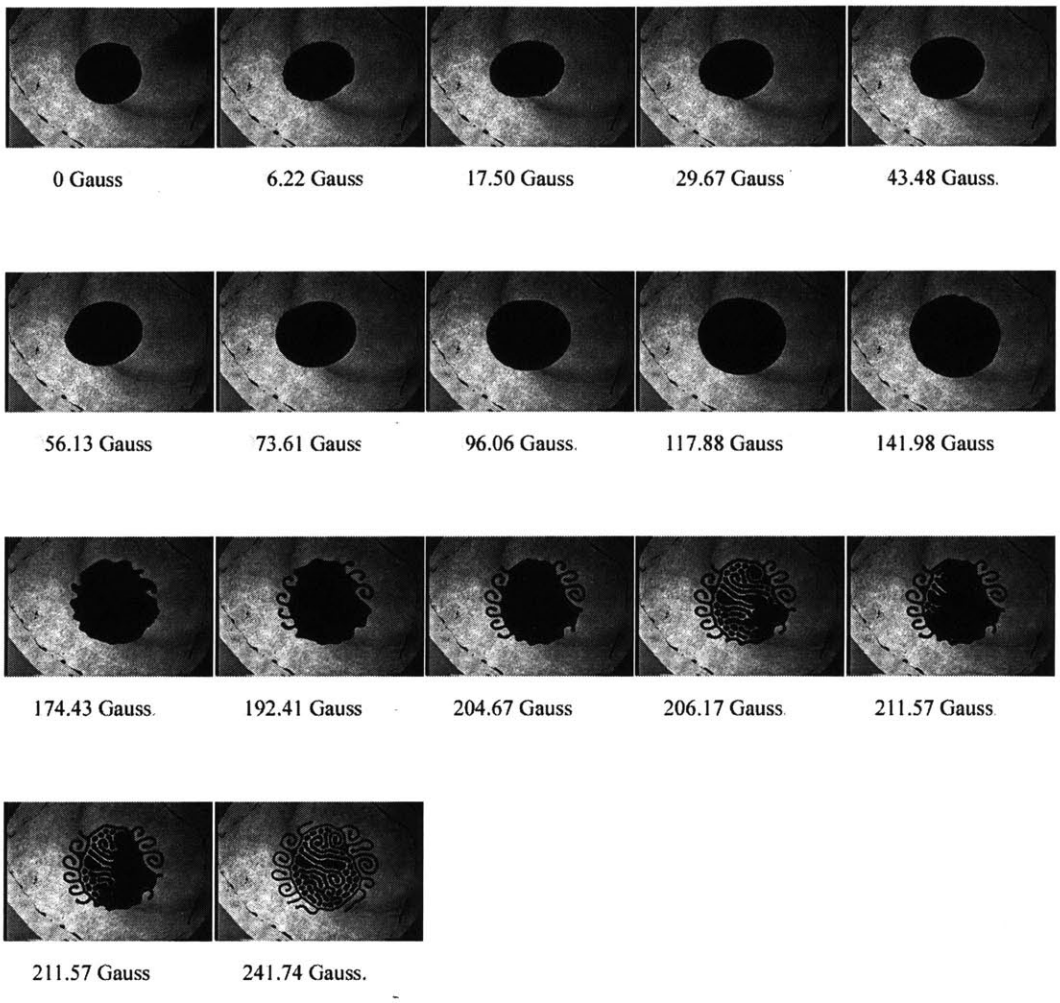

Figure D-12: Sequence 2: 200 μl, 0.9 mm, 25 Hz, 58.9 Gauss (rms)

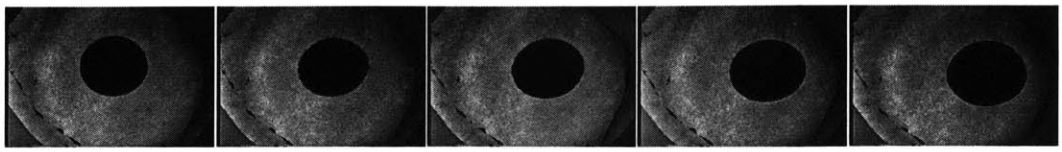

0 Gauss 12.75 Gauss 33.04 Gauss 51.36 Gauss 73.22 Gauss

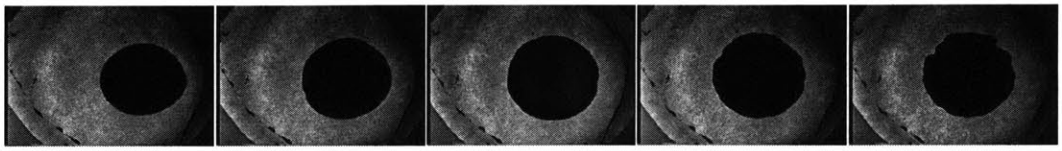

97.83 Gauss 122.76 Gauss 137.60 Gauss 161.85 Gauss 170.47 Gauss

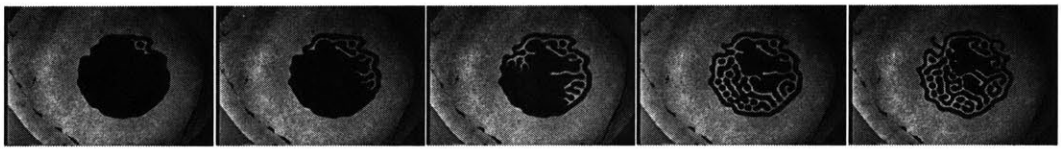

173.82 Gauss 175.27 Gauss 175.96 Gauss 179.08 Gauss 197.97 Gauss

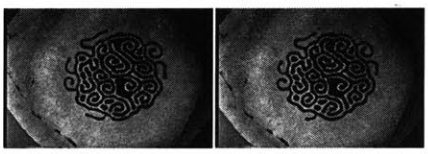

203.50 Gauss 226.45 Gauss

Figure D-13: Sequence 1: 200 μl, 0.9 mm, 25 Hz, 62.7 Gauss (rms)

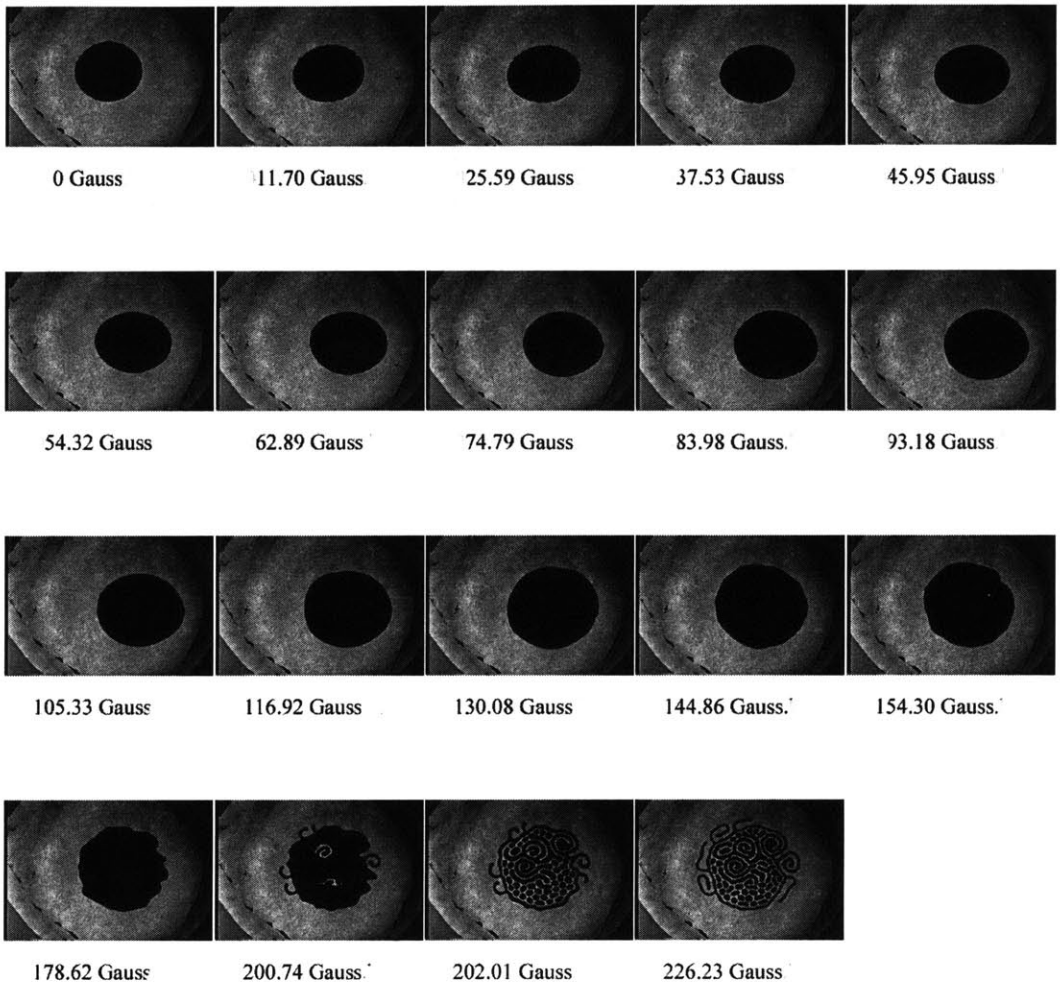

Figure D-14: Sequence 2: 200 μl, 0.9 mm, 25 Hz, 62.7 Gauss (rms)

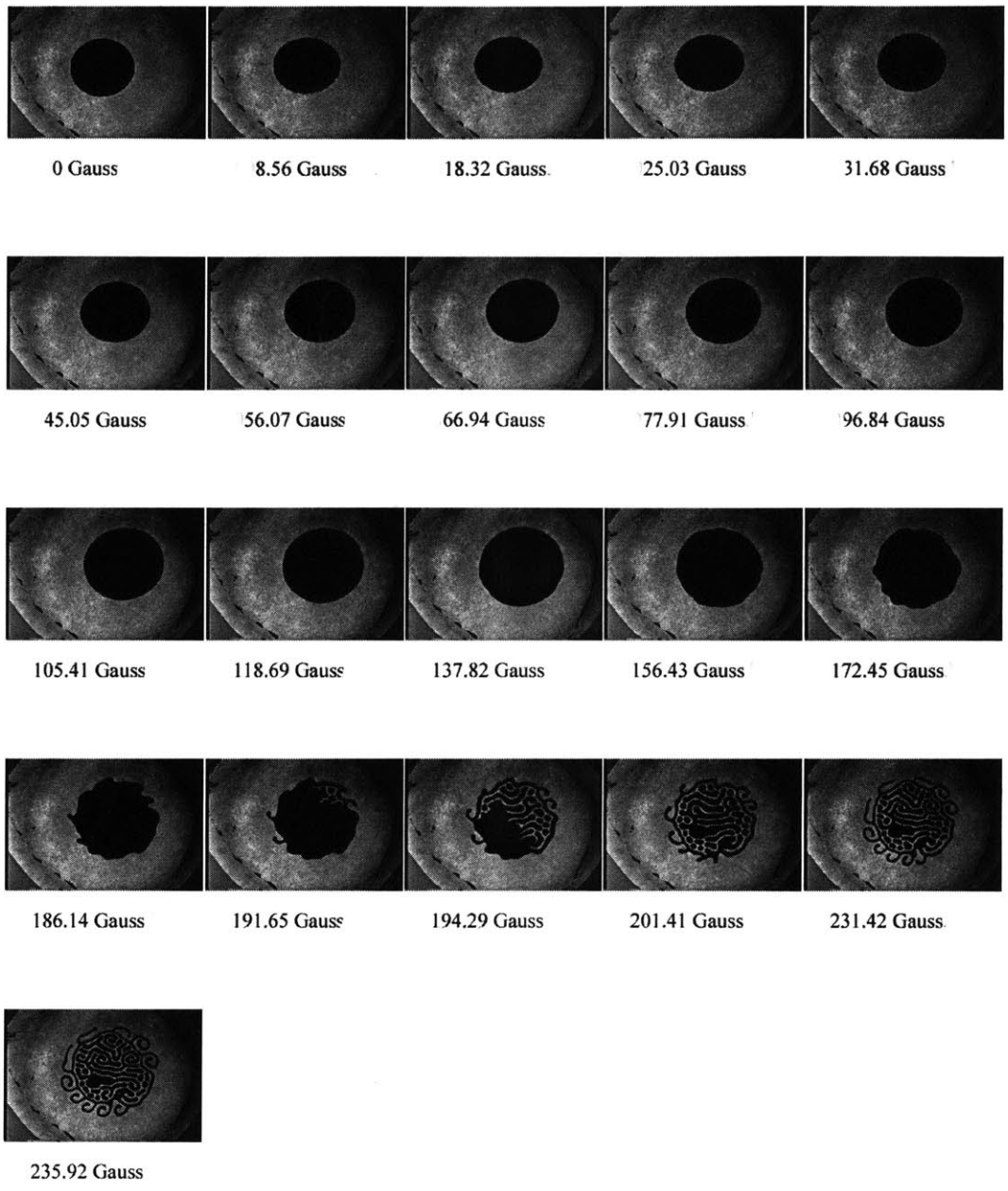

Figure D-15: Sequence 1: 200 μl, 0.9 mm, 25 Hz, 66.5 Gauss (rms)

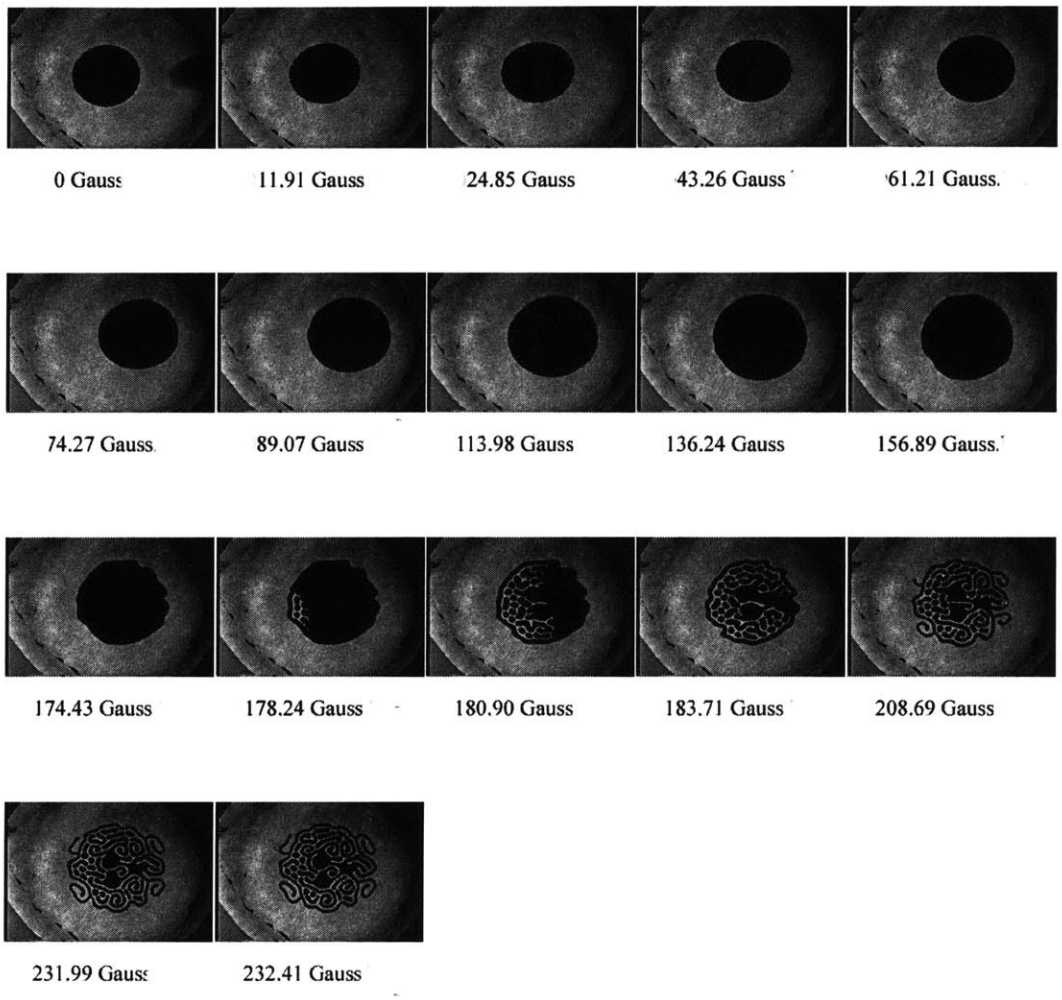

Figure D-16: Sequence 2: 200 μl, 0.9 mm, 25 Hz, 66.5 Gauss (rms)

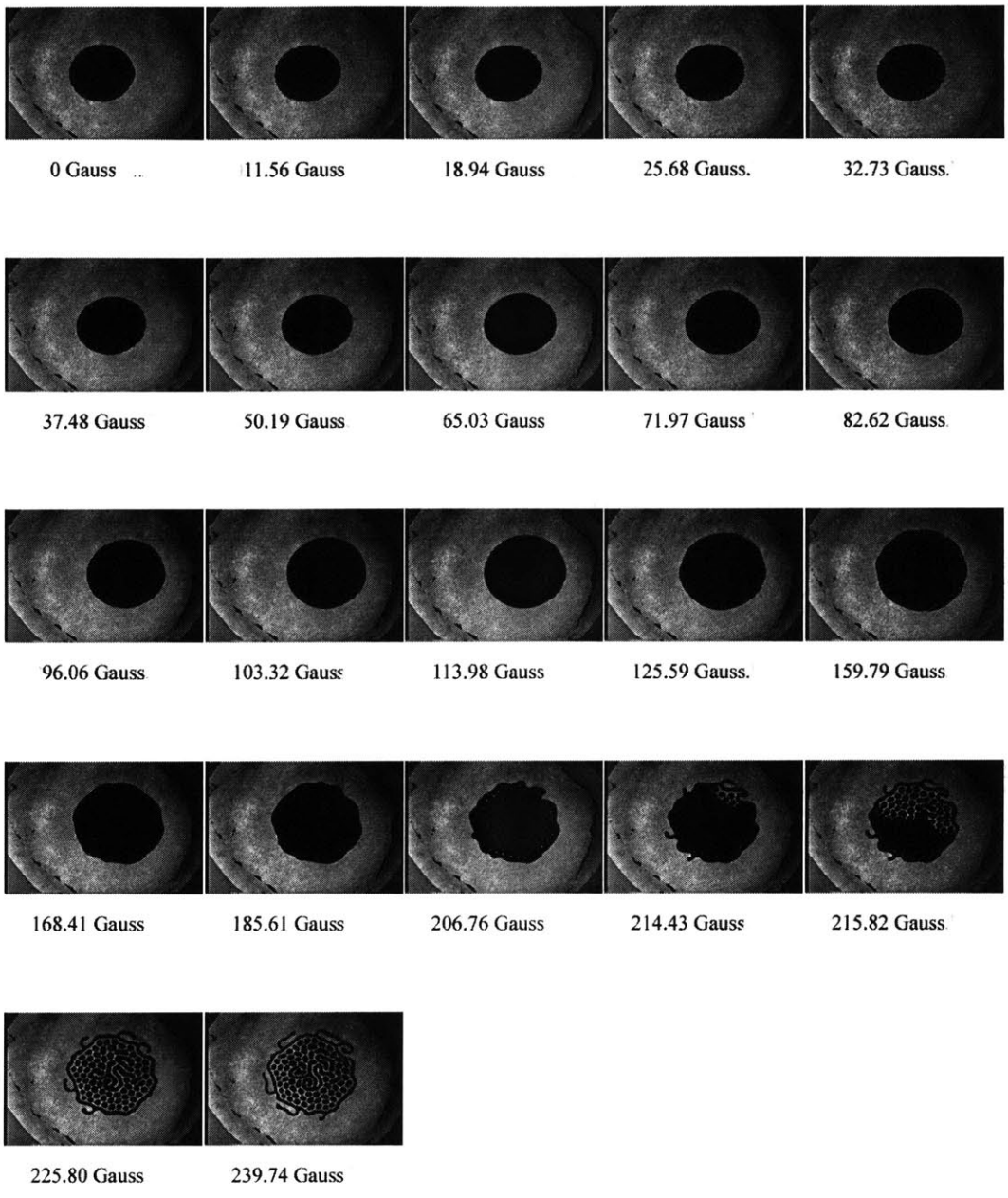

Figure D-17: Sequence 1: 200 μl, 0.9 mm, 25 Hz, 70.3 Gauss (rms)

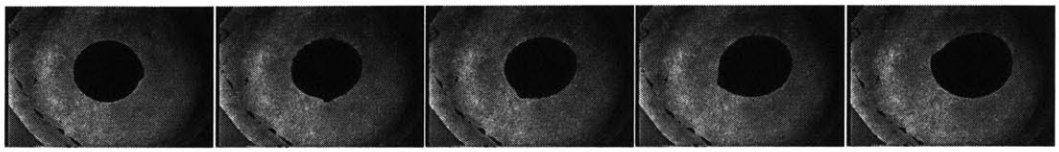

0 Gauss 6.79 Gauss 18.24 Gauss 36.27 Gauss 63.27 Gauss

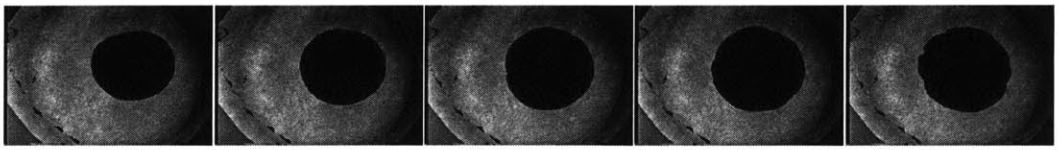

83.58 Gauss 102.46 Gauss 129.03 Gauss. 147.83 Gauss 169.94 Gauss.

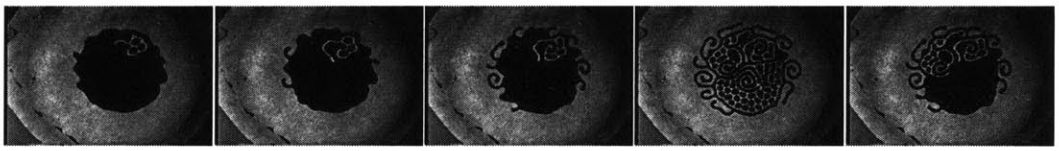

194.67 Gauss 204.84 Gauss 220.04 Gauss 222.14 Gauss. 226.45 Gauss

227.66 Gauss

Figure D-18: Sequence 2: 200 μl, 0.9 mm, 25 Hz, 70.3 Gauss (rms)

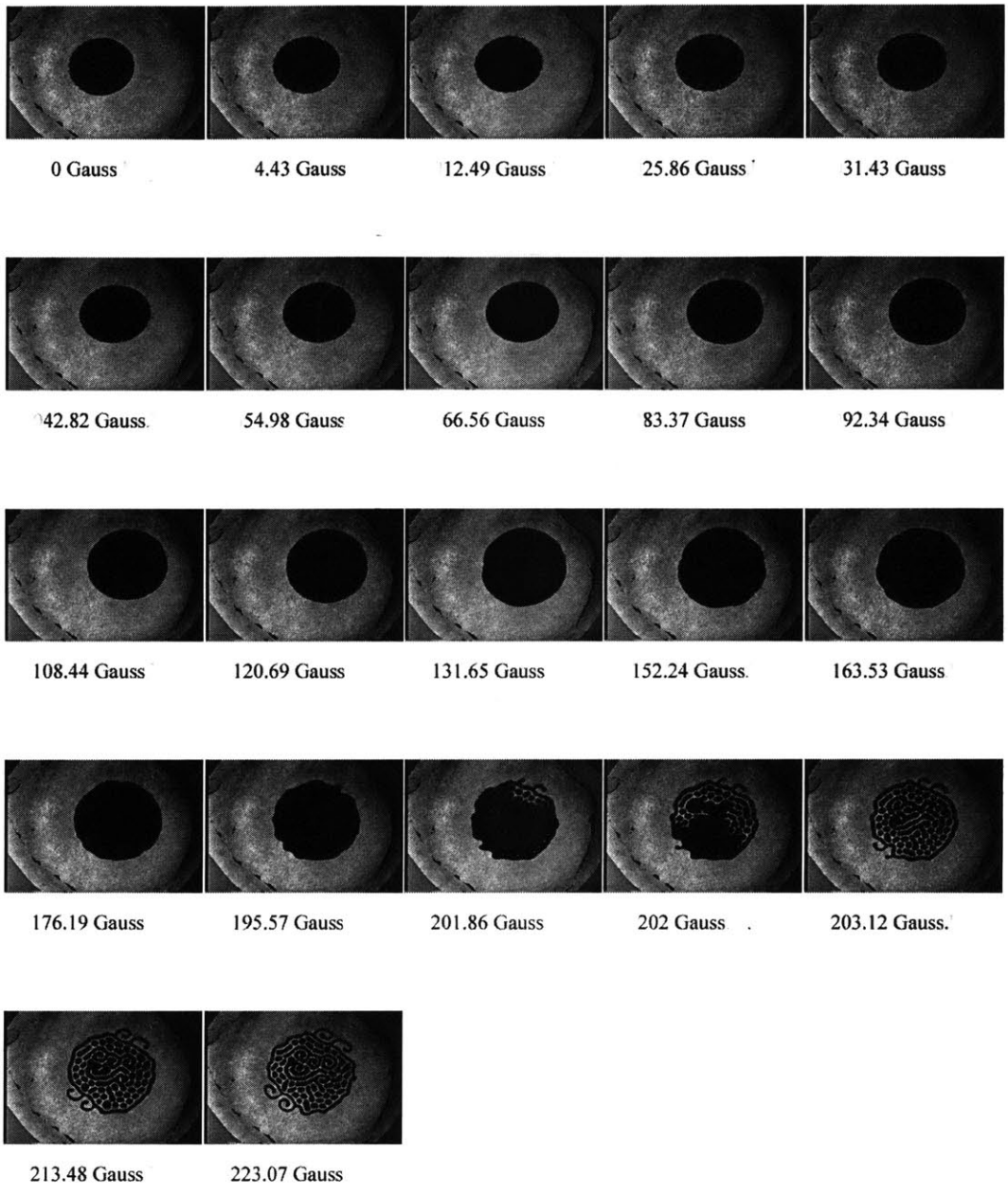

Figure D-19: Sequence 1: 200 μl, 0.9 mm, 25 Hz, 74.1 Gauss (rms)

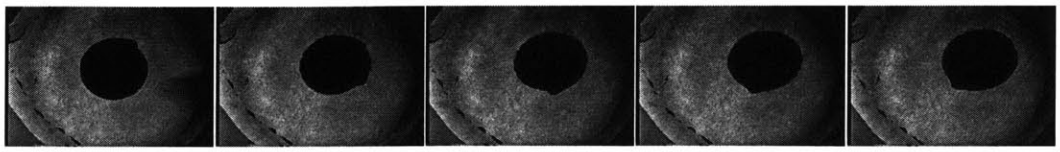

0 Gauss 4.96 Gauss 12.60 Gauss. 26.10 Gauss 42.16 Gauss

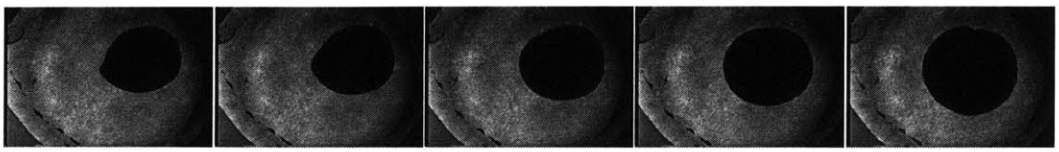

65.79 Gauss 82.83 Gauss 99.74 Gauss 113.76 Gauss 138.88 Gauss.

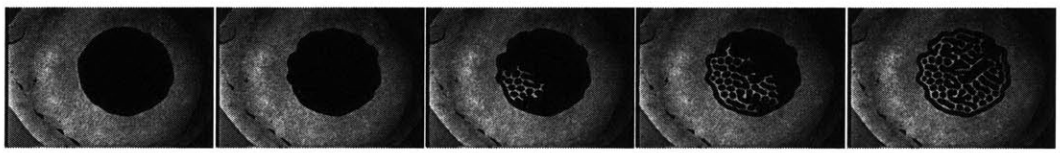

155.13 Gauss 181.51 Gauss. 188.26 Gauss. 189.62 Gauss 190.75 Gauss.

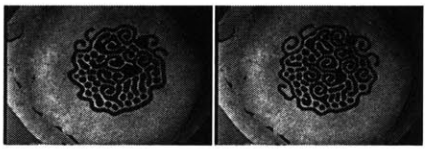

207.21 Gauss 232.83 Gauss

Figure D-20: Sequence 2: 200 μl, 0.9 mm, 25 Hz, 74.1 Gauss (rms)

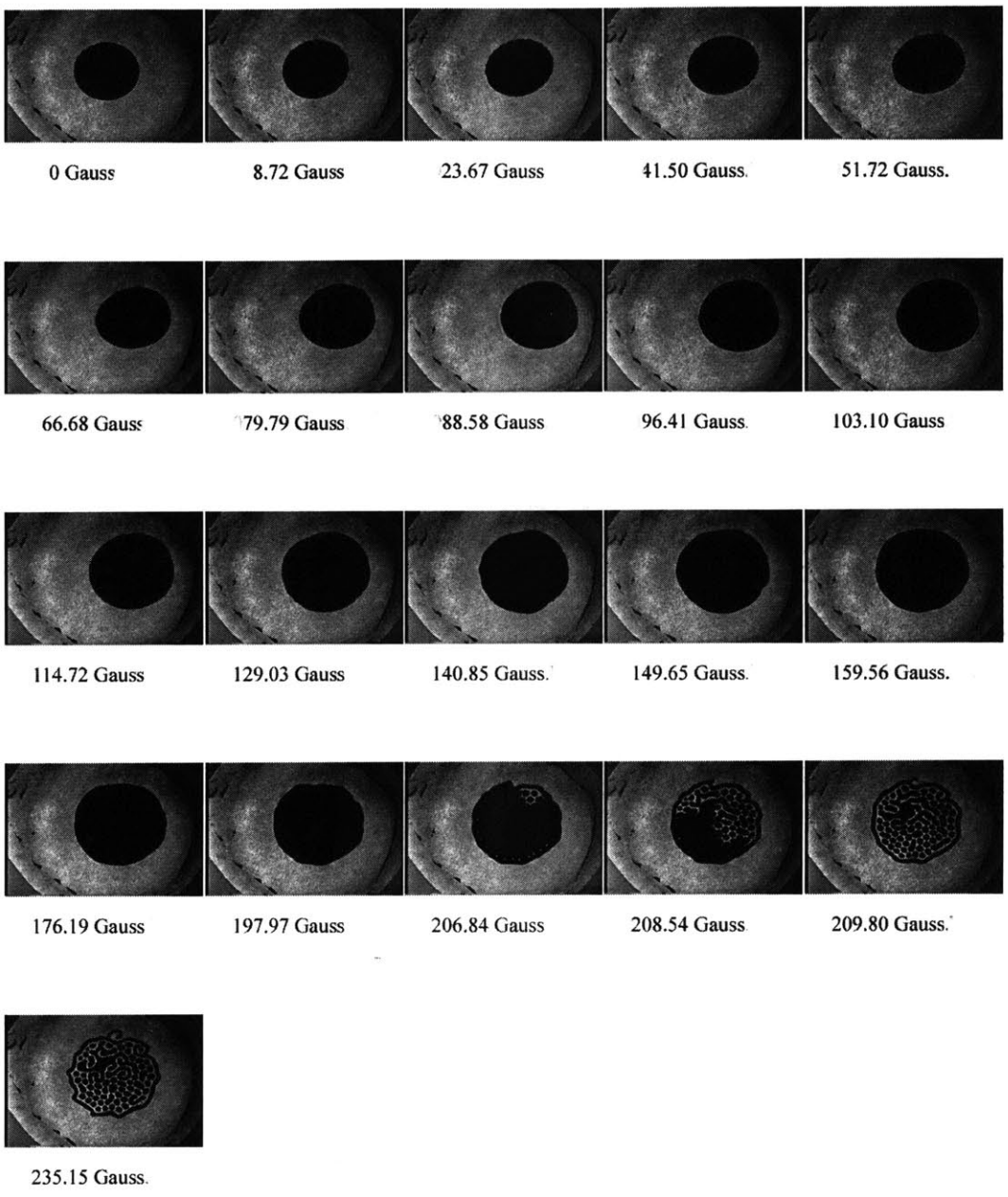

Figure D-21: Sequence 1: 200 μl, 0.9 mm, 25 Hz, 77.9 Gauss (rms)

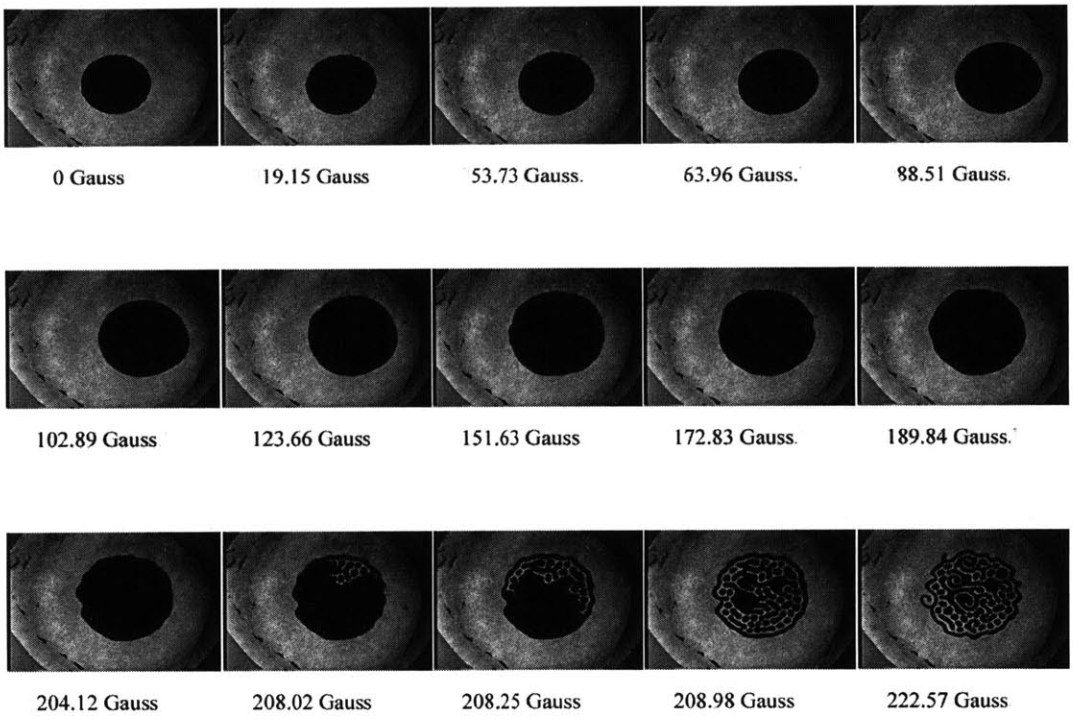

Figure D-22: Sequence 2: 200 μl, 0.9 mm, 25 Hz, 77.9 Gauss (rms)

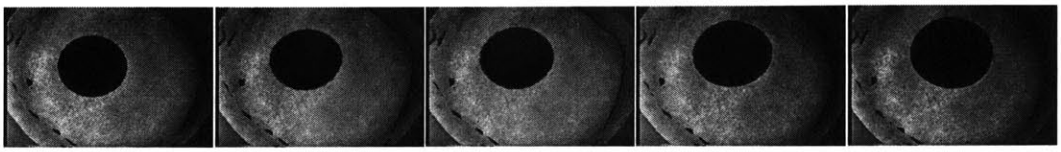

0 Gauss 14.51 Gauss 28.70 Gauss 56.43 Gauss 79.45 Gauss

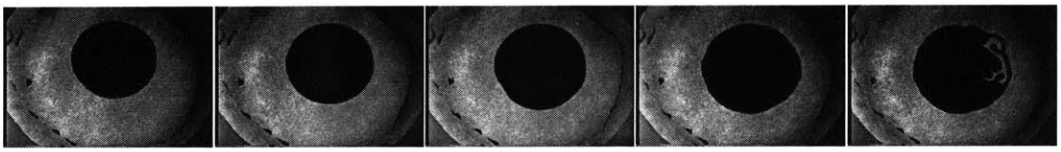

100.31 Gauss 115.74 Gauss 136.24 Gauss 159.18 Gauss. 165.97 Gauss.

174.66 Gauss 199.70 Gauss 226.87 Gauss 230.57 Gauss 232.06 Gauss

232.69 Gauss

Figure D-23: Sequence 1: 200 μl, 0.9 mm, 25 Hz, 81.7 Gauss (rms)

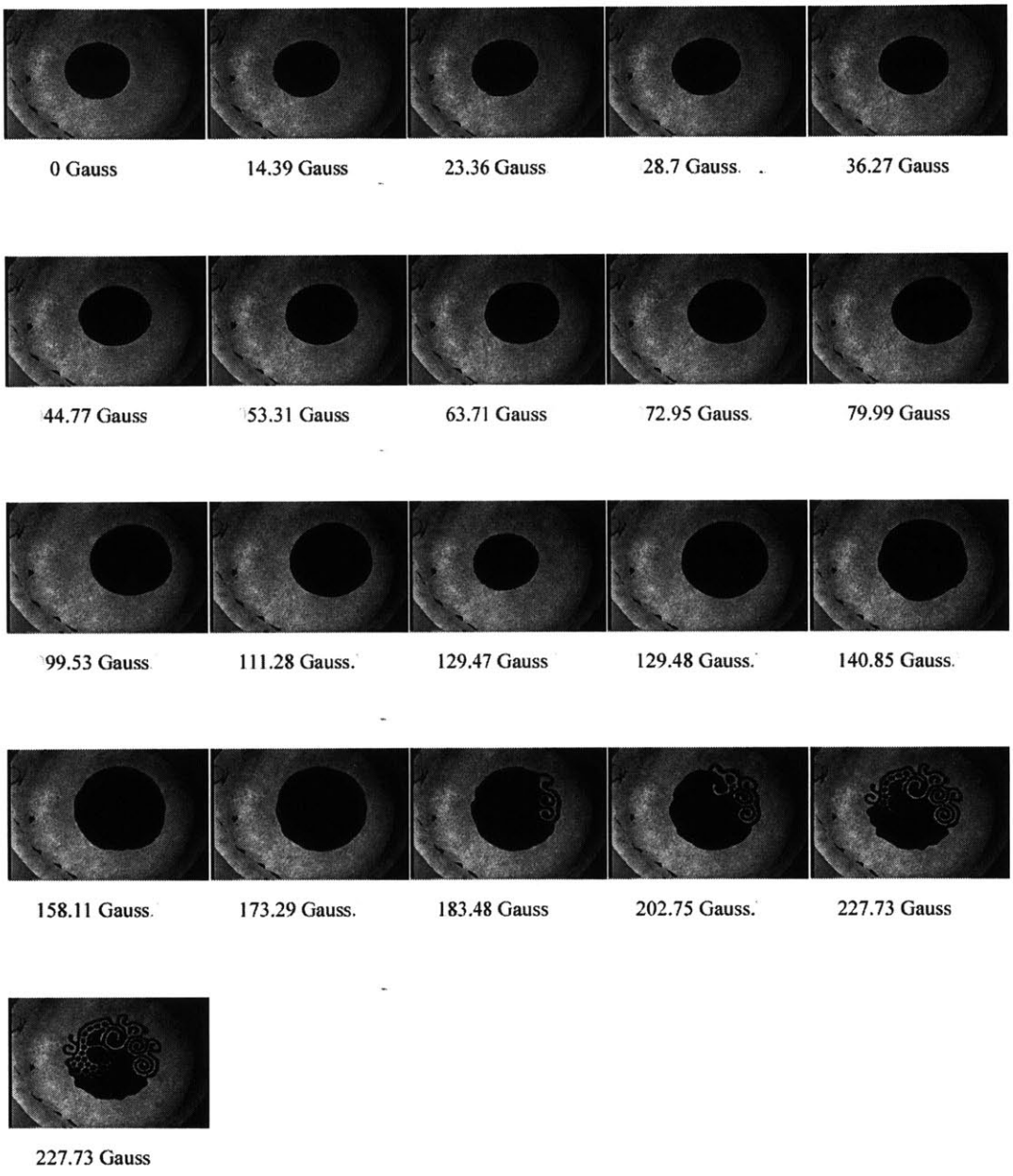

Figure D-24: Sequence 2: 200 μl, 0.9 mm, 25 Hz, 81.7 Gauss (rms)

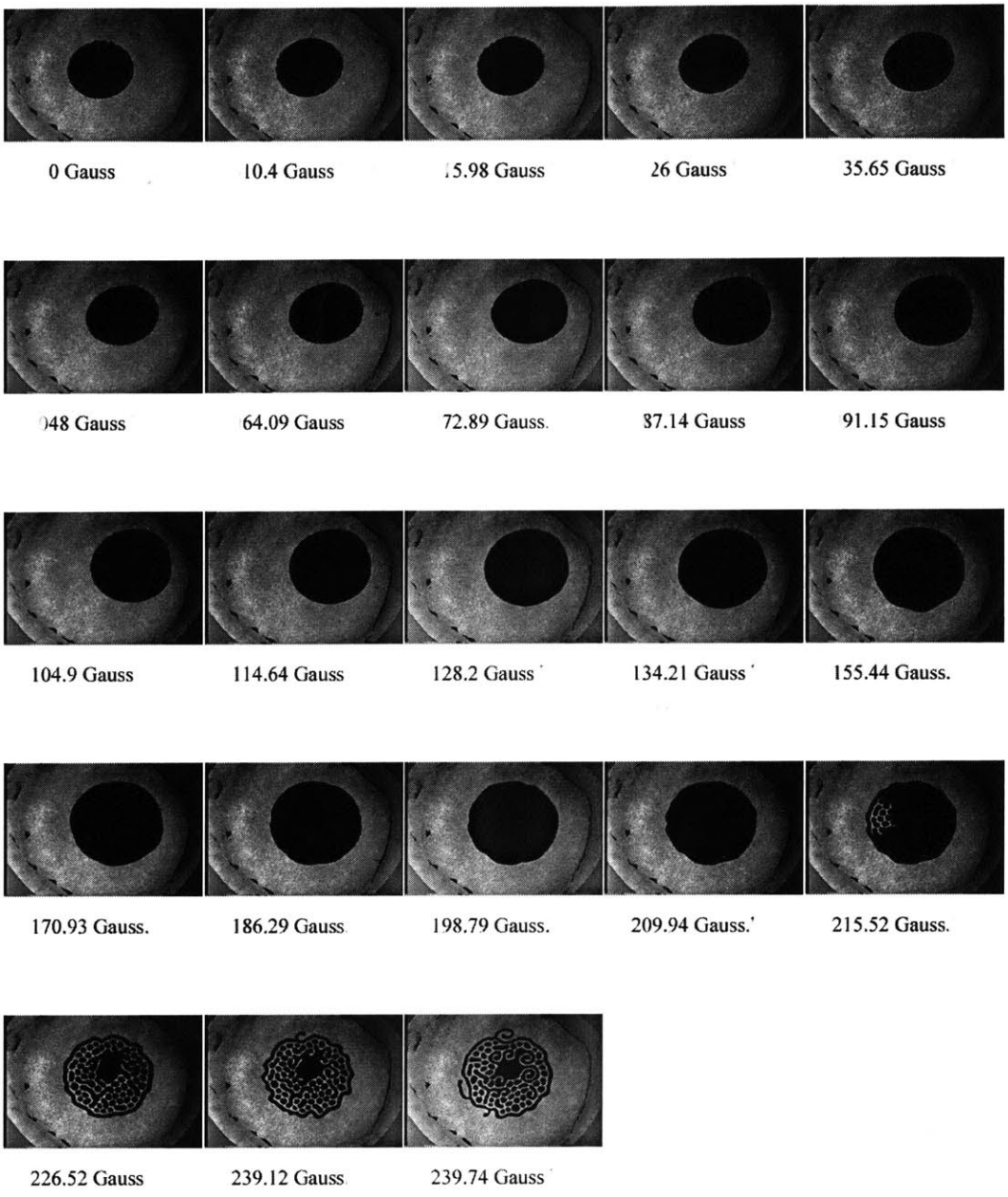

Figure D-25: Sequence 1: 200 μl, 0.9 mm, 25 Hz, 85.5 Gauss (rms)

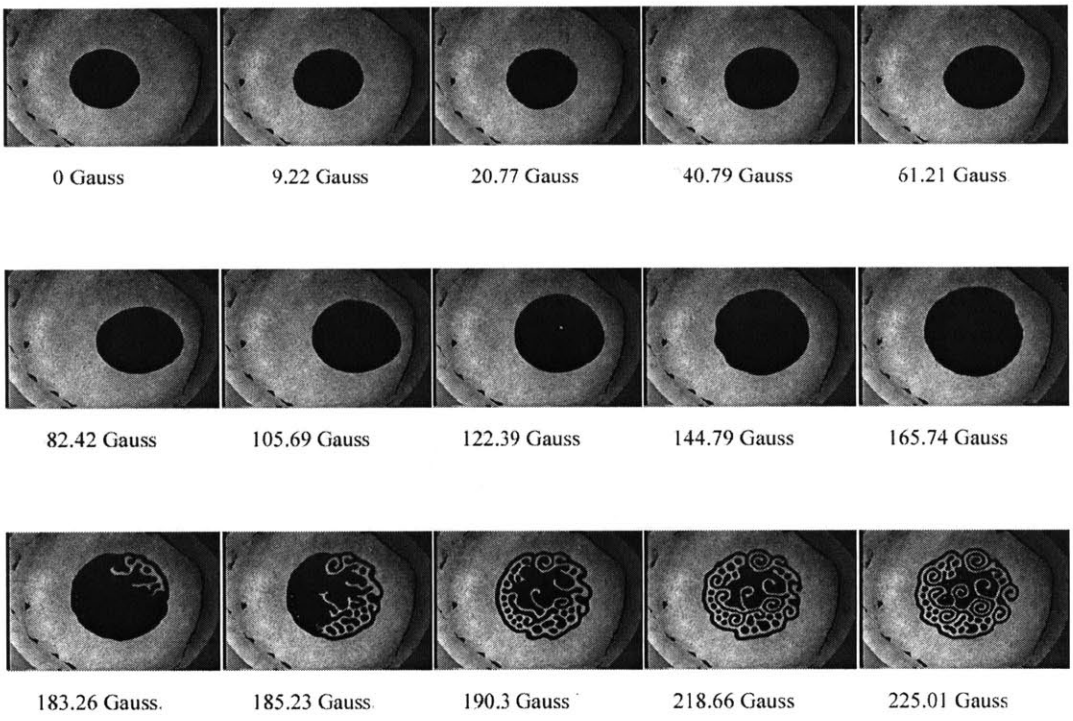

Figure D-26: Sequence 2: 200 μl, 0.9 mm, 25 Hz, 85.5 Gauss (rms)

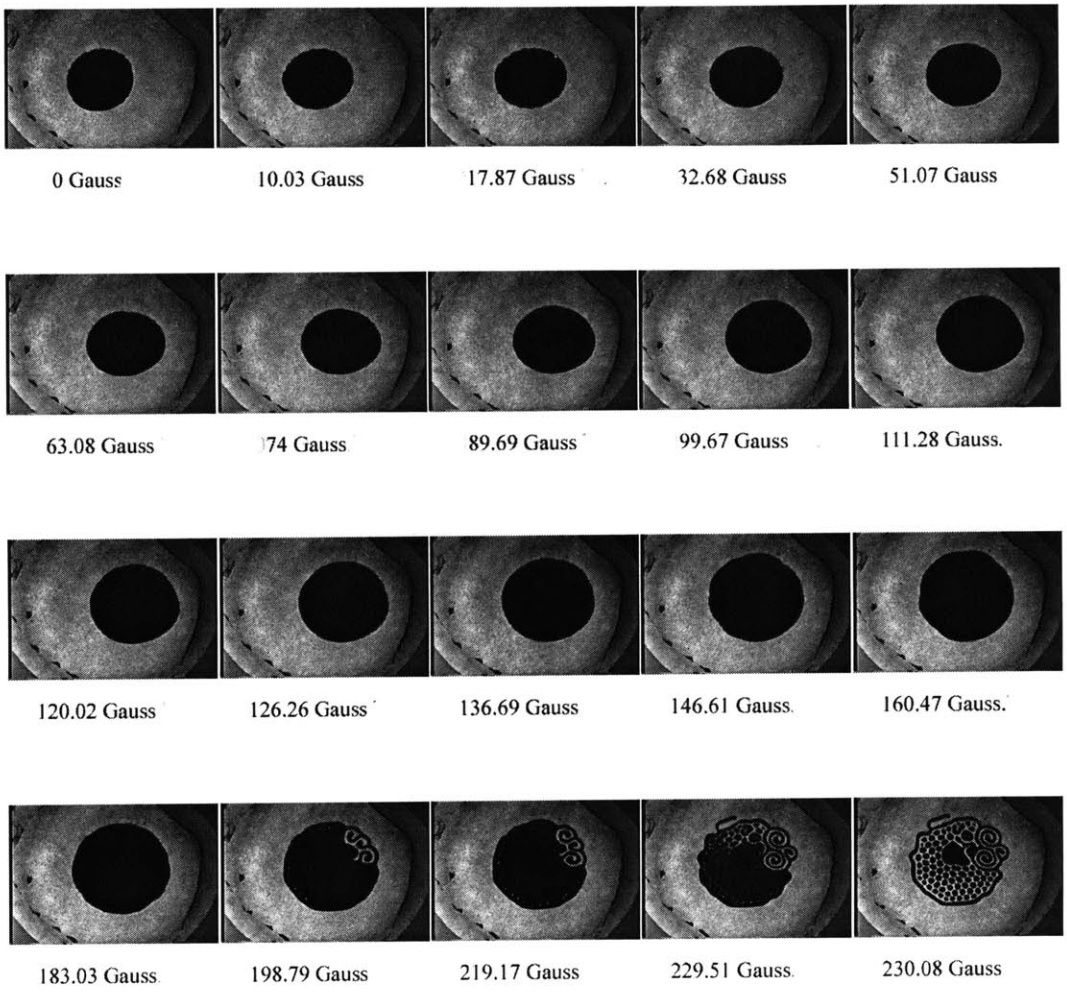

Figure D-27: Sequence 1: 200 μl, 0.9 mm, 25 Hz, 89.3 Gauss (rms)

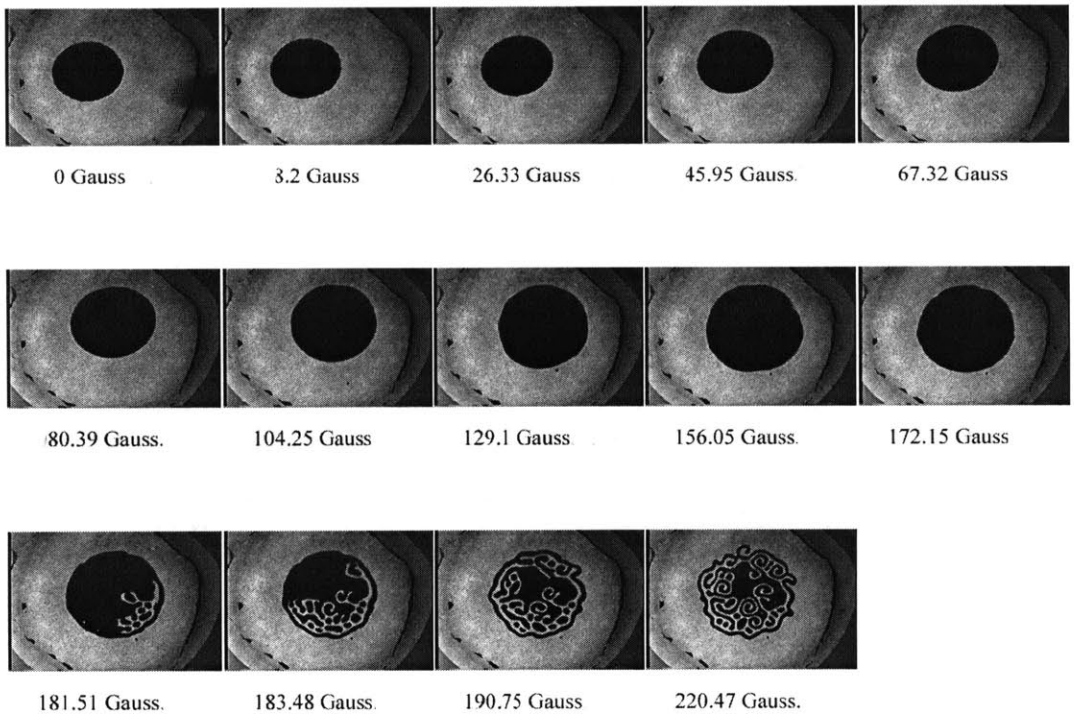

Figure D-28: Sequence 2: 200 μl, 0.9 mm, 25 Hz, 89.3 Gauss (rms)

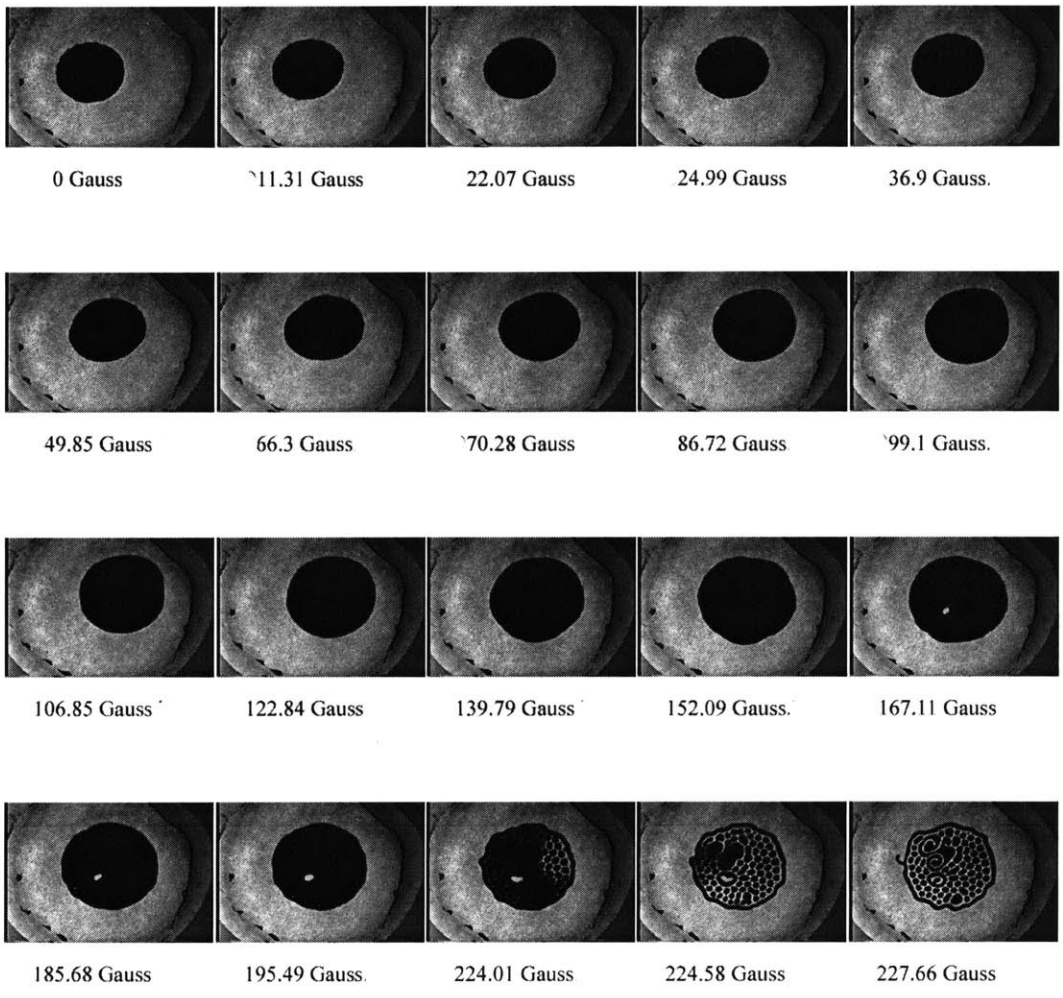

Figure D-29: Sequence 1: 200 μl, 0.9 mm, 25 Hz, 93.1 Gauss (rms)

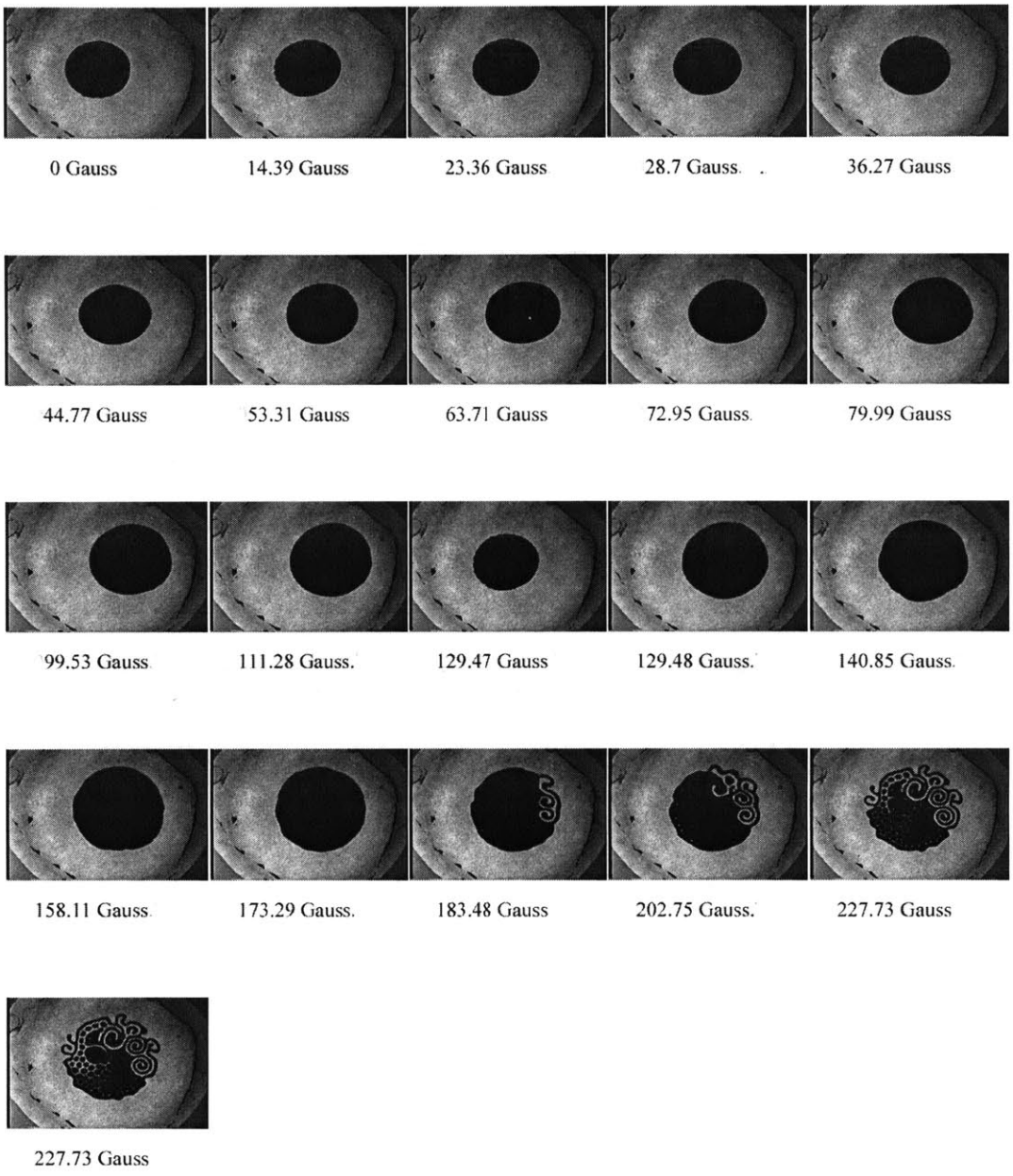

Figure D-30: Sequence 2: 200 μl, 0.9 mm, 25 Hz, 93.1 Gauss (rms)

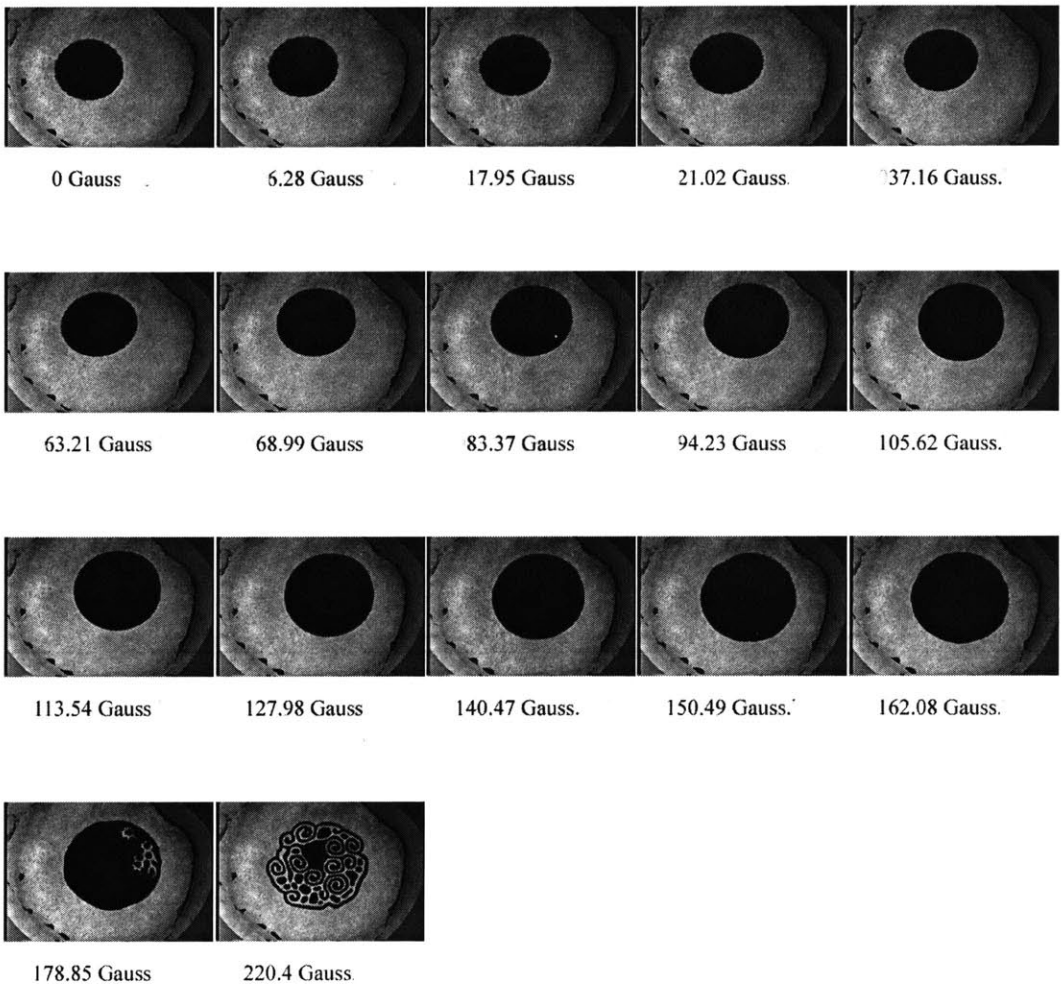

Figure D-31: Sequence 1: 200 μl, 0.9 mm, 25 Hz, 96.9 Gauss (rms)

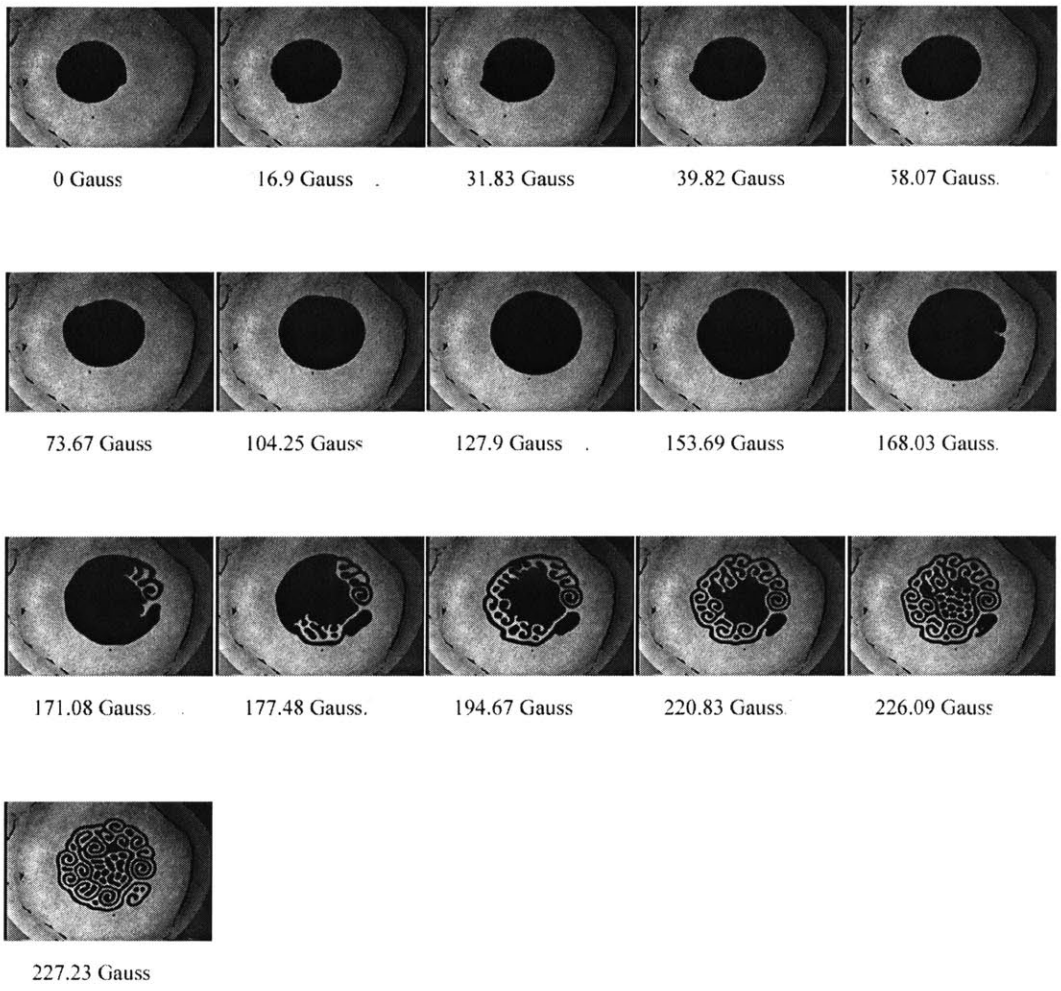

Figure D-32: Sequence 2: 200 μl, 0.9 mm, 25 Hz, 96.9 Gauss (rms)

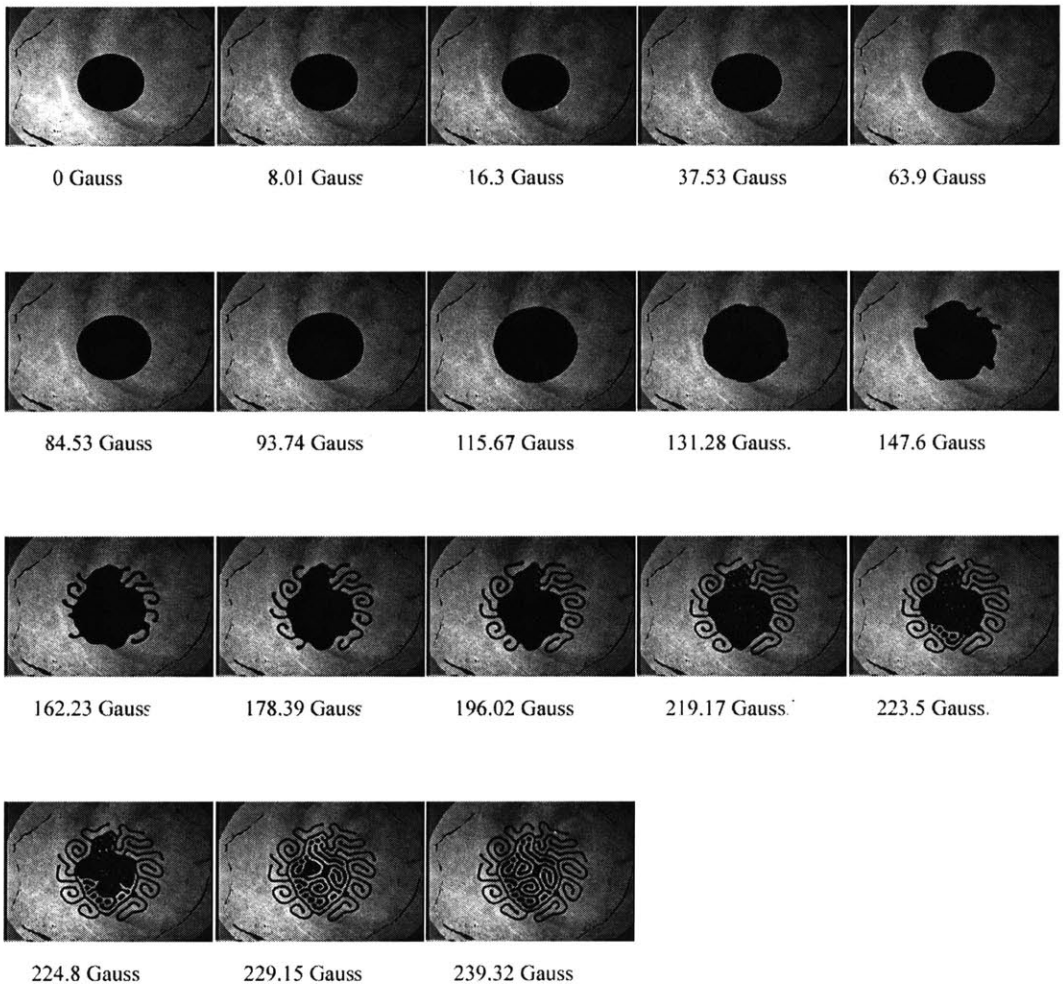

Figure D-33: Sequence 1: 200 μl, 0.9 mm, 30 Hz, 43.7 Gauss (rms)

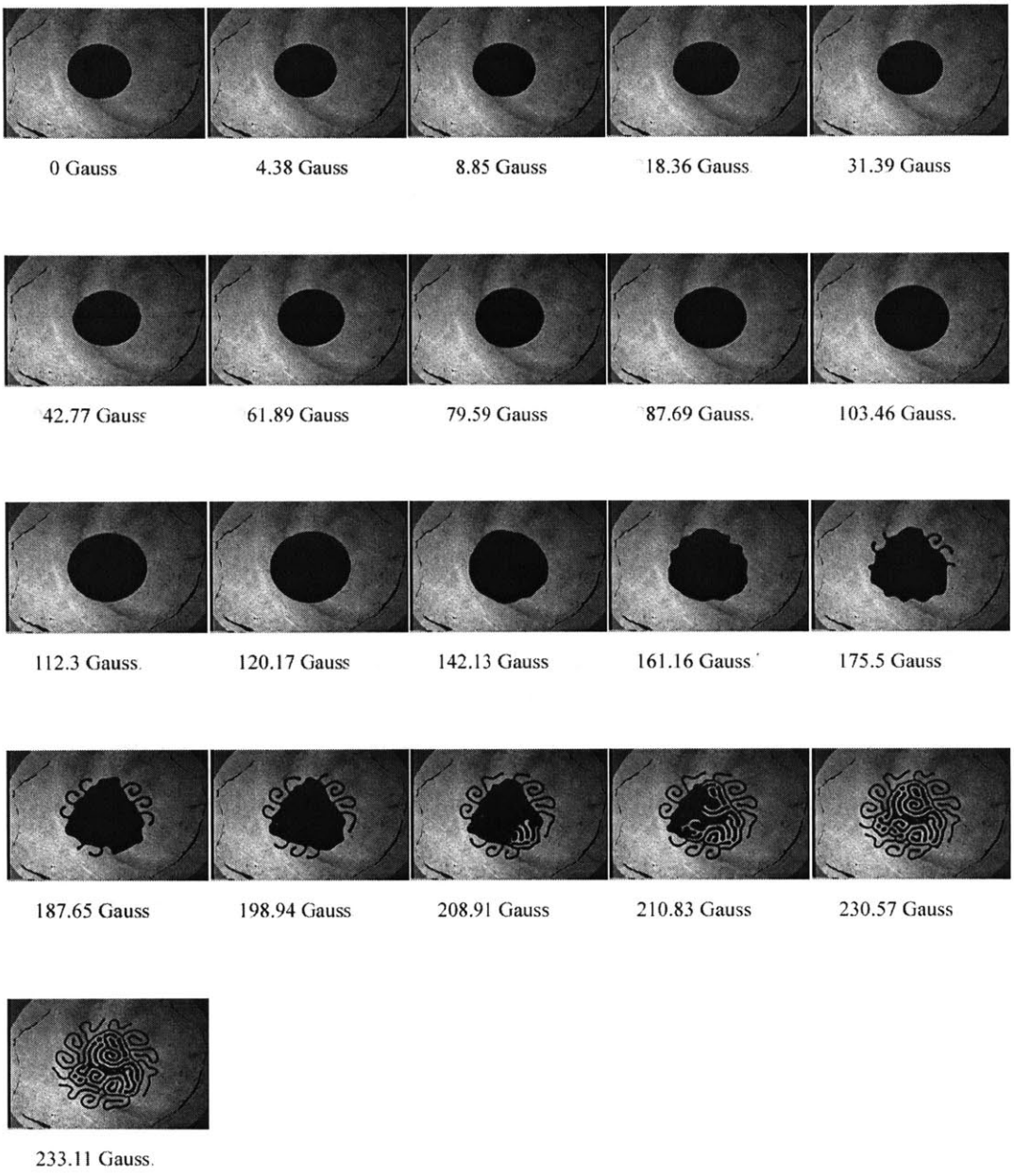

Figure D-34: Sequence 2: 200 μl, 0.9 mm, 30 Hz, 43.7 Gauss (rms)

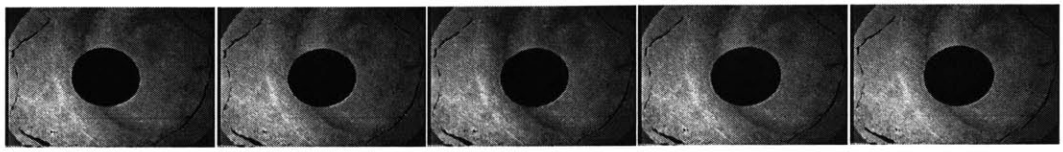

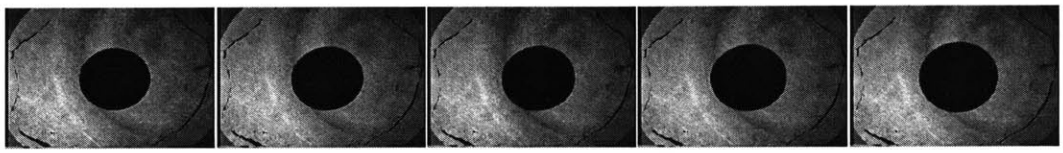

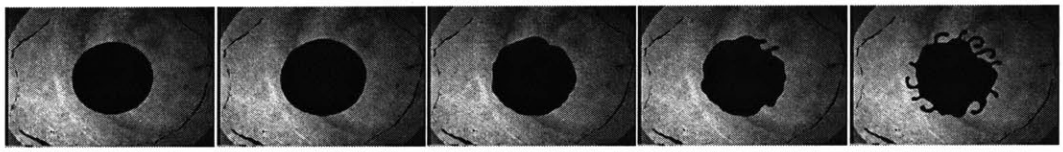

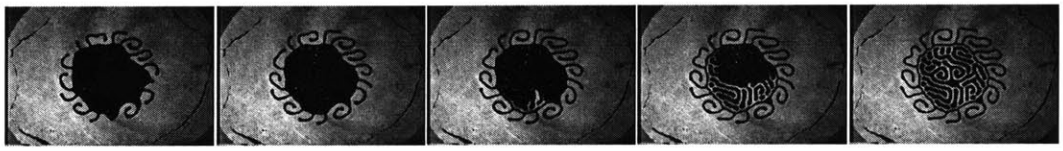

Figure D-35: Sequence 1: 200 μl, 0.9 mm, 30 Hz, 47.5 Gauss (rms)

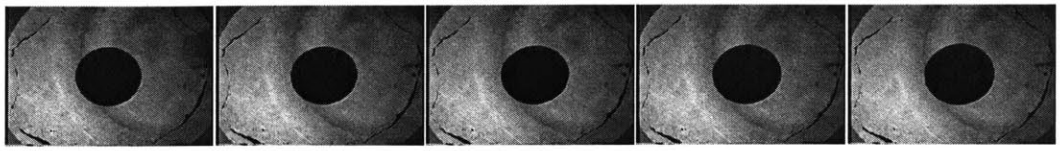

0 Gauss 5.92 Gauss 13.53 Gauss 30.99 Gauss. 50.14 Gauss.

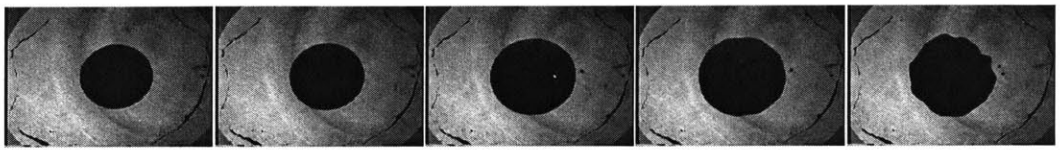

74 Gauss 91.01 Gauss 118.91 Gauss. 140.39 Gauss 156.51 Gauss.

184.39 Gauss 200.36 Gauss 214.87 Gauss 220.47 Gauss 220.62 Gauss.

220.98 Gauss. 245.69 Gauss 246.51 Gauss

Figure D-36: Sequence 2: 200 μl, 0.9 mm, 30 Hz, 47.5 Gauss (rms)

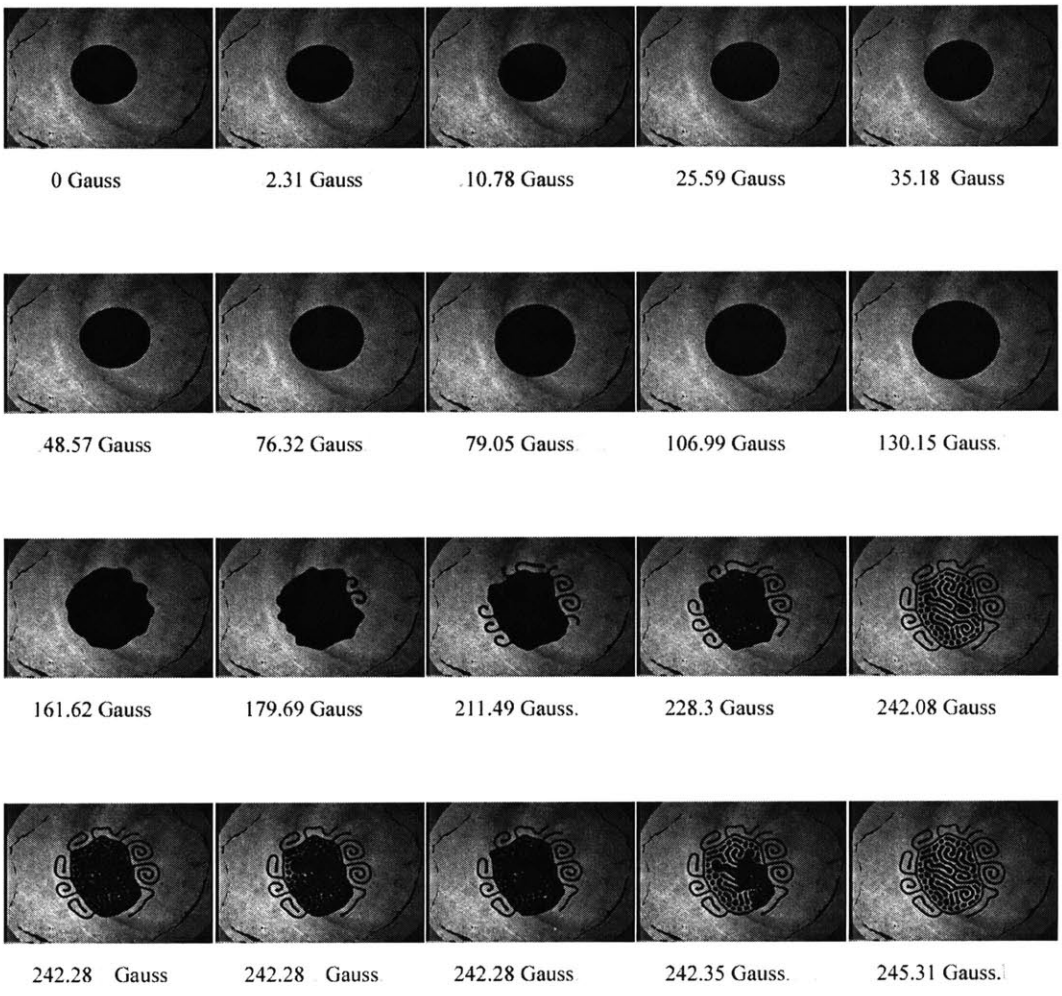

Figure D-37: Sequence 1: 200 μl, 0.9 mm, 30 Hz, 51.3 Gauss (rms)

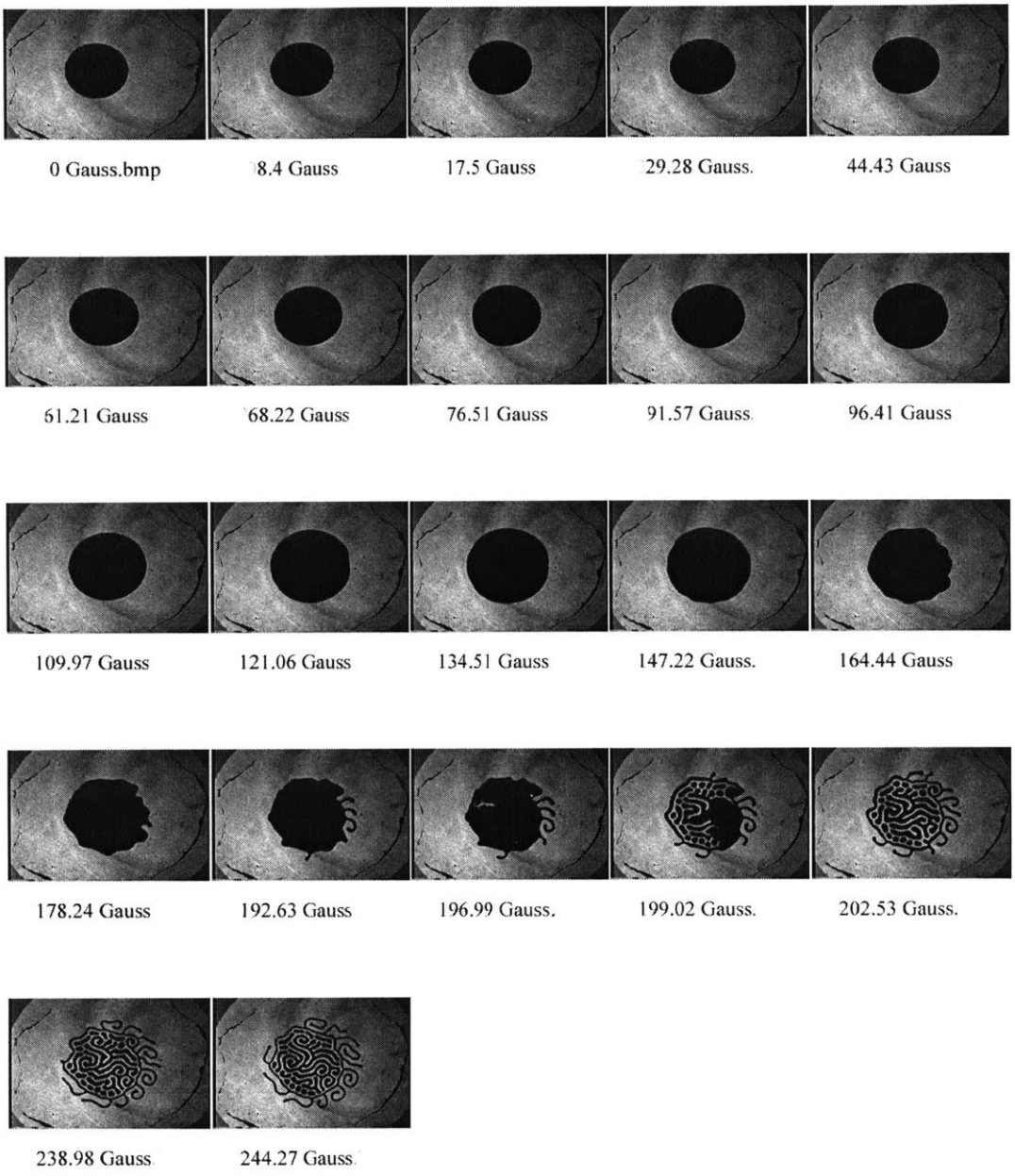

Figure D-38: Sequence 2: 200 μl, 0.9 mm, 30 Hz, 51.3 Gauss (rms)

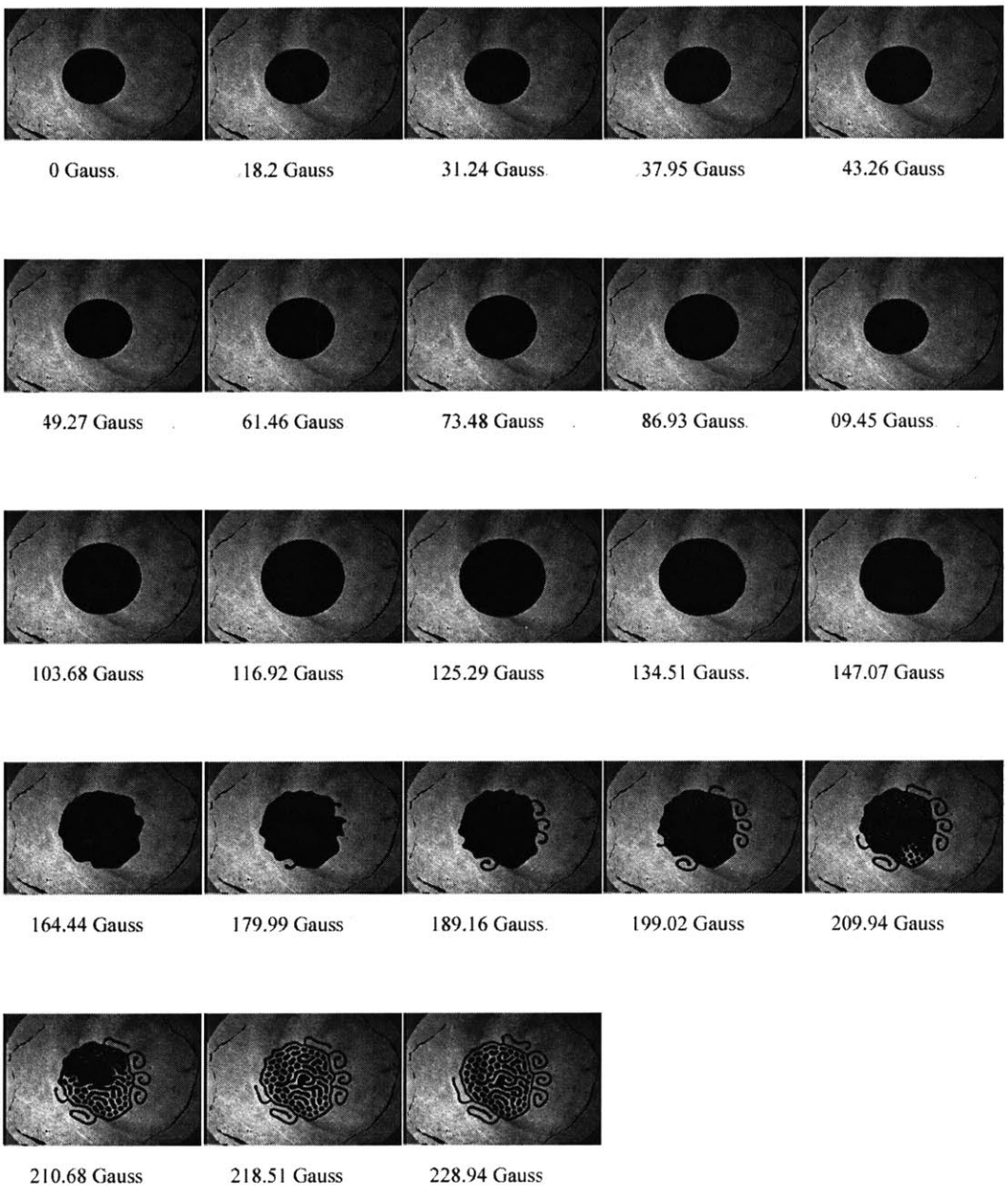

Figure D-39: Sequence 1: 200 μl, 0.9 mm, 30 Hz, 55.1 Gauss (rms)

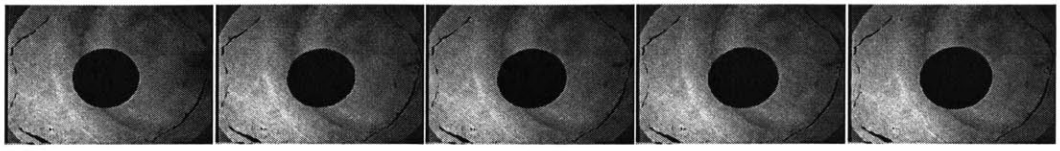

0 Gauss 10.2 Gauss 19.74 Gauss 40.63 Gauss 56.31 Gauss

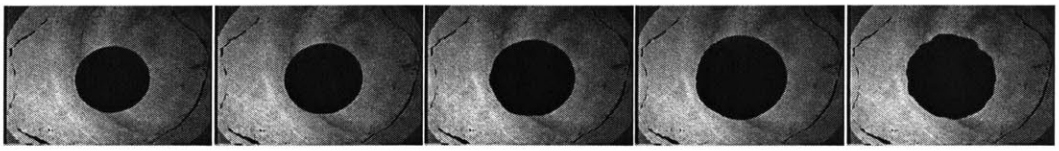

78.11 Gauss 97.05 Gauss 118.32 Gauss 128.2 Gauss 151.4 Gauss

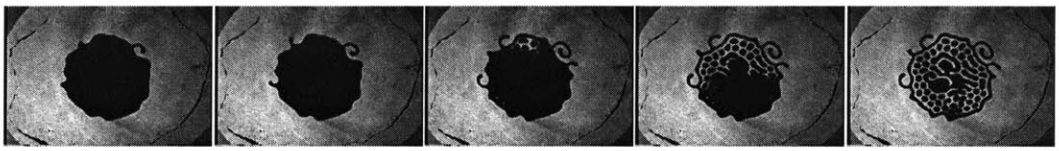

176.19 Gauss 182.34 Gauss 195.34 Gauss 197.52 Gauss 200.06 Gauss.

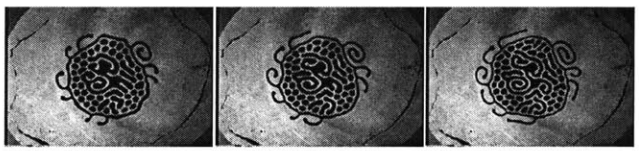

204.24 Gauss 217.64 Gauss 244.13 Gauss

Figure D-40: Sequence 2: 200 μl, 0.9 mm, 30 Hz, 55.1 Gauss (rms)

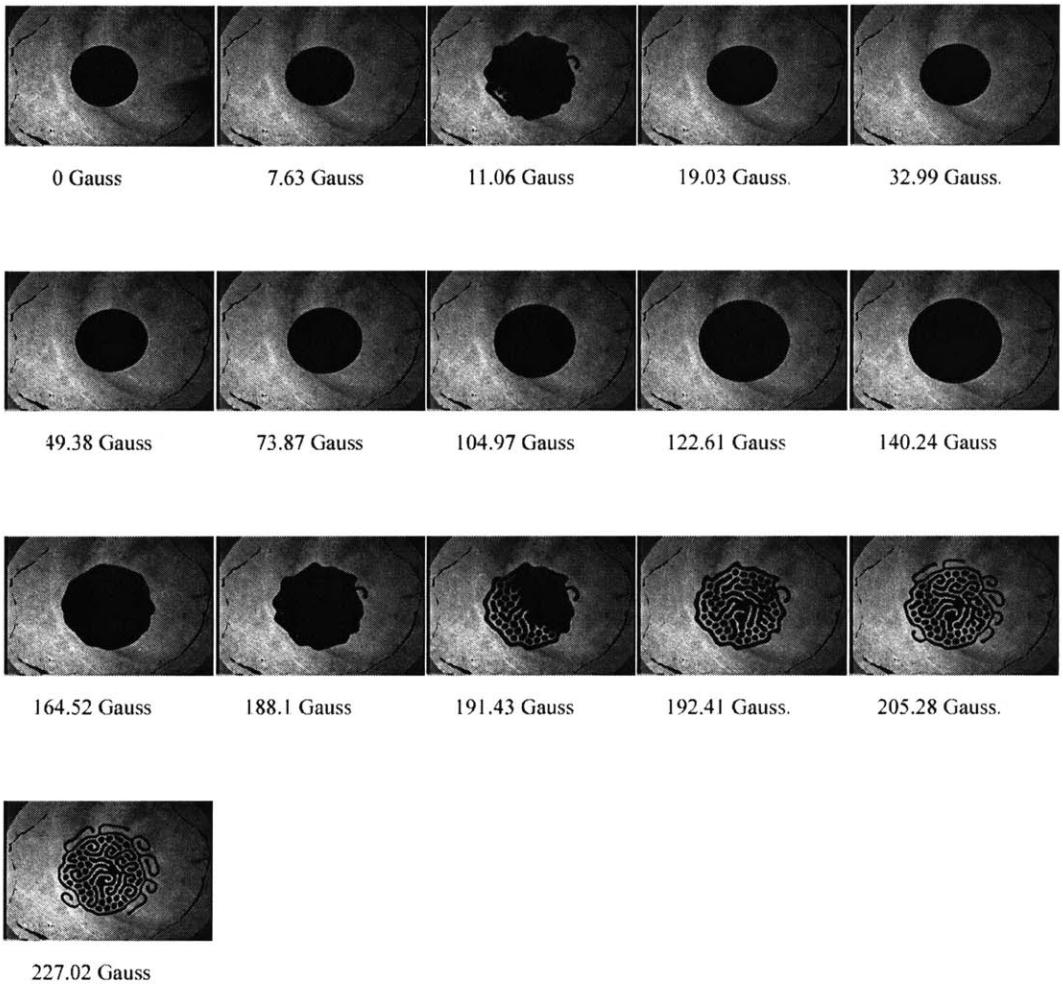

Figure D-41: Sequence 1: 200 μl, 0.9 mm, 30 Hz, 58.9 Gauss (rms)

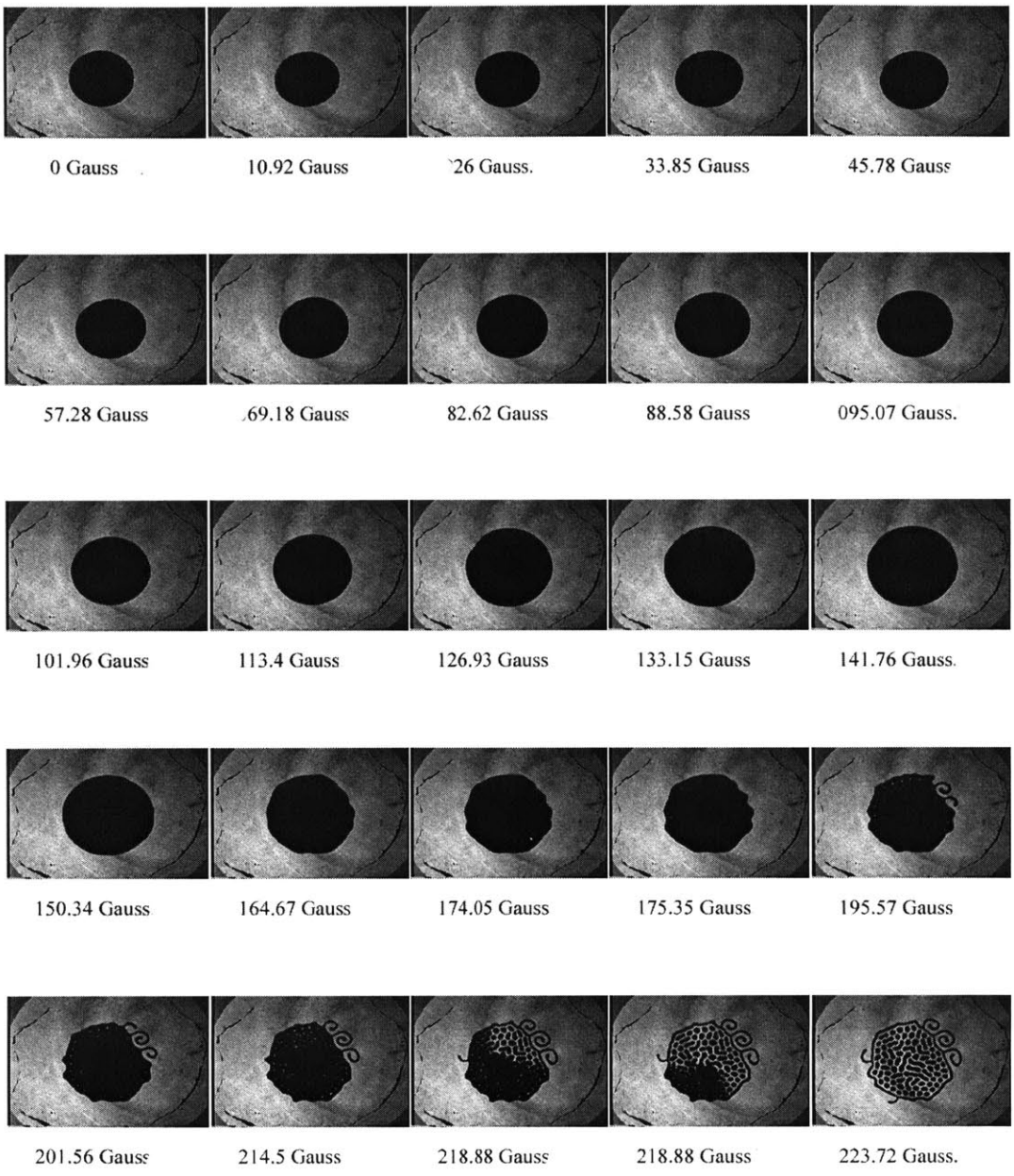

Figure D-42: Sequence 2: 200 μl, 0.9 mm, 30 Hz, 58.9 Gauss (rms)

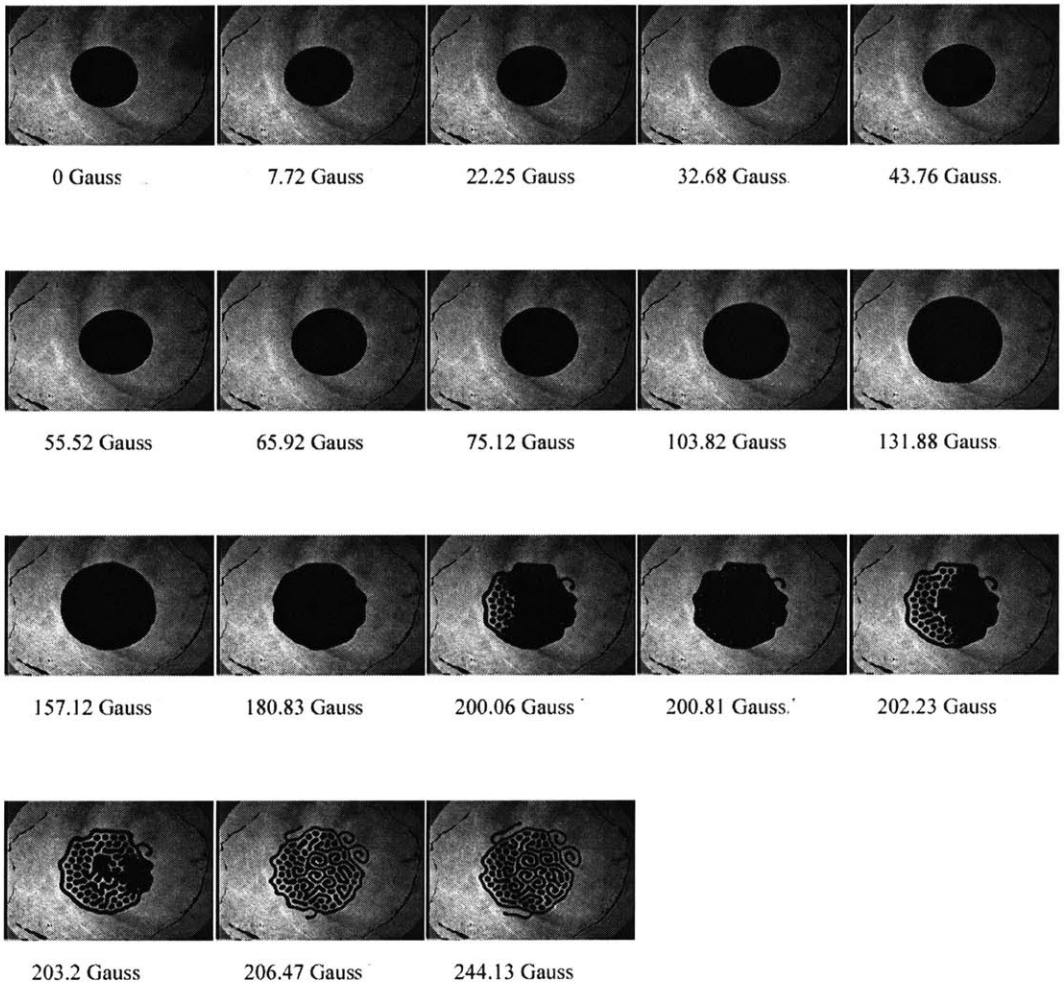

Figure D-43: Sequence 1: 200 μl, 0.9 mm, 30 Hz, 62.7 Gauss (rms)

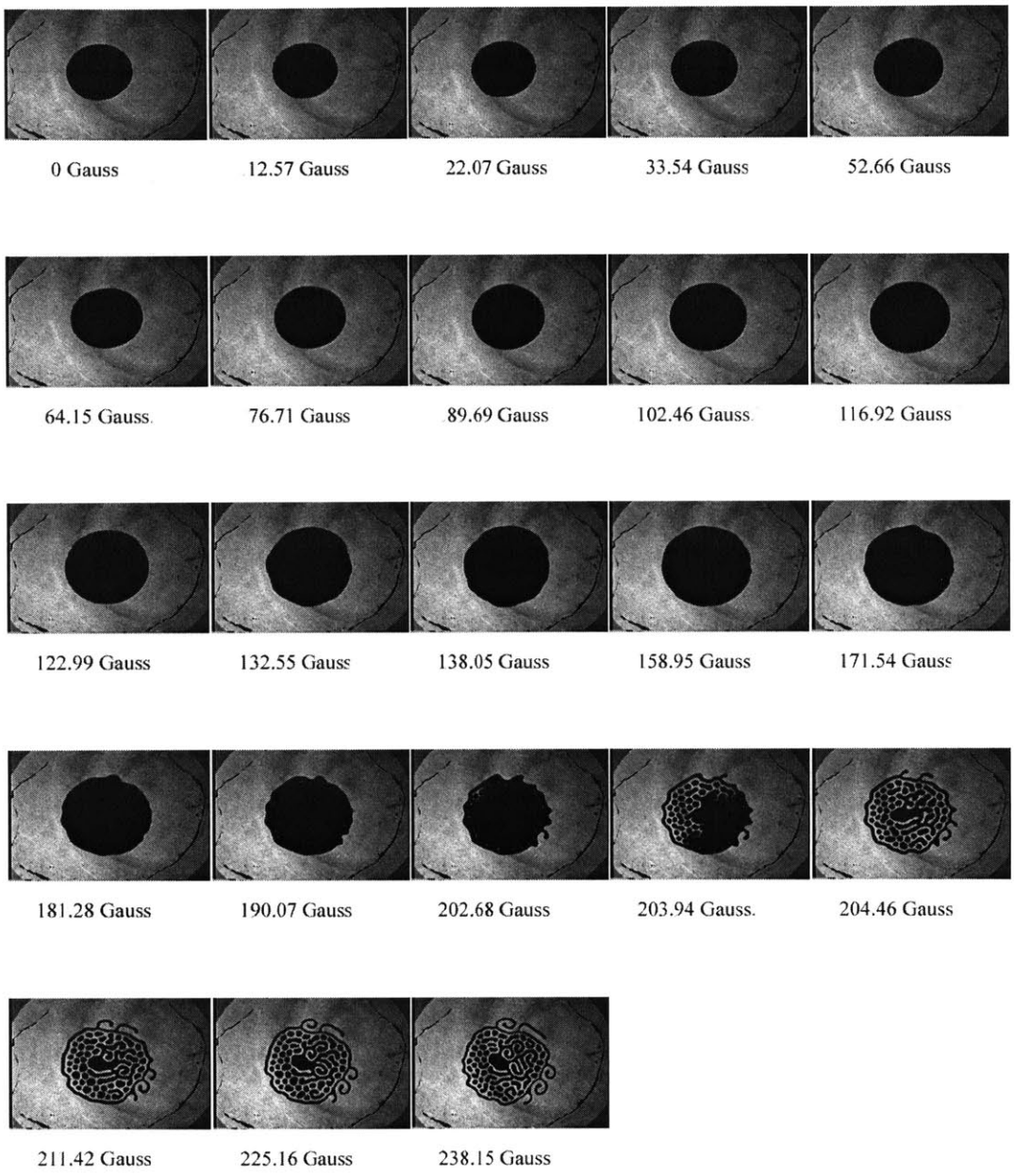

Figure D-44: Sequence 2: 200 μl, 0.9 mm, 30 Hz, 62.7 Gauss (rms)

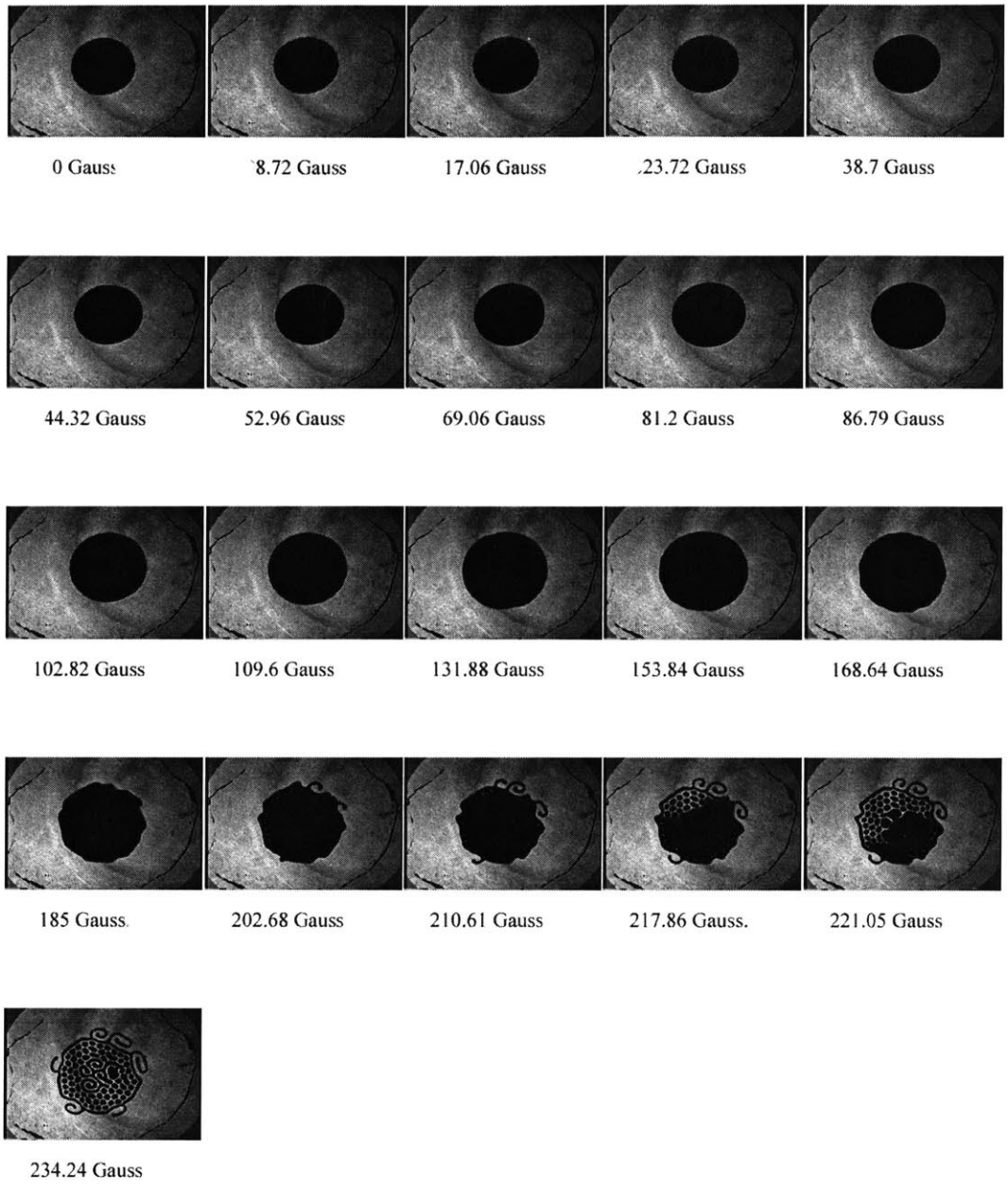

Figure D-45: Sequence 1: 200 μl, 0.9 mm, 30 Hz, 66.5 Gauss (rms)

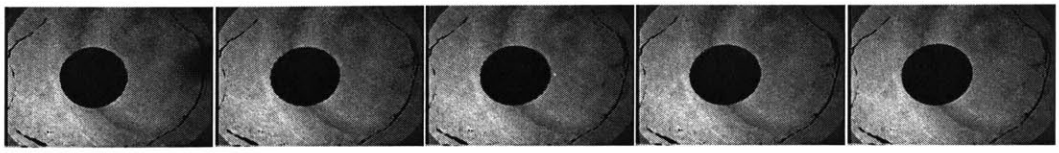

0 Gauss 3.41 Gauss 14.55 Gauss 25.13 Gauss. 34.31 Gauss

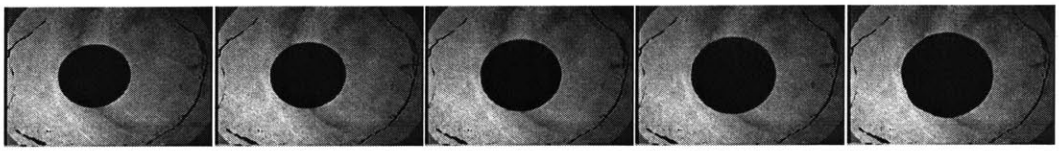

49.67 Gauss 65.1 Gauss 92.2 Gauss 107.5 Gauss. 125.96 Gauss

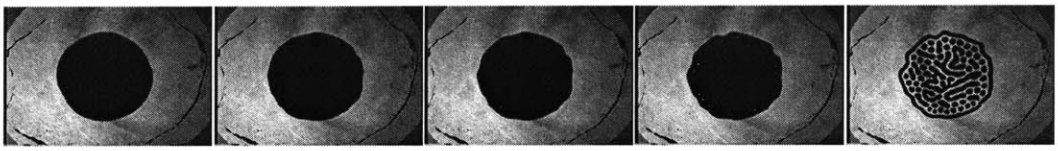

139.79 Gauss 167.57 Gauss 179.23 Gauss 190.97 Gauss 195.49 Gauss

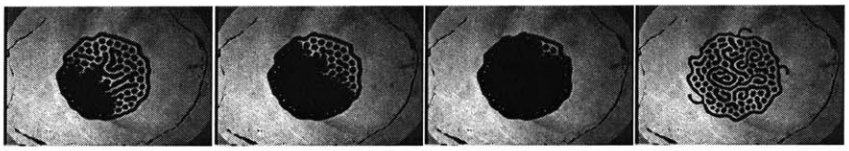

195.49 Gauss 195.57 Gauss 196.02 Gauss 232.62 Gauss

Figure D-46: Sequence 2: 200 μl, 0.9 mm, 30 Hz, 66.5 Gauss (rms)

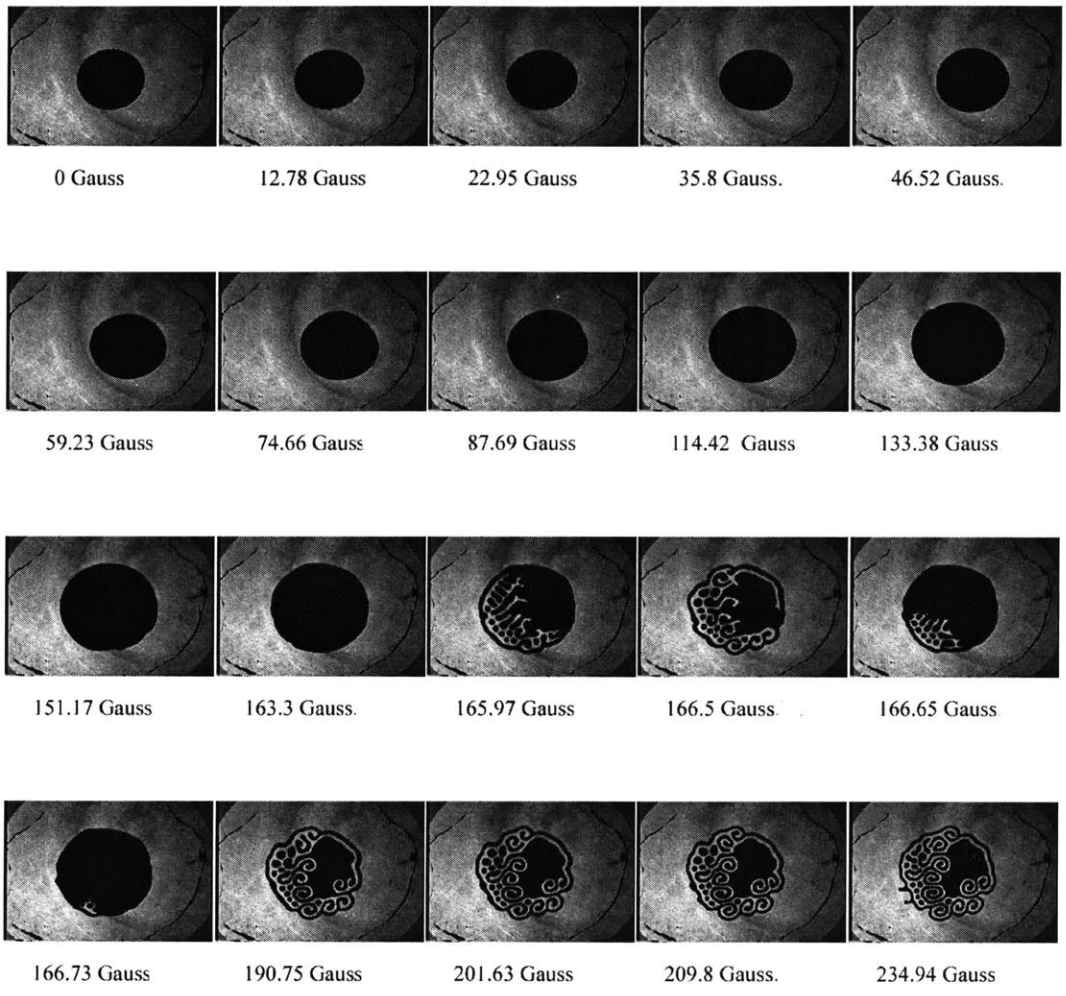

Figure D-47: Sequence 1: 200 μl, 0.9 mm, 30 Hz, 70.3 Gauss (rms)

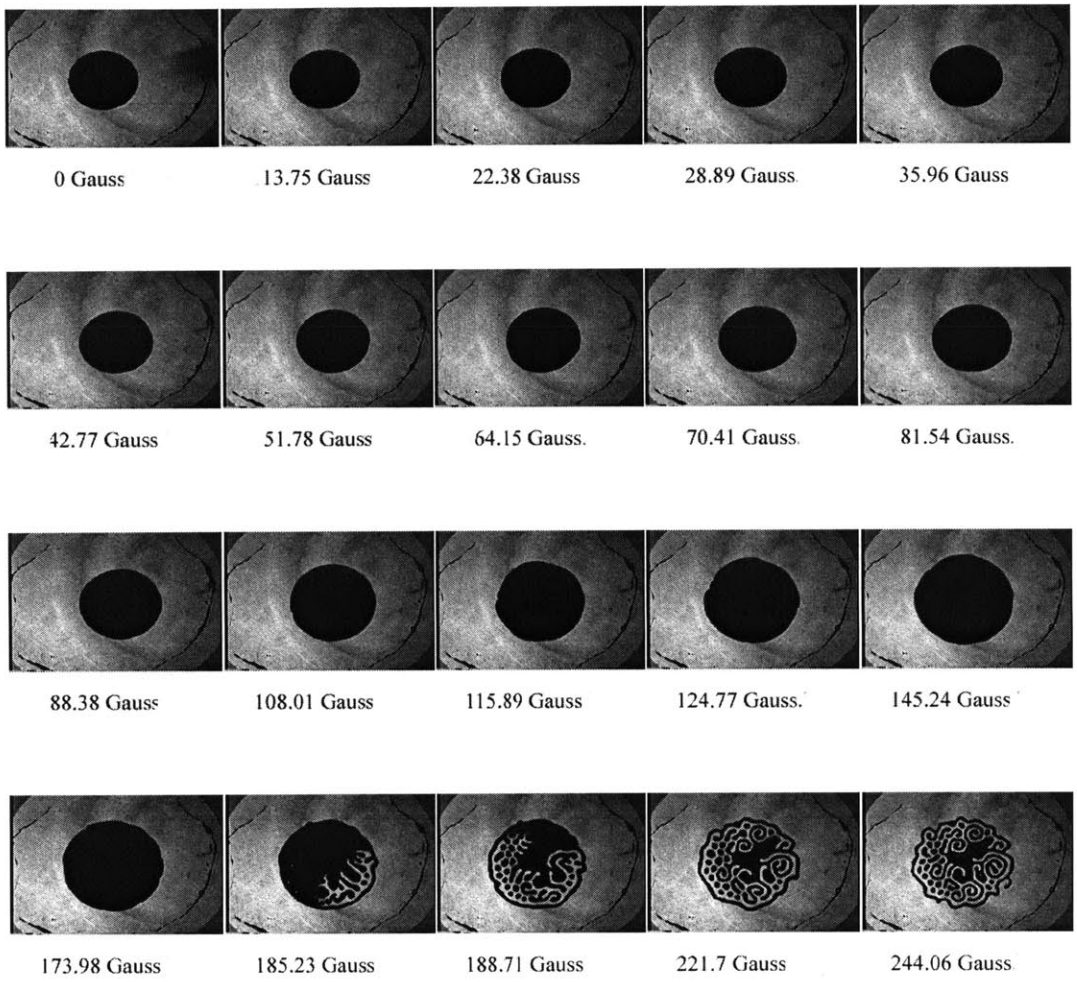

Figure D-48: Sequence 2: 200 μl, 0.9 mm, 30 Hz, 70.3 Gauss (rms)

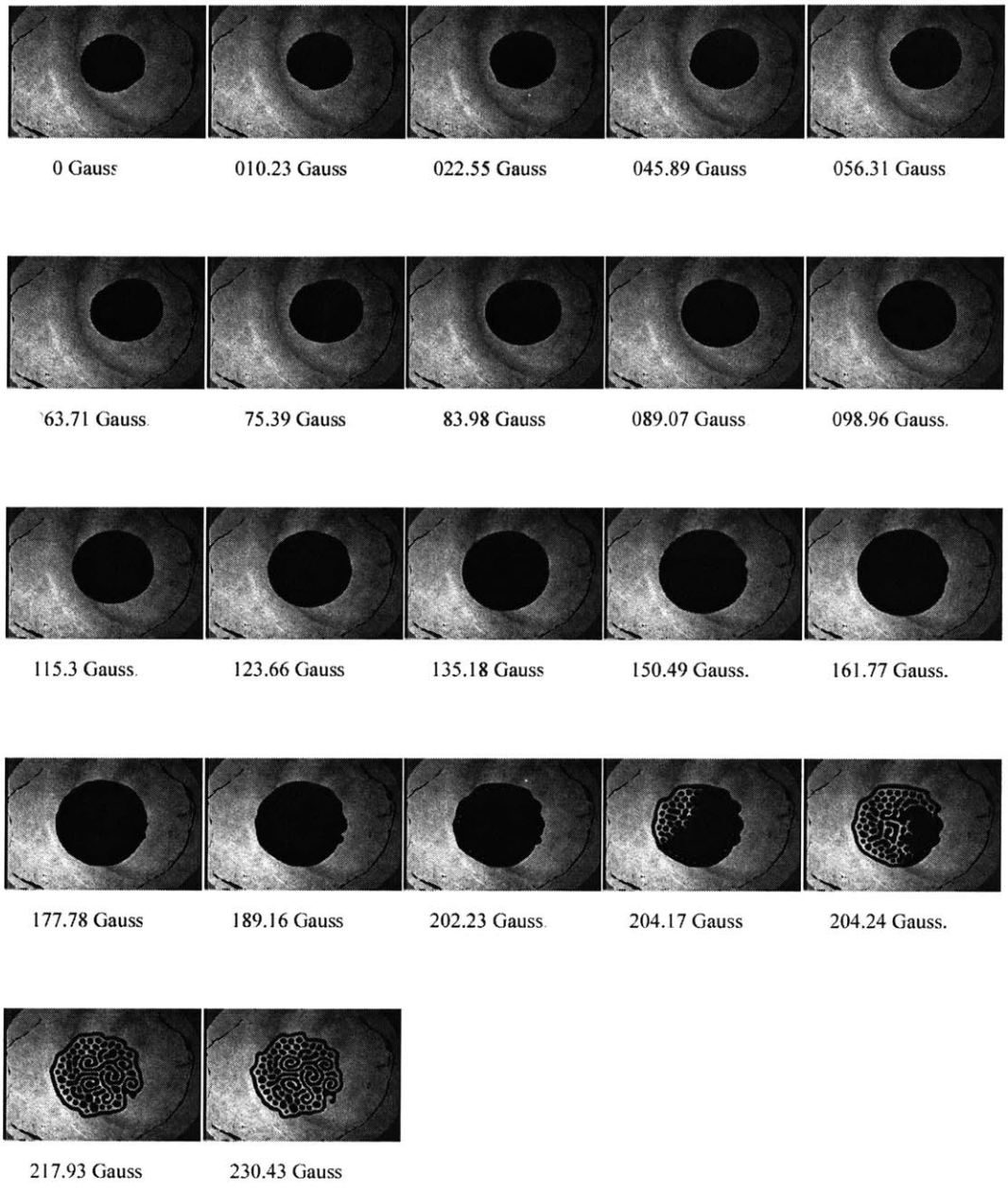

Figure D-49: Sequence 1: 200 μl, 0.9 mm, 30 Hz, 74.1 Gauss (rms)

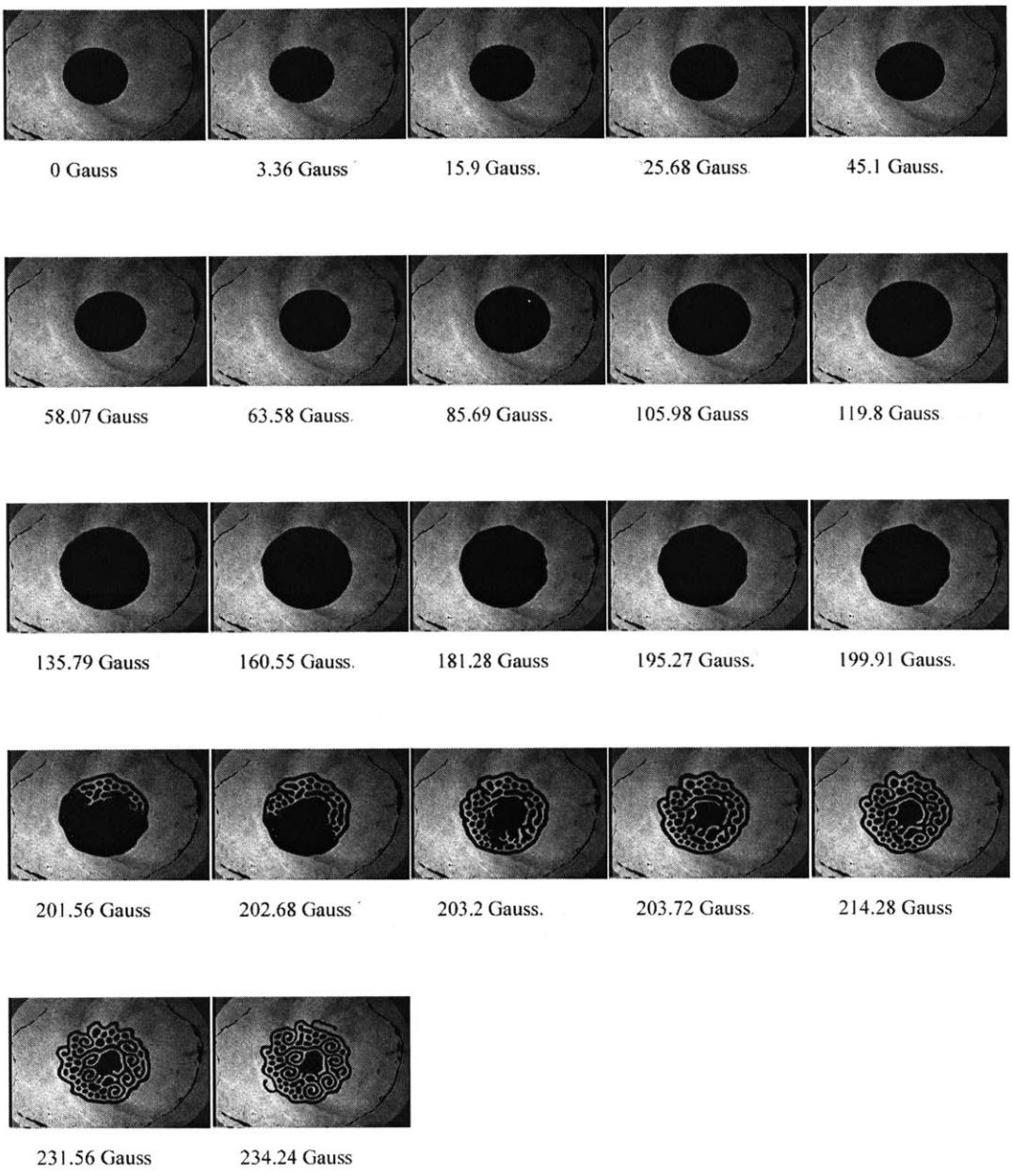

Figure D-50: Sequence 2: 200 μl, 0.9 mm, 30 Hz, 74.1 Gauss (rms)

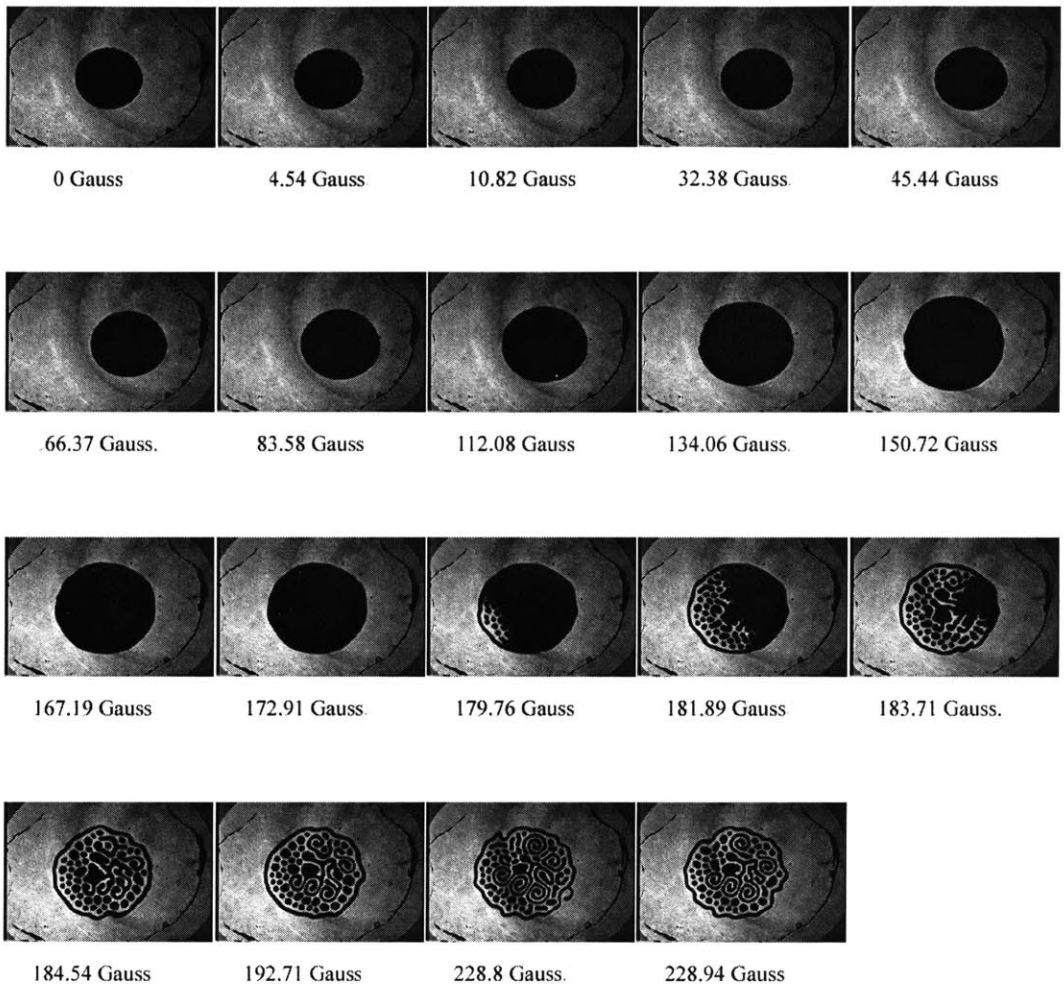

Figure D-51: Sequence 1: 200 μl, 0.9 mm, 30 Hz, 77.9 Gauss (rms)

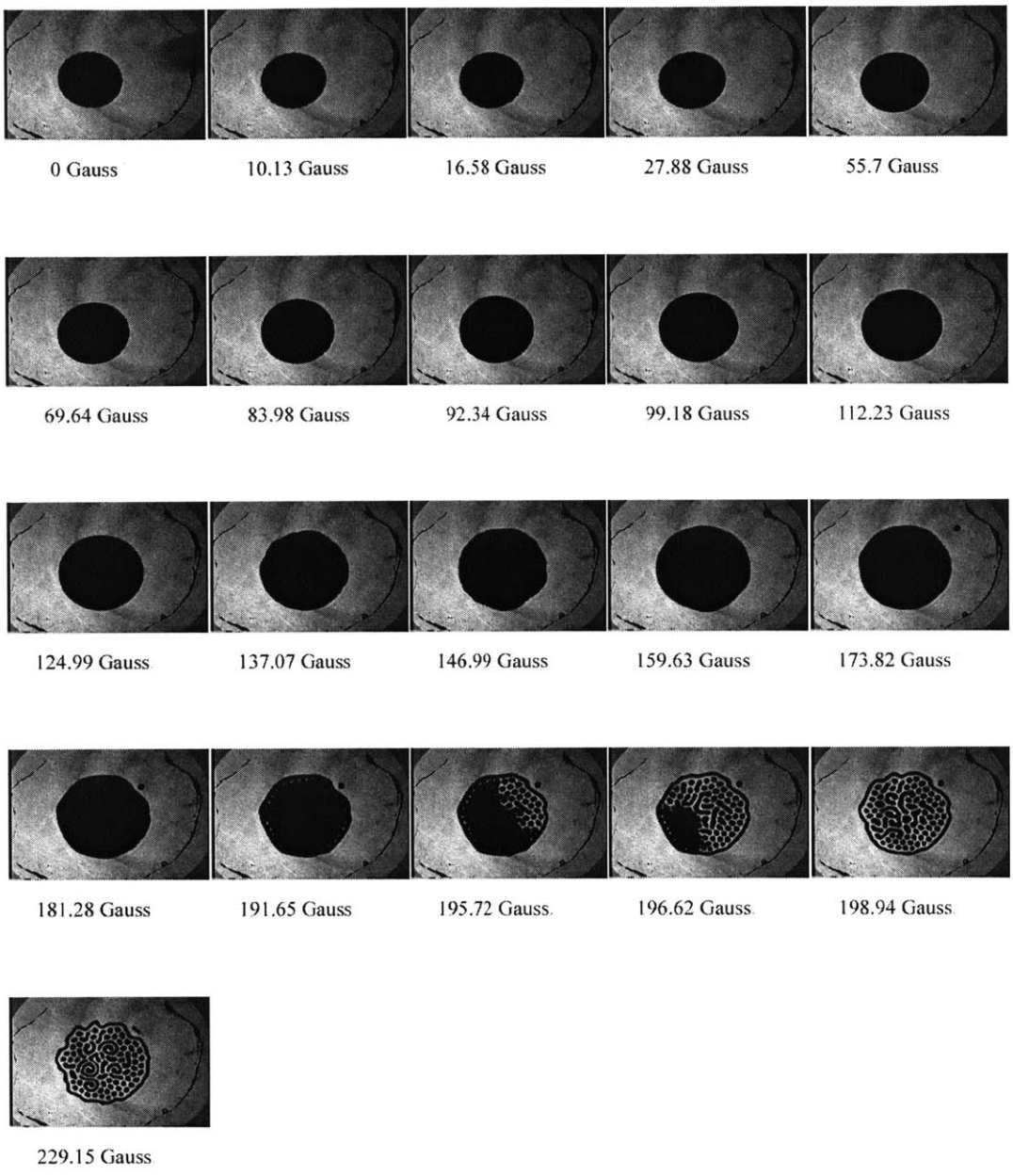

Figure D-52: Sequence 2: 200 μl, 0.9 mm, 30 Hz, 77.9 Gauss (rms)

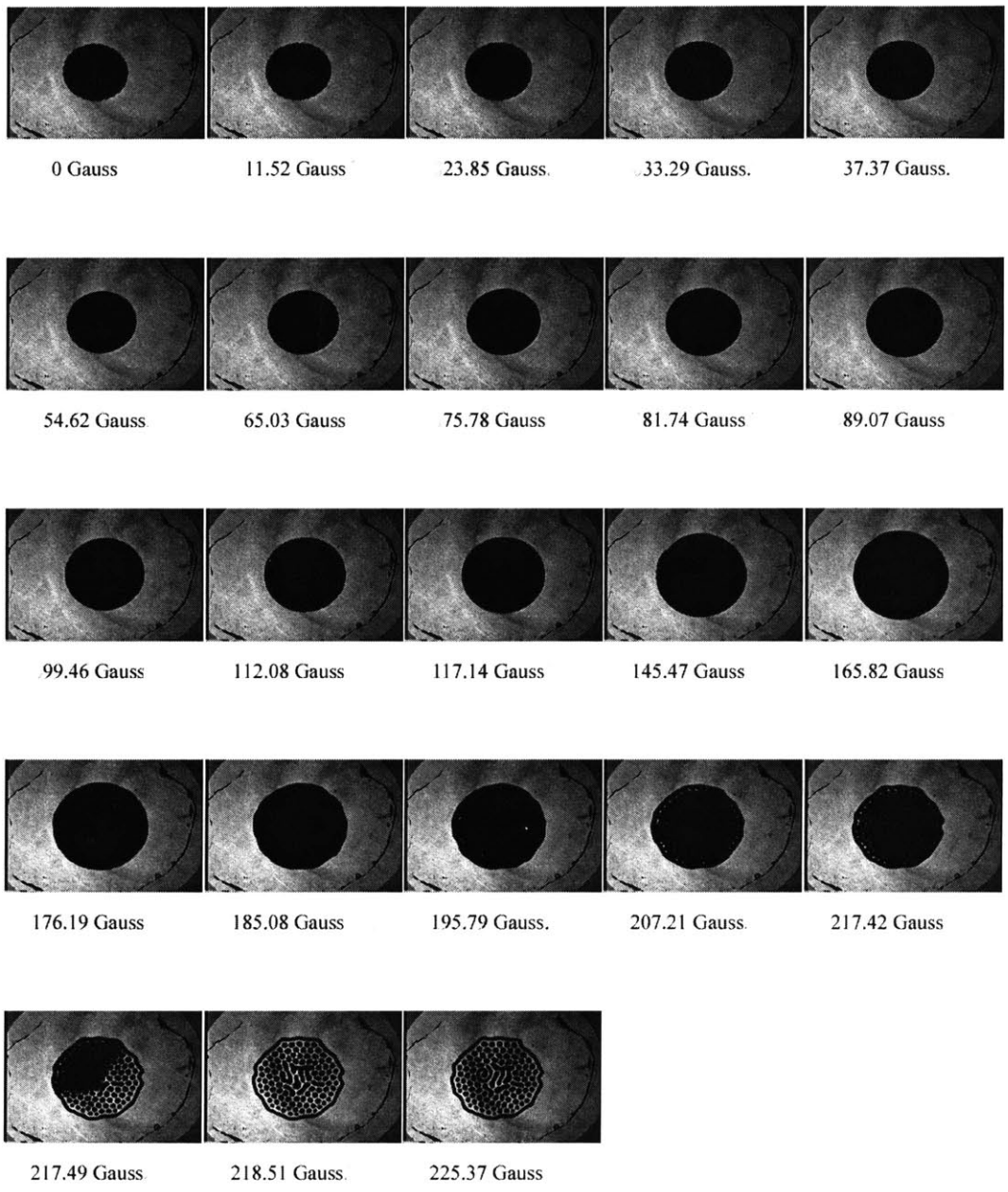

Figure D-53: Sequence 1: 200 μl, 0.9 mm, 30 Hz, 81.7 Gauss (rms)

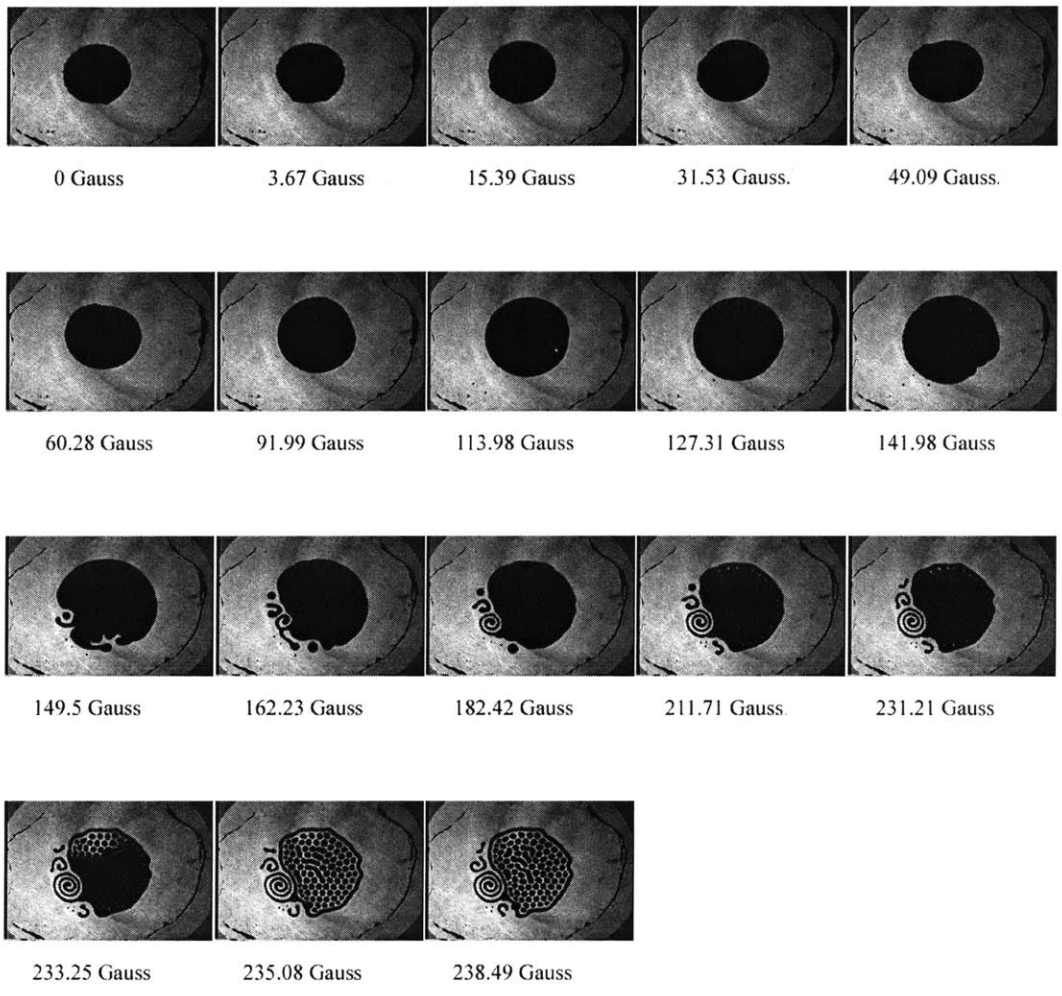

Figure D-54: Sequence 2: 200 μl, 0.9 mm, 30 Hz, 81.7 Gauss (rms)

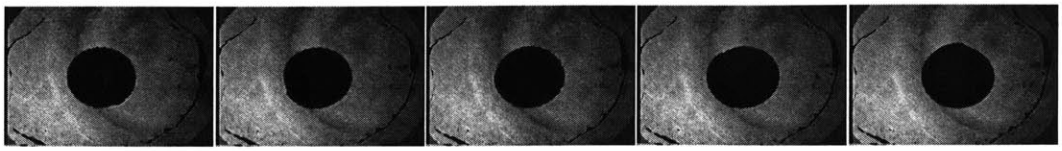

0 Gauss 3.07 Gauss 10.2 Gauss 31.39 Gauss 42.99 Gauss.

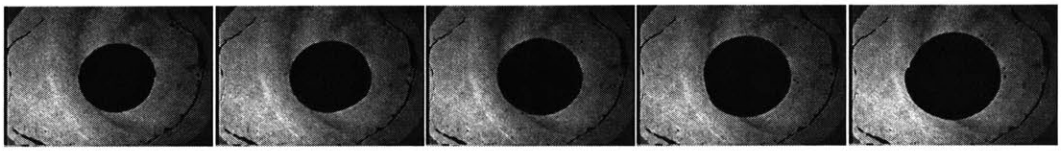

66.75 Gauss 86.58 Gauss 100.39 Gauss 115.89 Gauss 146.08 Gauss

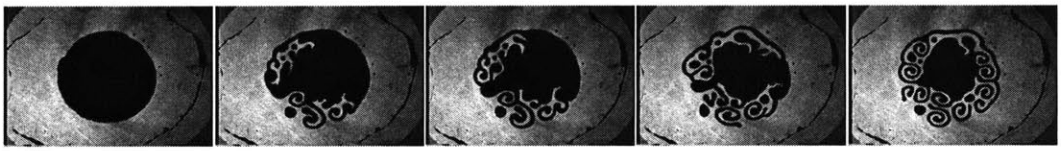

162.53 Gauss 173.75 Gauss 174.2 Gauss 179.91 Gauss 206.54 Gauss

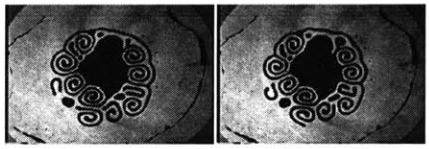

230.57 Gauss 234.1 Gauss

Figure D-55: Sequence 1: 200 μl, 0.9 mm, 30 Hz, 85.5 Gauss (rms)

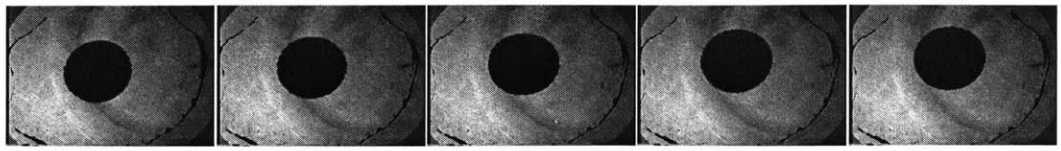

0 Gauss 6.64 Gauss 18.12 Gauss 28.55 Gauss 37.85 Gauss

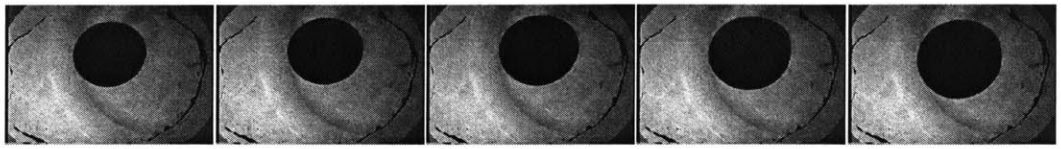

51.72 Gauss 63.96 Gauss 79.18 Gauss. 96.48 Gauss 108.44 Gauss

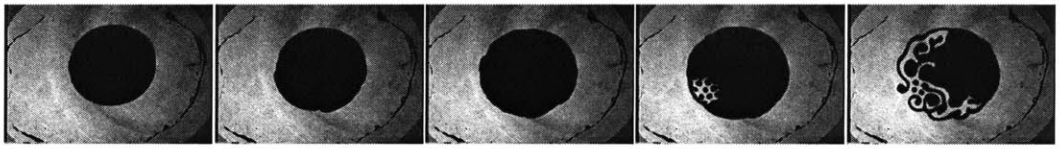

123.43 Gauss 145.47 Gauss 165.97 Gauss 176.26 Gauss 183.48 Gauss

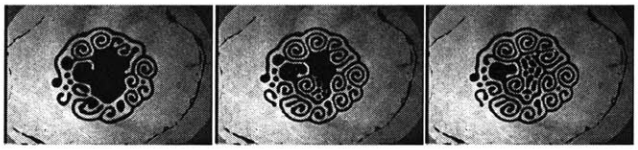

216.84 Gauss 241.12 Gauss 241.19 Gauss.

Figure D-56: Sequence 2: 200 μl, 0.9 mm, 30 Hz, 85.5 Gauss (rms)

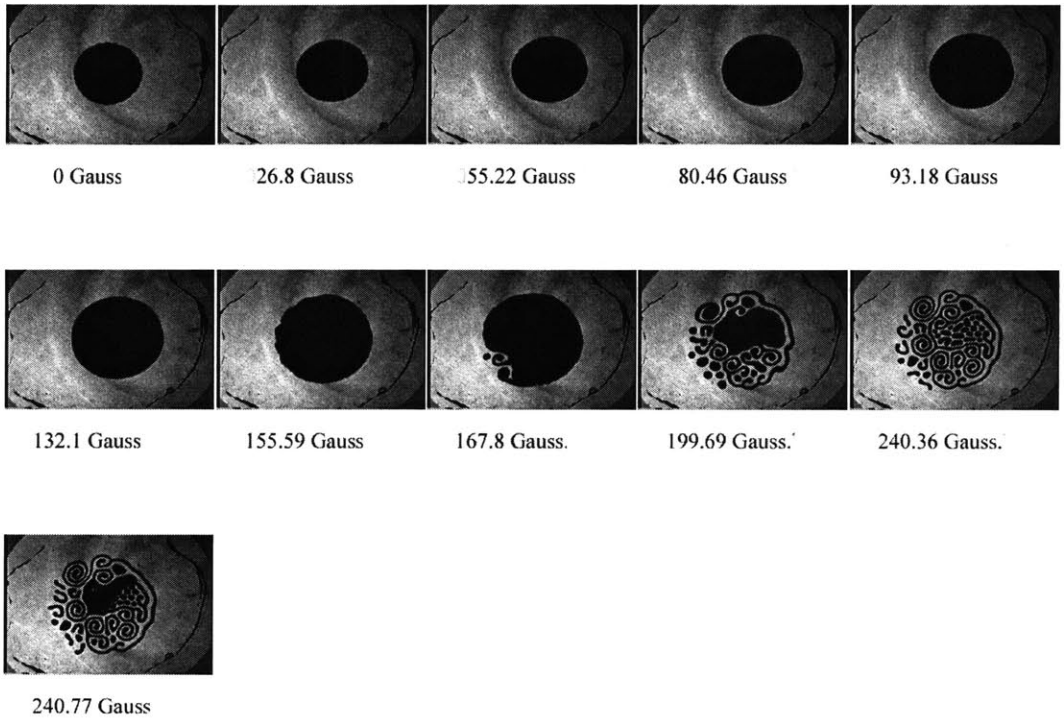

Figure D-57: Sequence 1: 200 μl, 0.9 mm, 30 Hz, 89.3 Gauss (rms)

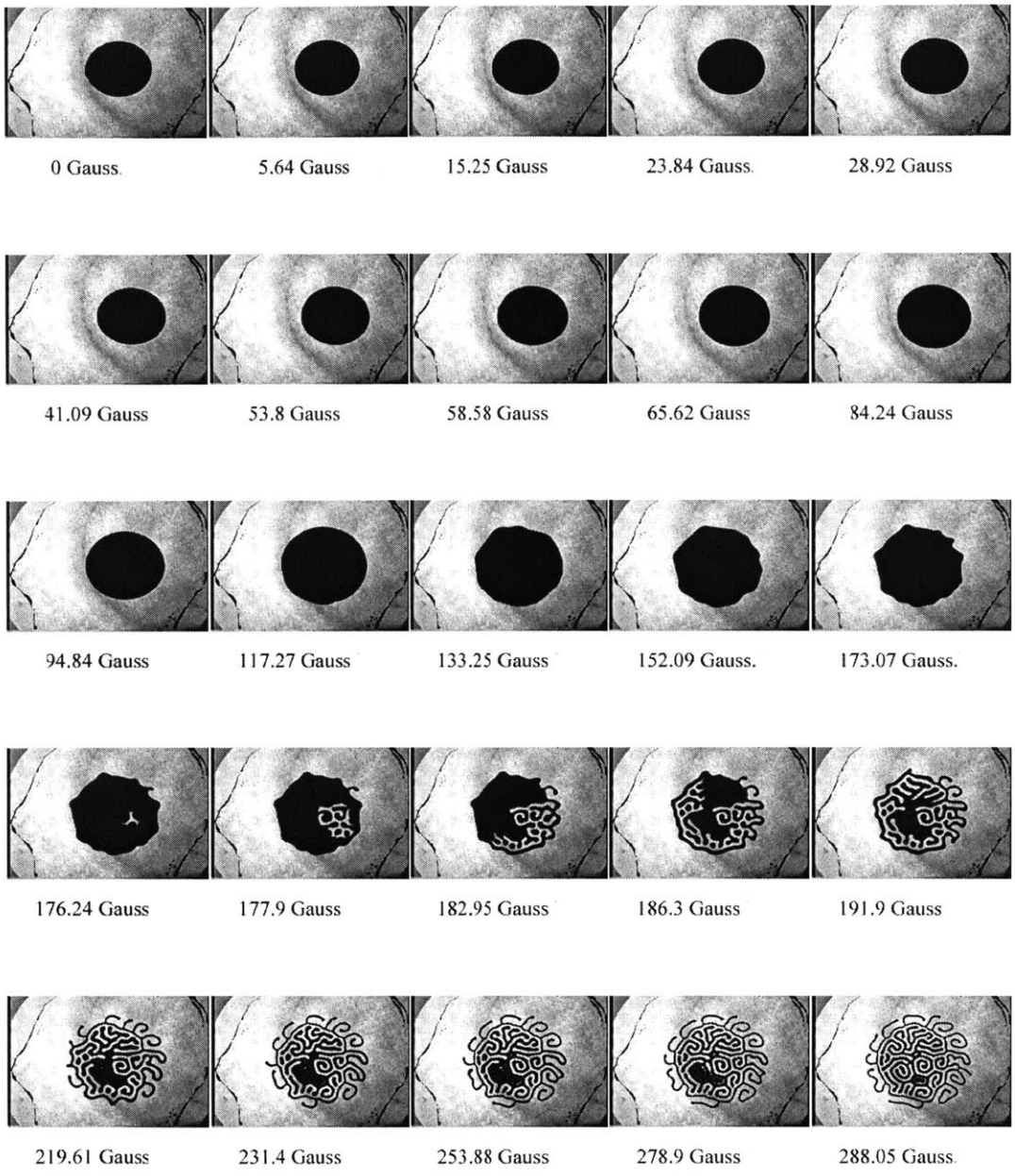

Figure D-58: Sequence 1: 200 μl, 0.9 mm, 35 Hz, 39.9 Gauss (rms)

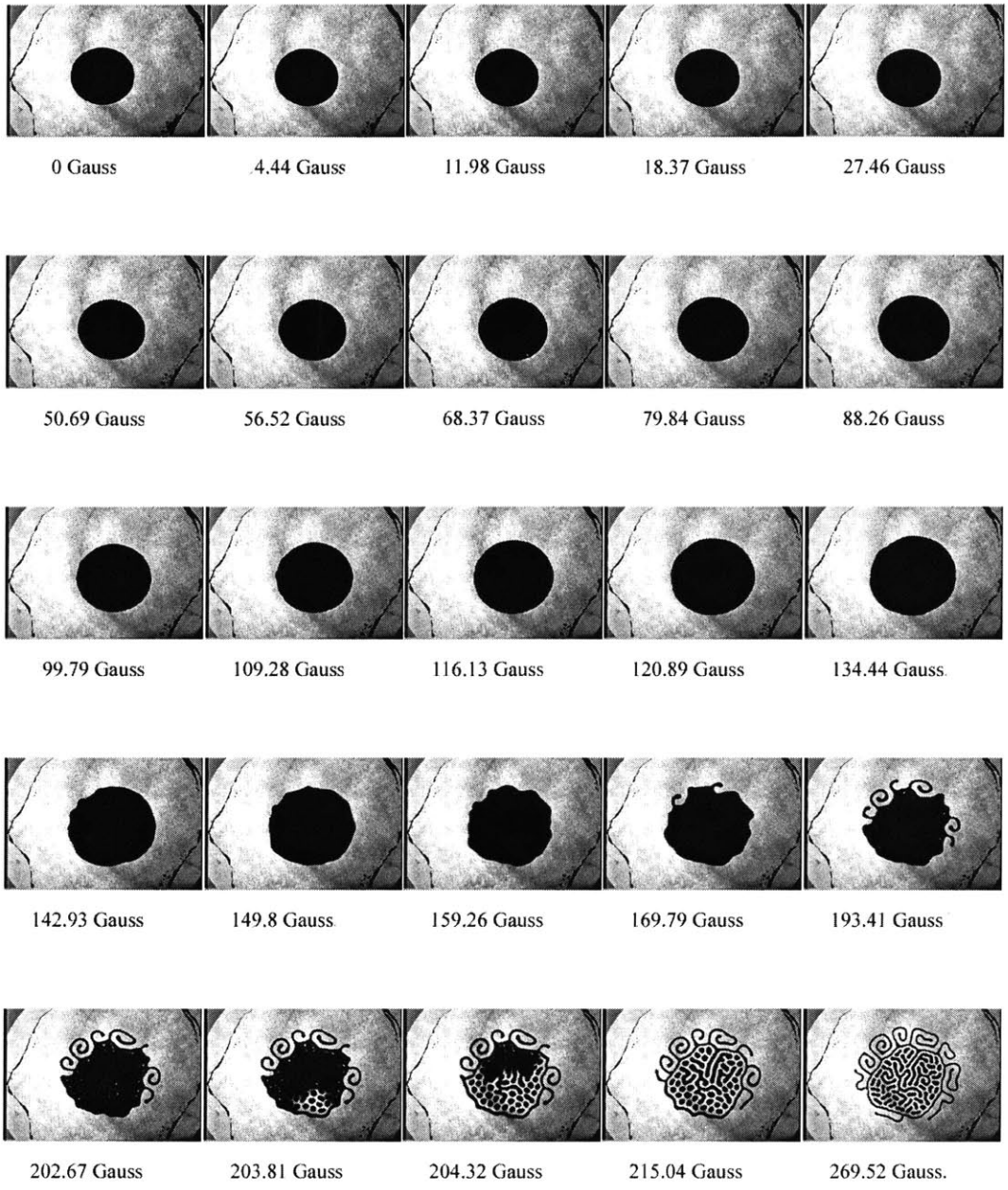

Figure D-59: Sequence 2: 200 μl, 0.9 mm, 35 Hz, 39.9 Gauss (rms)

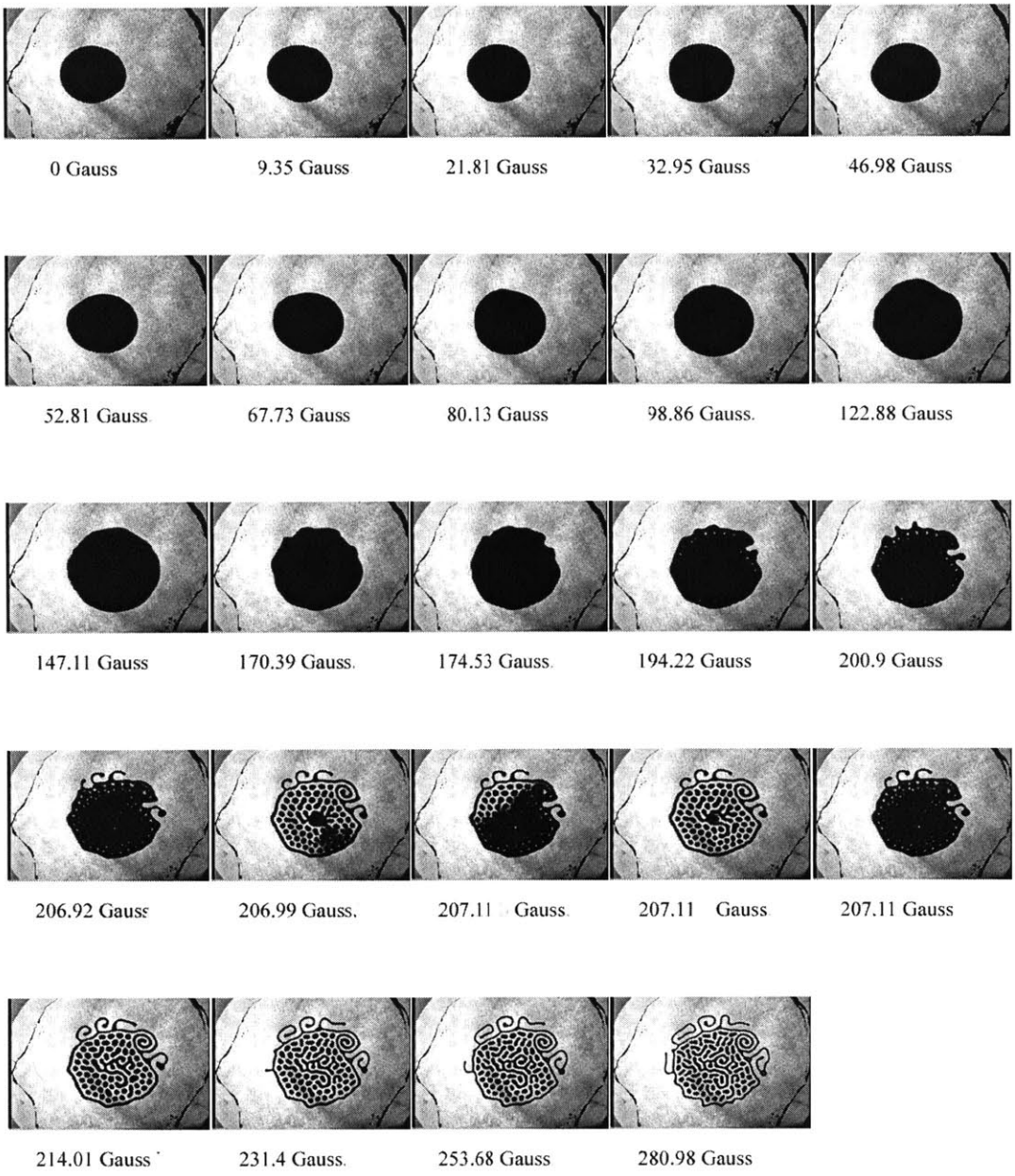

Figure D-60: Sequence 1: 200 μl, 0.9 mm, 35 Hz, 43.7 Gauss (rms)

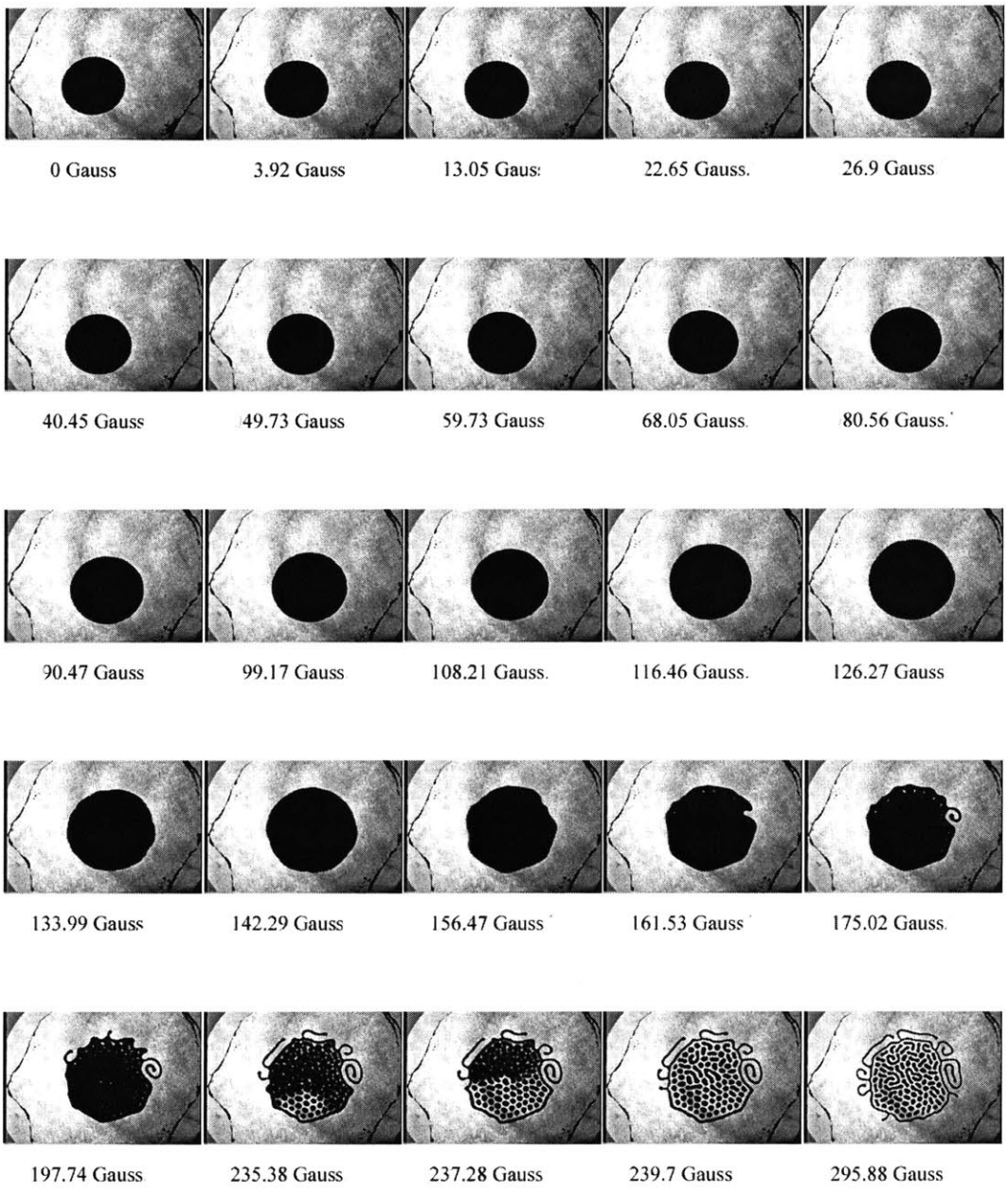

Figure D-61: Sequence 2: 200 μl, 0.9 mm, 35 Hz, 43.7 Gauss (rms)

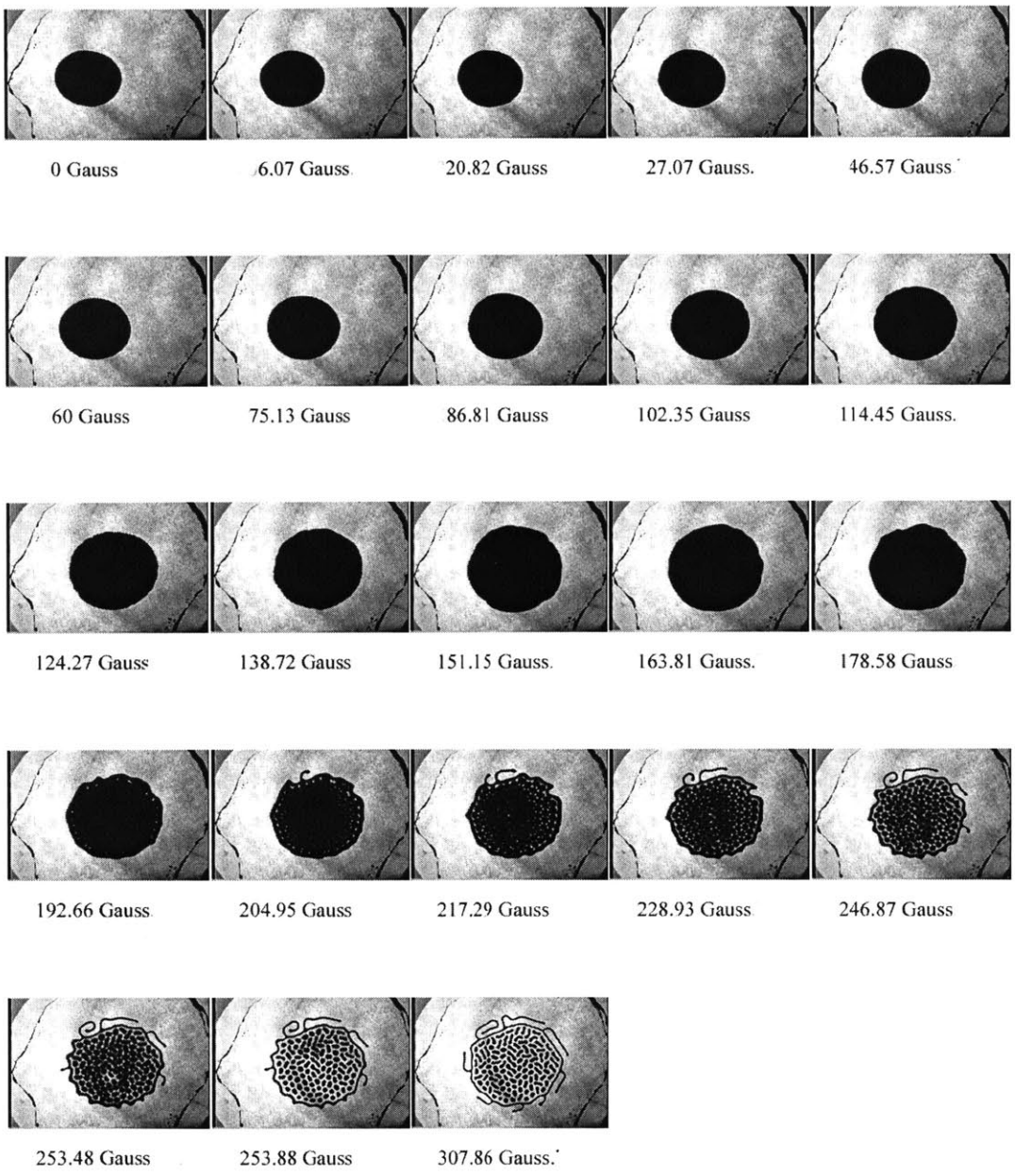

Figure D-62: Sequence 1: 200 μl, 0.9 mm, 35 Hz, 47.5 Gauss (rms)

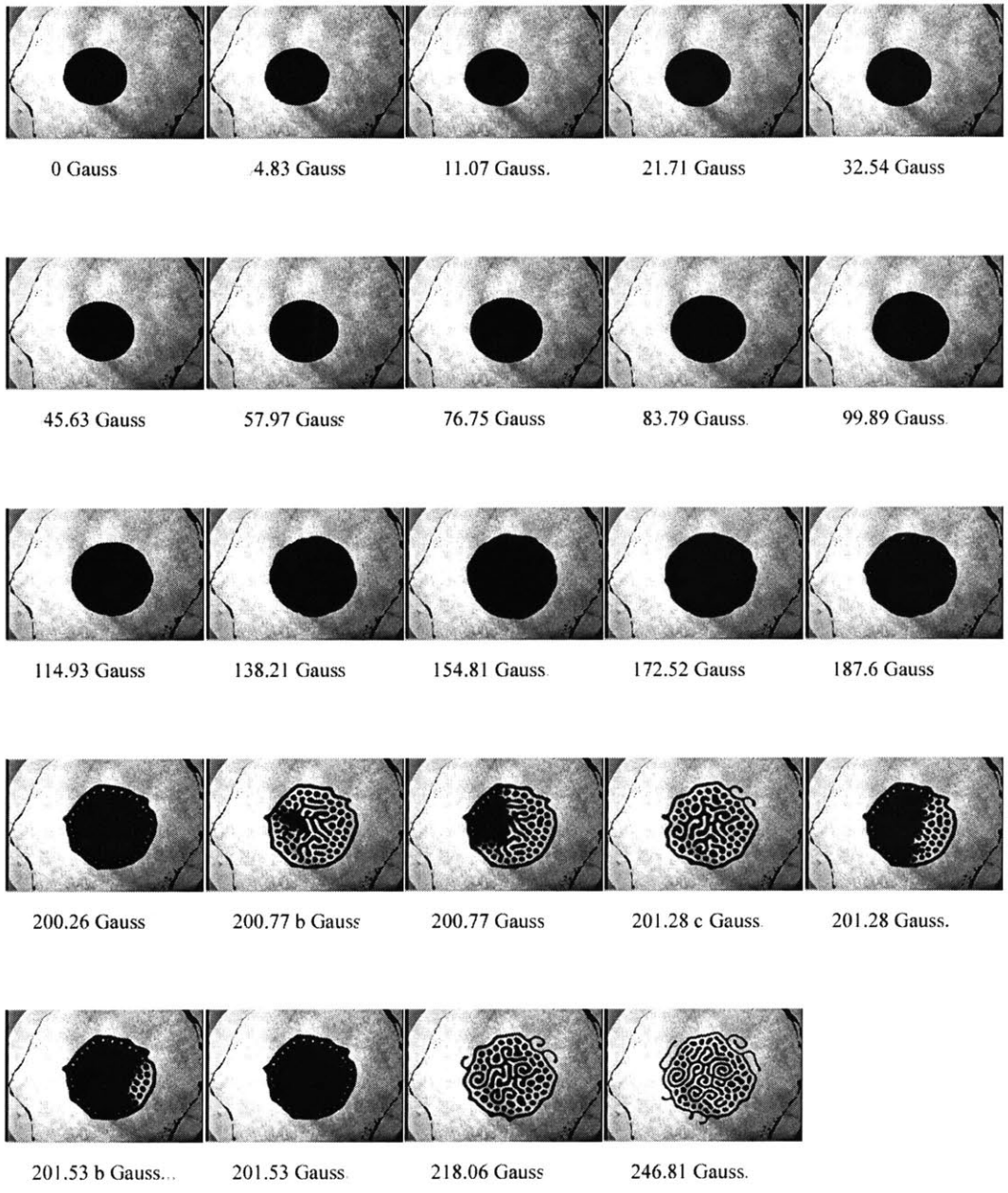

Figure D-63: Sequence 2: 200 μl, 0.9 mm, 35 Hz, 47.5 Gauss (rms)

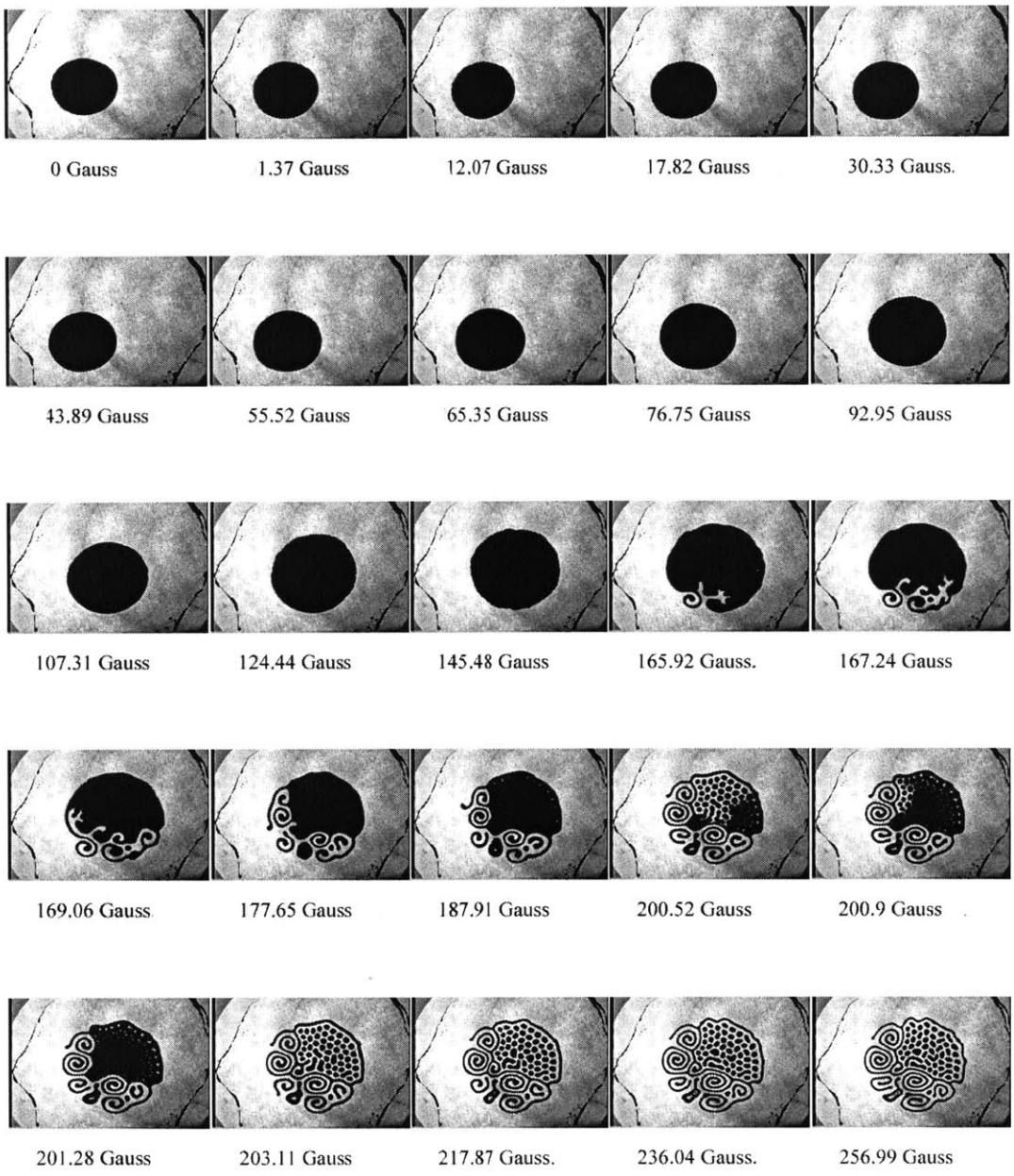

Figure D-64: Sequence 1: 200 μl, 0.9 mm, 35 Hz, 51.3 Gauss (rms)

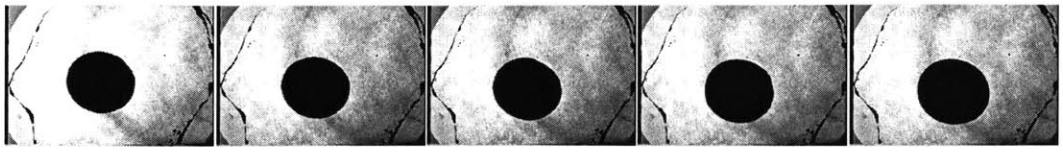

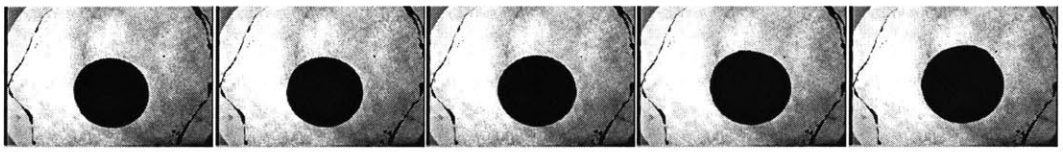

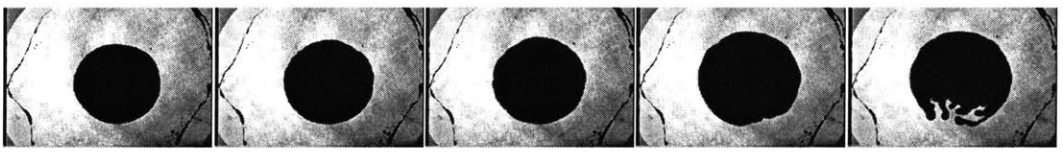

Figure D-65: Sequence 2: 200 μl, 0.9 mm, 35 Hz, 51.3 Gauss (rms)

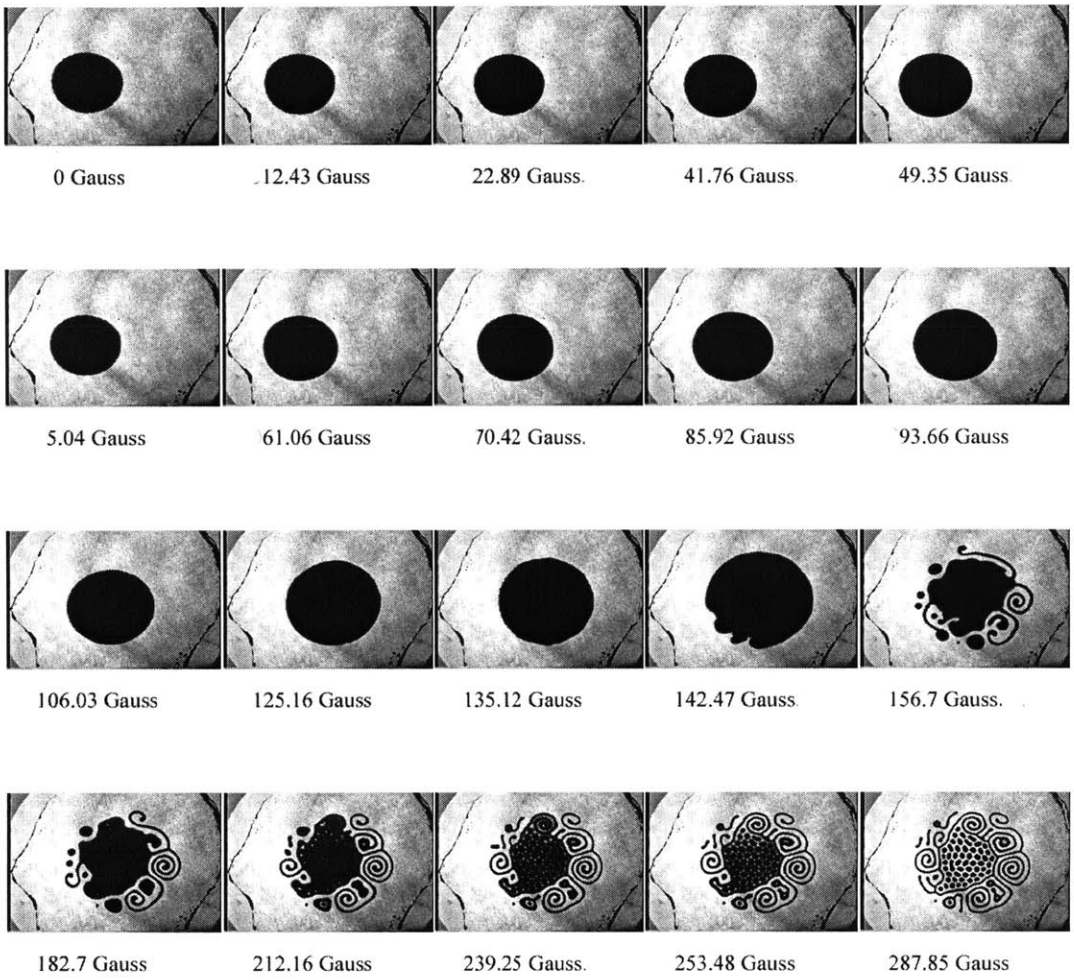

Figure D-66: Sequence 1: 200 μl, 0.9 mm, 35 Hz, 55.1 Gauss (rms)

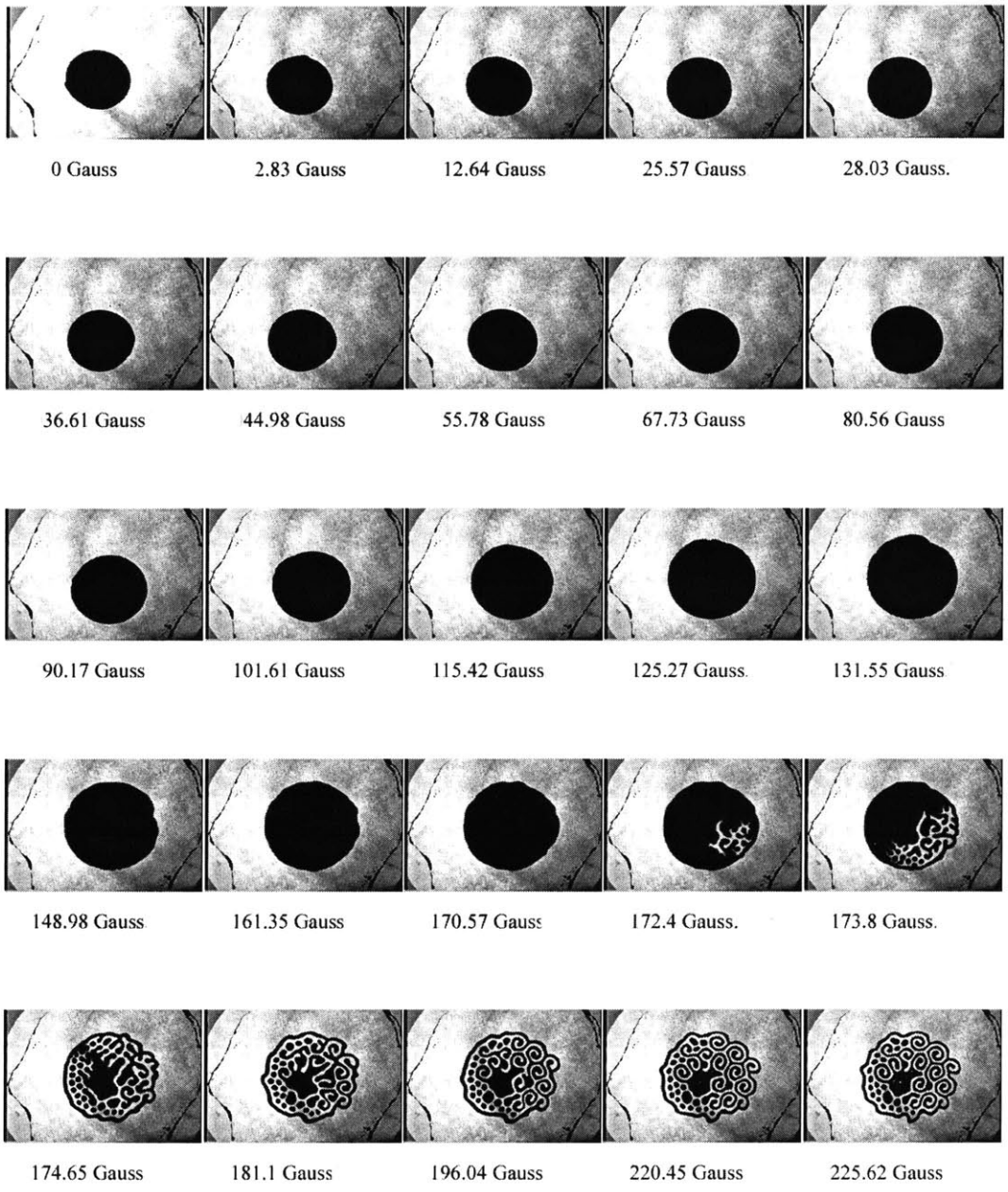

Figure D-67: Sequence 2: 200 μl, 0.9 mm, 35 Hz, 55.1 Gauss (rms)

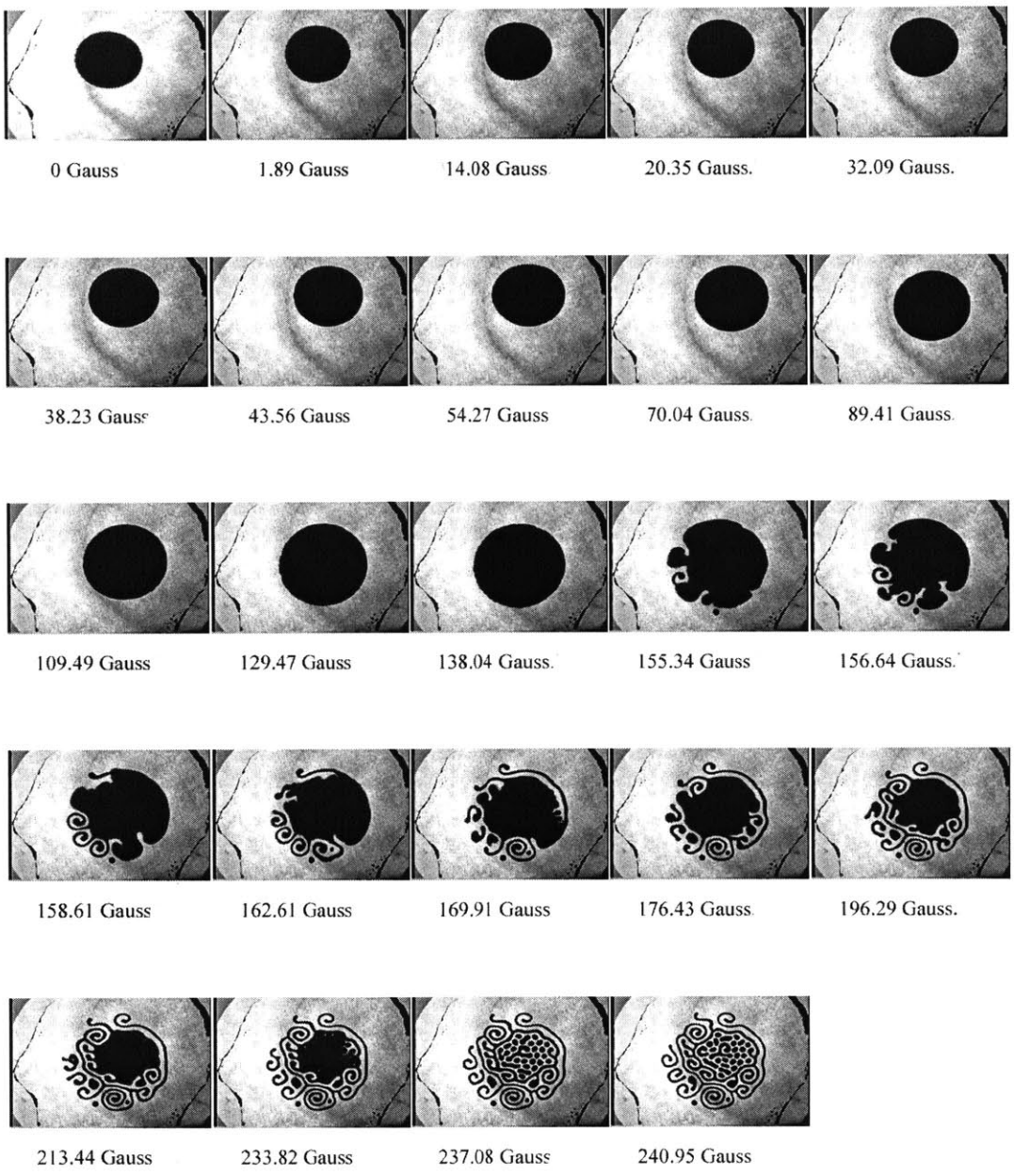

Figure D-68: Sequence 1: 200 μl, 0.9 mm, 35 Hz, 58.9 Gauss (rms)

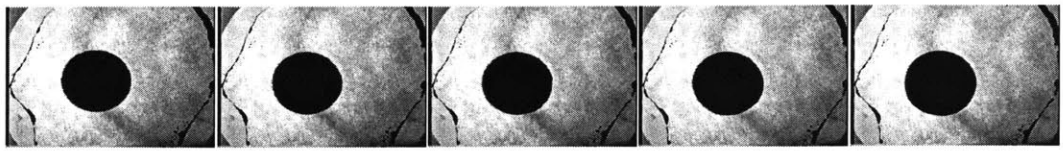

0 Gauss 11.48 Gauss 19.7 Gauss. 29.07 Gauss. 42.04 Gauss.

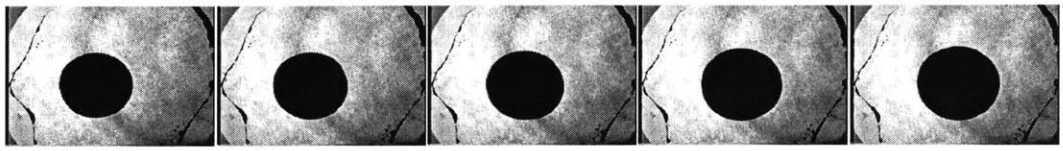

48.02 Gauss 58.58 Gauss 71.82 Gauss 88.01 Gauss. 94.58 Gauss.

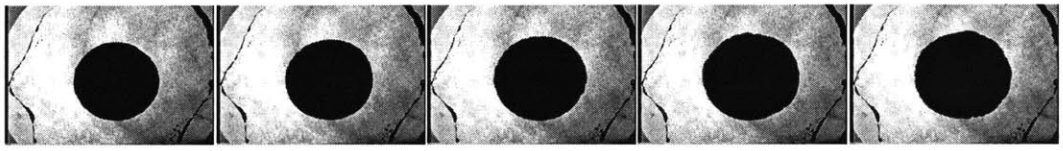

110.83 Gauss 120.95 Gauss 131.33 Gauss 140.05 Gauss 146.82 Gauss

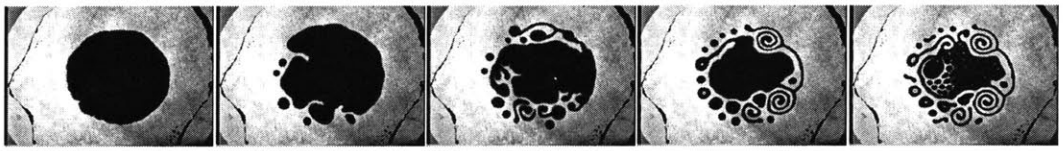

151.21 Gauss 158.43 Gauss 165.92 Gauss 192.78 Gauss 231.4 Gauss

234.4 Gauss

Figure D-69: Sequence 2: 200 μl, 0.9 mm, 35 Hz, 58.9 Gauss (rms)

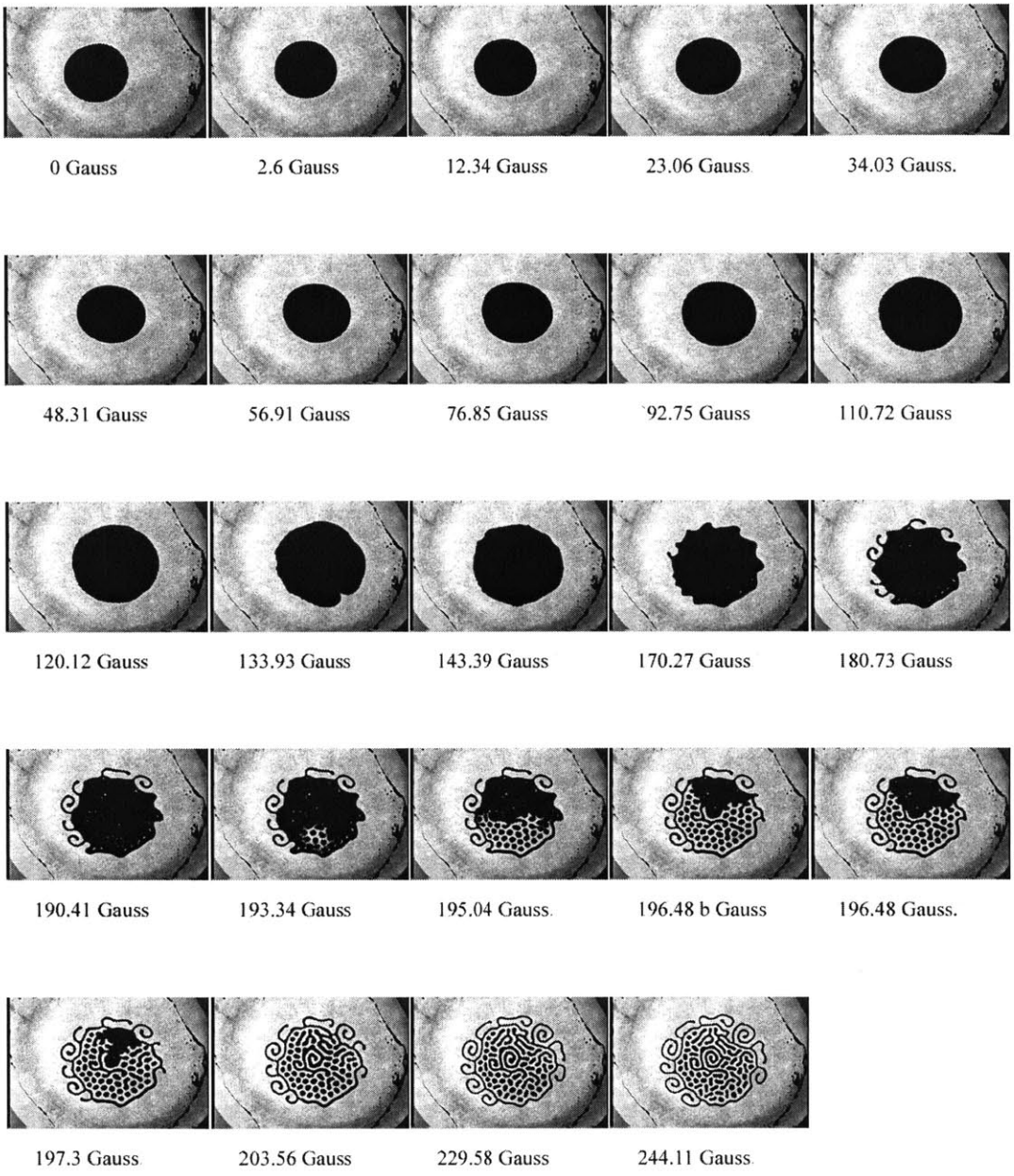

Figure D-70: Sequence 1: 200 μl, 0.9 mm, 40 Hz, 39.9 Gauss (rms)

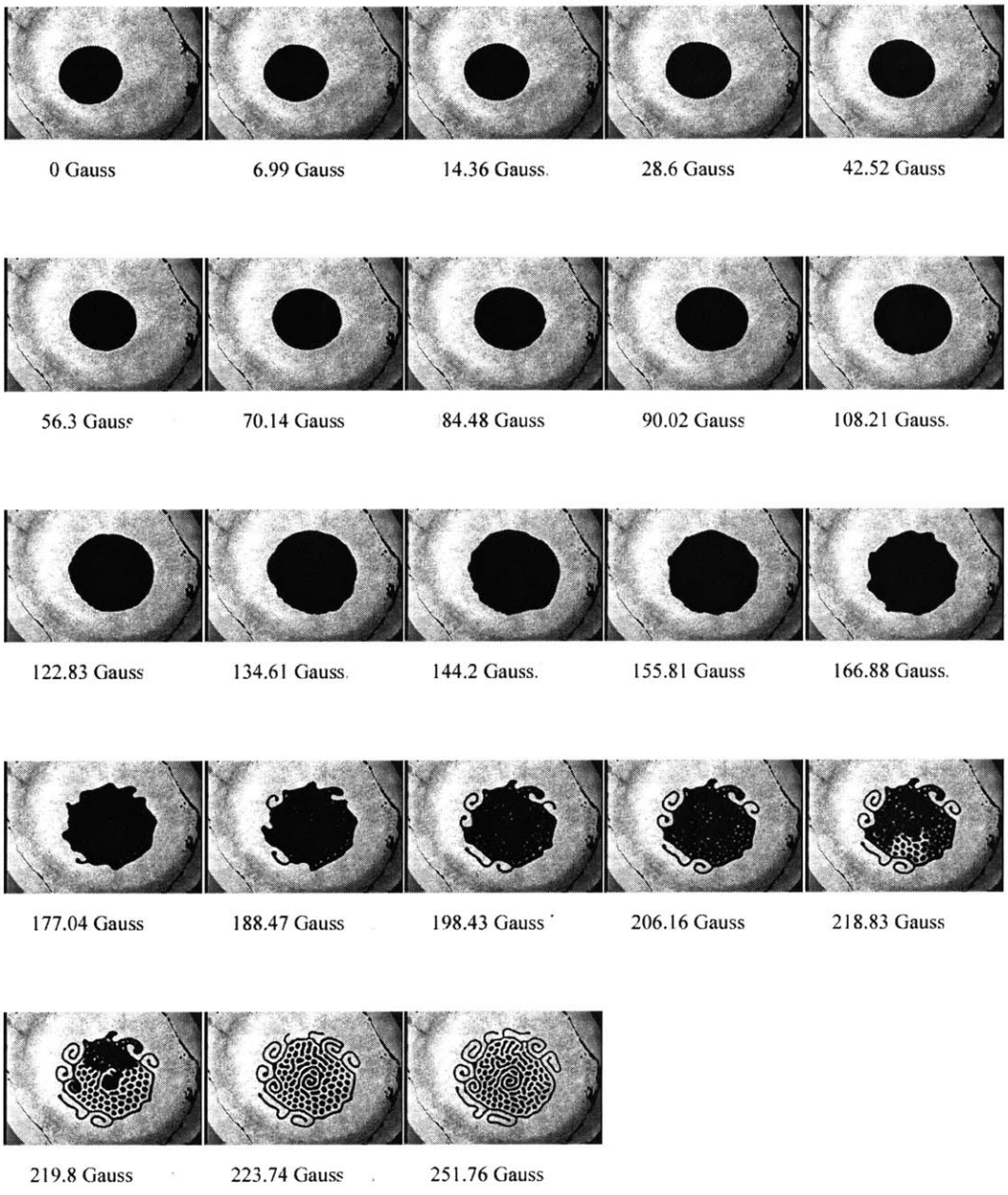

Figure D-71: Sequence 2: 200 μl, 0.9 mm, 40 Hz, 39.9 Gauss (rms)

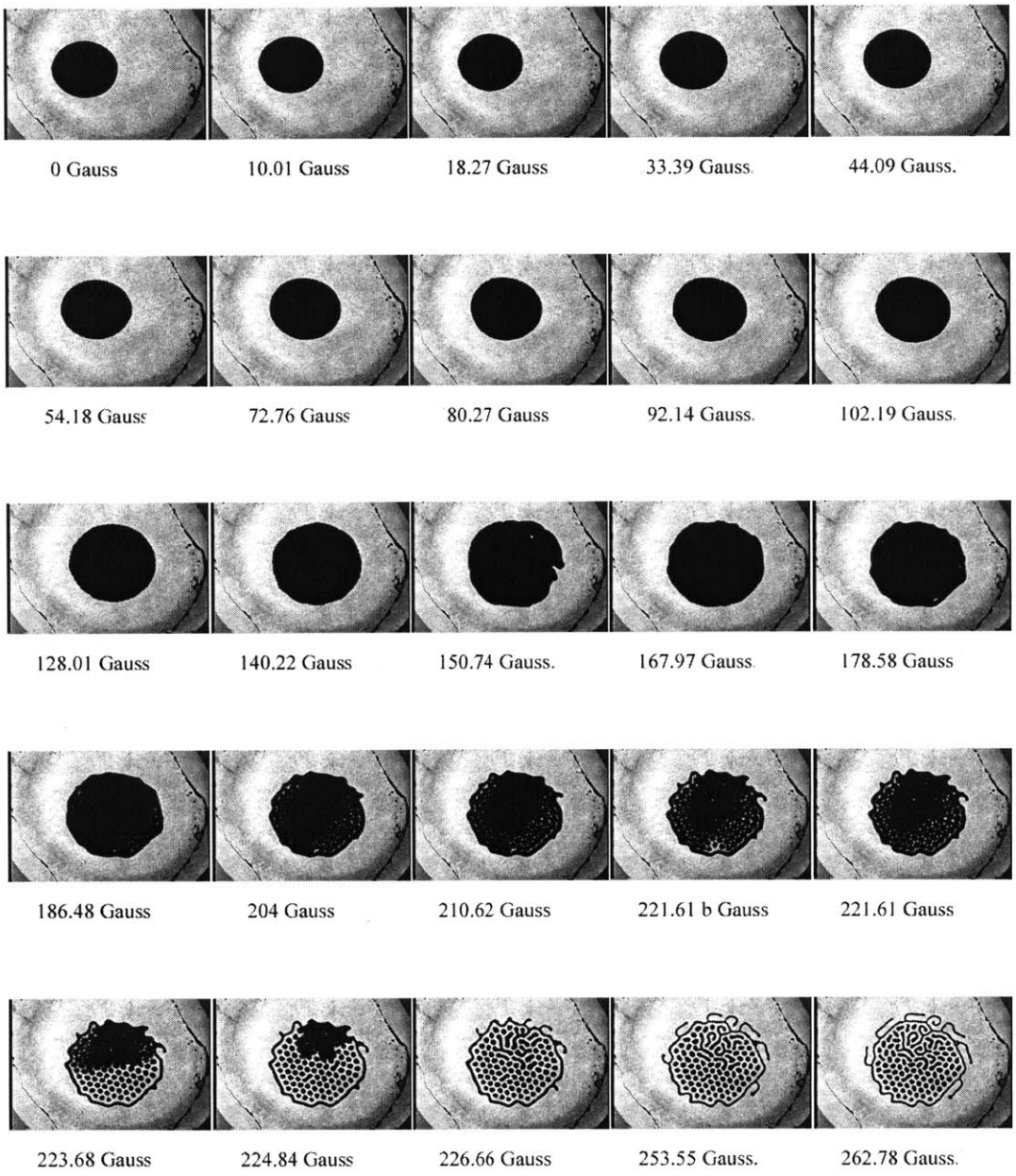

Figure D-72: Sequence 1: 200 μl, 0.9 mm, 40 Hz, 43.7 Gauss (rms)

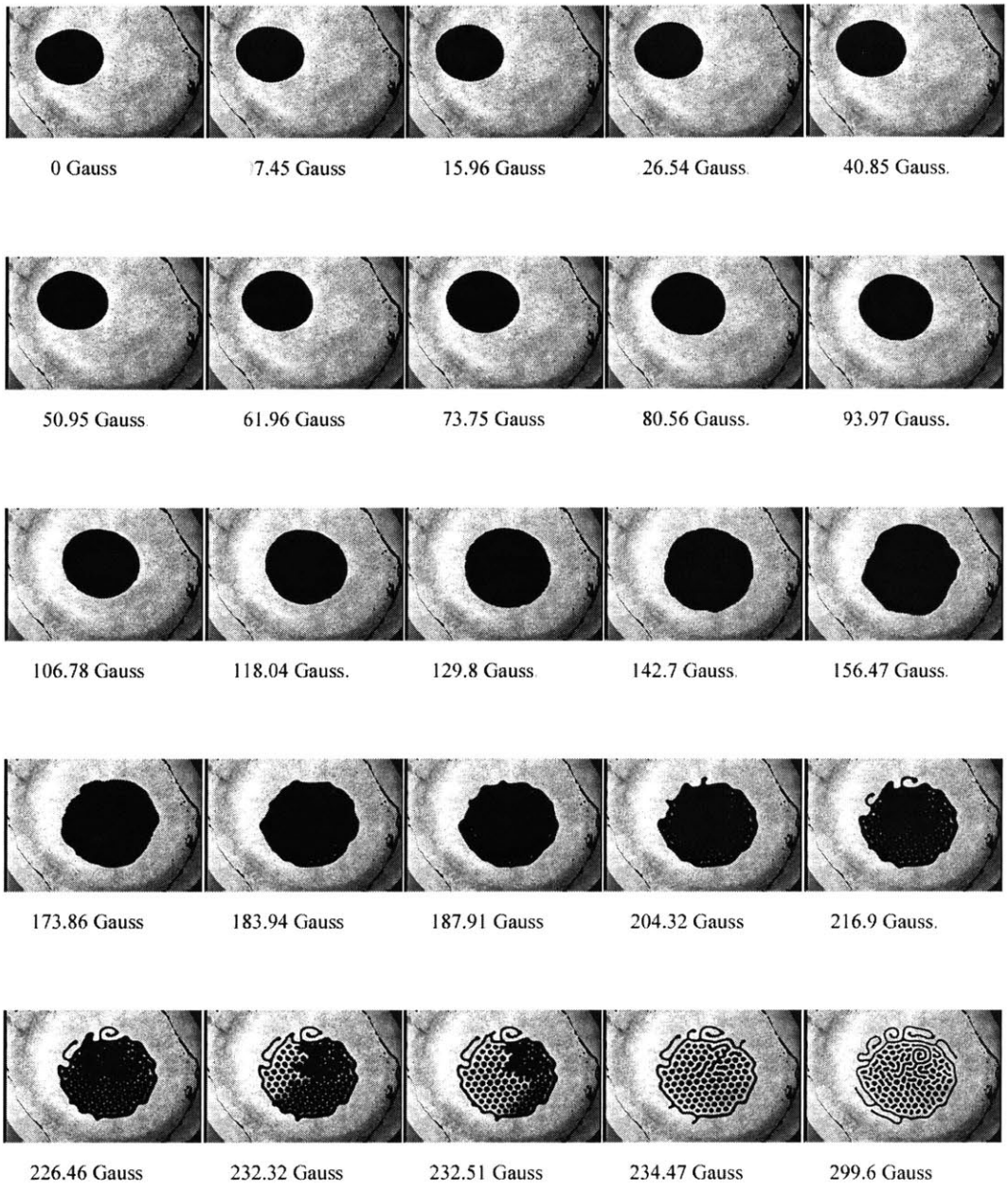

Figure D-73: Sequence 2: 200 μl, 0.9 mm, 40 Hz, 43.7 Gauss (rms)

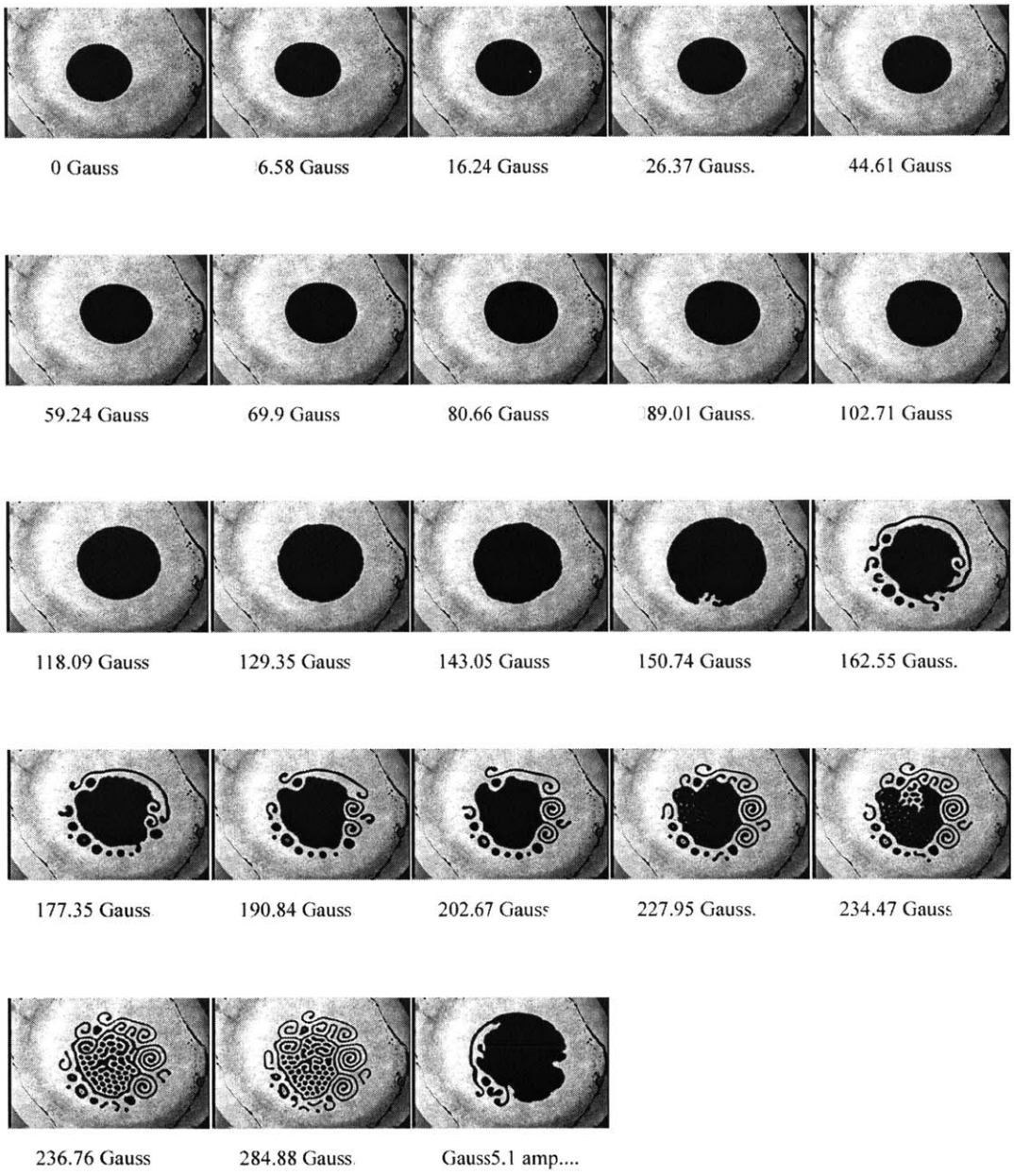

Figure D-74: Sequence 1: 200 μl, 0.9 mm, 40 Hz, 47.5 Gauss (rms)

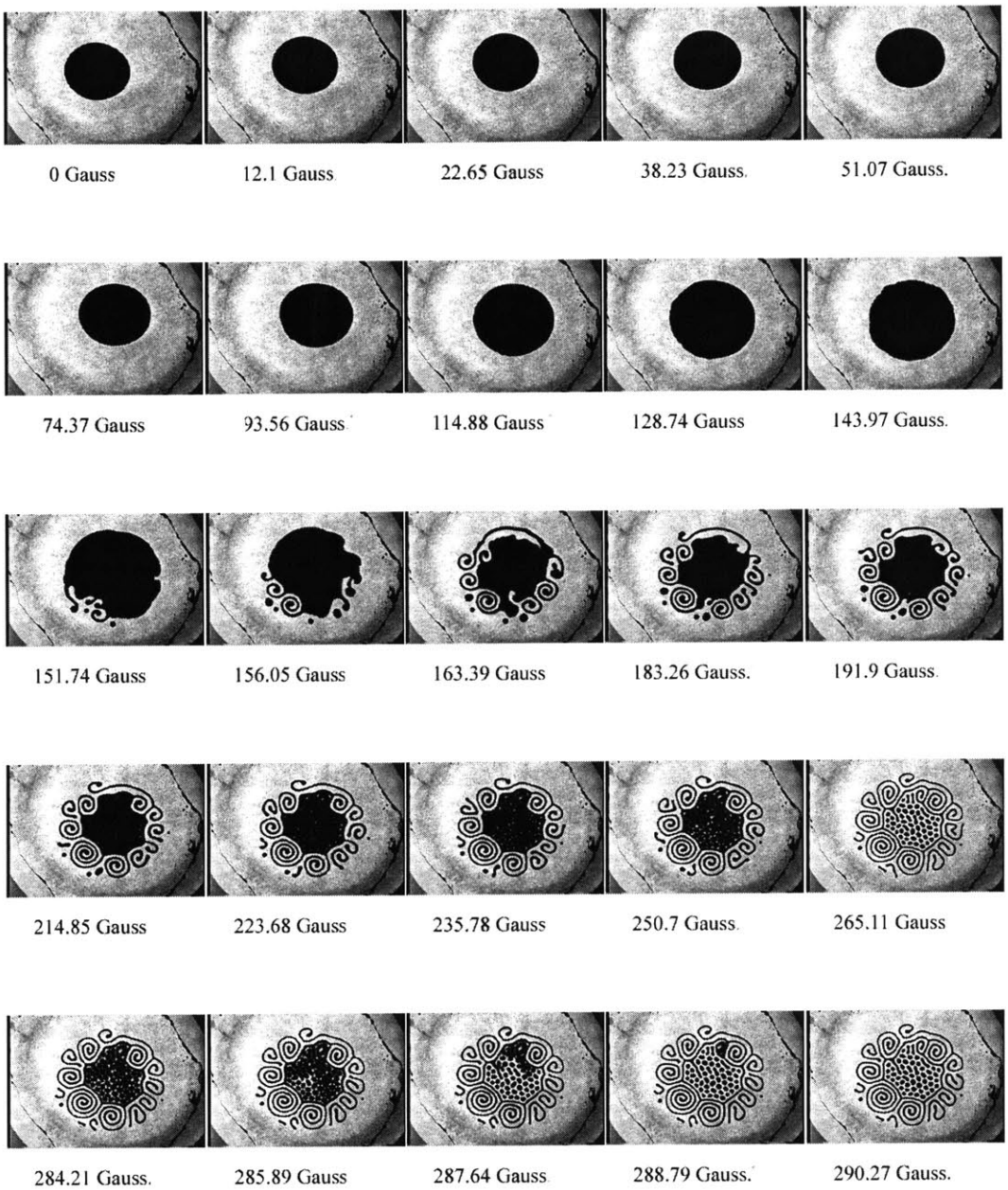

Figure D-75: Sequence 2: 200 μl, 0.9 mm, 40 Hz, 47.5 Gauss (rms)

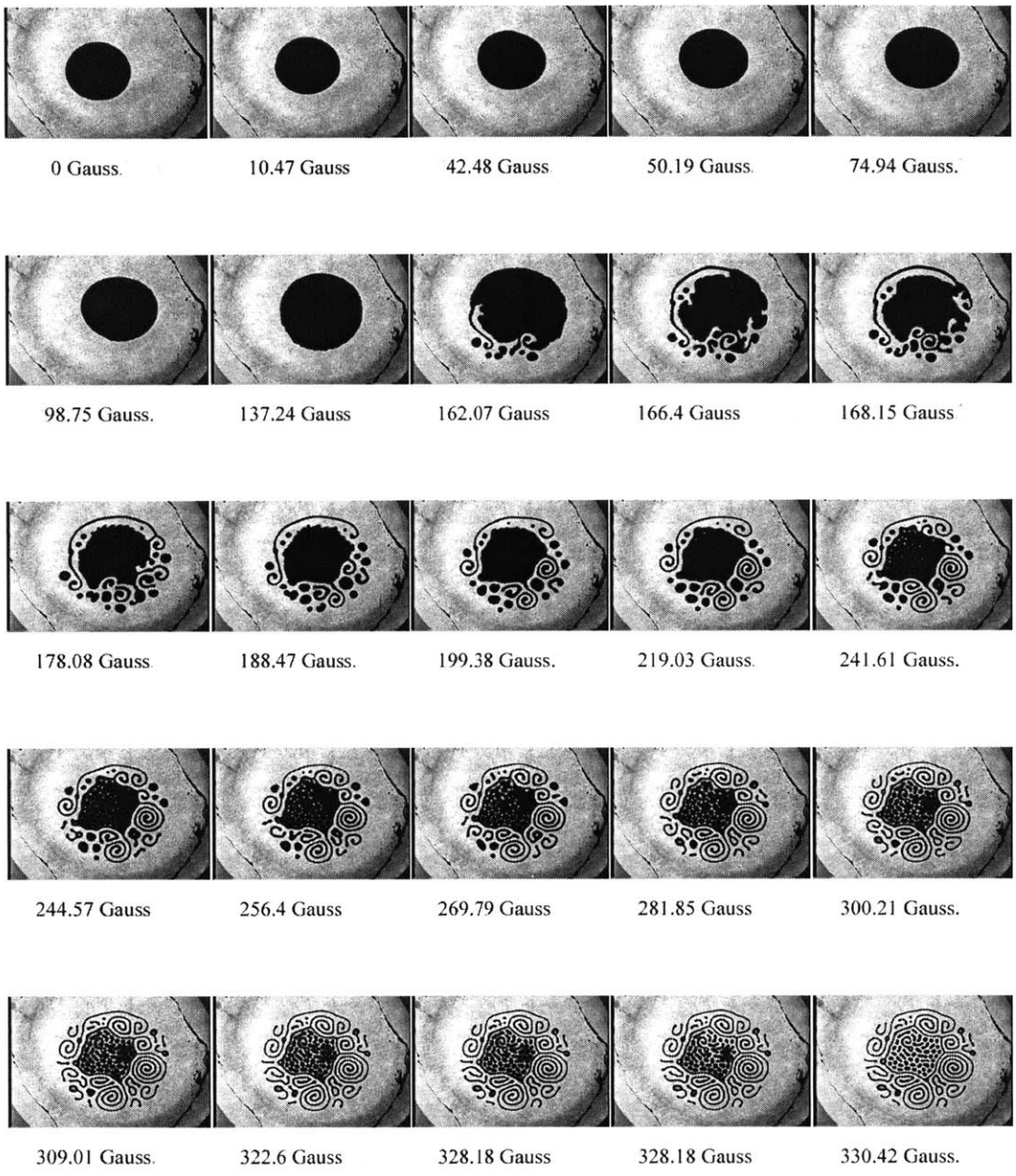

Figure D-76: Sequence 1: 200 μl, 0.9 mm, 40 Hz, 51.3 Gauss (rms)

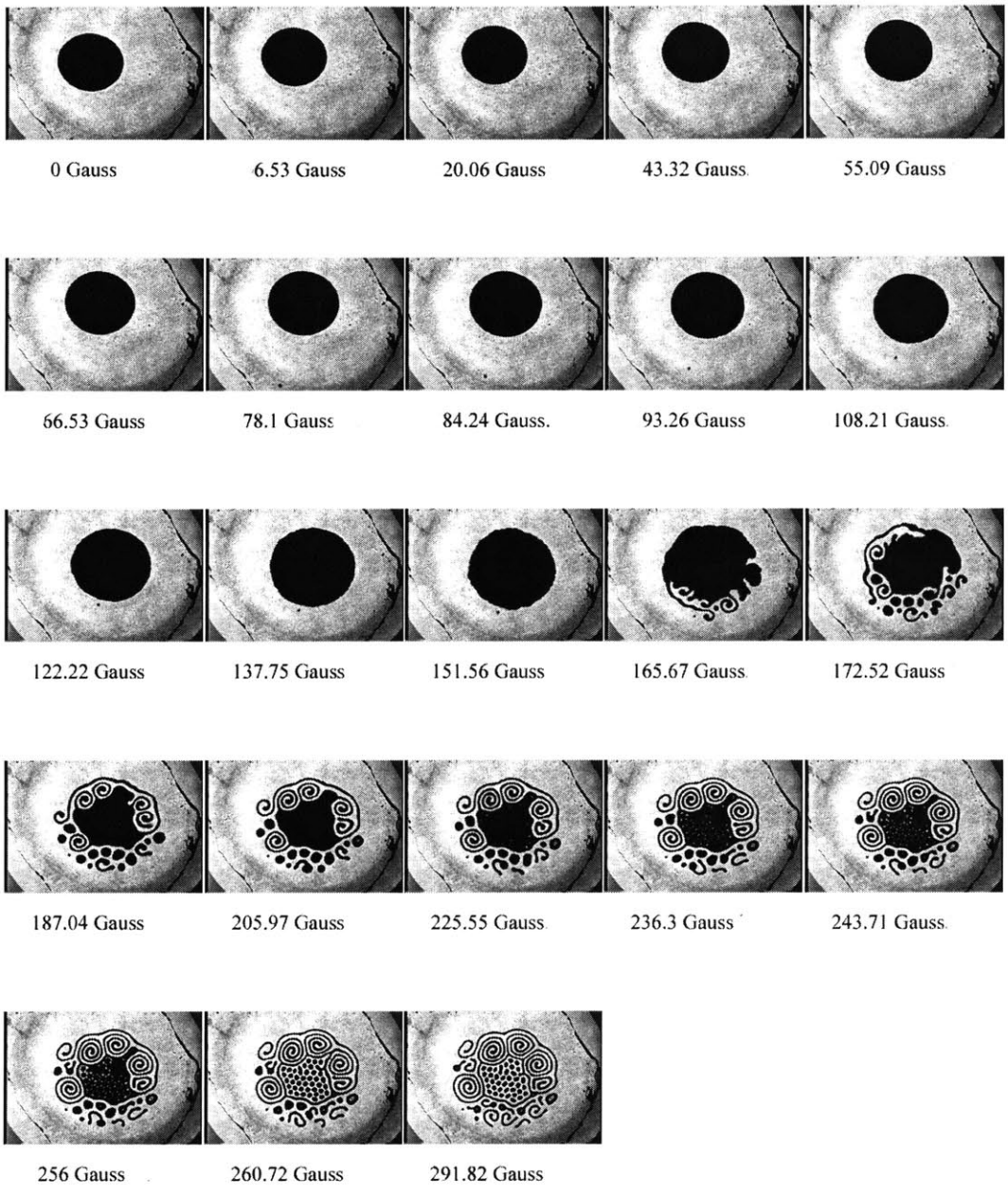

Figure D-77: Sequence 2: 200 μl, 0.9 mm, 40 Hz, 51.3 Gauss (rms)

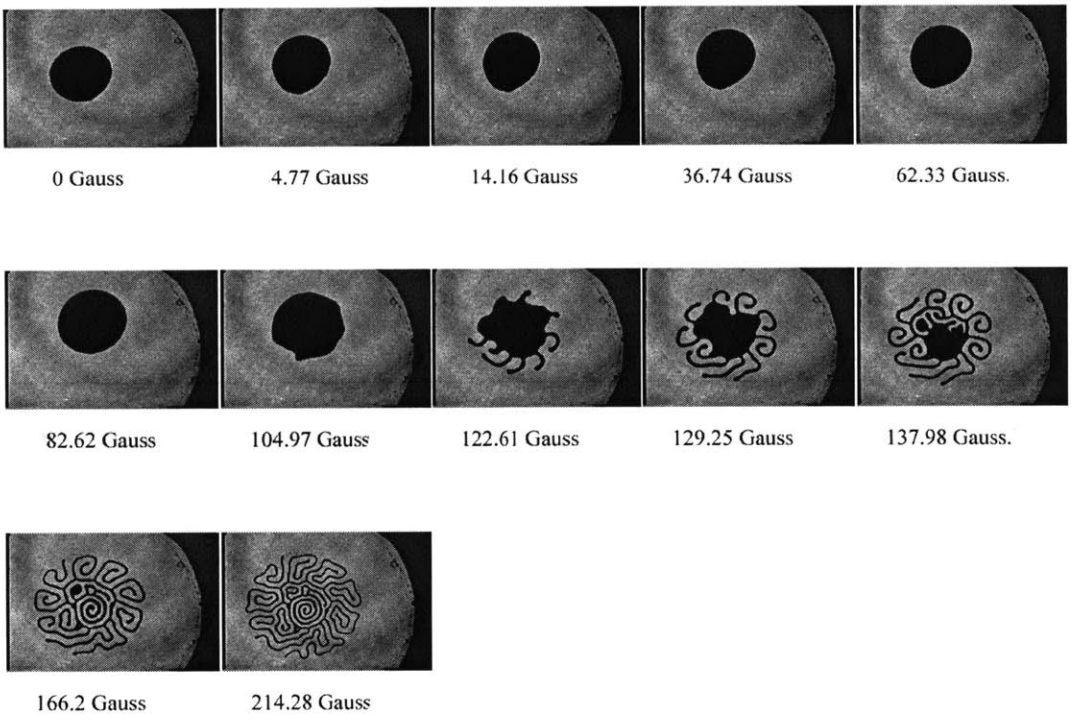

Figure D-78: Sequence 1: 200 μl, 1.15 mm, 20 Hz, 24.7 Gauss (rms)

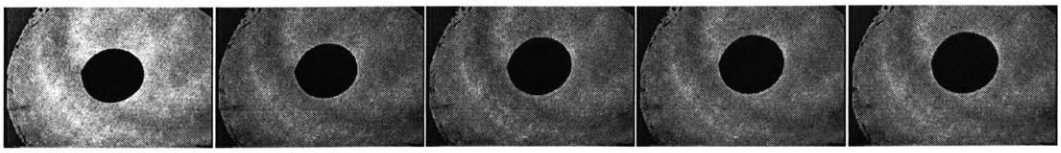

0 Gauss 9.79 Gauss 42.32 Gauss 51.89 Gauss 72.95 Gauss.

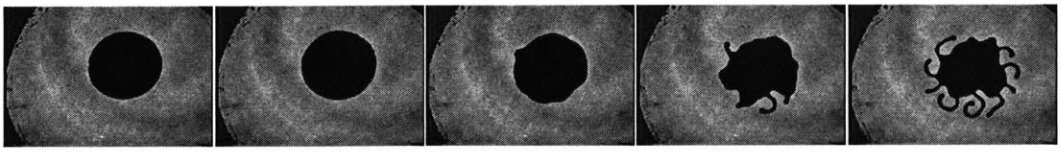

83.71 Gauss 90.59 Gauss 100.96 Gauss 112.23 Gauss 117.14 Gauss

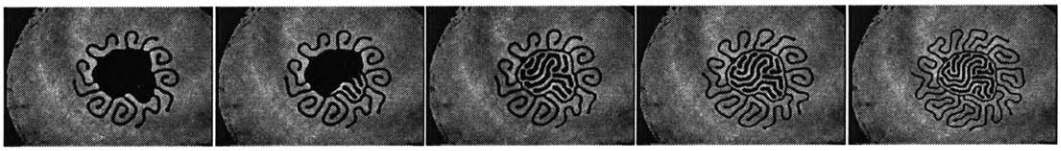

139.26 Gauss 151.25 Gauss 151.86 Gauss 169.1 Gauss 217.2 Gauss.

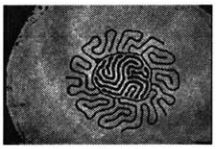

228.51 Gauss

Figure D-79: Sequence 2: 200 μl, 1.15 mm, 20 Hz, 24.7 Gauss (rms)

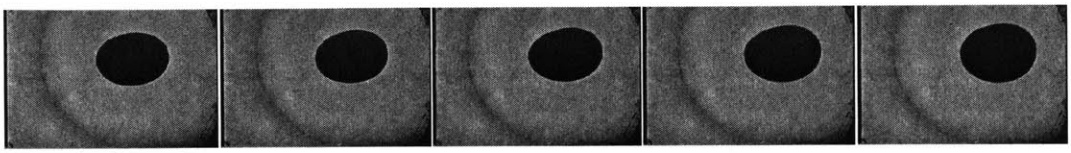

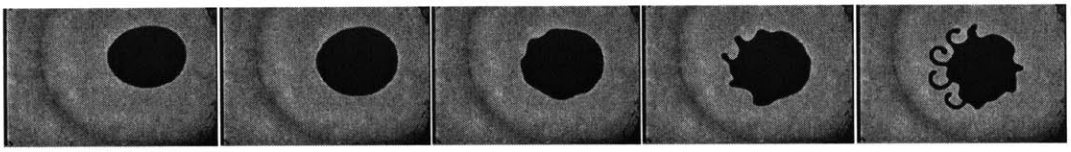

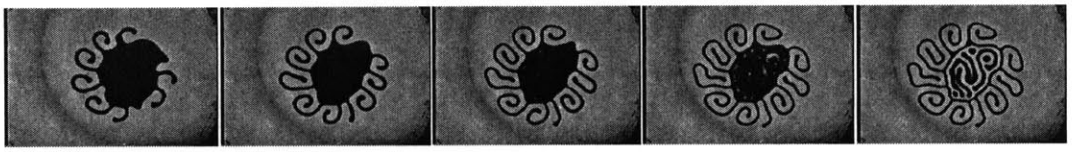

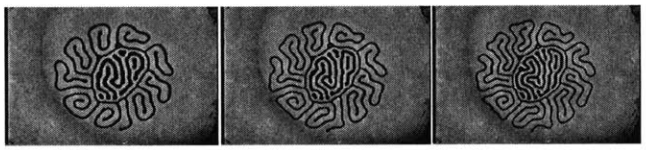

Figure D-80: Sequence 1: 200 μl, 1.15 mm, 20 Hz, 28.5 Gauss (rms)

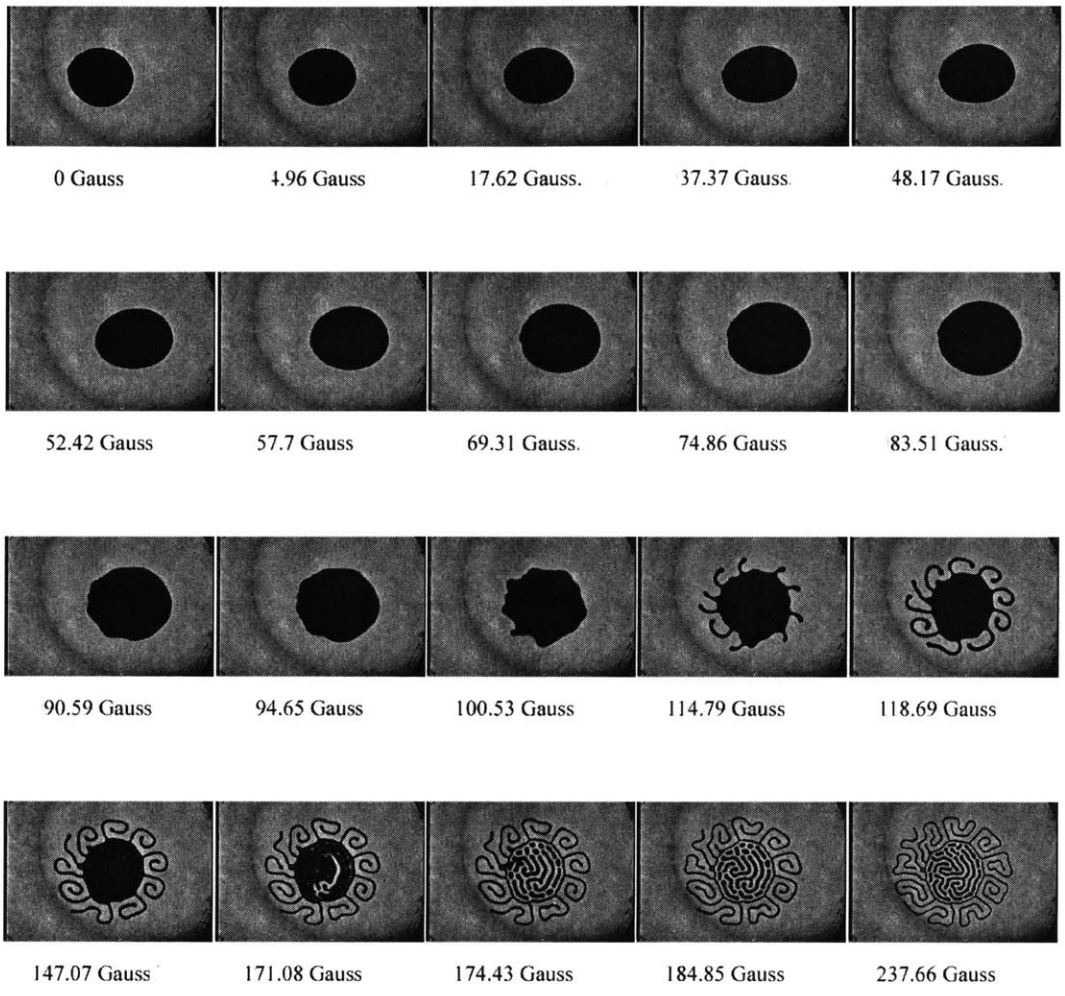

Figure D-81: Sequence 2: 200 μl, 1.15 mm, 20 Hz, 28.5 Gauss (rms)

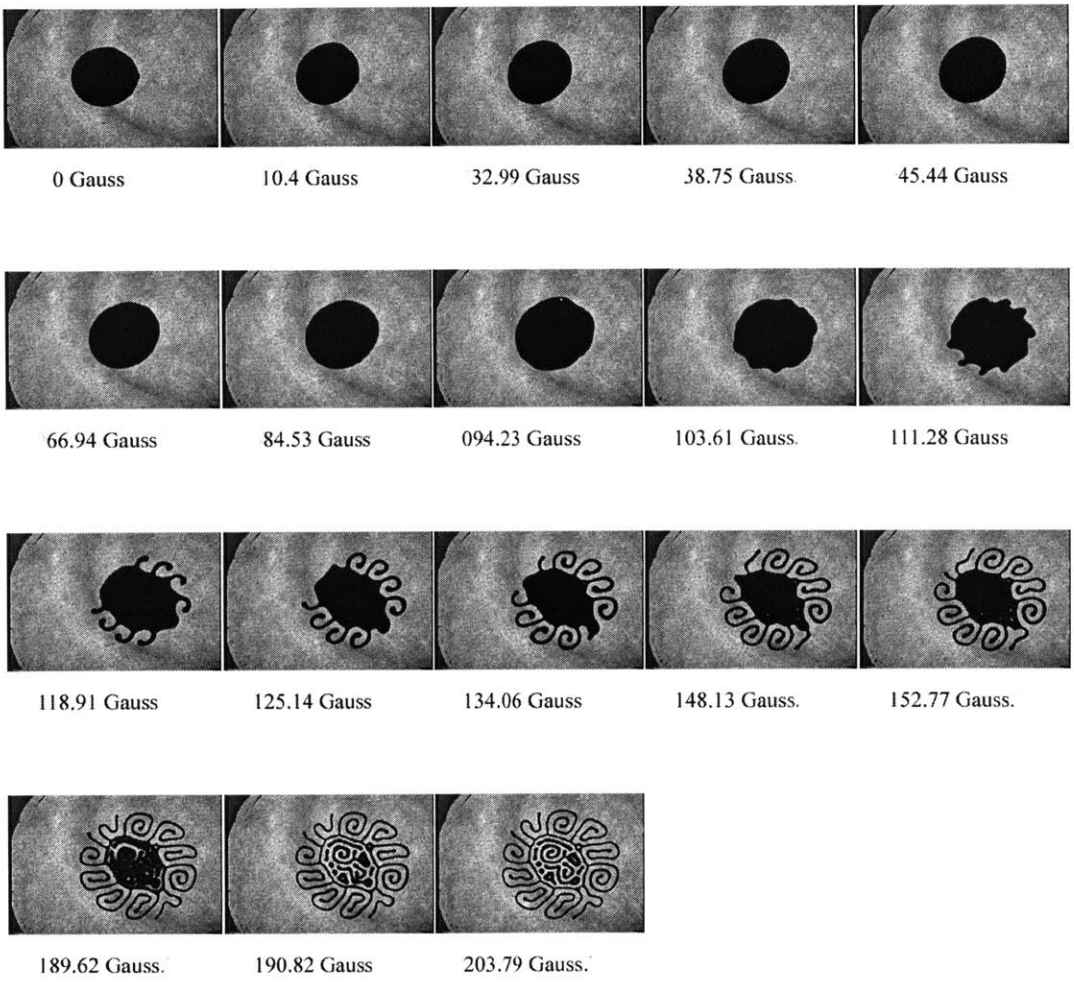

Figure D-82: Sequence 1: 200 μl, 1.15 mm, 20 Hz, 32.3 Gauss (rms)

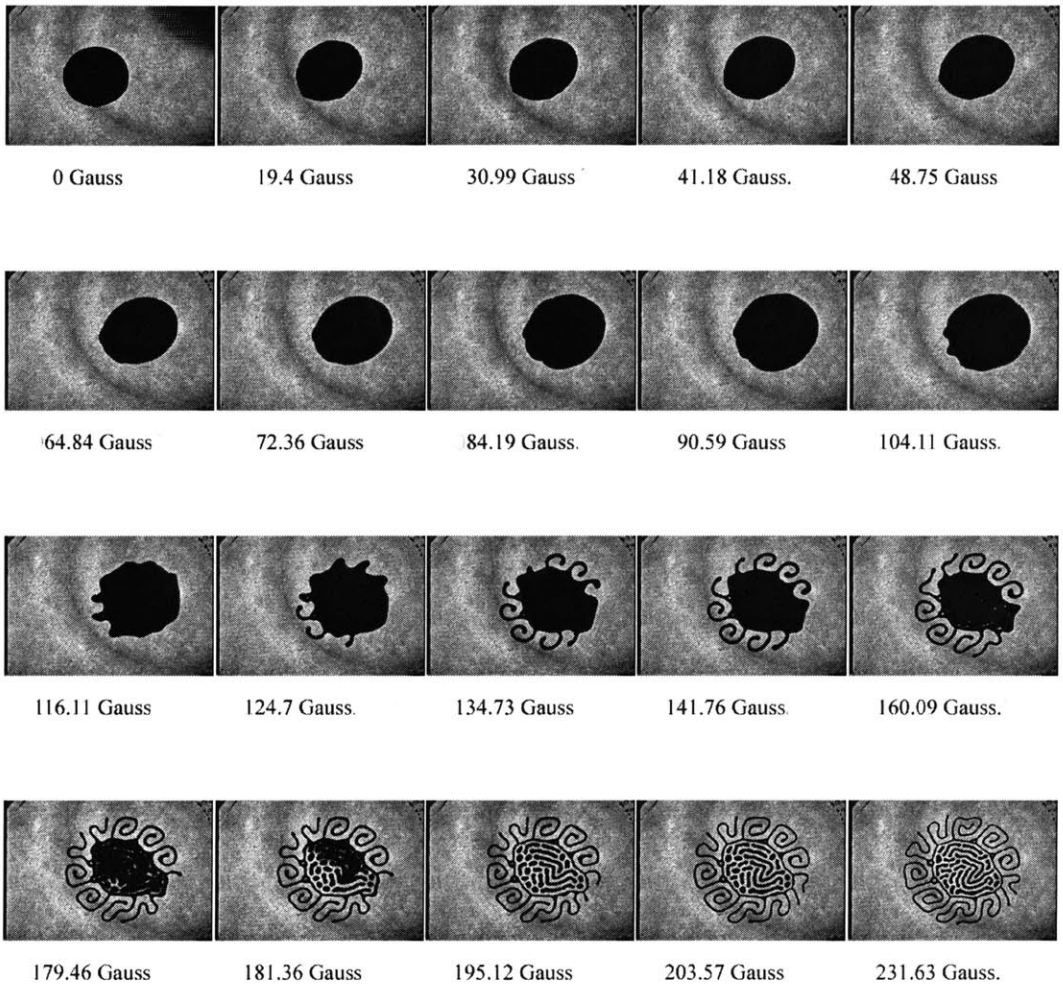

Figure D-83: Sequence 2: 200 μl, 1.15 mm, 20 Hz, 32.3 Gauss (rms)

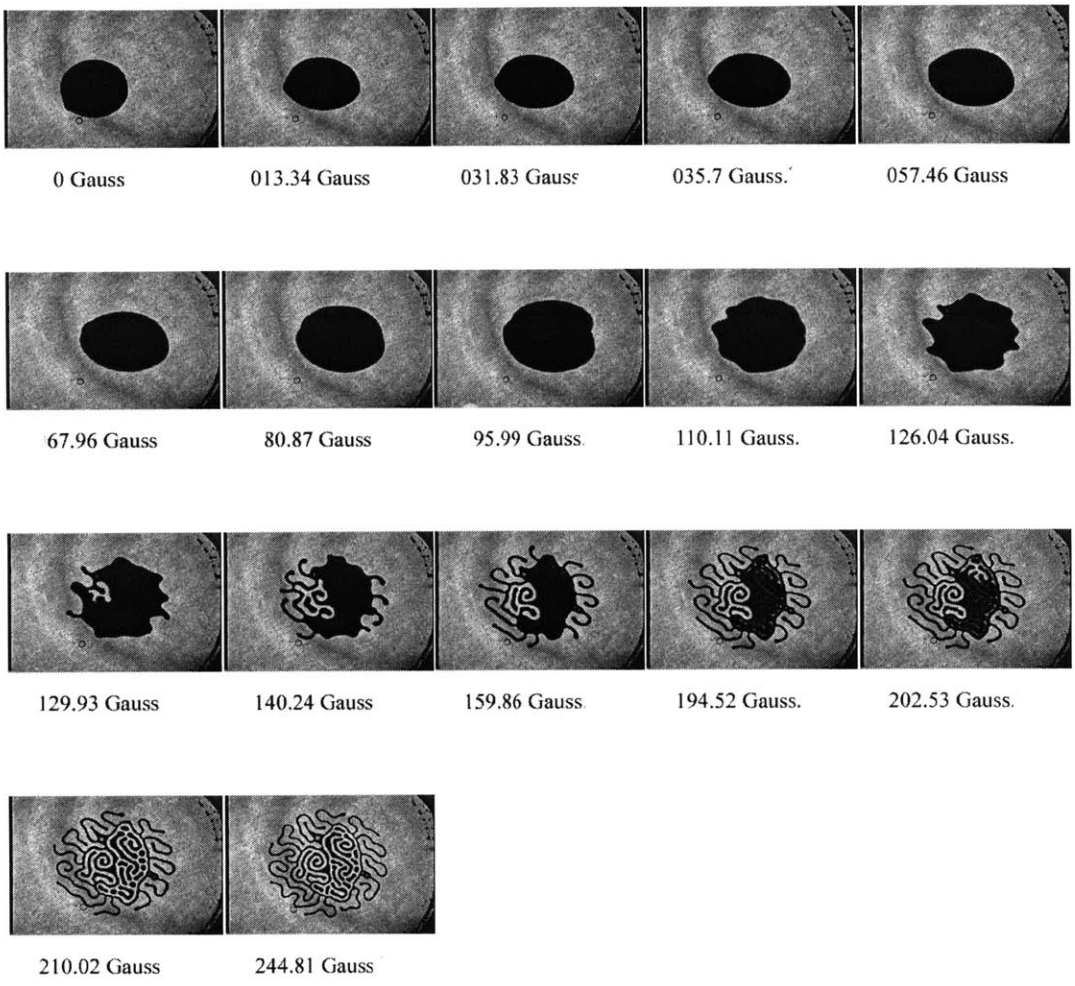

Figure D-84: Sequence 1: 200 μl, 1.15 mm, 20 Hz, 36.1 Gauss (rms)

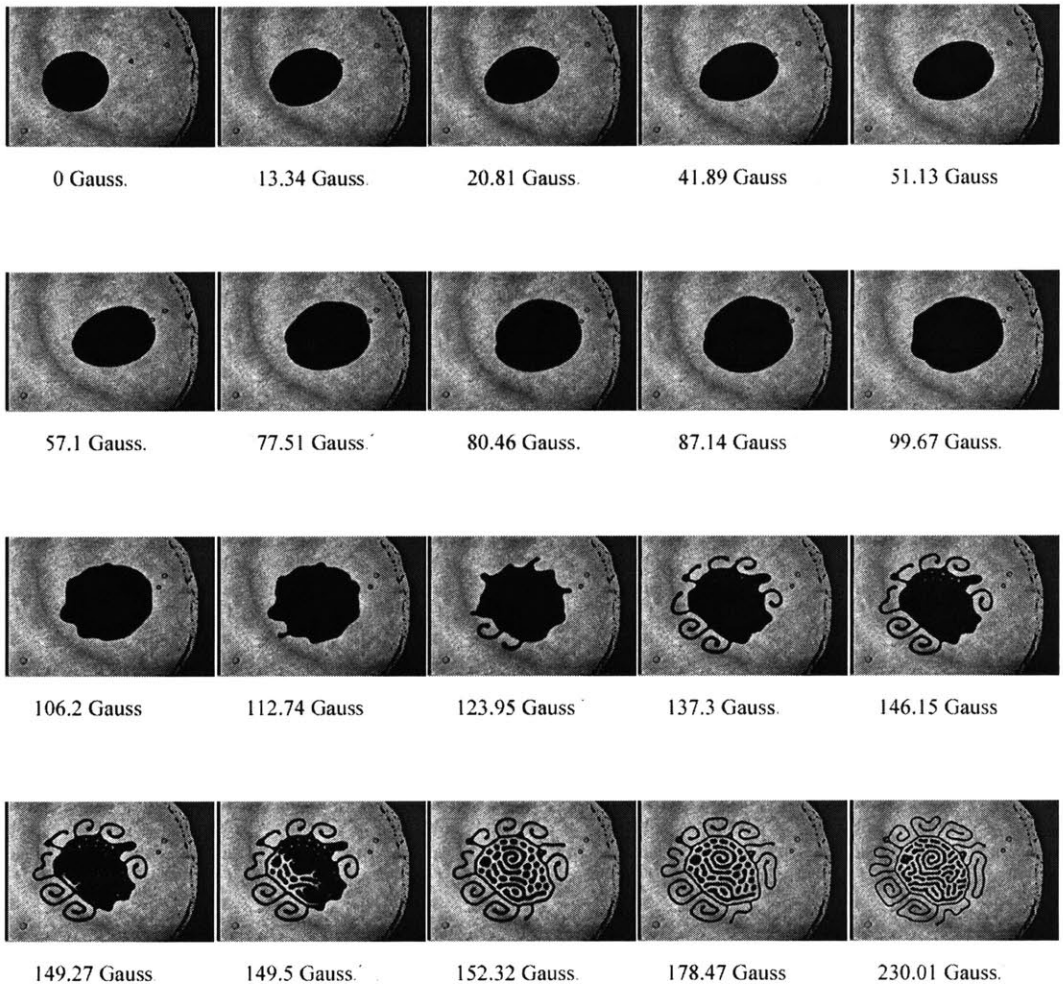

Figure D-85: Sequence 2: 200 μl, 1.15 mm, 20 Hz, 36.1 Gauss (rms)

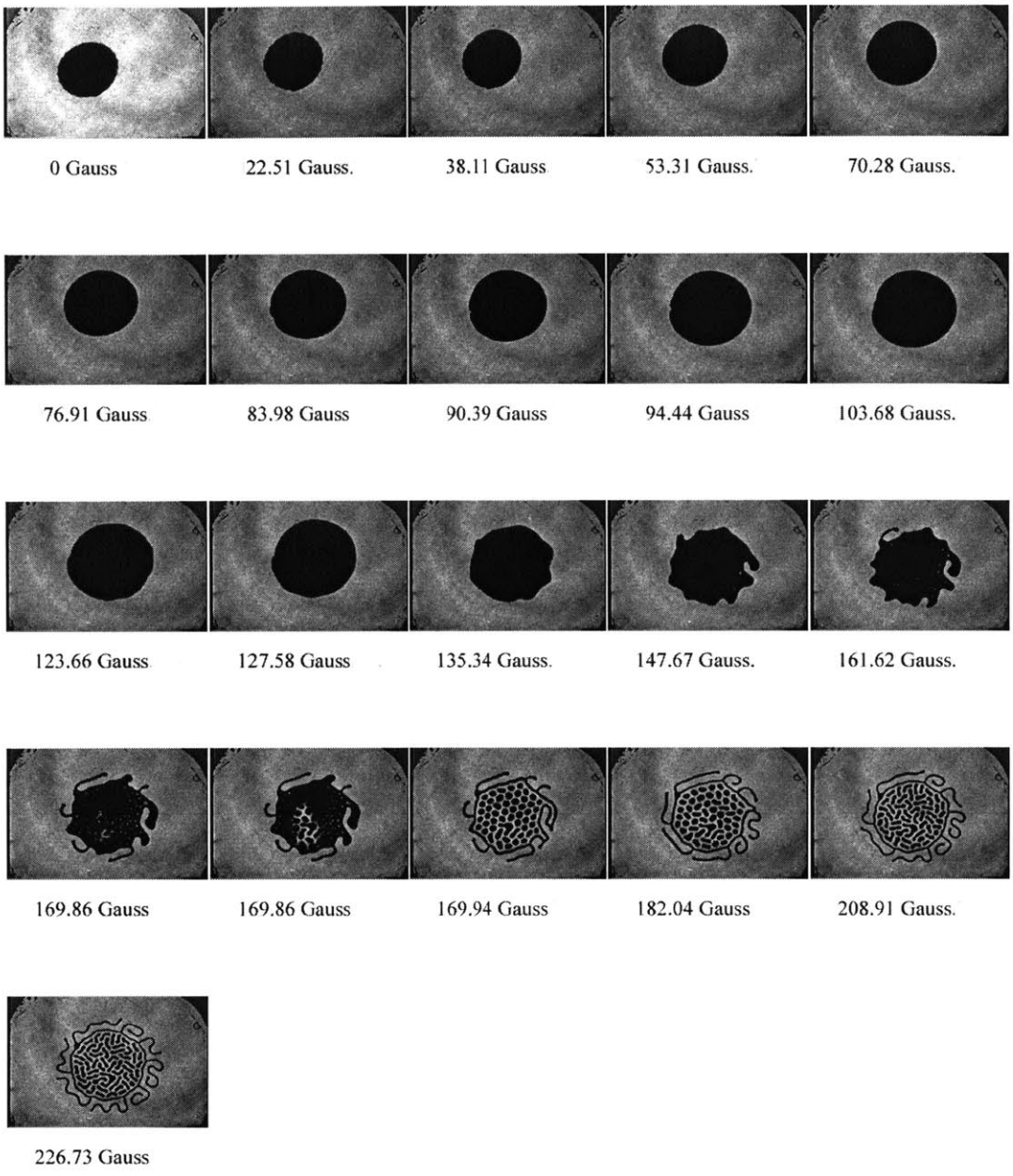

Figure D-86: Sequence 1: 200 μl, 1.15 mm, 20 Hz, 39.9 Gauss (rms)

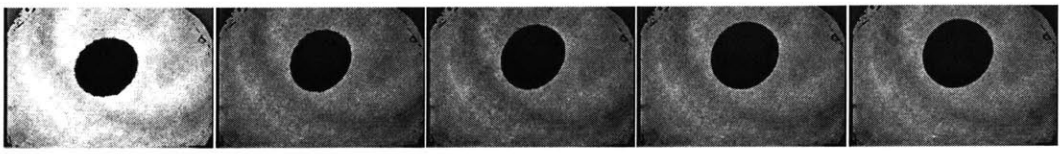

0 Gauss 12.24 Gauss 38.43 Gauss 52.66 Gauss. 57.16 Gauss.

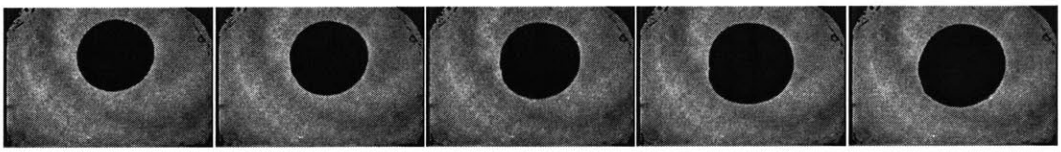

74 Gauss. 81.2 Gauss 87.34 Gauss 96.48 Gauss. 112.23 Gauss.

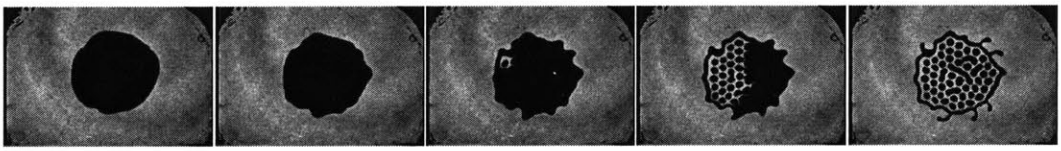

126.71 Gauss 139.79 Gauss 153.15 Gauss. 153.23 Gauss. 153.46 Gauss.

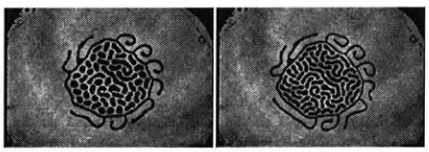

187.04 Gauss 228.59 Gauss.

Figure D-87: Sequence 2: 200 μl, 1.15 mm, 20 Hz, 39.9 Gauss (rms)

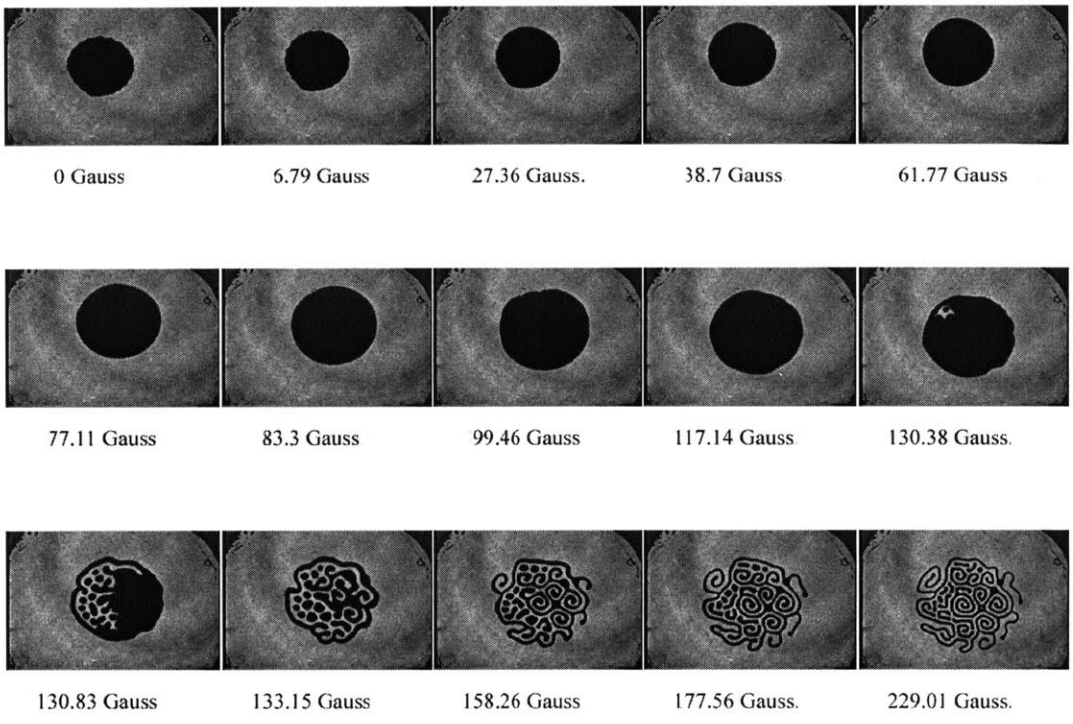

Figure D-88: Sequence 1: 200 μl, 1.15 mm, 20 Hz, 43.7 Gauss (rms)

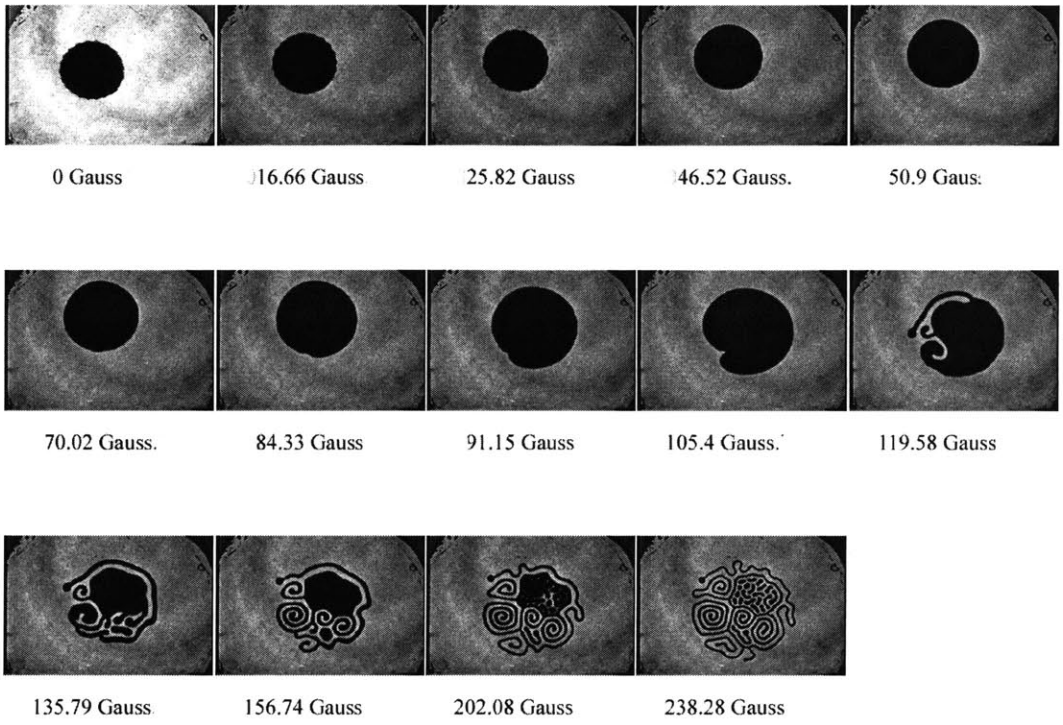

Figure D-89: Sequence 2: 200 μl, 1.15 mm, 20 Hz, 43.7 Gauss (rms)

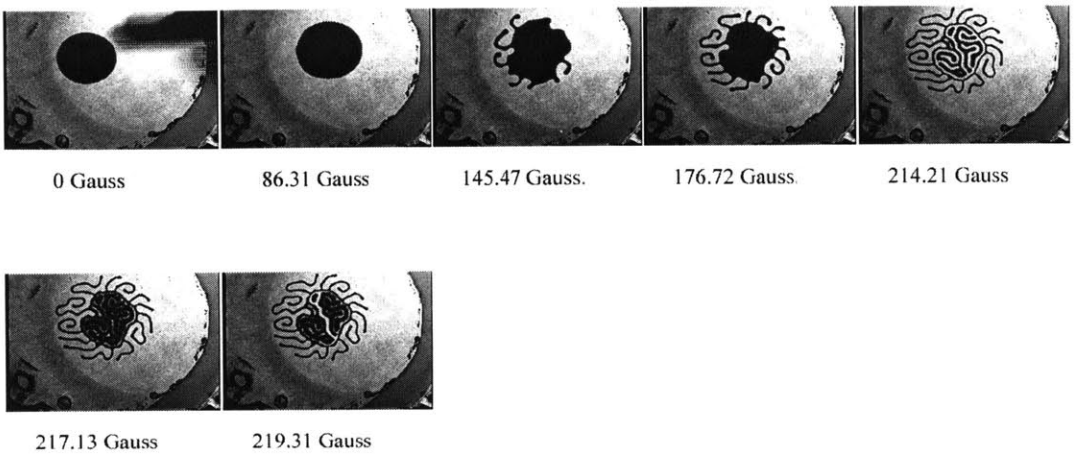

Figure D-90: Sequence 1: 200 μl, 1.15 mm, 25 Hz, 28.5 Gauss (rms)

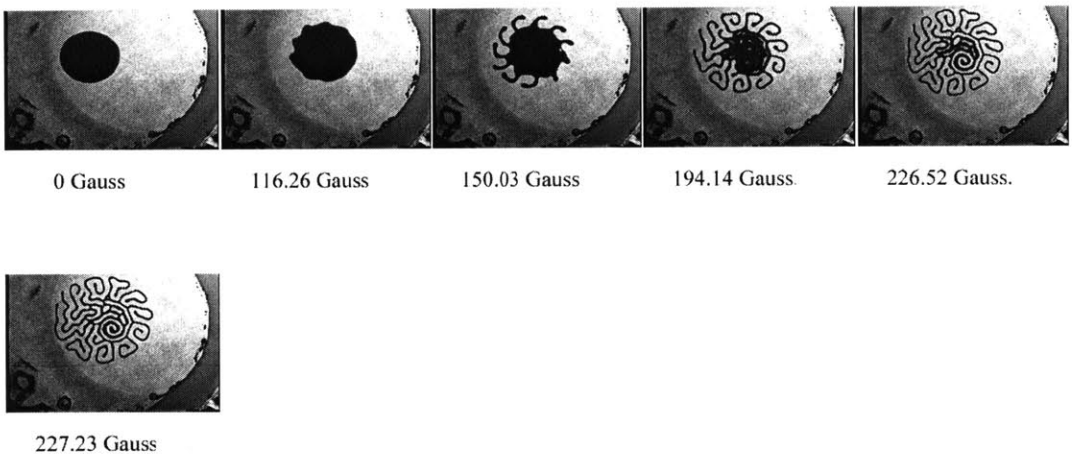

Figure D-91: Sequence 2: 200 μl, 1.15 mm, 25 Hz, 28.5 Gauss (rms)

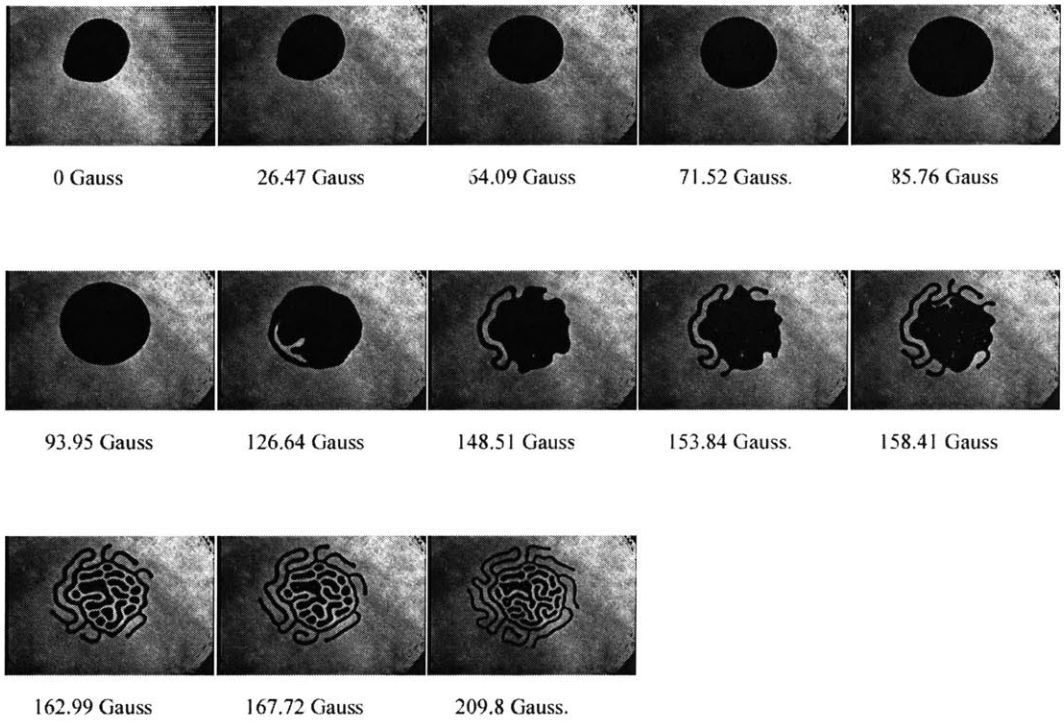

Figure D-92: Sequence 1: 200 μl, 1.15 mm, 25 Hz, 32.3 Gauss (rms)

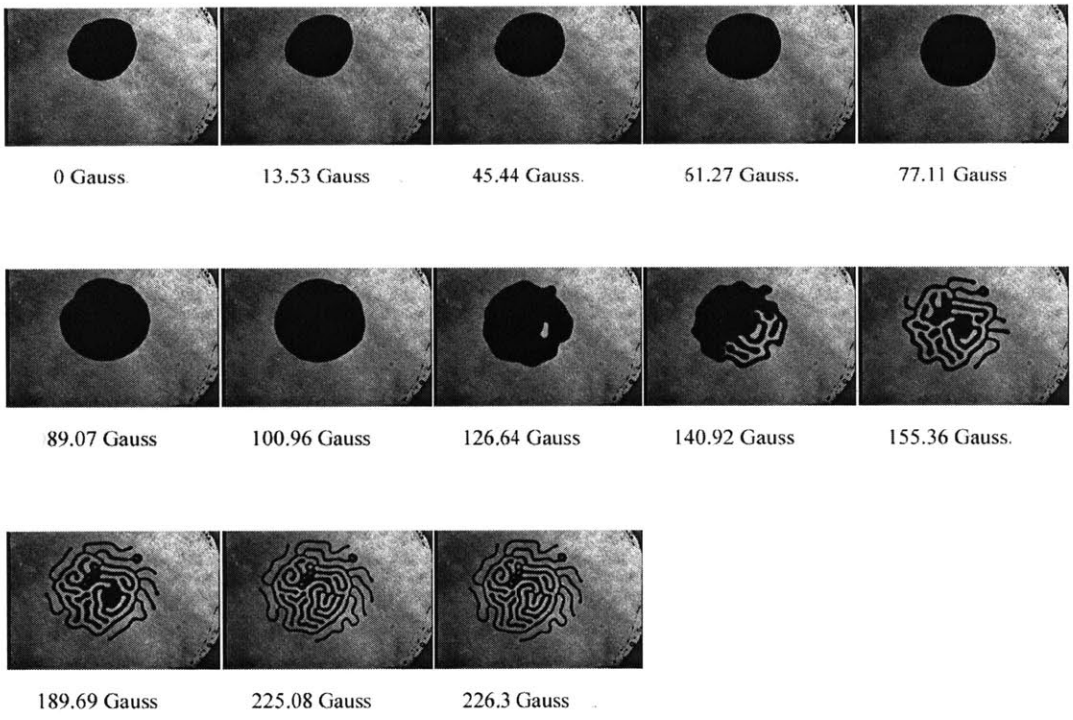

Figure D-93: Sequence 2: 200 μl, 1.15 mm, 25 Hz, 32.3 Gauss (rms)

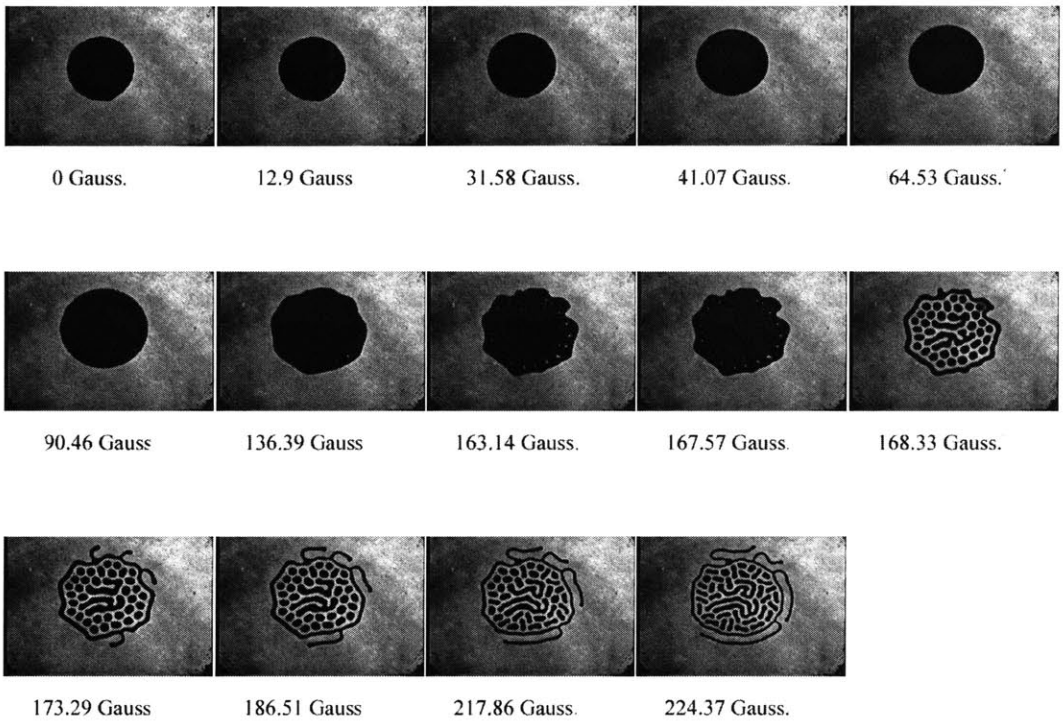

Figure D-94: Sequence 1: 200 μl, 1.15 mm, 25 Hz, 36.1 Gauss (rms)

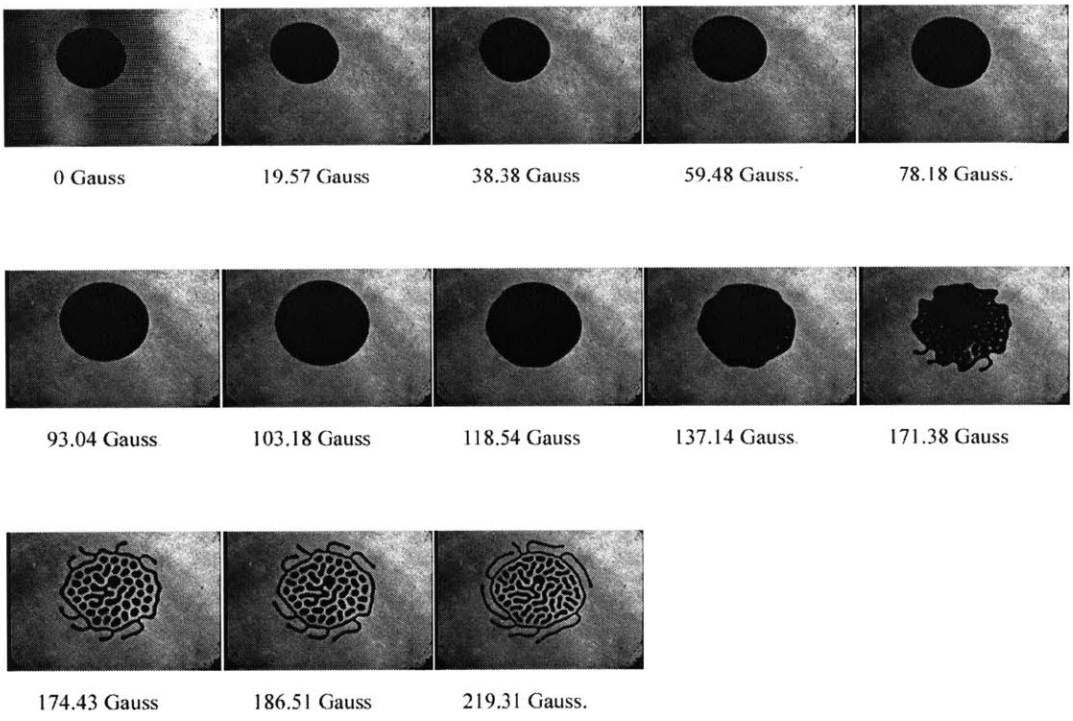

Figure D-95: Sequence 2: 200 μl, 1.15 mm, 25 Hz, 36.1 Gauss (rms)

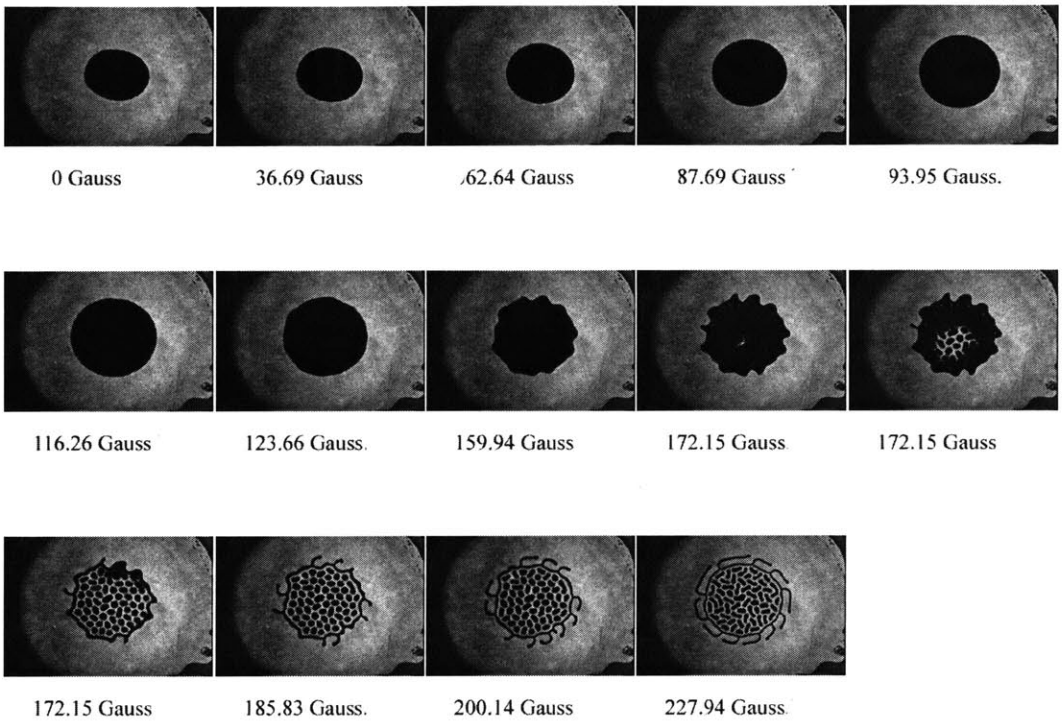

Figure D-96: Sequence 1: 200 μl, 1.15 mm, 25 Hz, 39.9 Gauss (rms)

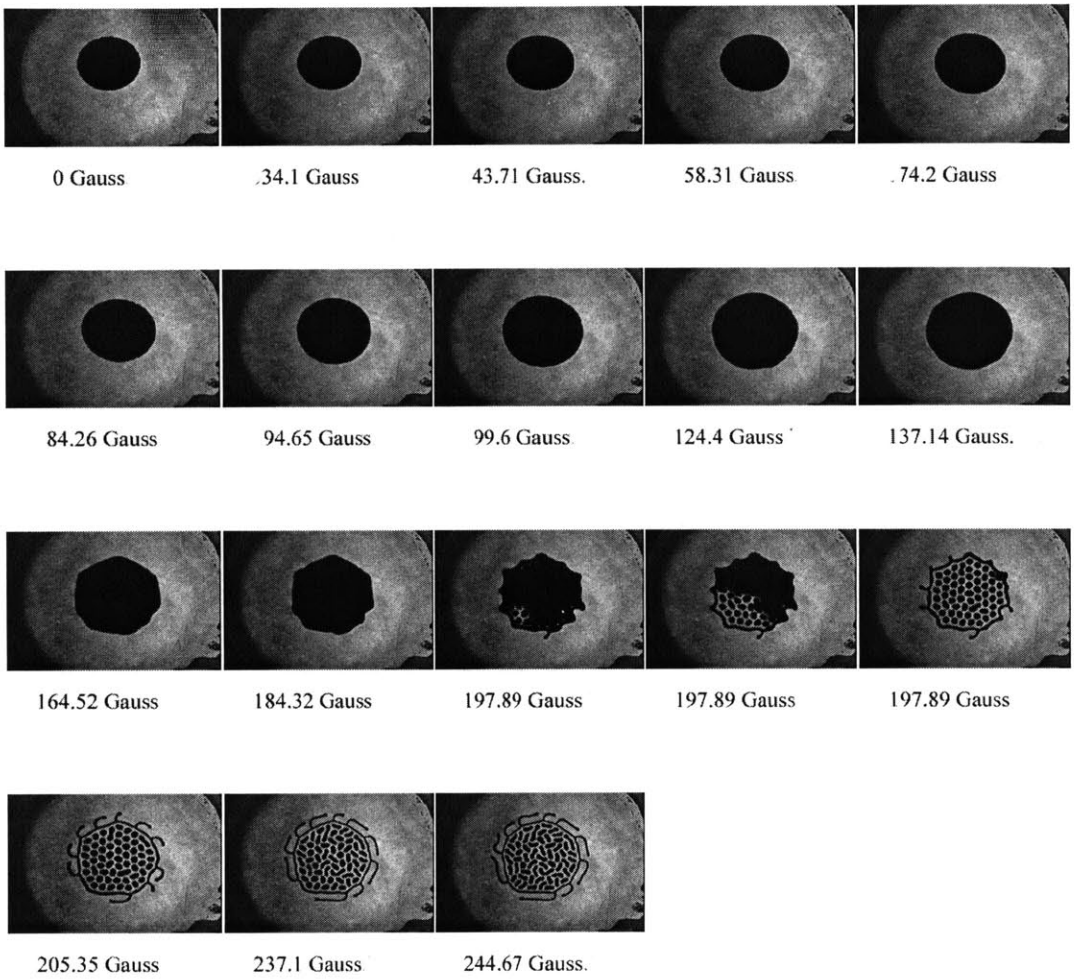

Figure D-97: Sequence 2: 200 μl, 1.15 mm, 25 Hz, 39.9 Gauss (rms)

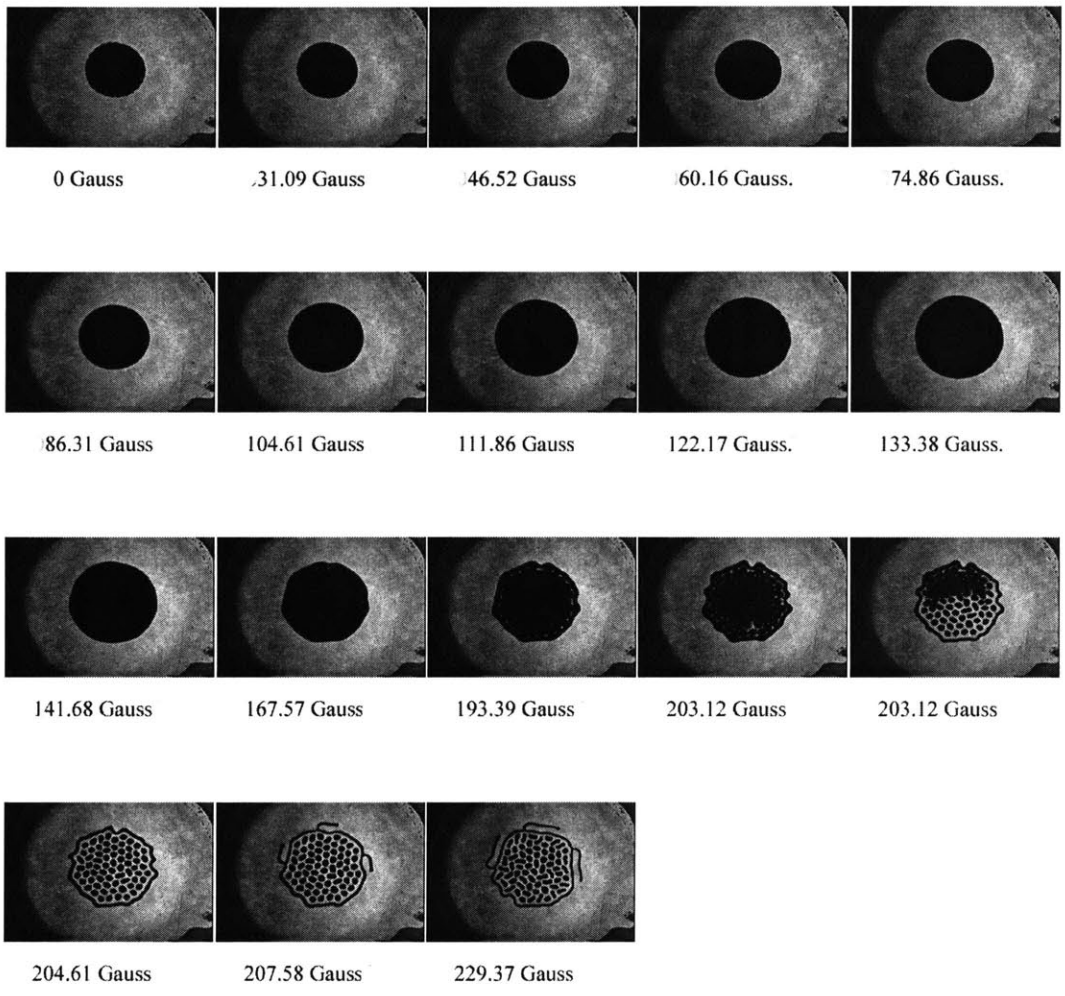

Figure D-98: Sequence 1: 200 μl, 1.15 mm, 25 Hz, 43.7 Gauss (rms)

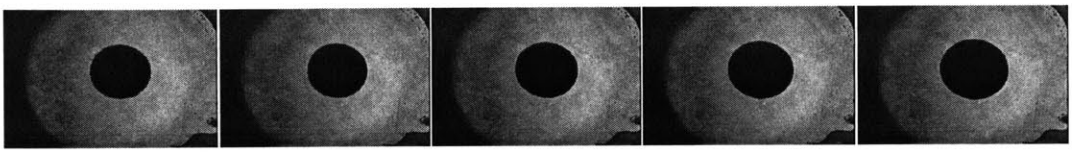

0 Gauss 16.34 Gauss 29.13 Gauss 49.38 Gauss. 62.64 Gauss

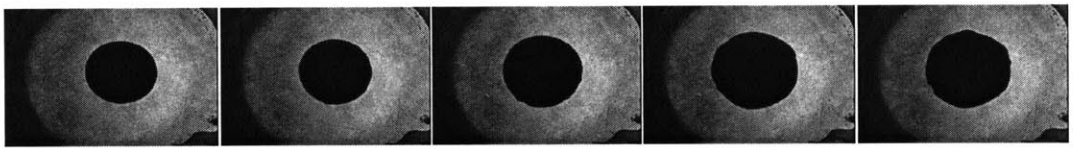

80.19 Gauss. 85.62 Gauss 101.03 Gauss. 125.89 Gauss. 150.79 Gauss.

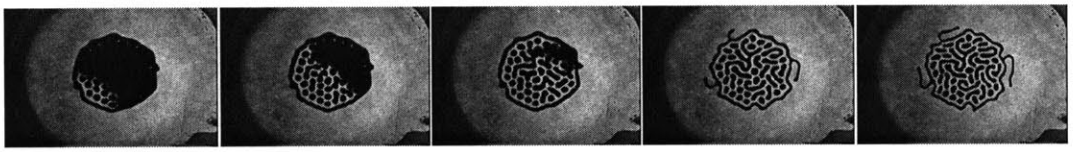

167.57 Gauss 167.57 Gauss 172.15 Gauss 198.64 Gauss 216.4 Gauss

223.65 Gauss.

Figure D-99: Sequence 2: 200 μl, 1.15 mm, 25 Hz, 43.7 Gauss (rms)

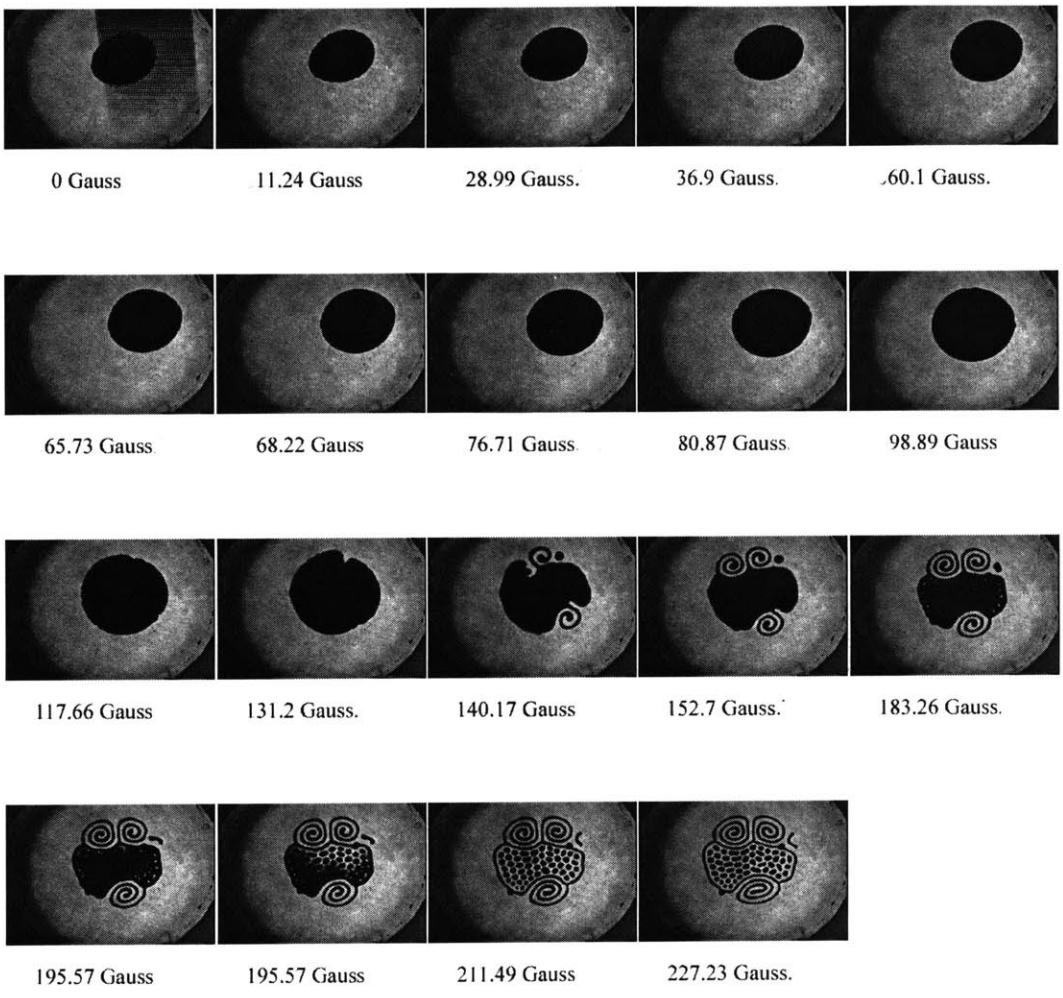

Figure D-100: Sequence 1: 200 μl, 1.15 mm, 25 Hz, 51.3 Gauss (rms)

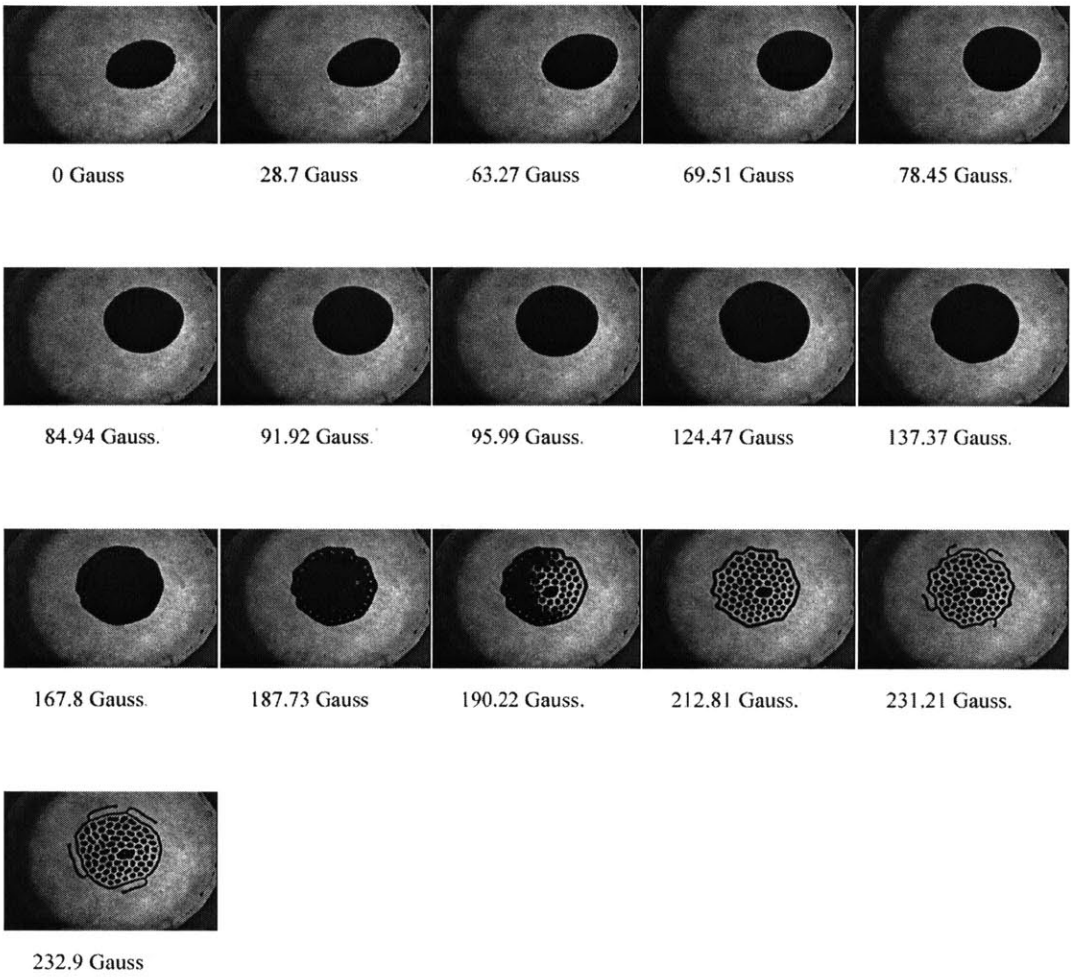

Figure D-101: Sequence 2: 200 μl, 1.15 mm, 25 Hz, 51.3 Gauss (rms)

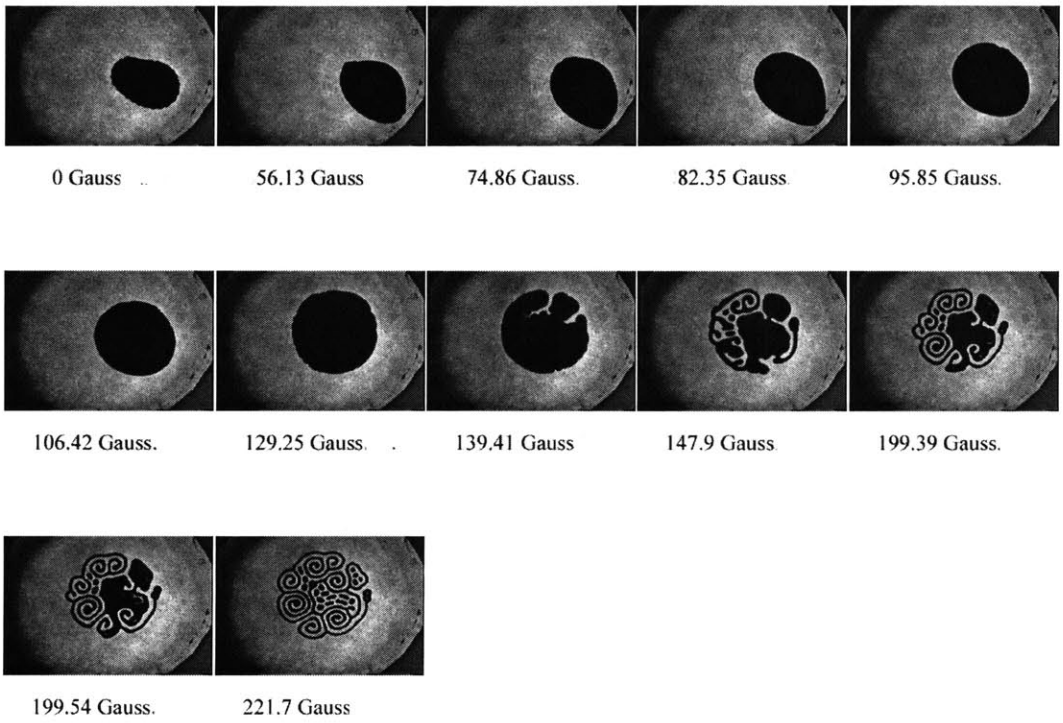

Figure D-102: Sequence 1: 200 μl, 1.15 mm, 25 Hz, 55.1 Gauss (rms)

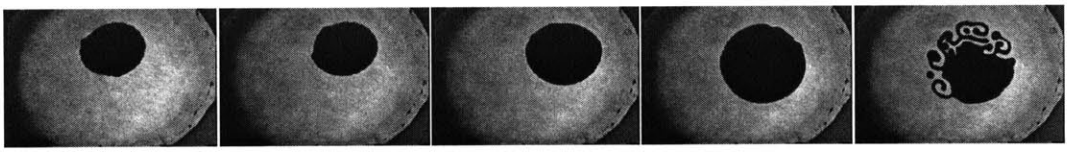

0 Gauss 16.9 Gauss. 67.26 Gauss 115.3 Gauss. 173.82 Gauss

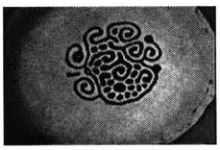

197.07 Gauss

Figure D-103: Sequence 2: 200 μl, 1.15 mm, 25 Hz, 55.1 Gauss (rms)

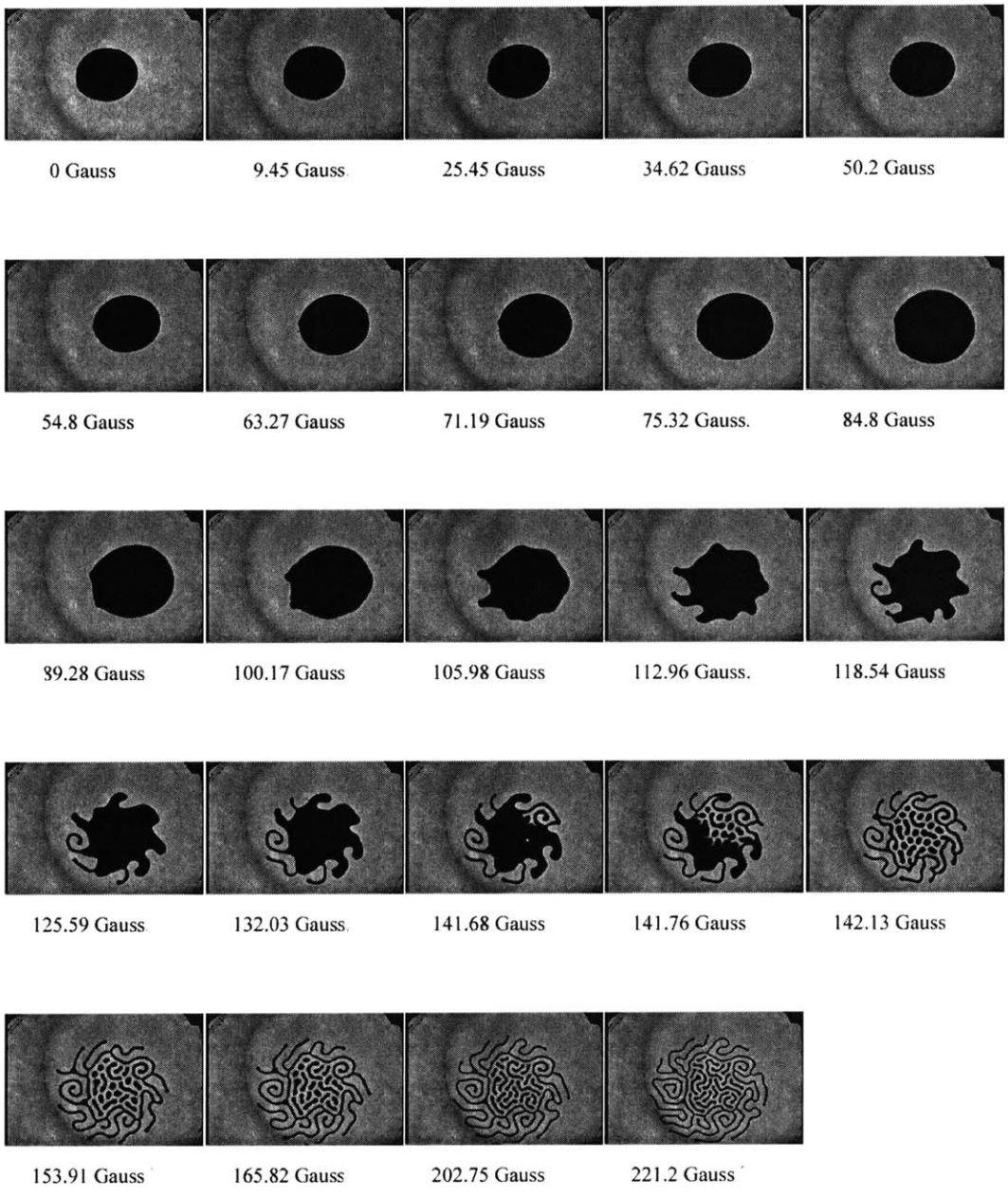

Figure D-104: Sequence 1: 200 μl, 1.15 mm, 30 Hz, 20.9 Gauss (rms)

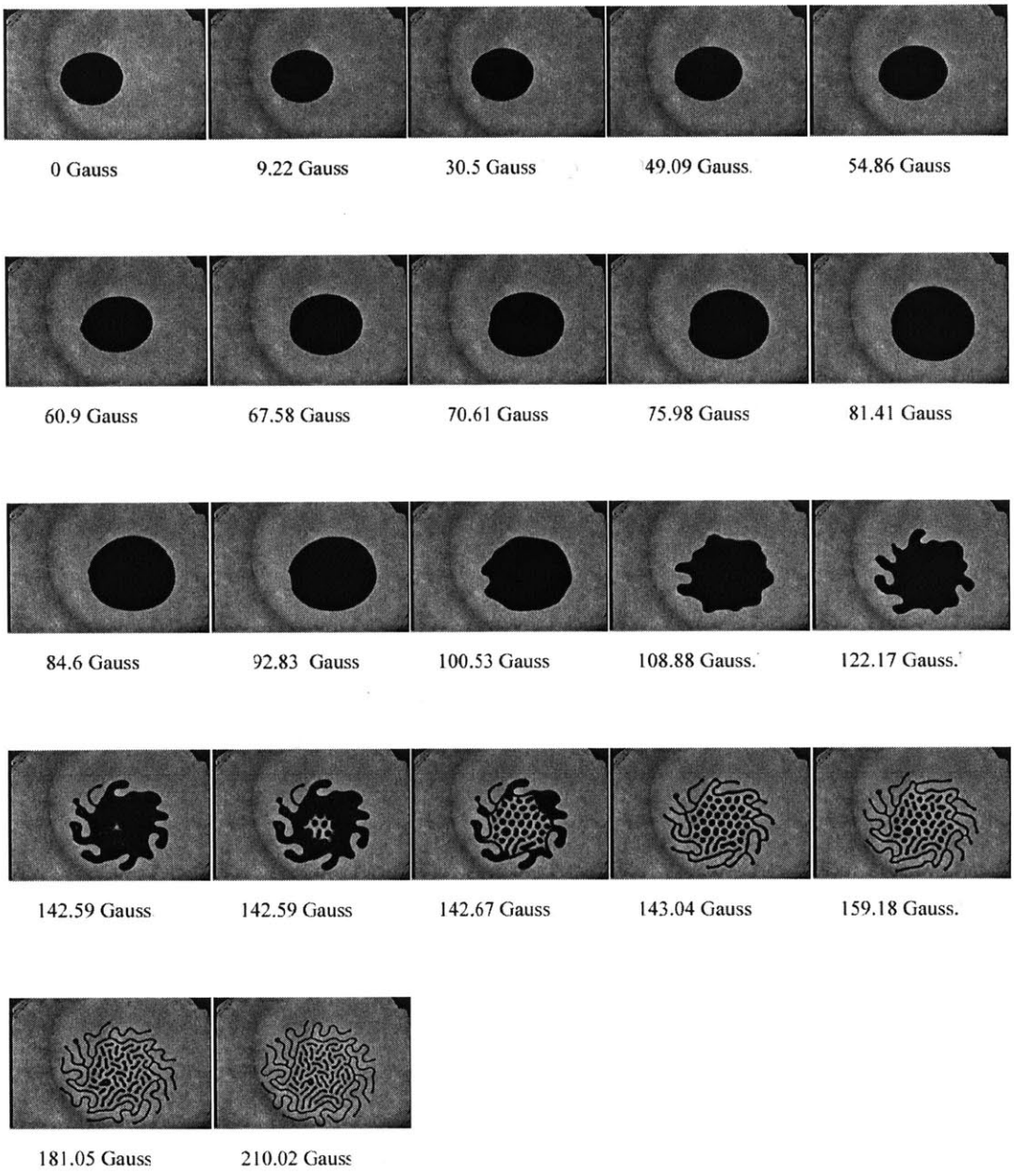

Figure D-105: Sequence 2: 200 μl, 1.15 mm, 30 Hz, 20.9 Gauss (rms)

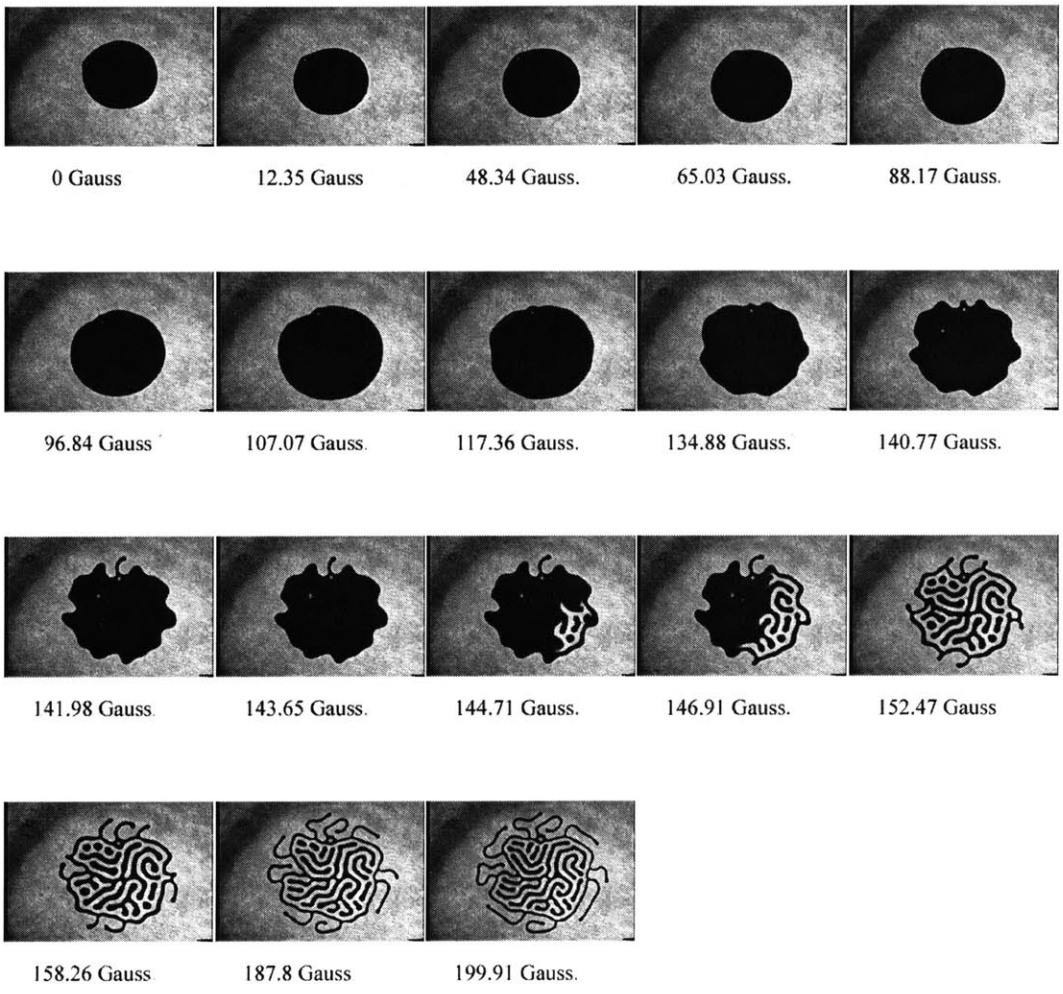

Figure D-106: Sequence 1: 200 μl, 1.15 mm, 30 Hz, 24.7 Gauss (rms)

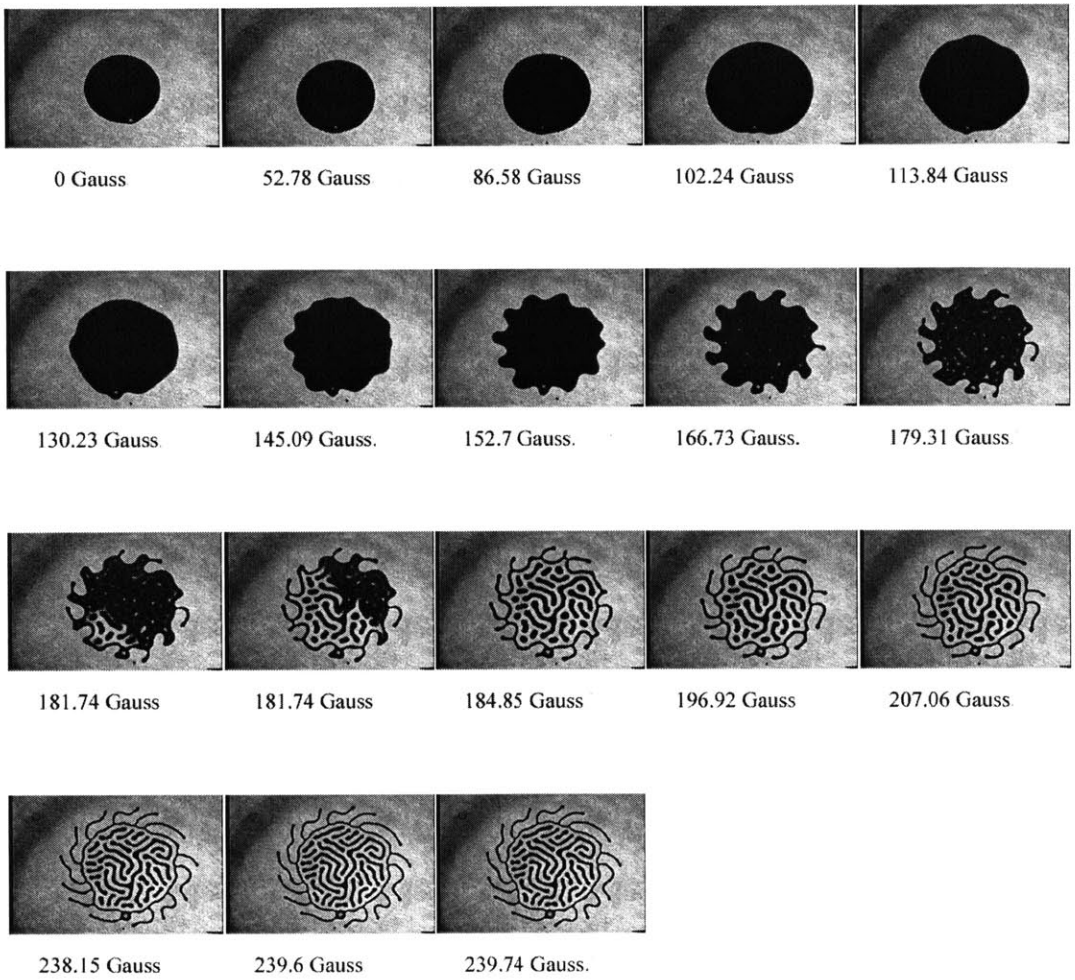

Figure D-107: Sequence 2: 200 μl, 1.15 mm, 30 Hz, 24.7 Gauss (rms)

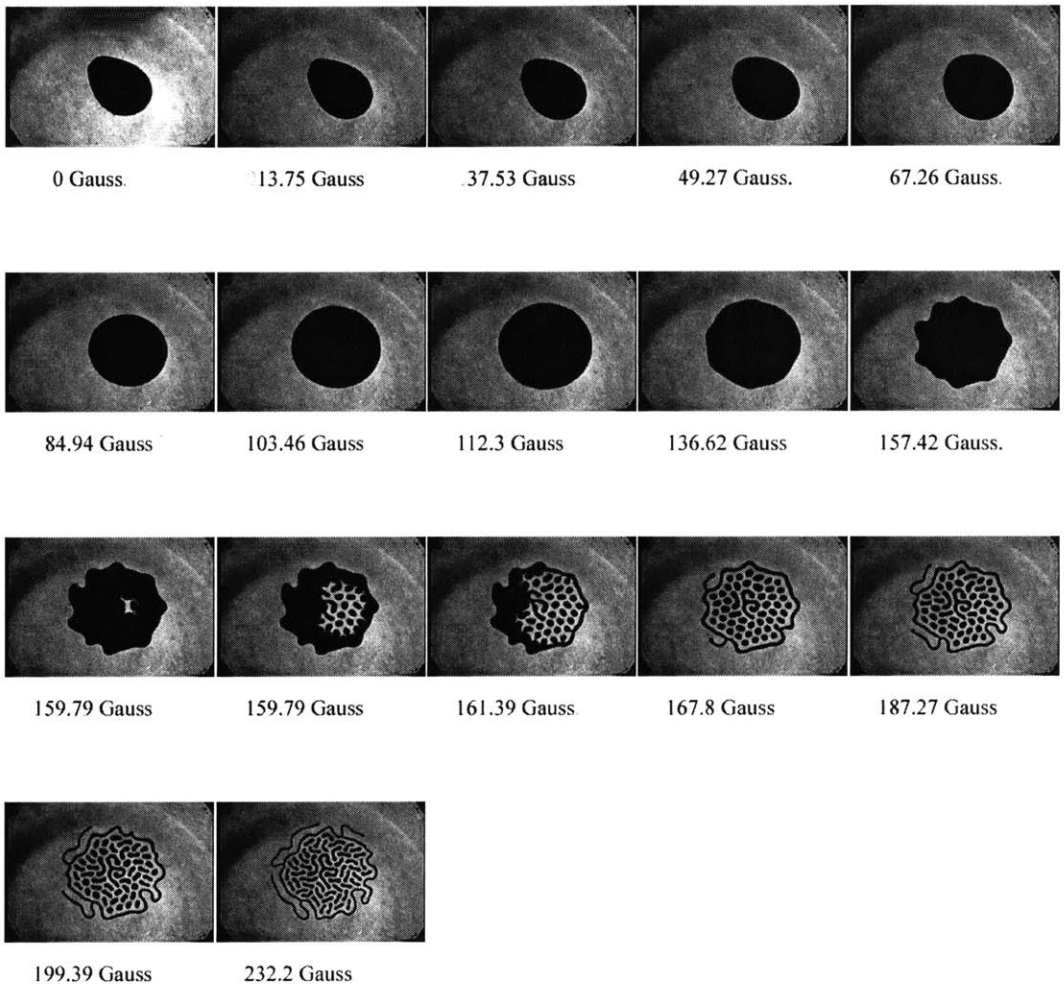

Figure D-108: Sequence 1: 200 μl, 1.15 mm, 30 Hz, 28.5 Gauss (rms)

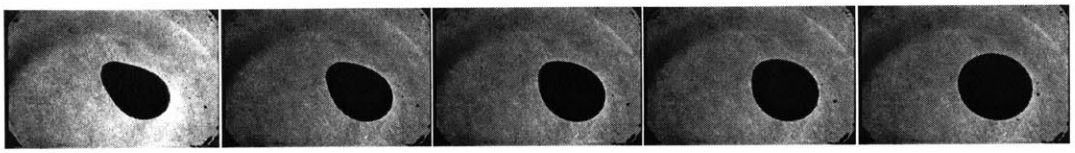

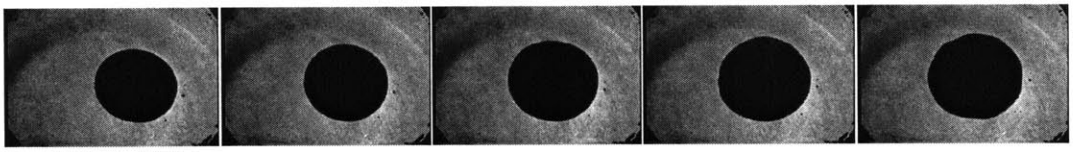

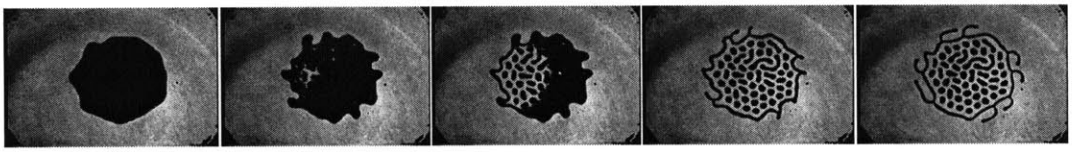

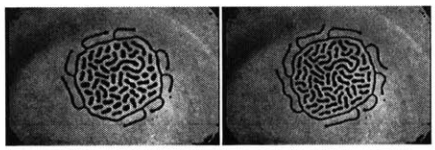

Figure D-109: Sequence 2: 200 μl, 1.15 mm, 30 Hz, 28.5 Gauss (rms)

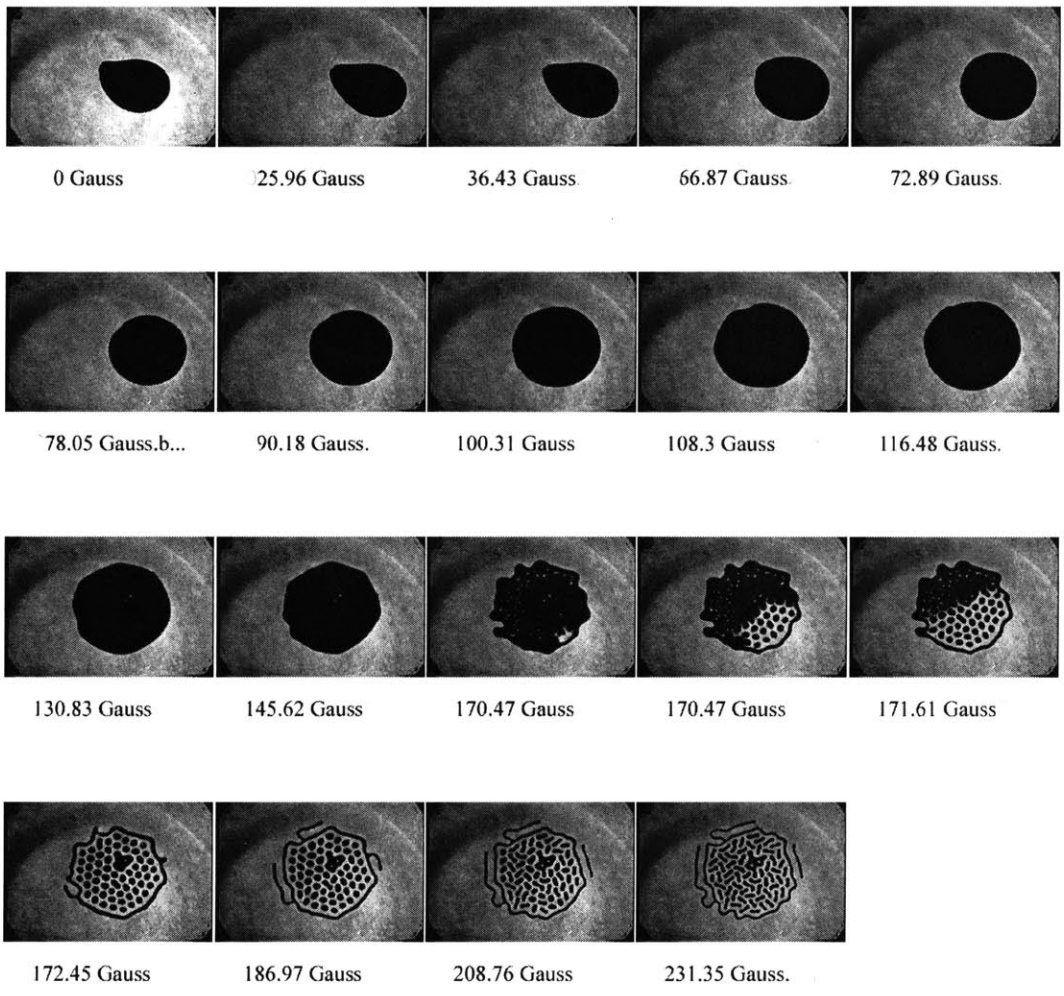

Figure D-110: Sequence 1: 200 μl, 1.15 mm, 30 Hz, 32.3 Gauss (rms)

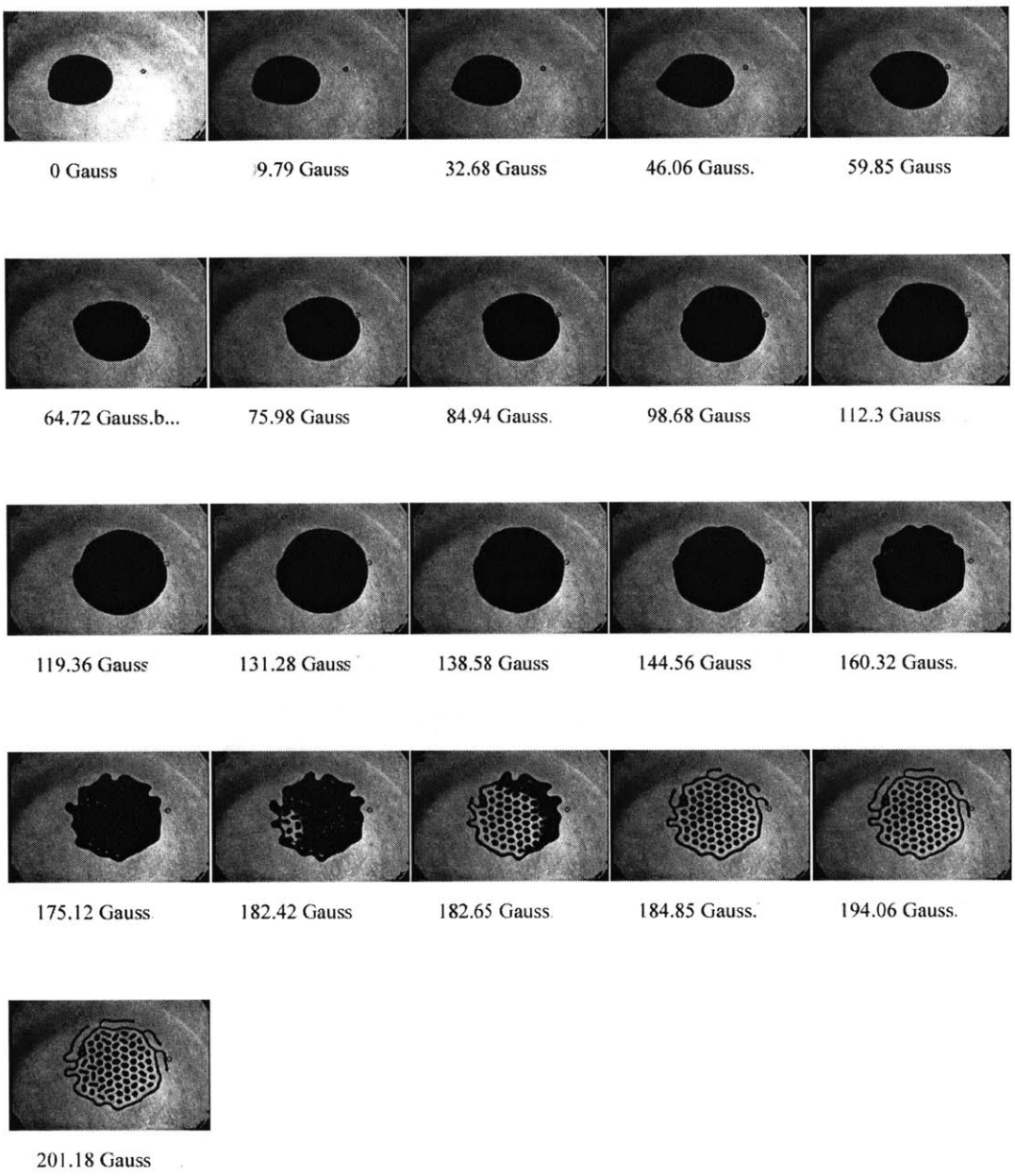

Figure D-111: Sequence 2: 200 μl, 1.15 mm, 30 Hz, 32.3 Gauss (rms)

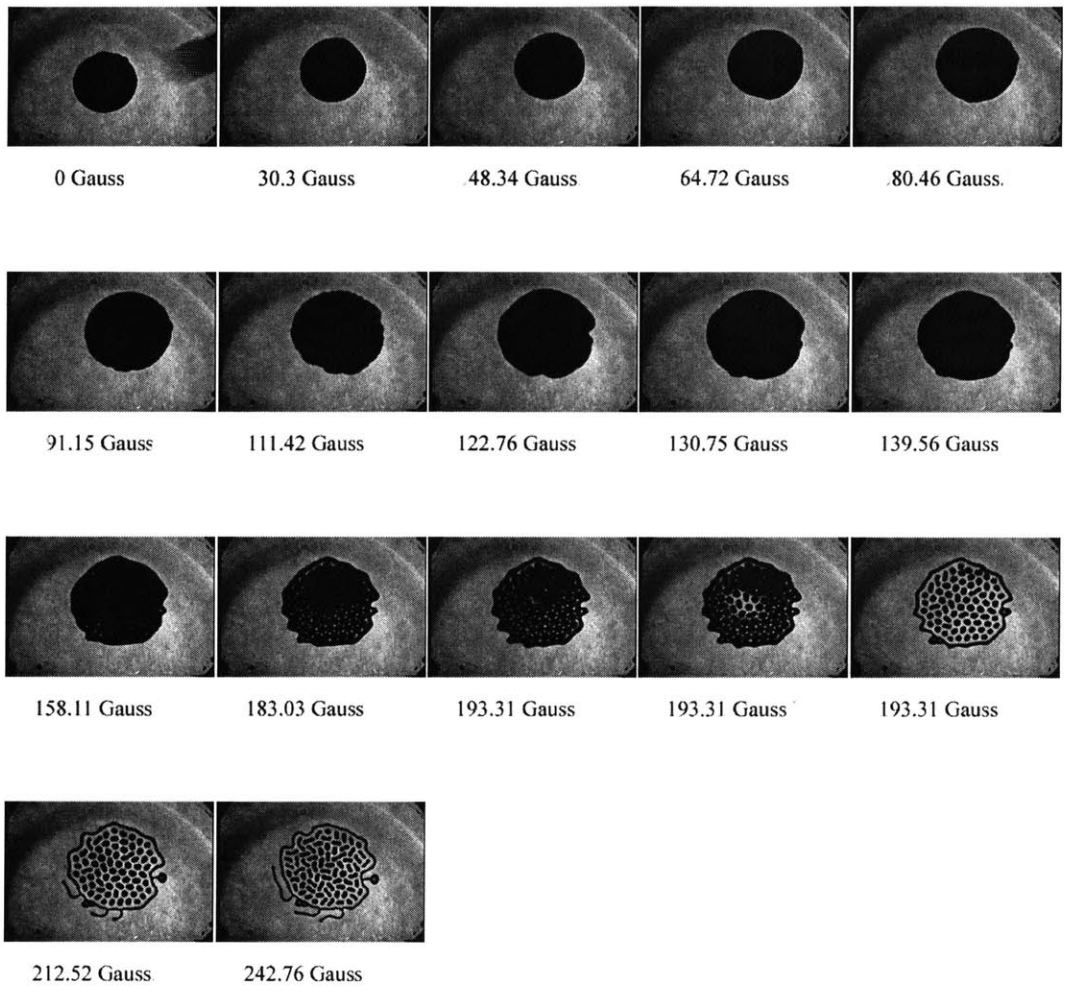

Figure D-112: Sequence 1: 200 μl, 1.15 mm, 30 Hz, 36.1 Gauss (rms)

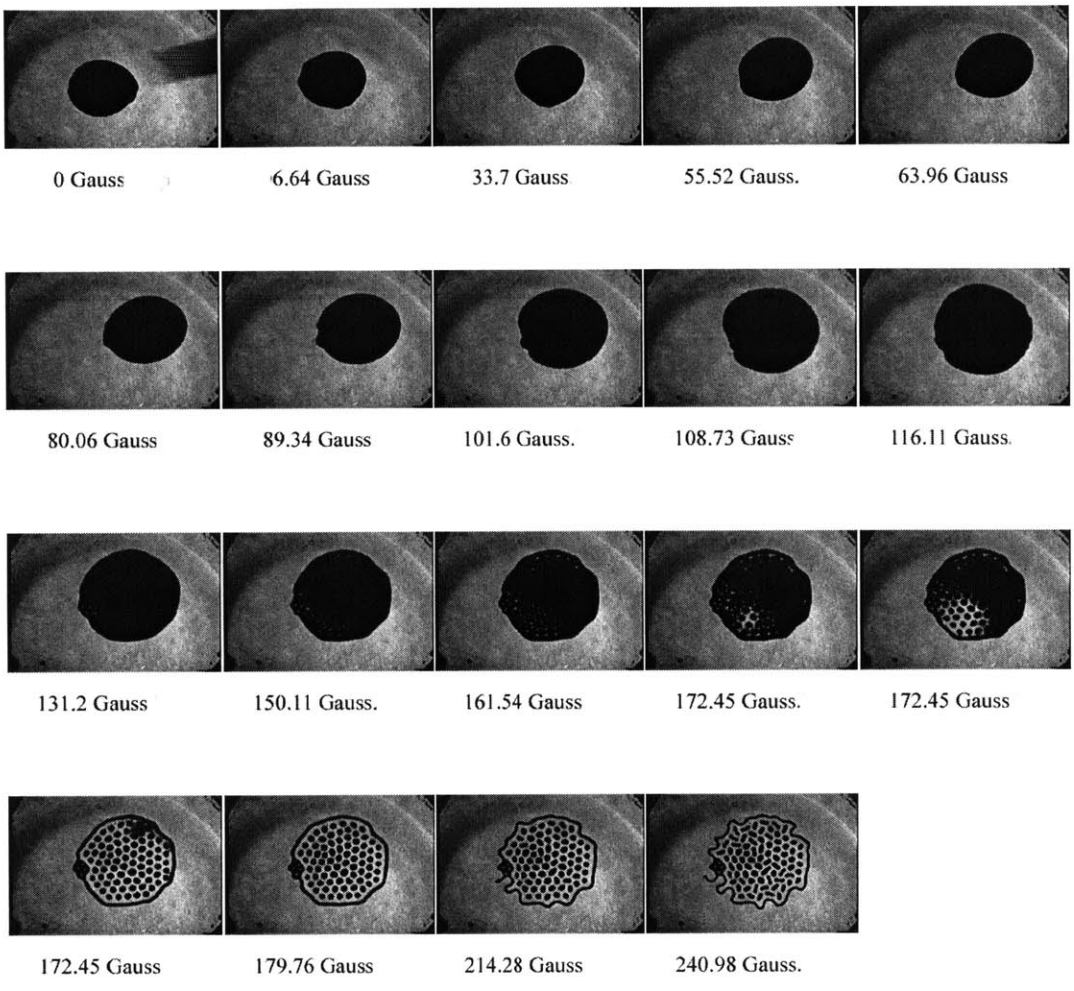

Figure D-113: Sequence 2: 200 μl, 1.15 mm, 30 Hz, 36.1 Gauss (rms)

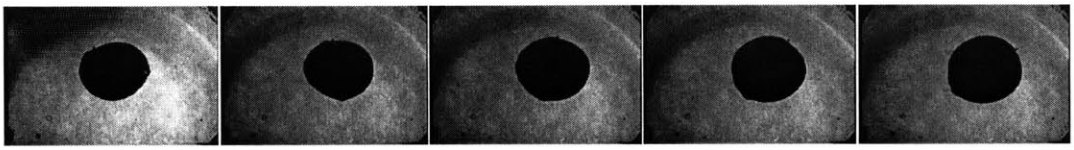

0 Gauss 23.22 Gauss. 54.5 Gauss. 59.29 Gauss. 65.1 Gauss.

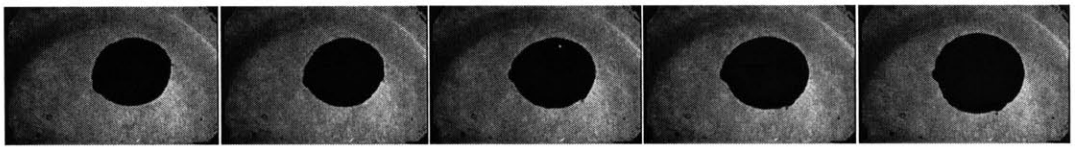

72.3 Gauss. 77.25 Gauss. 86.79 Gauss 92.2 Gauss. 103.53 Gauss.

117.44 Gauss 124.99 Gauss 130.38 Gauss. 142.13 Gauss. 181.28 Gauss

199.84 Gauss. 199.84 Gauss 238.08 Gauss.

Figure D-114: Sequence 1: 200 μl, 1.15 mm, 30 Hz, 39.9 Gauss (rms)

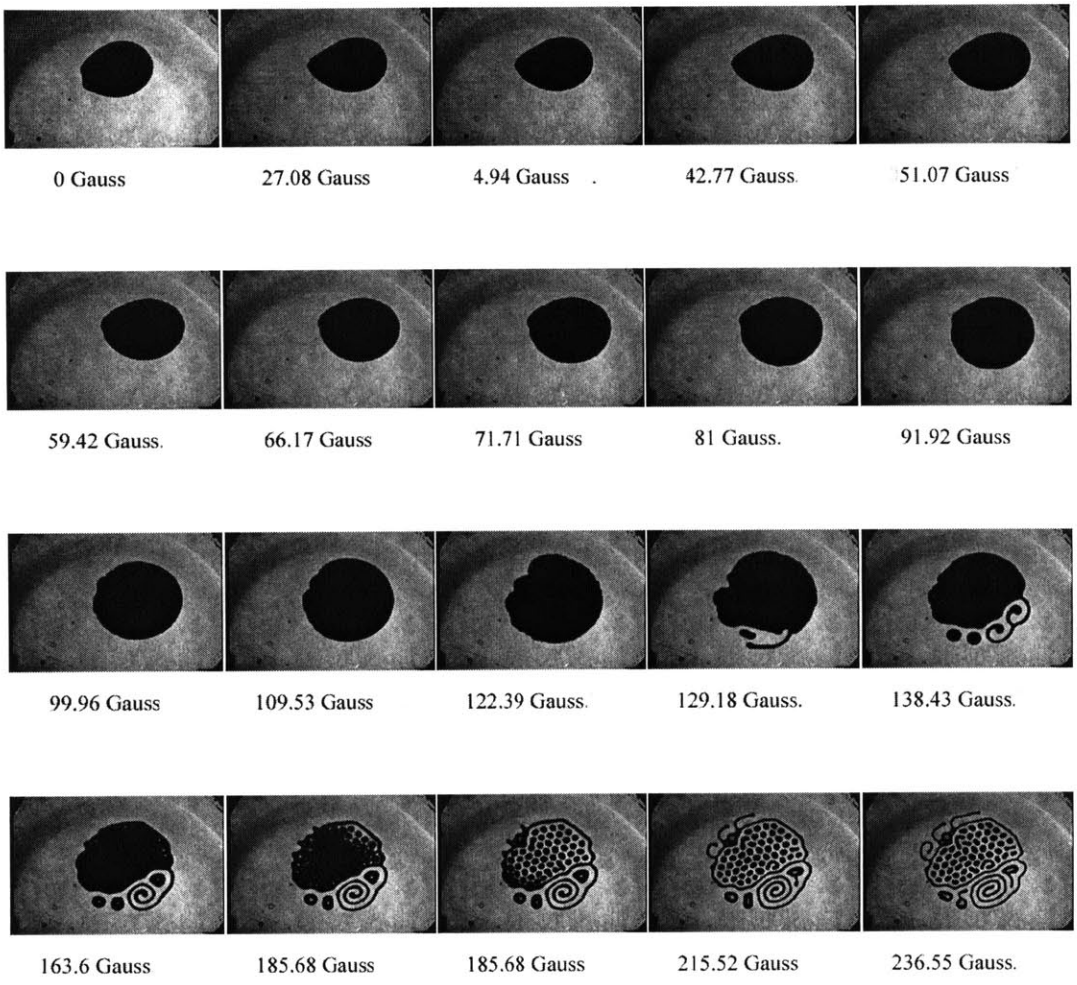

Figure D-115: Sequence 2: 200 μl, 1.15 mm, 30 Hz, 39.9 Gauss (rms)

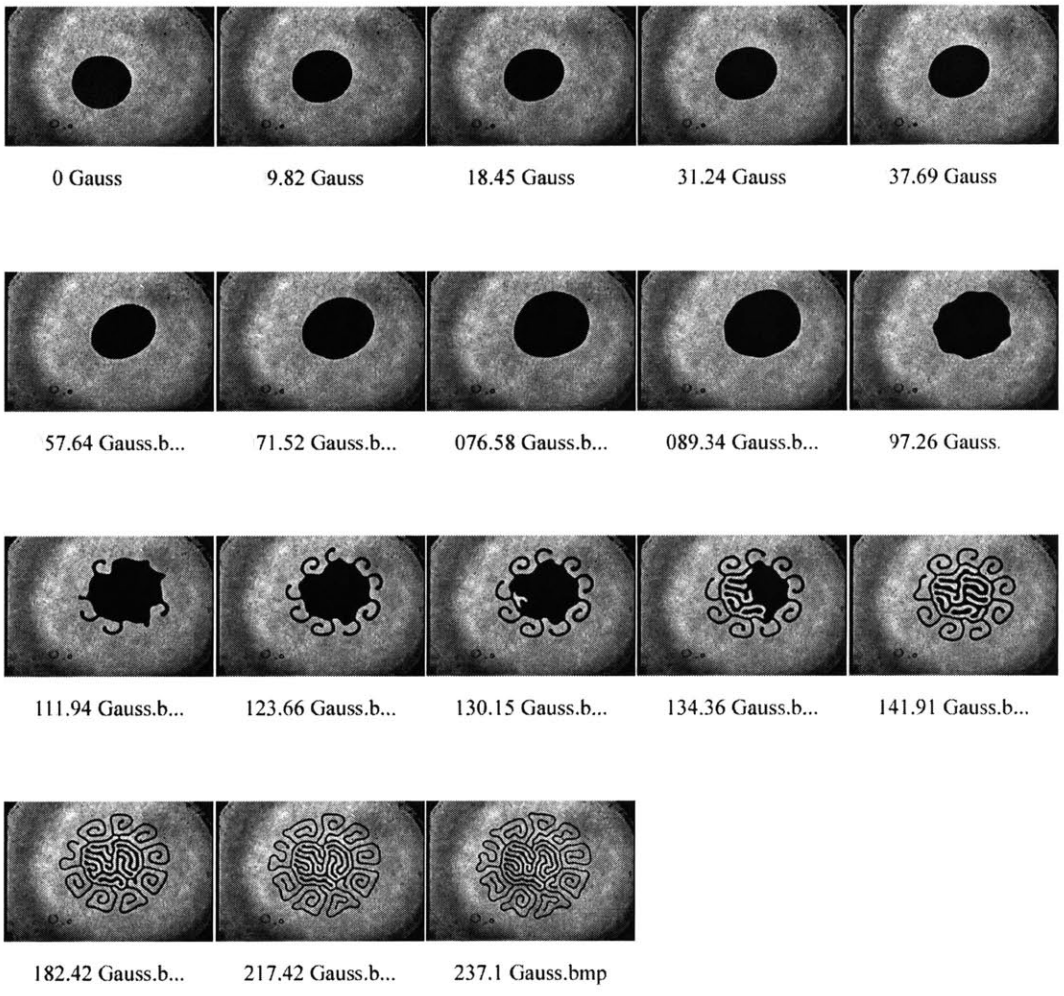

Figure D-116: Sequence 1: 200 μl, 1.15 mm, 35 Hz, 20.9 Gauss (rms)

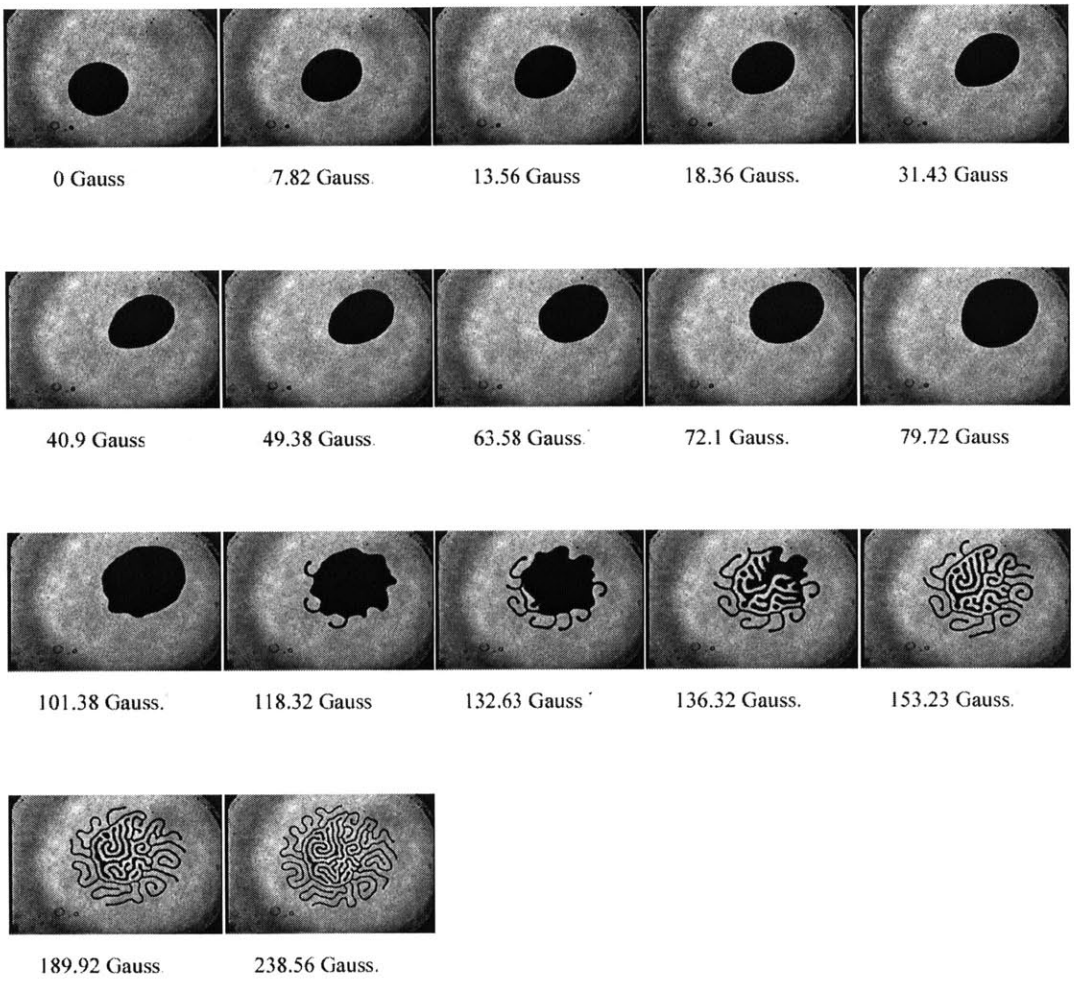

Figure D-117: Sequence 2: 200 μl, 1.15 mm, 35 Hz, 20.9 Gauss (rms)

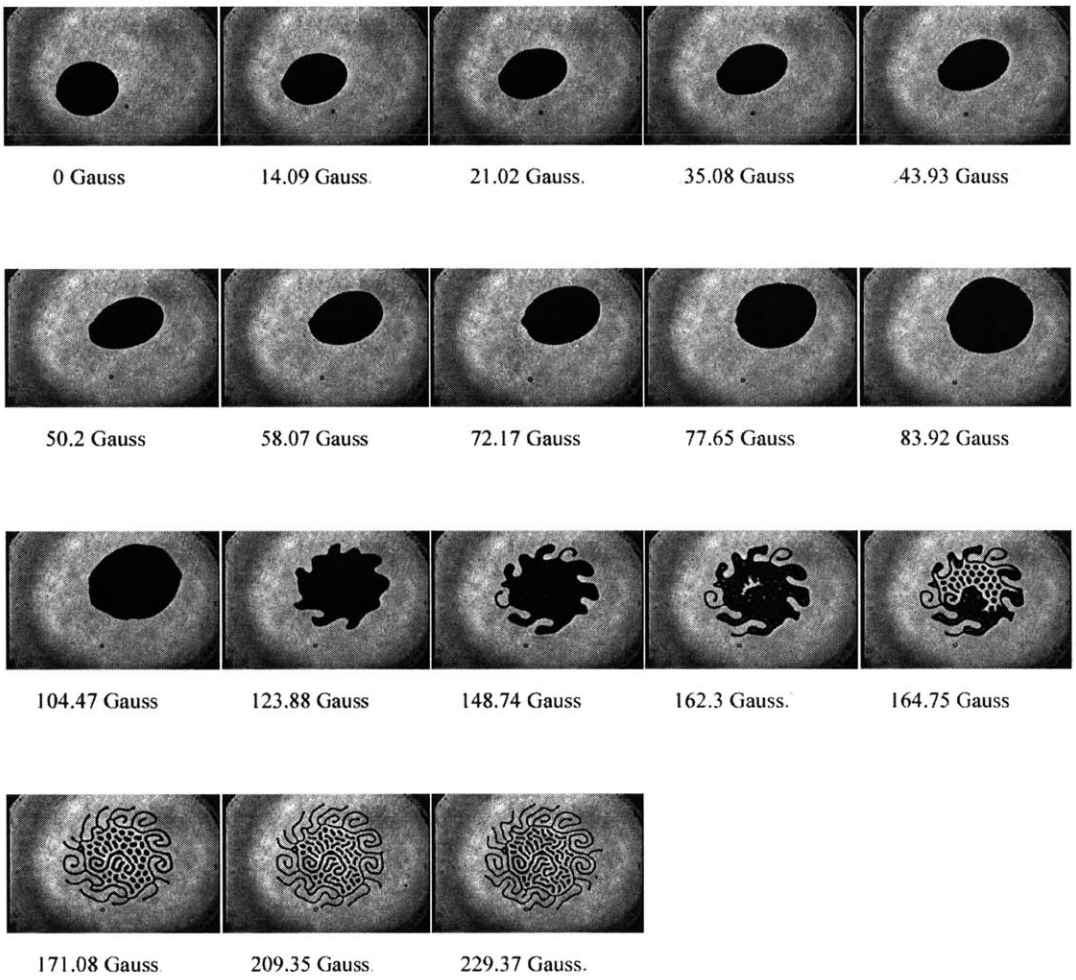

Figure D-118: Sequence 1: 200 μl, 1.15 mm, 35 Hz, 24.7 Gauss (rms)

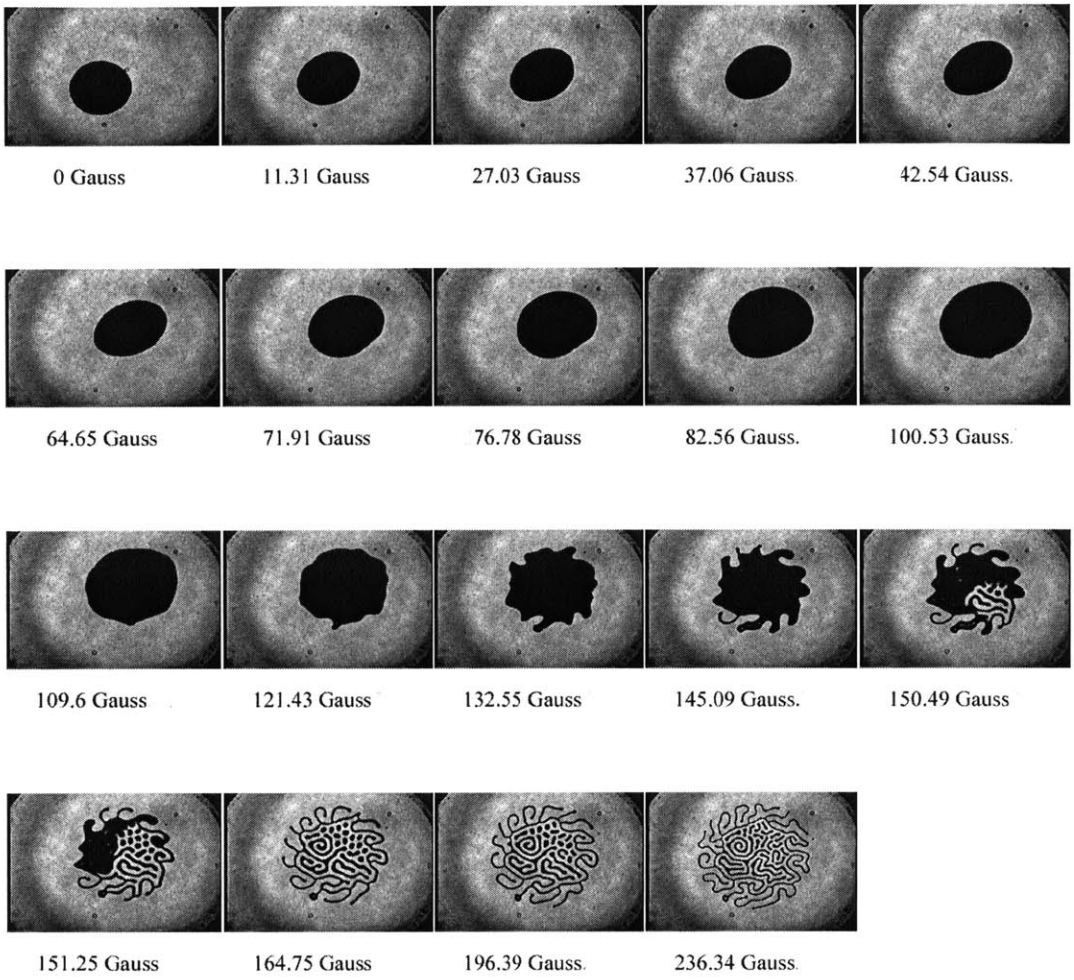

Figure D-119: Sequence 2: 200 μl, 1.15 mm, 35 Hz, 24.7 Gauss (rms)

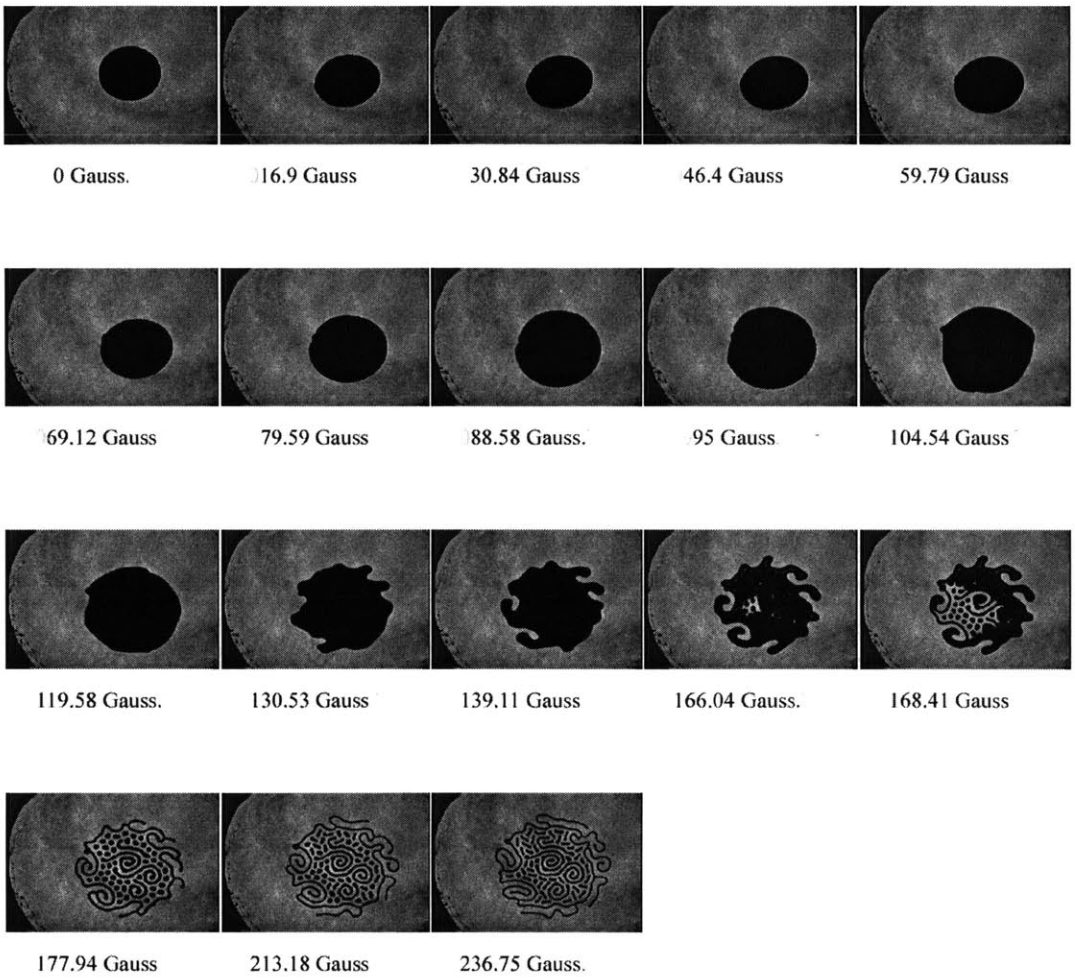

Figure D-120: Sequence 1: 200 μl, 1.15 mm, 35 Hz, 28.5 Gauss (rms)

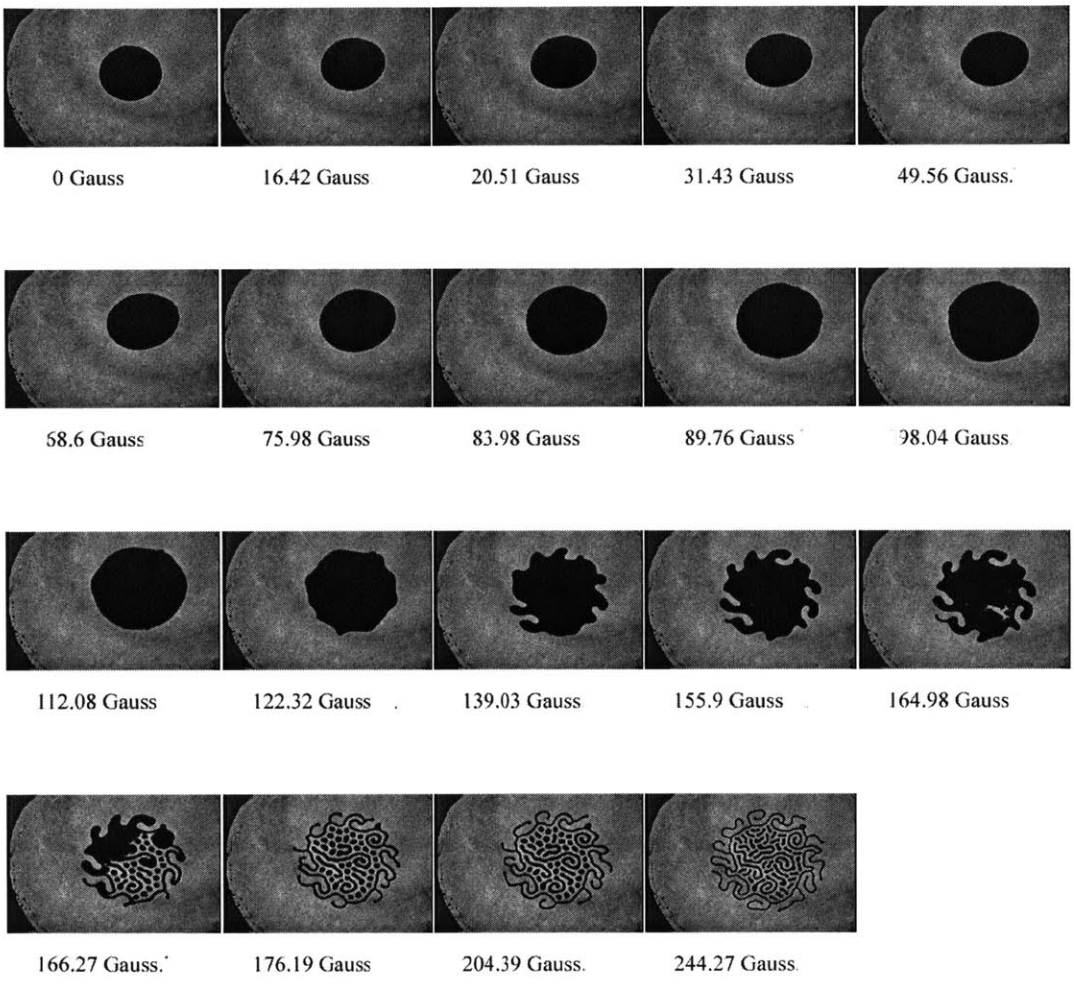

Figure D-121: Sequence 2: 200 μl, 1.15 mm, 35 Hz, 28.5 Gauss (rms)

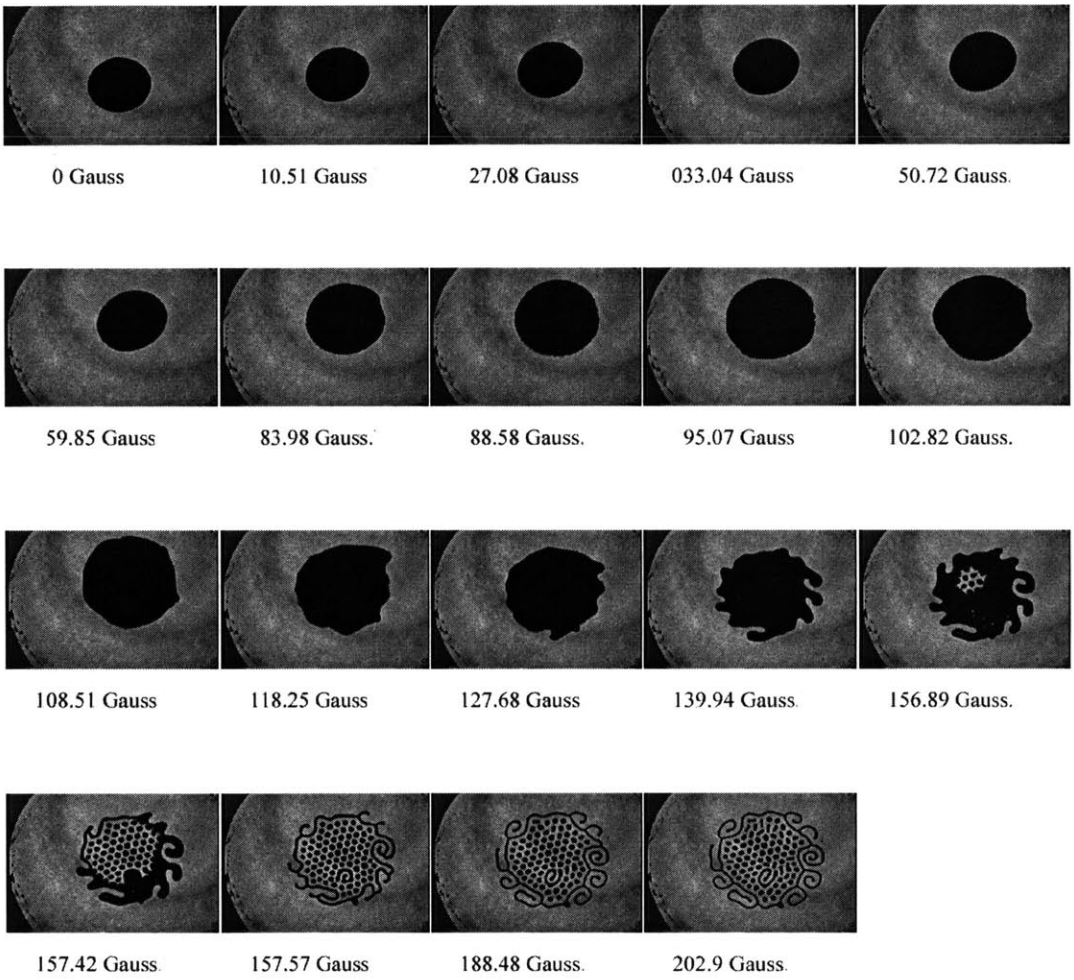

Figure D-122: Sequence 1: 200 μl, 1.15 mm, 35 Hz, 32.3 Gauss (rms)

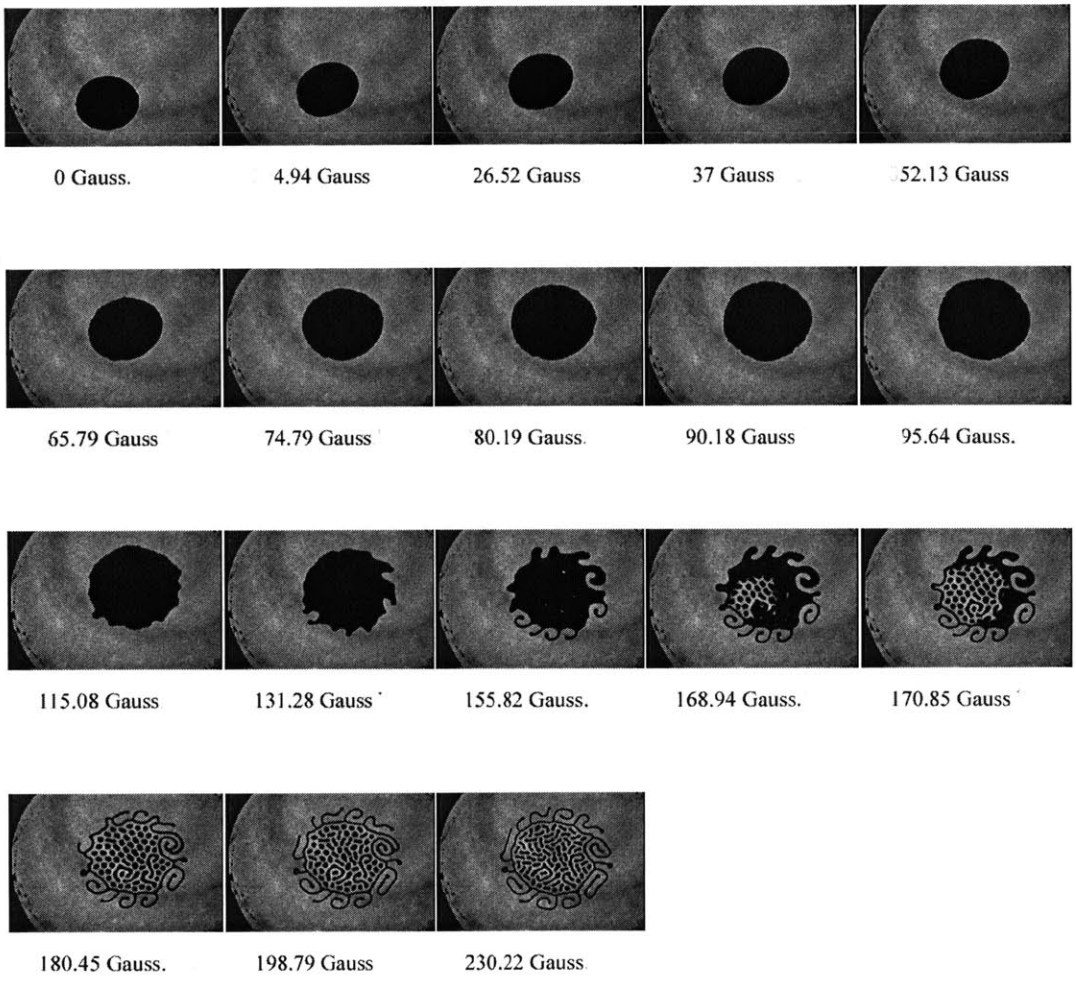

Figure D-123: Sequence 2: 200 μl, 1.15 mm, 35 Hz, 32.3 Gauss (rms)

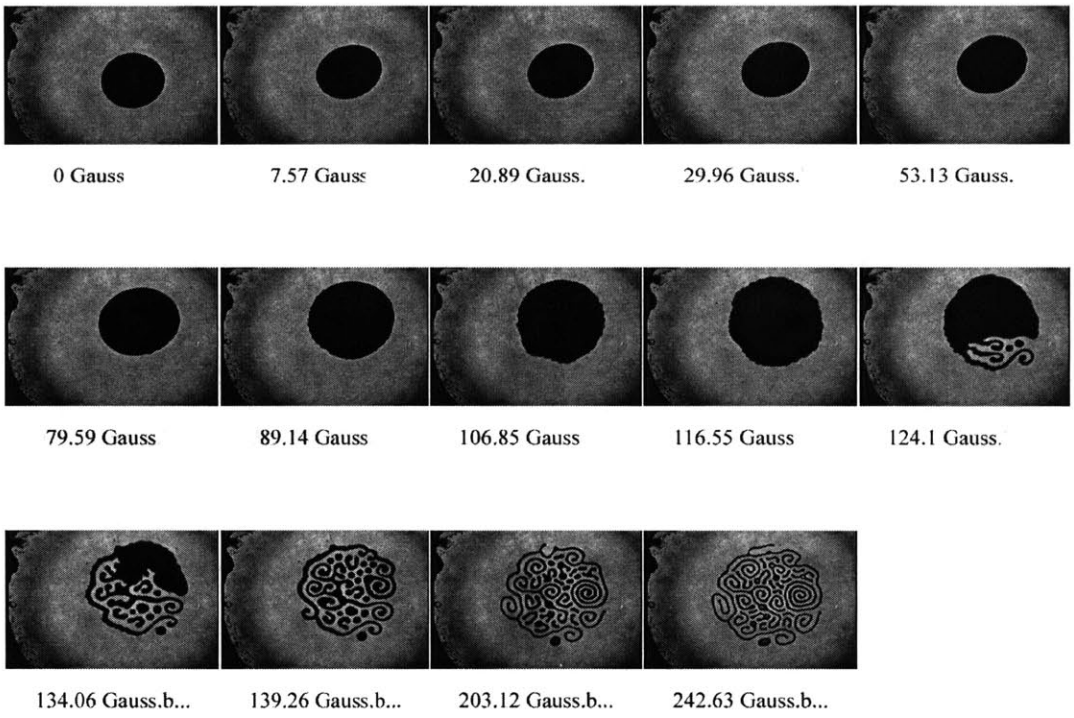

Figure D-124: Sequence 1: 200 μl, 1.15 mm, 35 Hz, 36.1 Gauss (rms)

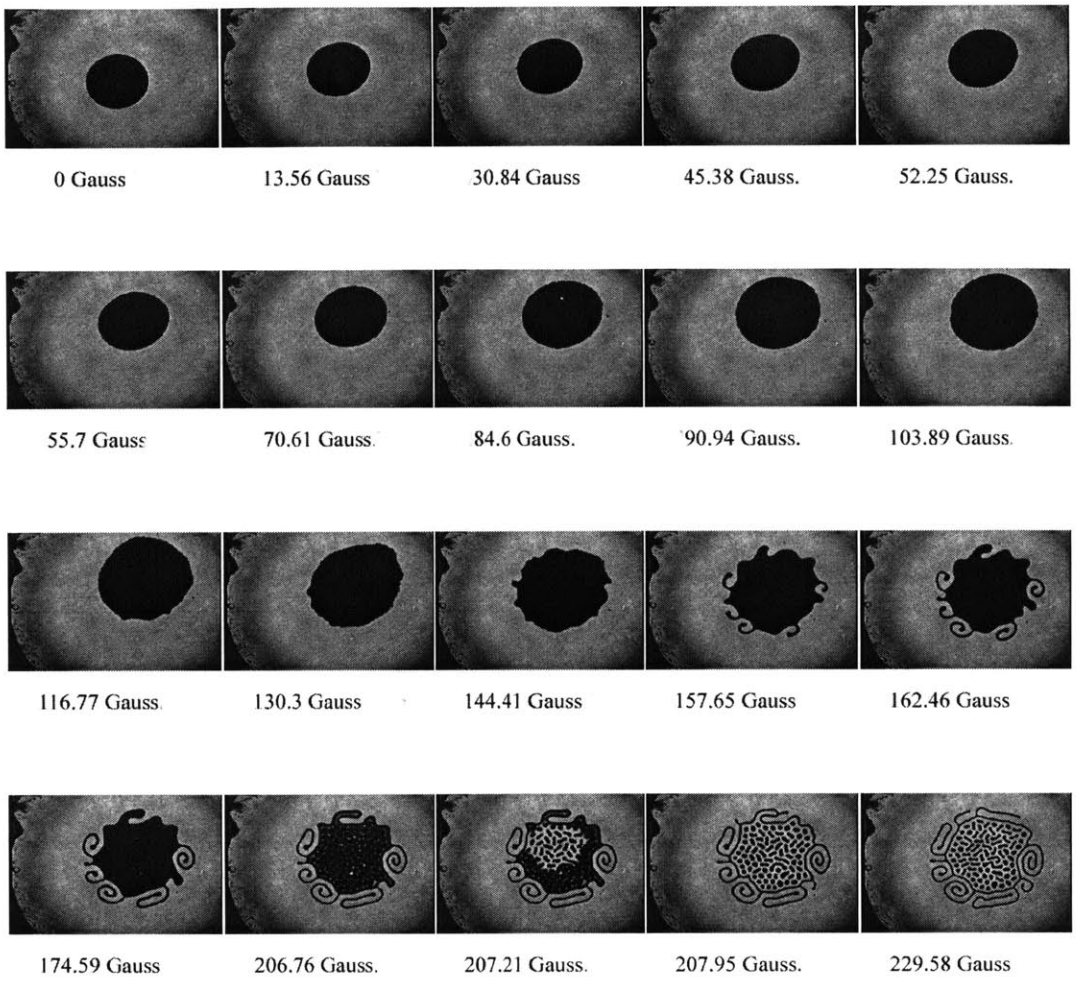

Figure D-125: Sequence 2: 200 μl, 1.15 mm, 35 Hz, 36.1 Gauss (rms)

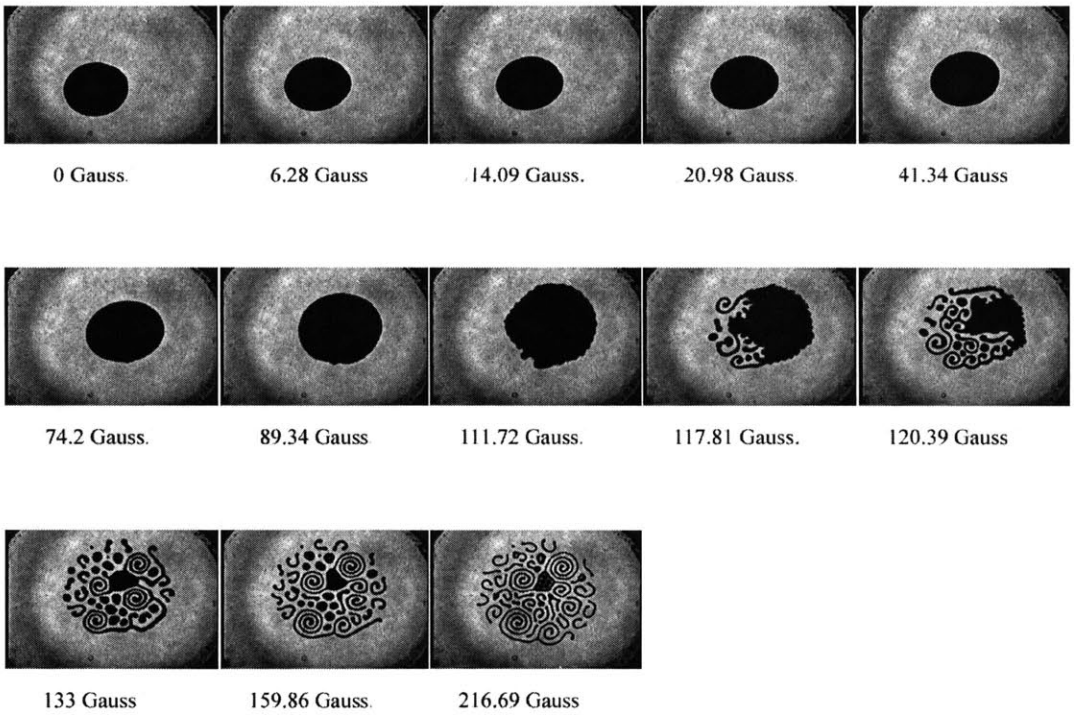

Figure D-126: Sequence 1: 200 μl, 1.15 mm, 35 Hz, 39.9 Gauss (rms)

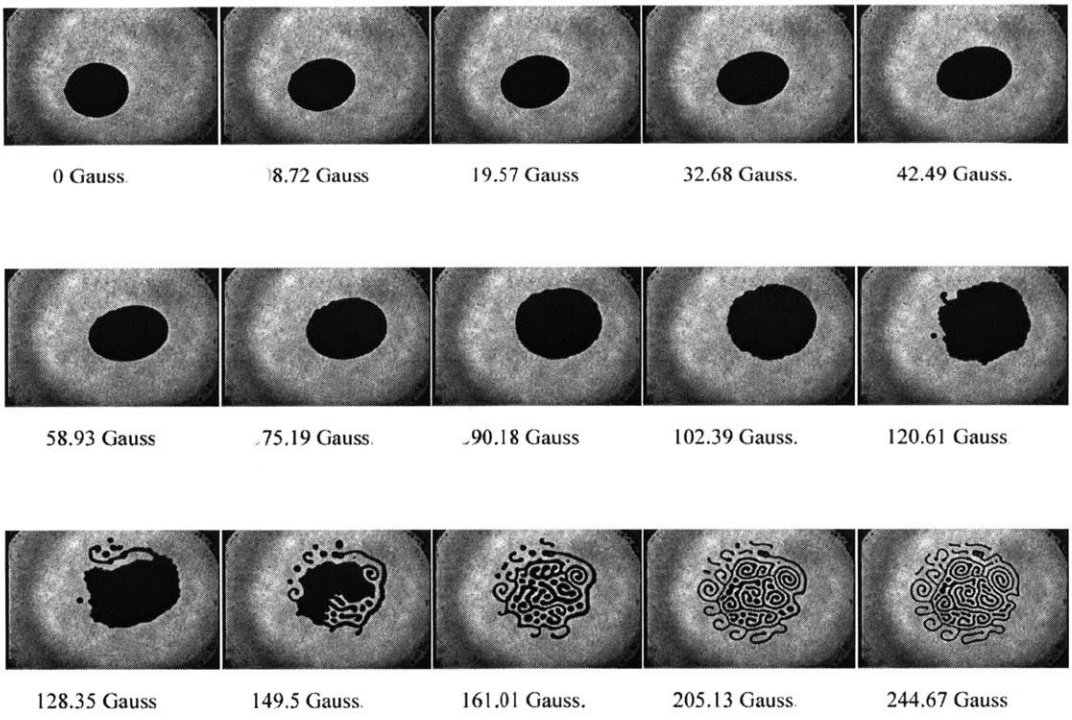

Figure D-127: Sequence 2: 200 μl, 1.15 mm, 35 Hz, 39.9 Gauss (rms)

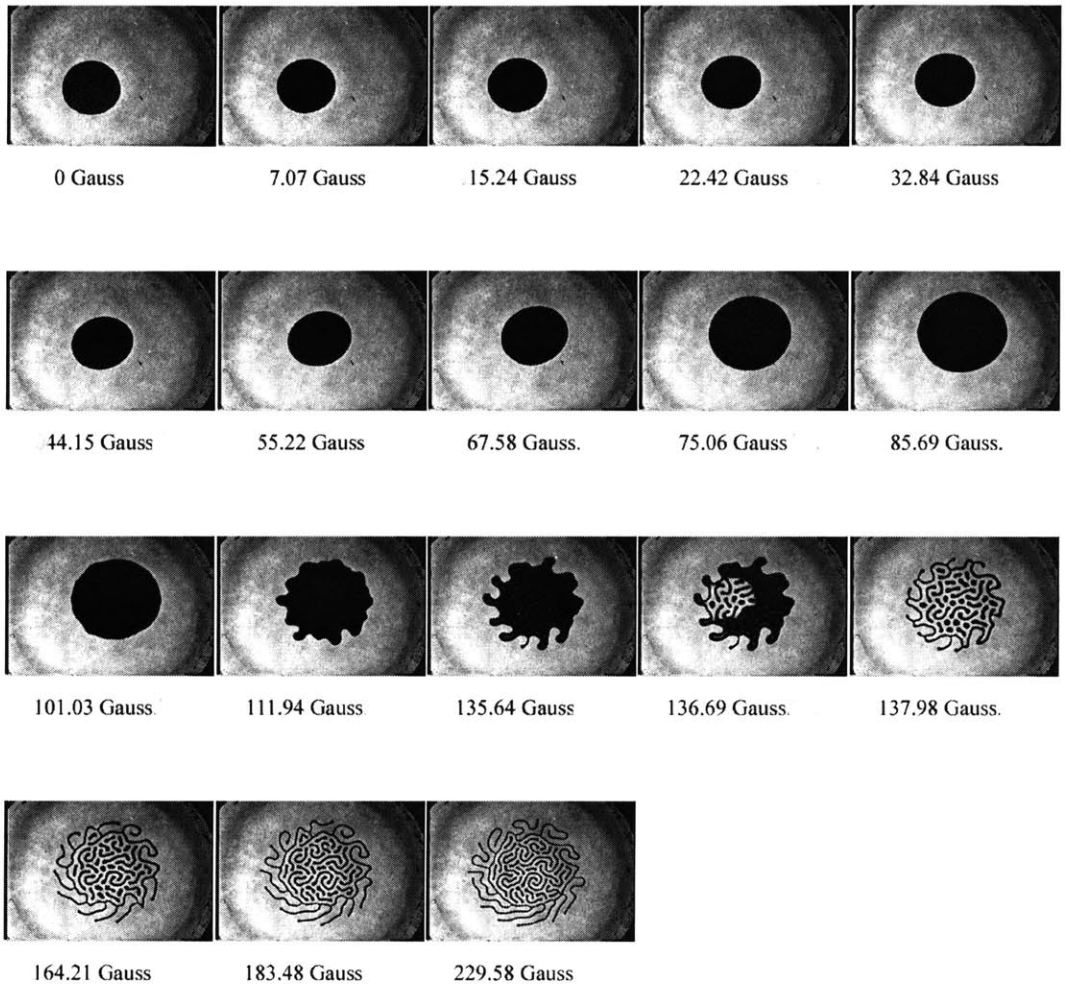

Figure D-128: Sequence 1: 200 μl, 1.15 mm, 40 Hz, 20.9 Gauss (rms)

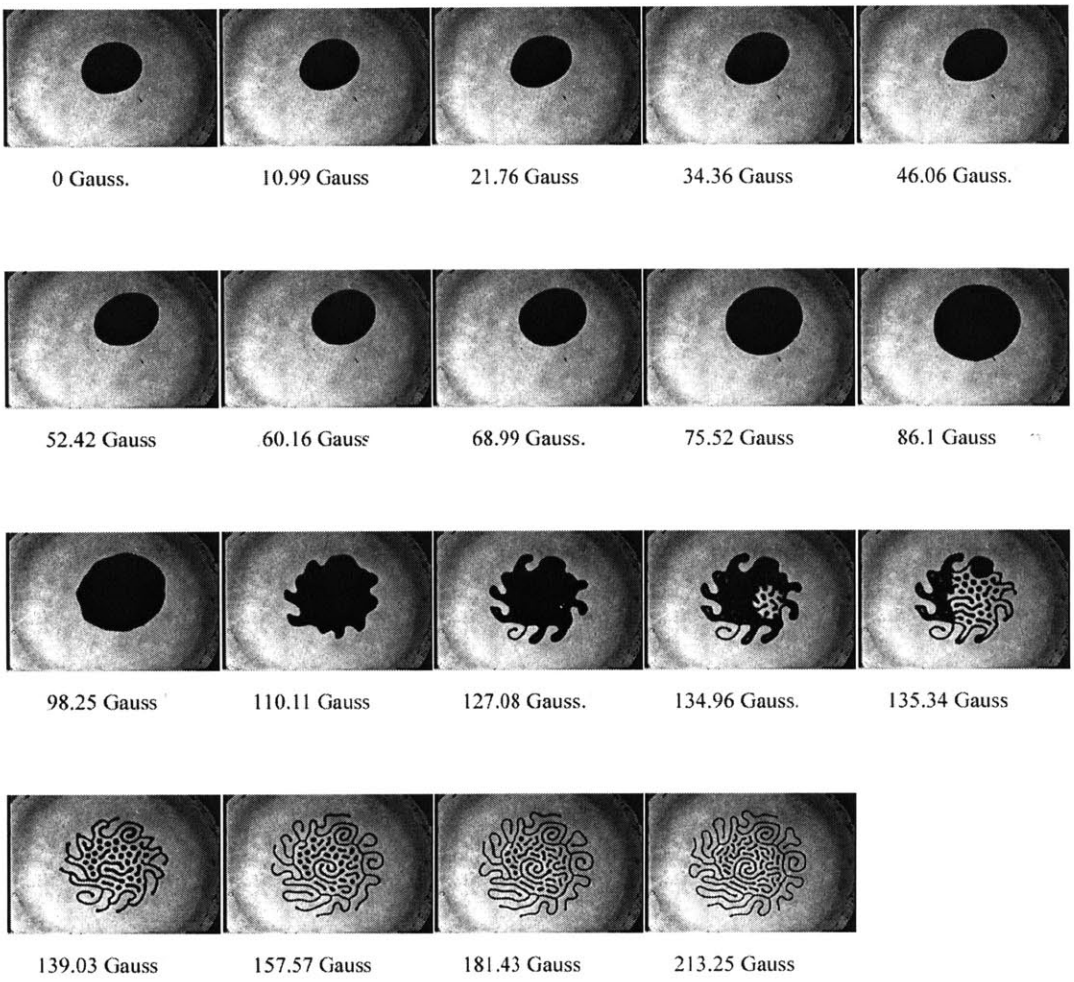

Figure D-129: Sequence 2: 200 μl, 1.15 mm, 40 Hz, 20.9 Gauss (rms)

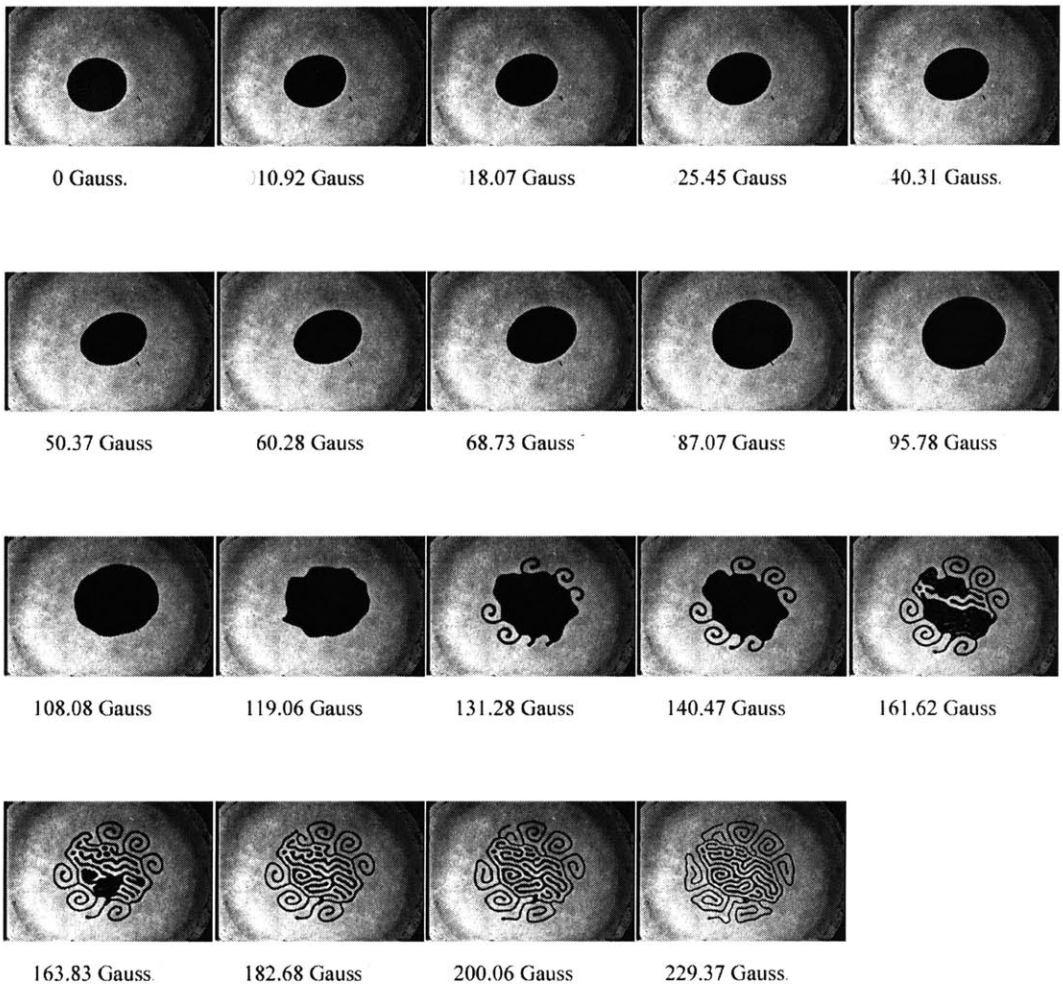

Figure D-130: Sequence 1: 200 μl, 1.15 mm, 40 Hz, 24.7 Gauss (rms)

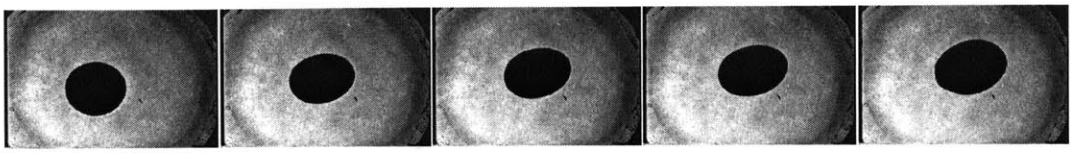

0 Gauss 22.38 Gauss 40.58 Gauss 53.31 Gauss. 70.41 Gauss

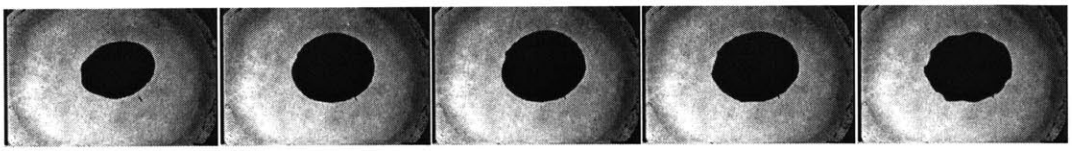

74.13 Gauss. 88.38 Gauss 94.79 Gauss. 105.62 Gauss. 114.79 Gauss

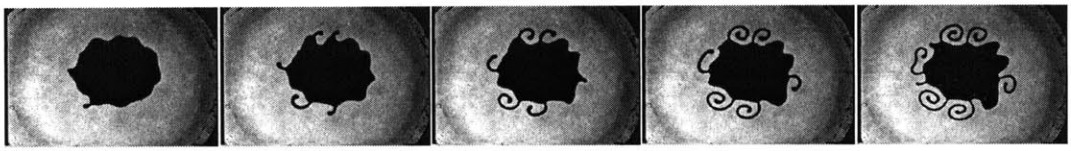

120.61 Gauss. 128.8 Gauss 132.1 Gauss. 142.97 Gauss. 159.63 Gauss.

176.79 ampos 177.18 Gauss. 180.14 Gauss. 194.67 Gauss. 213.47 Gauss.

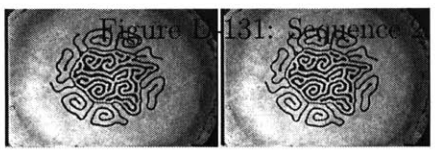

235.64 Gauss. 245.69 Gauss

Figure D-131: Sequence 200 μl, 1.15 mm, 40 Hz, 24.7 Gauss (rms)

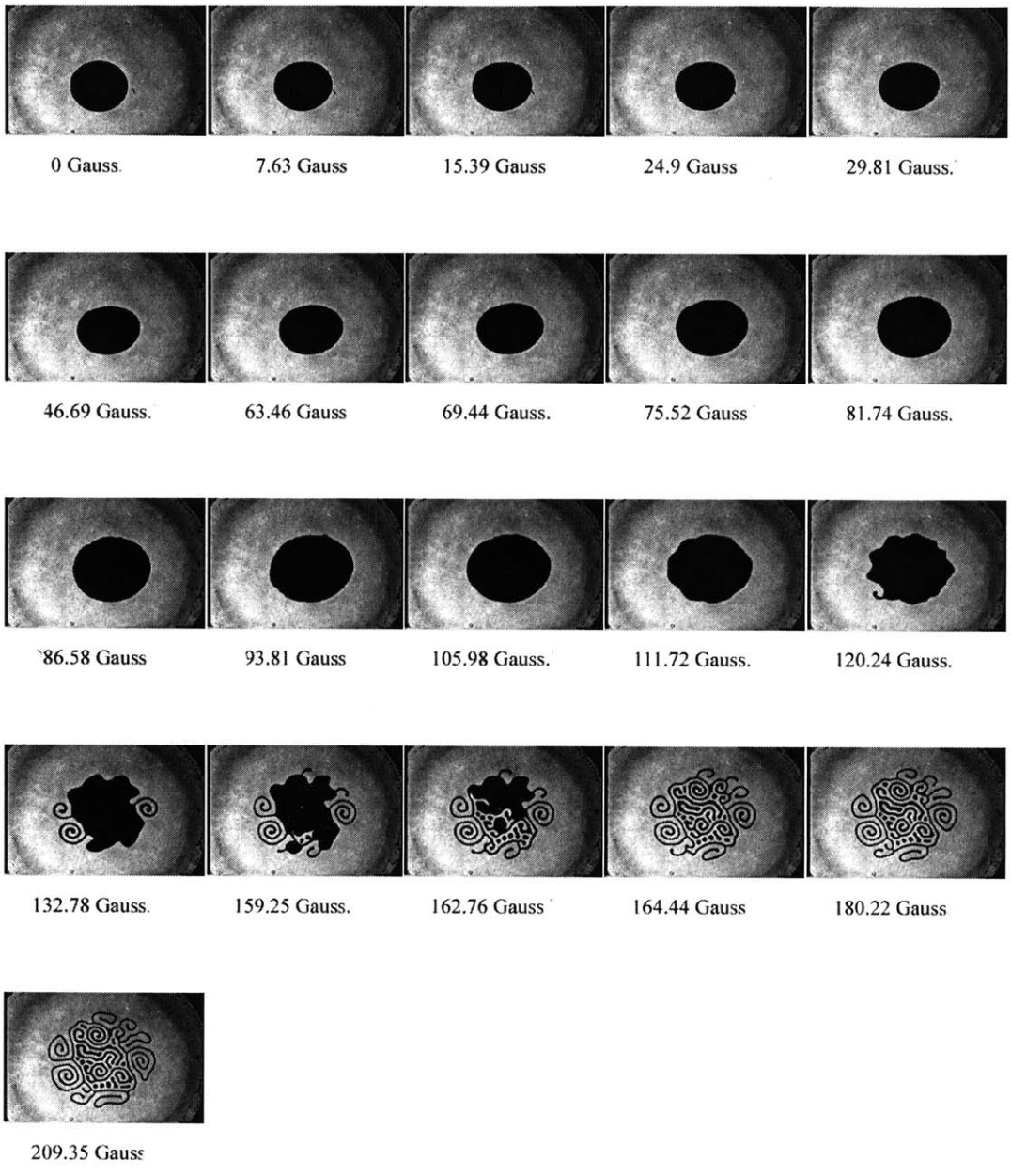

Figure D-132: Sequence 1: 200 μl, 1.15 mm, 40 Hz, 28.5 Gauss (rms)

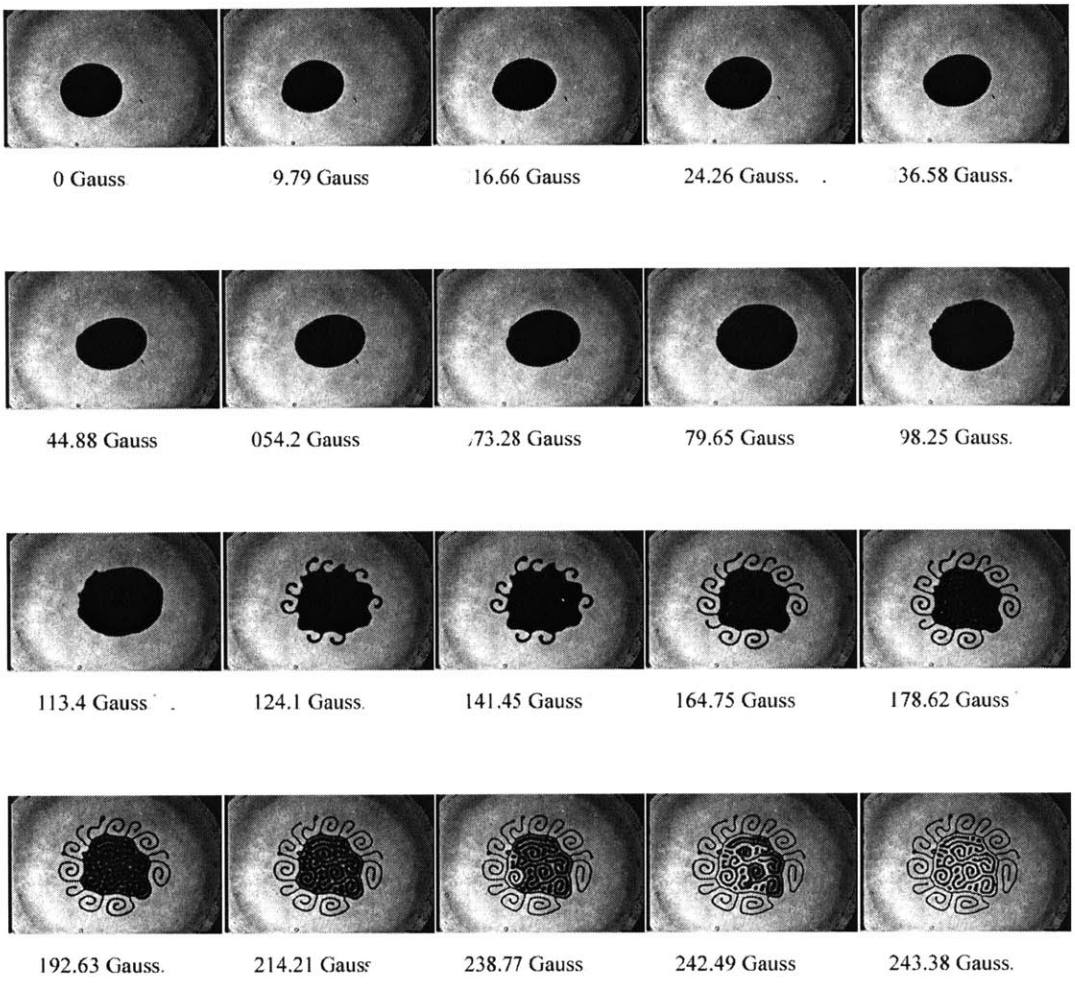

Figure D-133: Sequence 2: 200 μl, 1.15 mm, 40 Hz, 28.5 Gauss (rms)

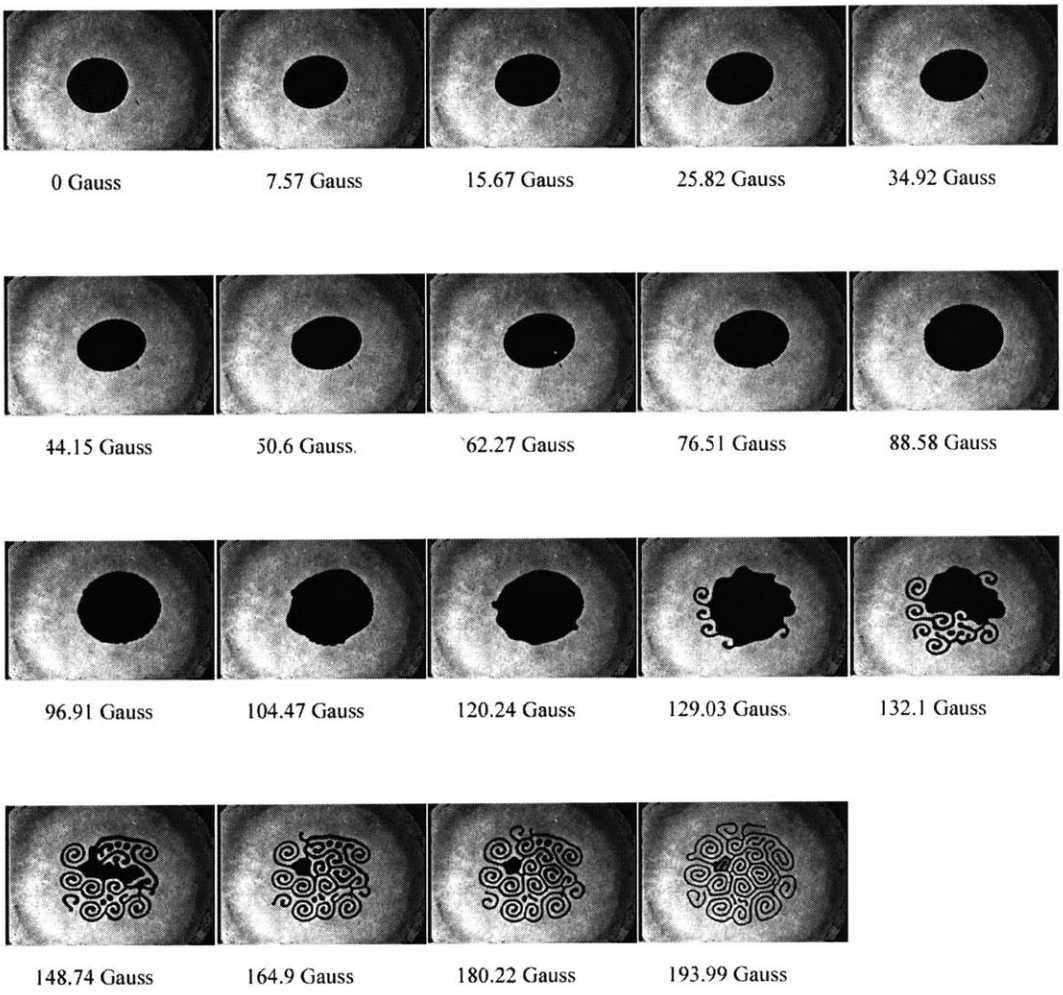

Figure D-134: Sequence 1: 200 μl, 1.15 mm, 40 Hz, 32.3 Gauss (rms)

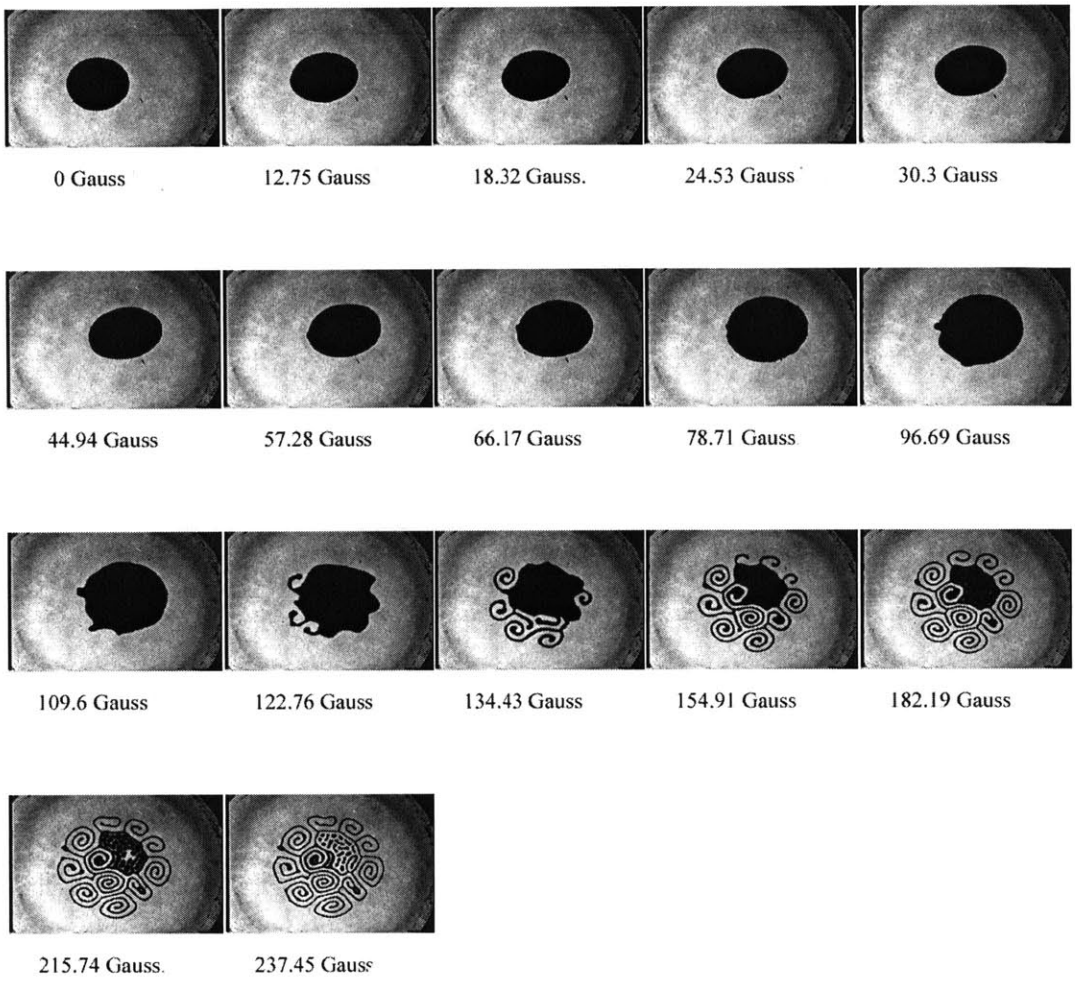

Figure D-135: Sequence 2: 200 μl, 1.15 mm, 40 Hz, 32.3 Gauss (rms)

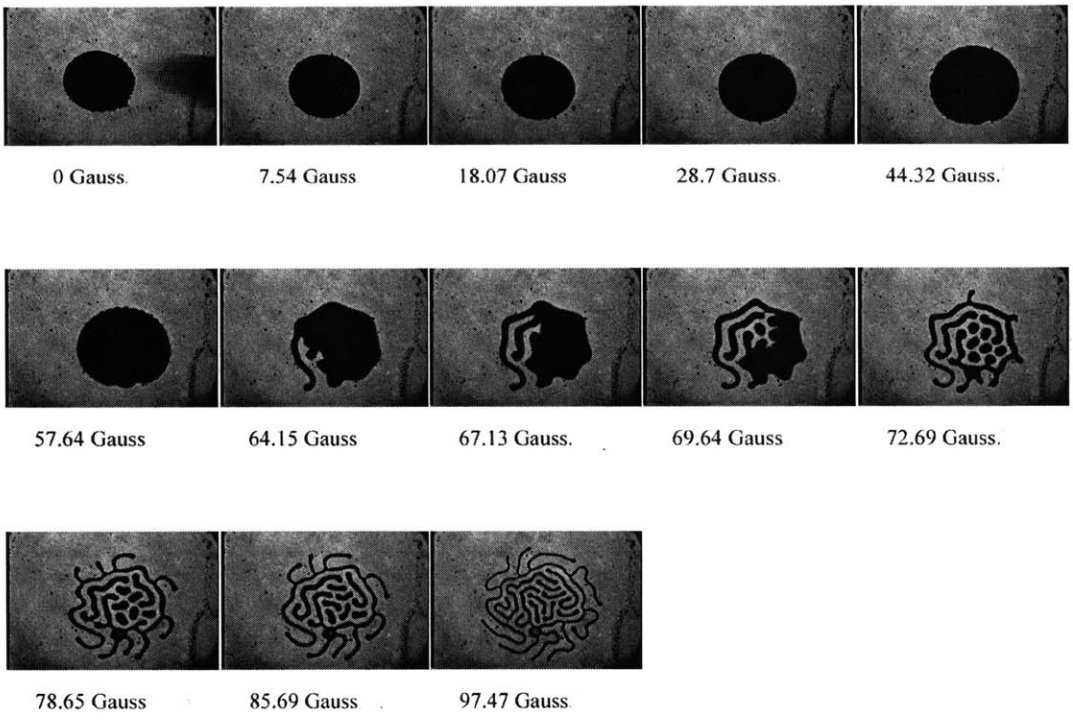

Figure D-136: Sequence 1: 200 μl, 1.4 mm, 20 Hz, 20.9 Gauss (rms)

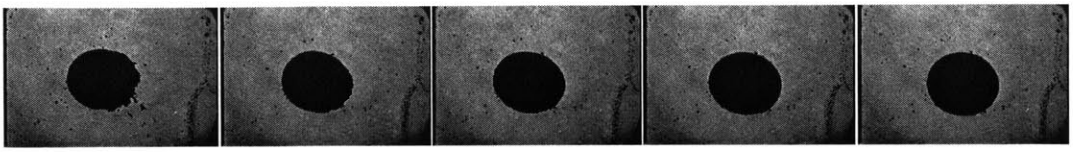

0 Gauss 4.79 Gauss 17.5 Gauss. 29.23 Gauss 44.54 Gauss

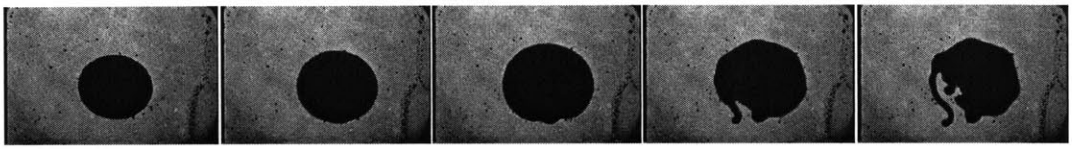

52.9 Gauss 71.78 Gauss. 81.34 Gauss. 97.61 Gauss. 100.74 Gauss.

101.96 Gauss.b... 109.39 Gauss.b... 119.8 Gauss.bmp 132.93 Gauss.b... 161.31 Gauss.b...

186.97 Gauss.b... 187.65 Gauss.b... 212.3 Gauss.bmp

Figure D-137: Sequence 2: 200 μl, 1.4 mm, 20 Hz, 20.9 Gauss (rms)

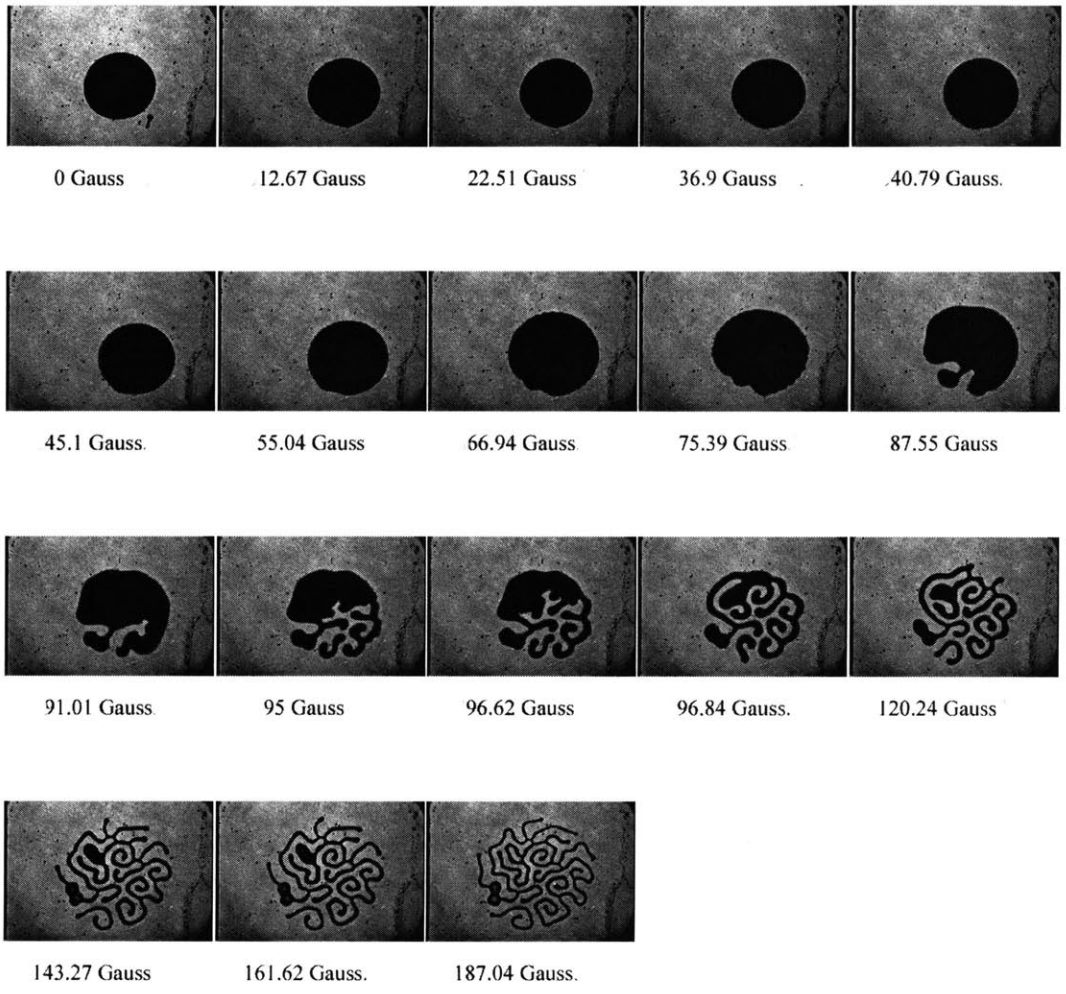

Figure D-138: Sequence 1: 200 μl, 1.4 mm, 20 Hz, 24.7 Gauss (rms)

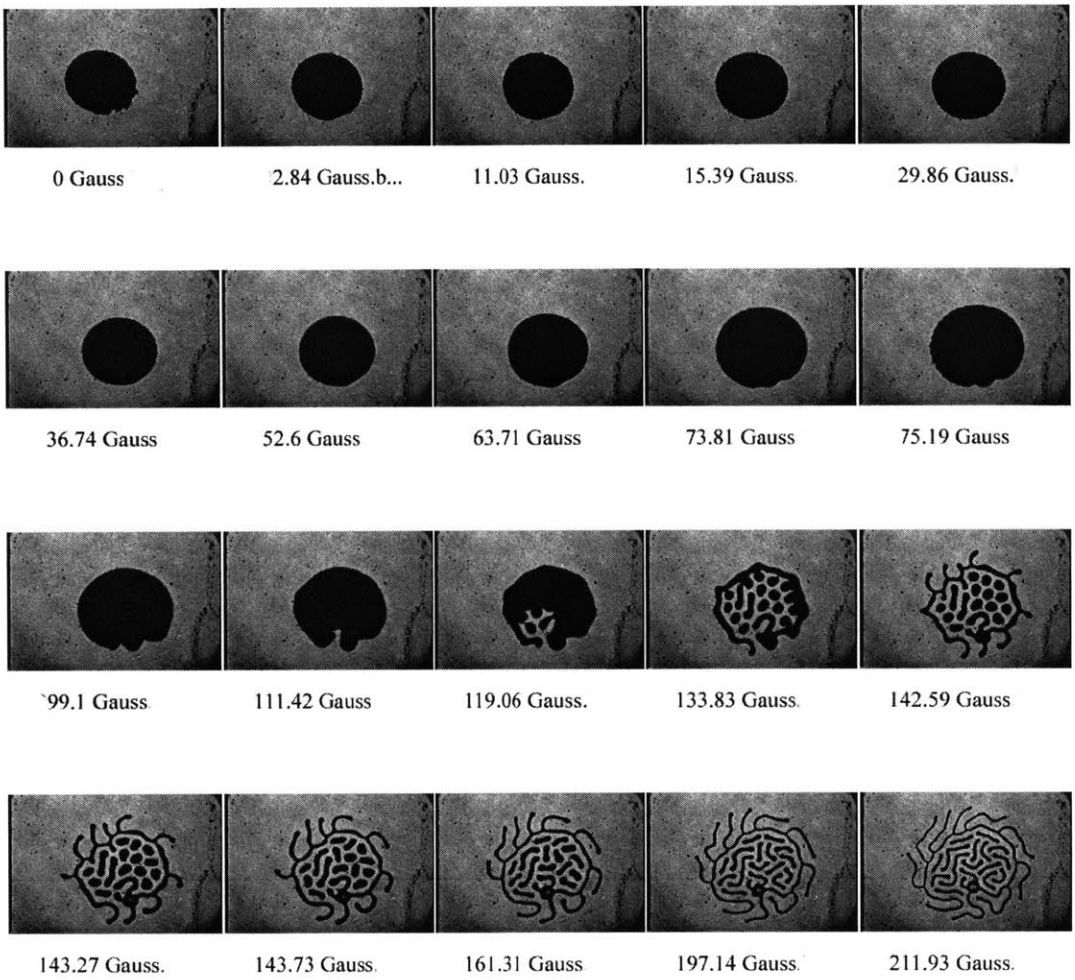

Figure D-139: Sequence 2: 200 μl, 1.4 mm, 20 Hz, 24.7 Gauss (rms)

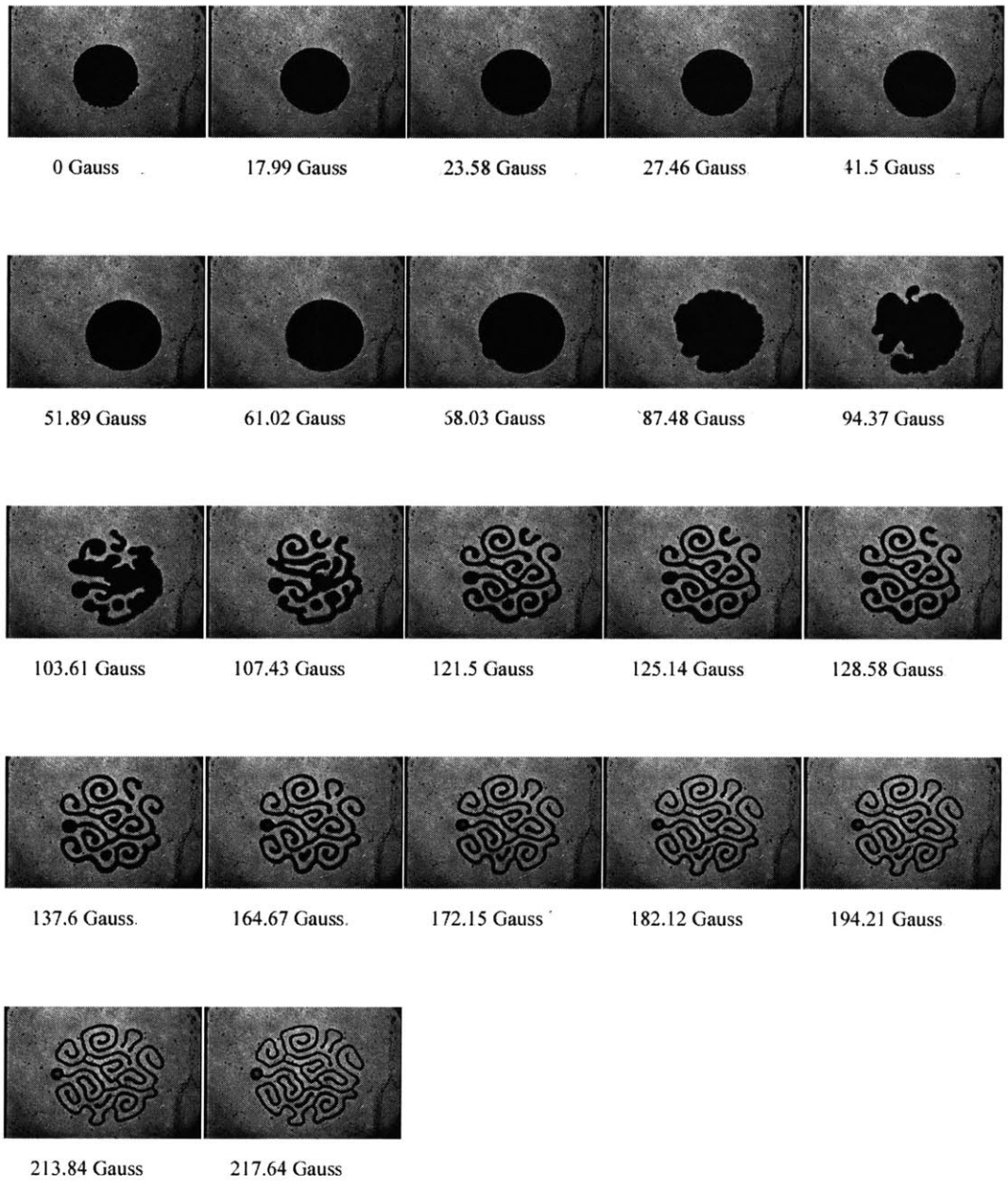

Figure D-140: Sequence 1: 200 μl, 1.4 mm, 20 Hz, 28.5 Gauss (rms)

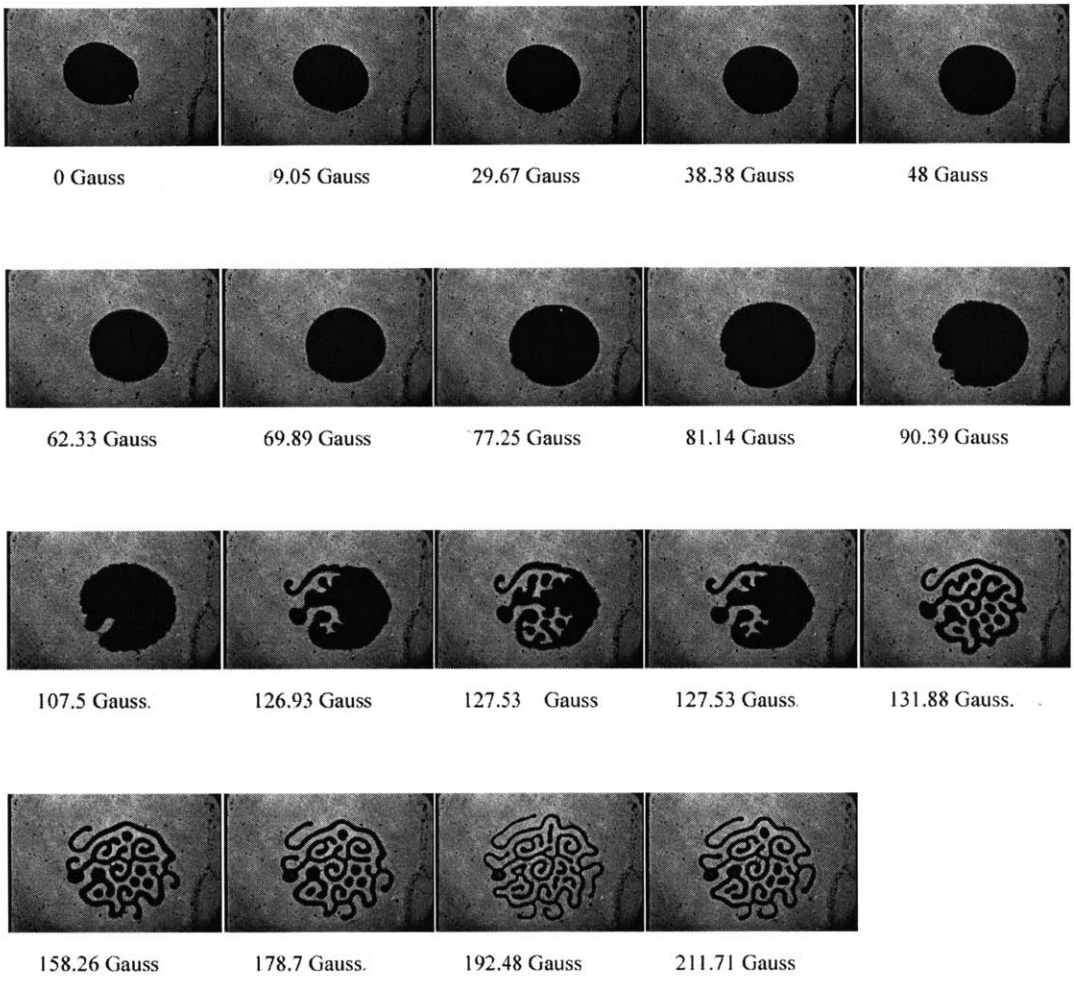

Figure D-141: Sequence 2: 200 μl, 1.4 mm, 20 Hz, 28.5 Gauss (rms)

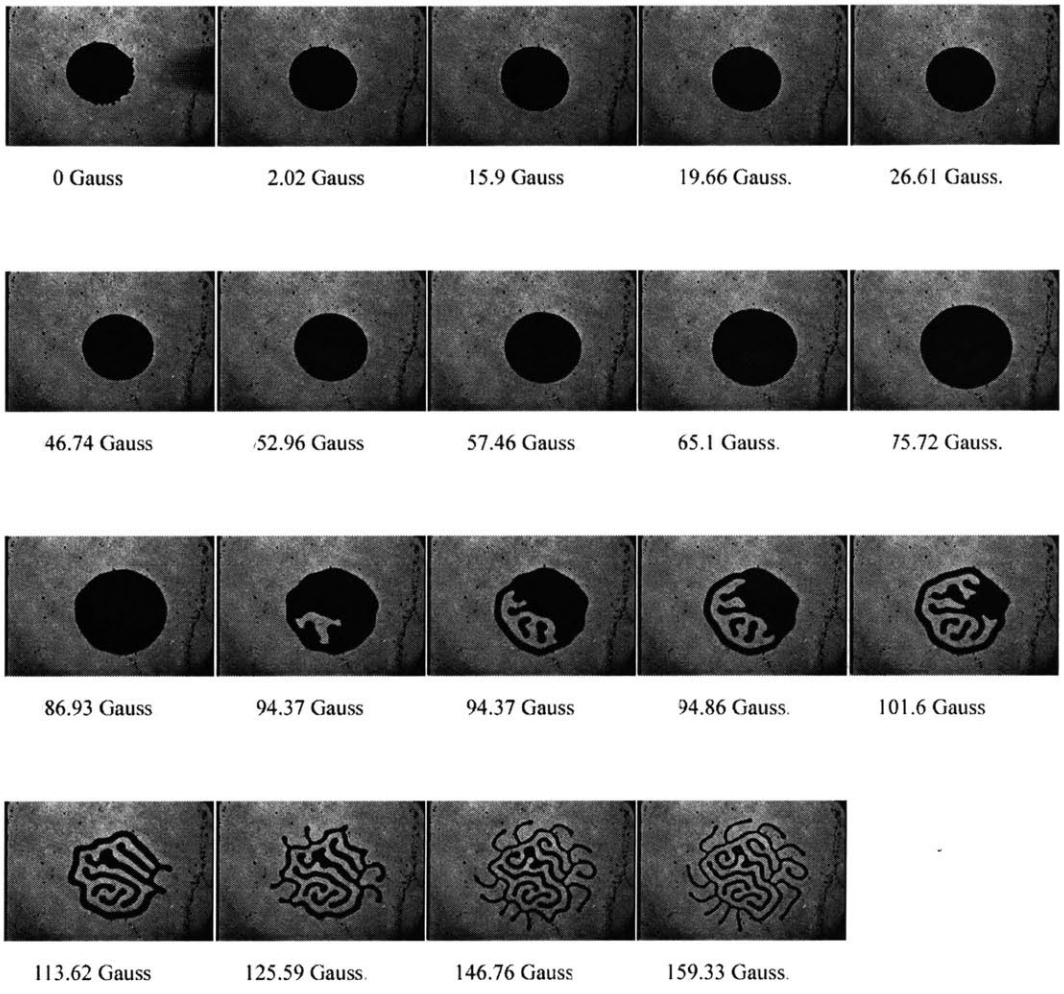

Figure D-142: Sequence 1: 200 μl, 1.4 mm, 25 Hz, 17.1 Gauss (rms)

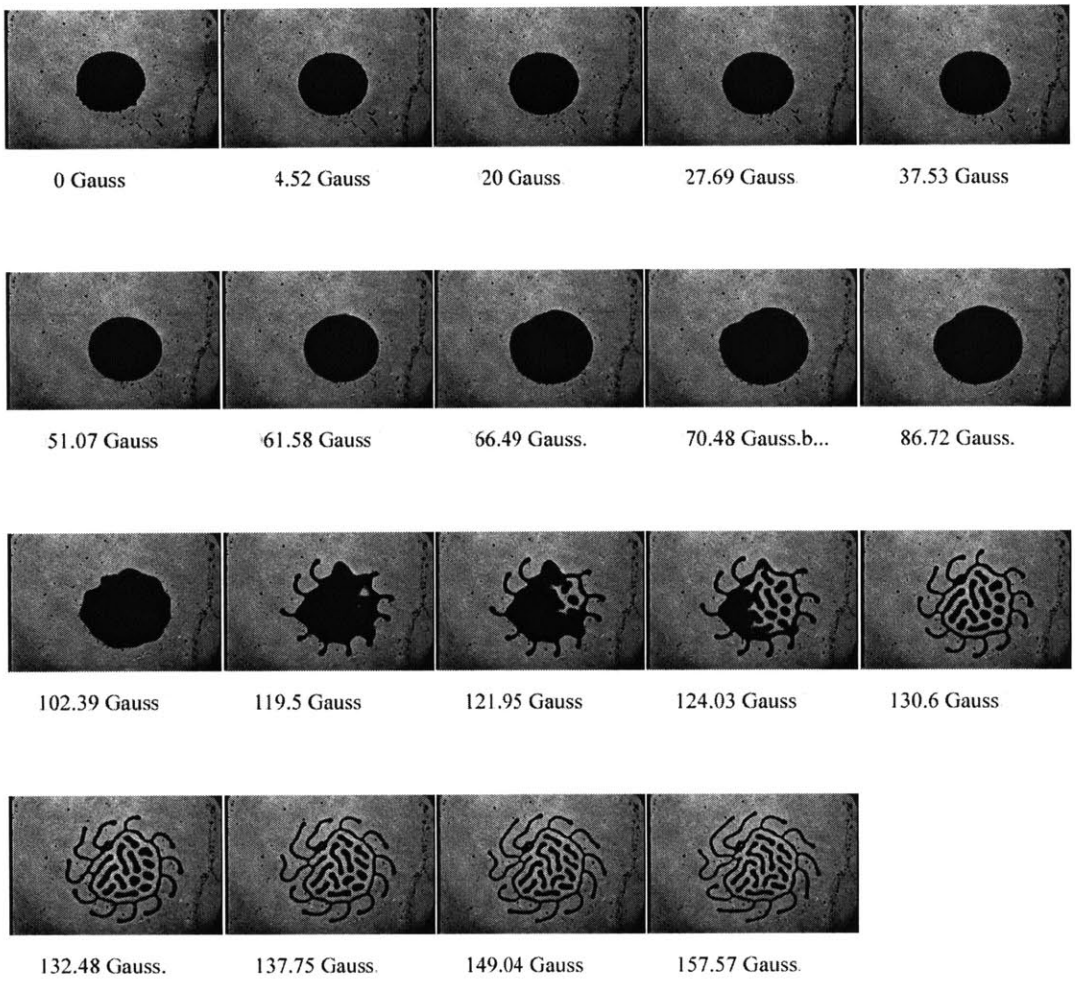

Figure D-143: Sequence 2: 200 μl, 1.4 mm, 25 Hz, 17.1 Gauss (rms)

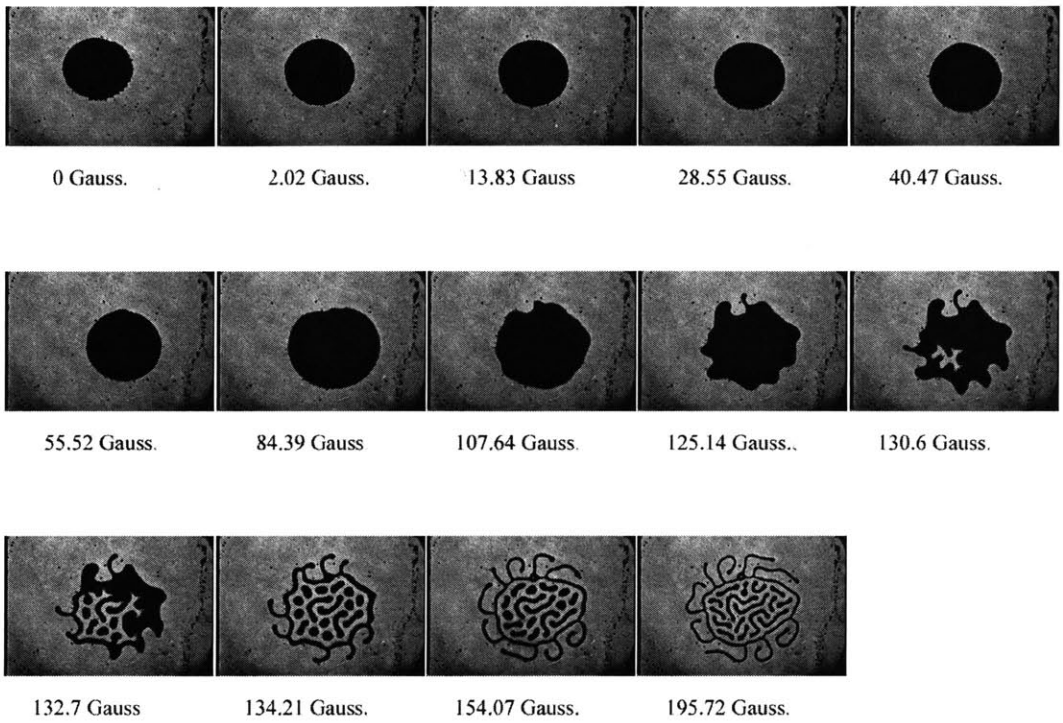

Figure D-144: Sequence 1: 200 μl, 1.4 mm, 25 Hz, 20.9 Gauss (rms)

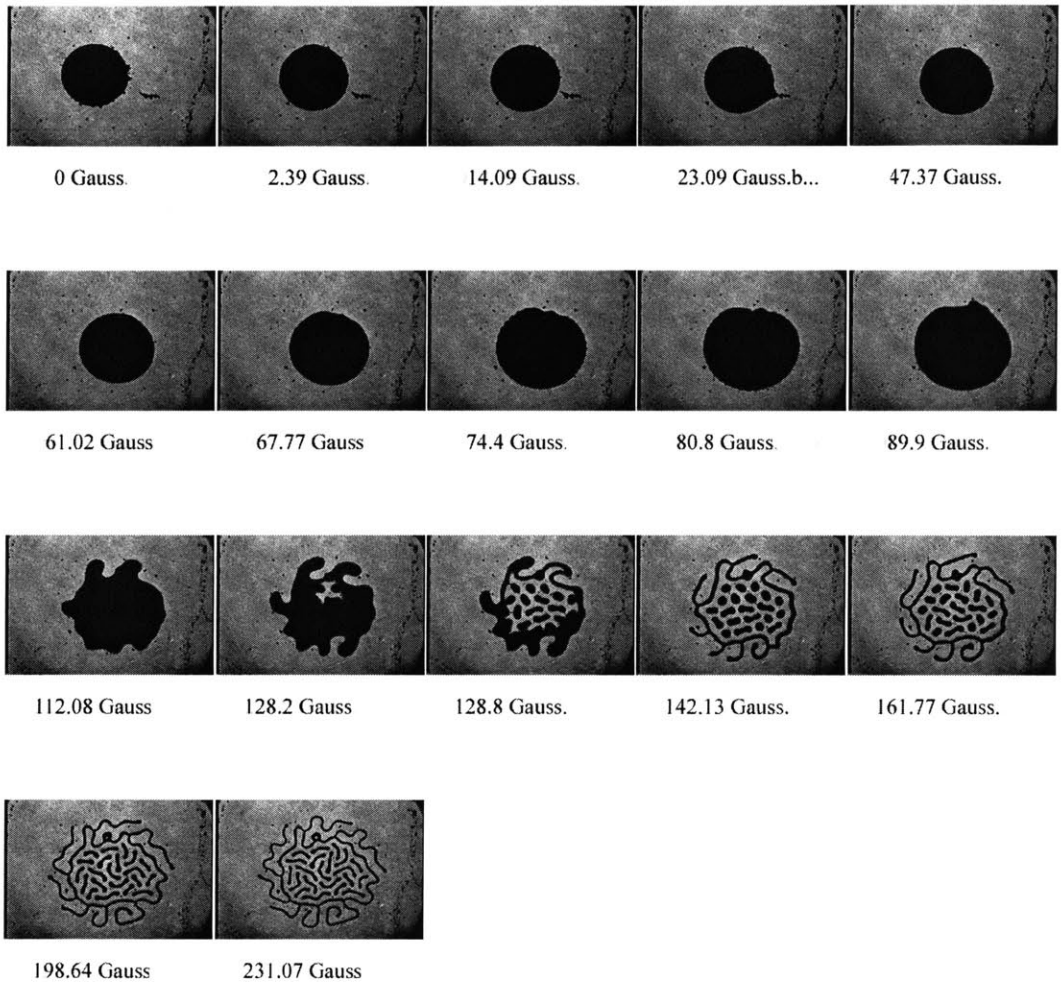

Figure D-145: Sequence 2: 200 μl, 1.4 mm, 25 Hz, 20.9 Gauss (rms)

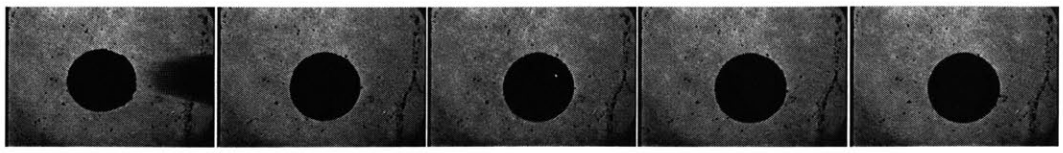

0 Gauss 11.03 Gauss. 25.96 Gauss 33.75 Gauss. 41.56 Gauss.

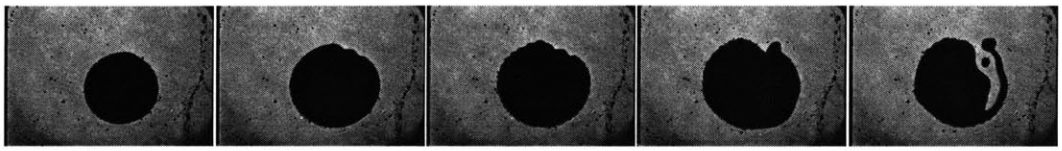

47.43 Gauss. 69.44 Gauss 75.78 Gauss. 98.96 Gauss. 106.78 Gauss.

115.23 Gauss 121.5 Gauss 125.74 Gauss. 132.55 Gauss. 155.59 Gauss.

185.45 Gauss.

Figure D-146: Sequence 1: 200 μl, 1.4 mm, 25 Hz, 24.7 Gauss (rms)

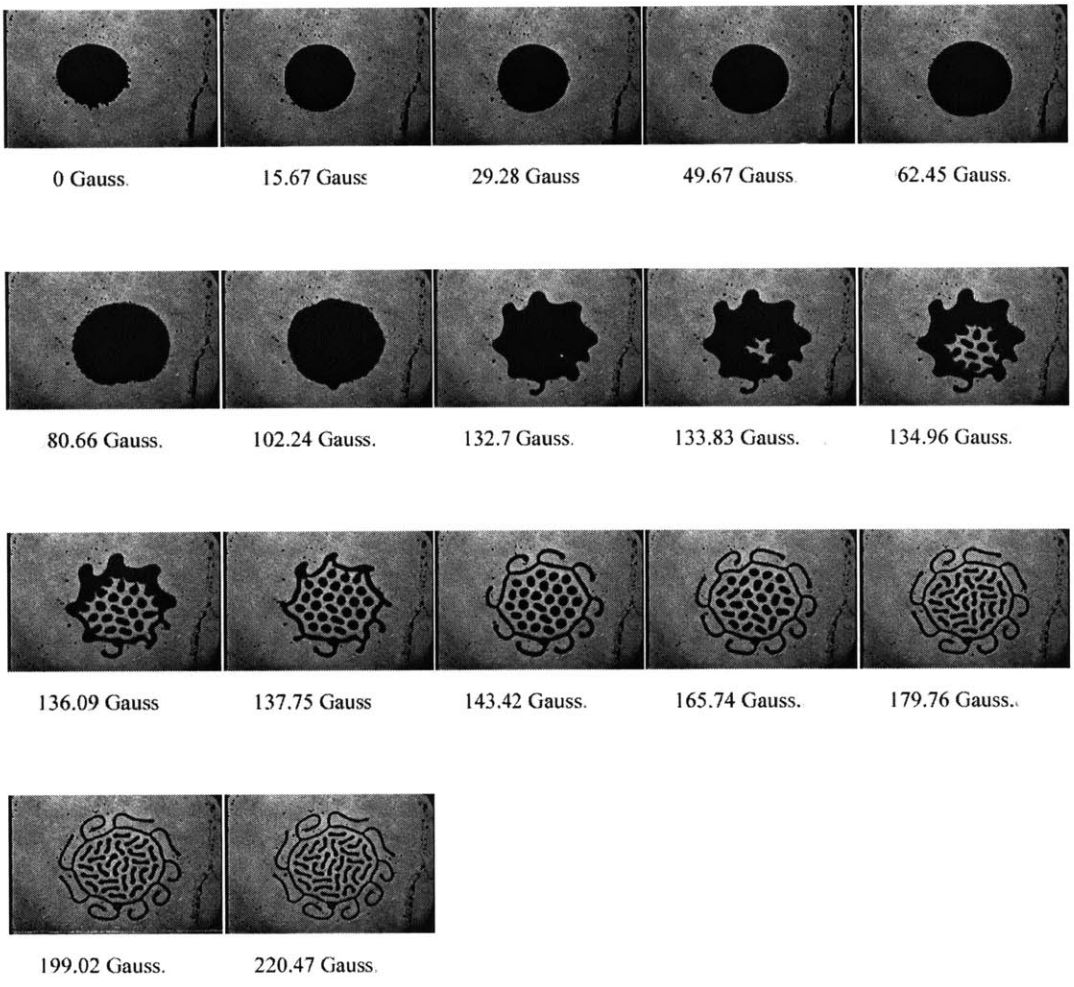

Figure D-147: Sequence 2: 200 μl, 1.4 mm, 25 Hz, 24.7 Gauss (rms)

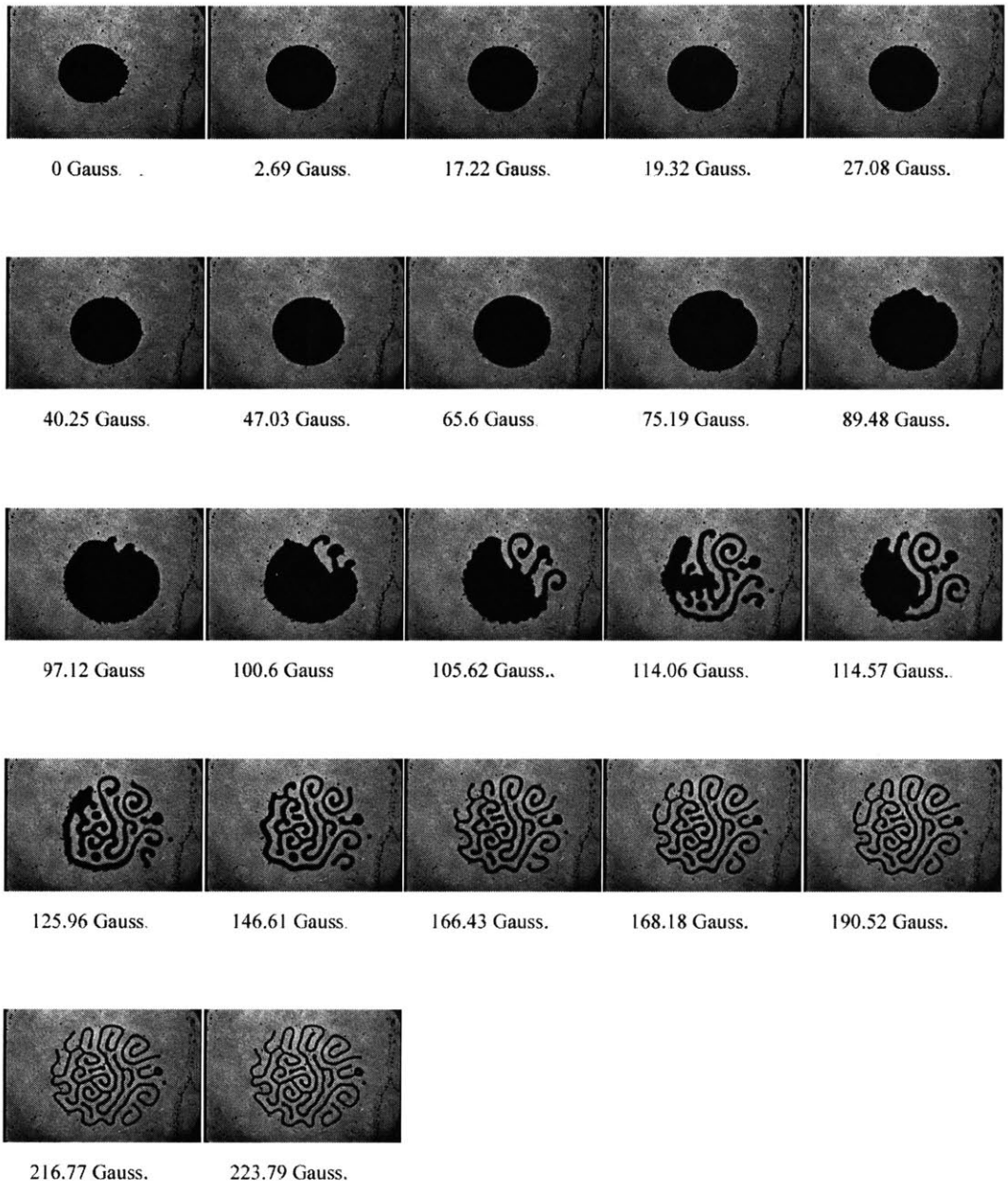

Figure D-148: Sequence 1: 200 μl, 1.4 mm, 25 Hz, 28.5 Gauss (rms)

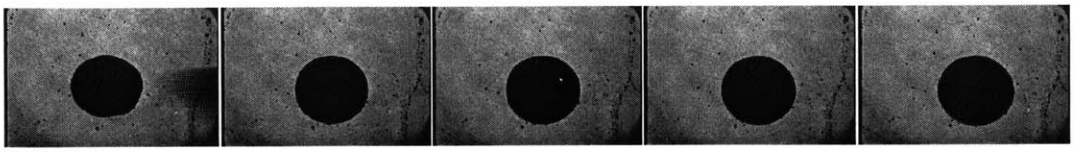

0 Gauss 10.09 Gauss 20.51 Gauss 26.75 Gauss. 38.7 Gauss.

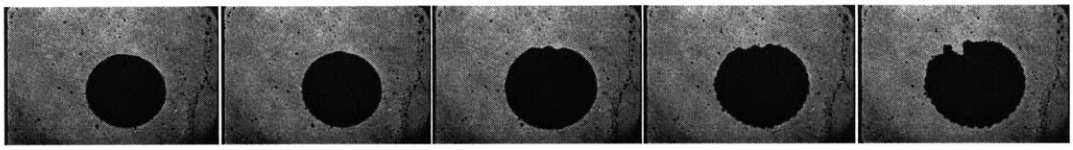

51.54 Gauss. 59.66 Gauss 73.41 Gauss 89.48 Gauss. 99.67 Gauss

115.67 Gauss. 118.54 Gauss 128.2 Gauss. 133.15 Gauss. 142.21 Gauss.

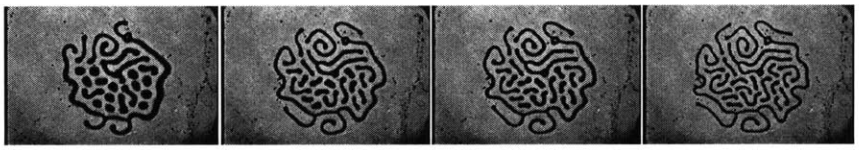

153 Gauss 183.03 Gauss 192.03 Gauss 234.1 Gauss.

Figure D-149: Sequence 2: 200 μl, 1.4 mm, 25 Hz, 28.5 Gauss (rms)

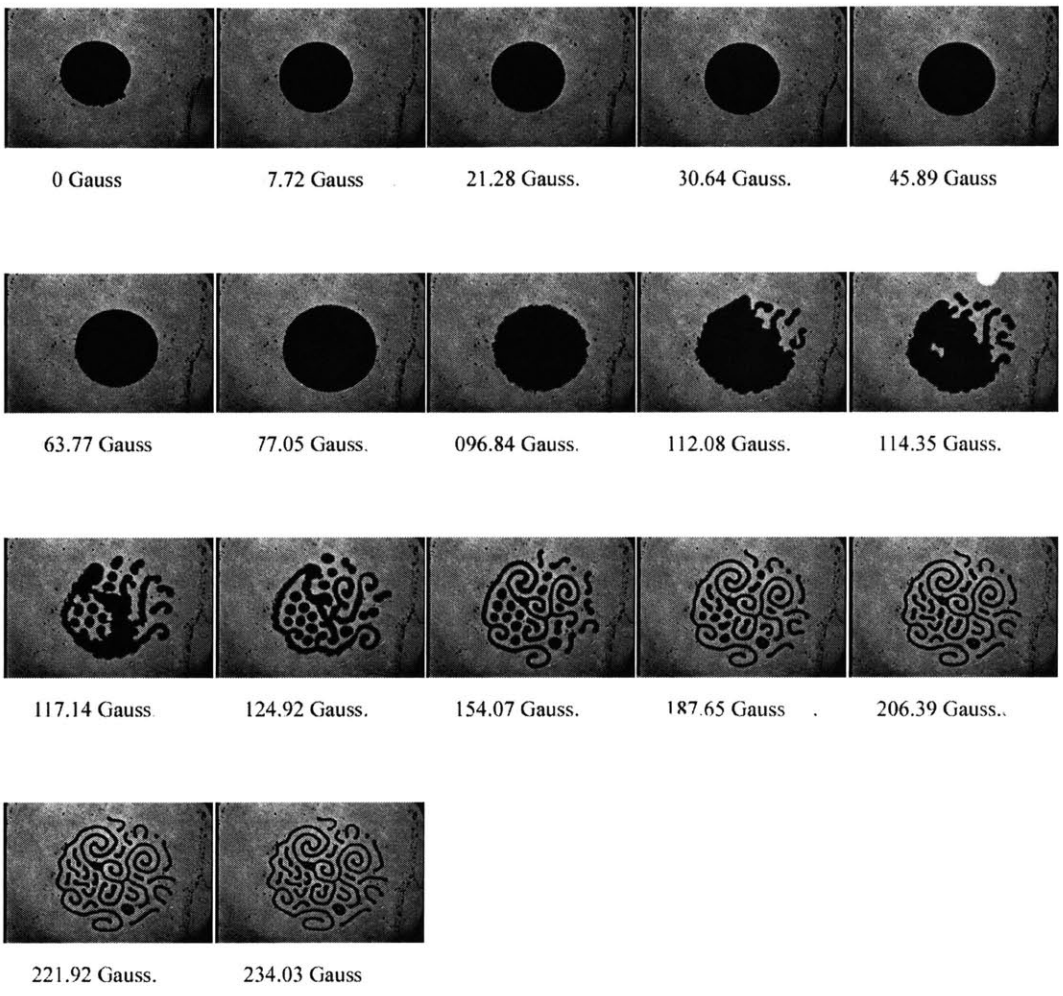

Figure D-150: Sequence 1: 200 μl, 1.4 mm, 25 Hz, 28.5 Gauss (rms)

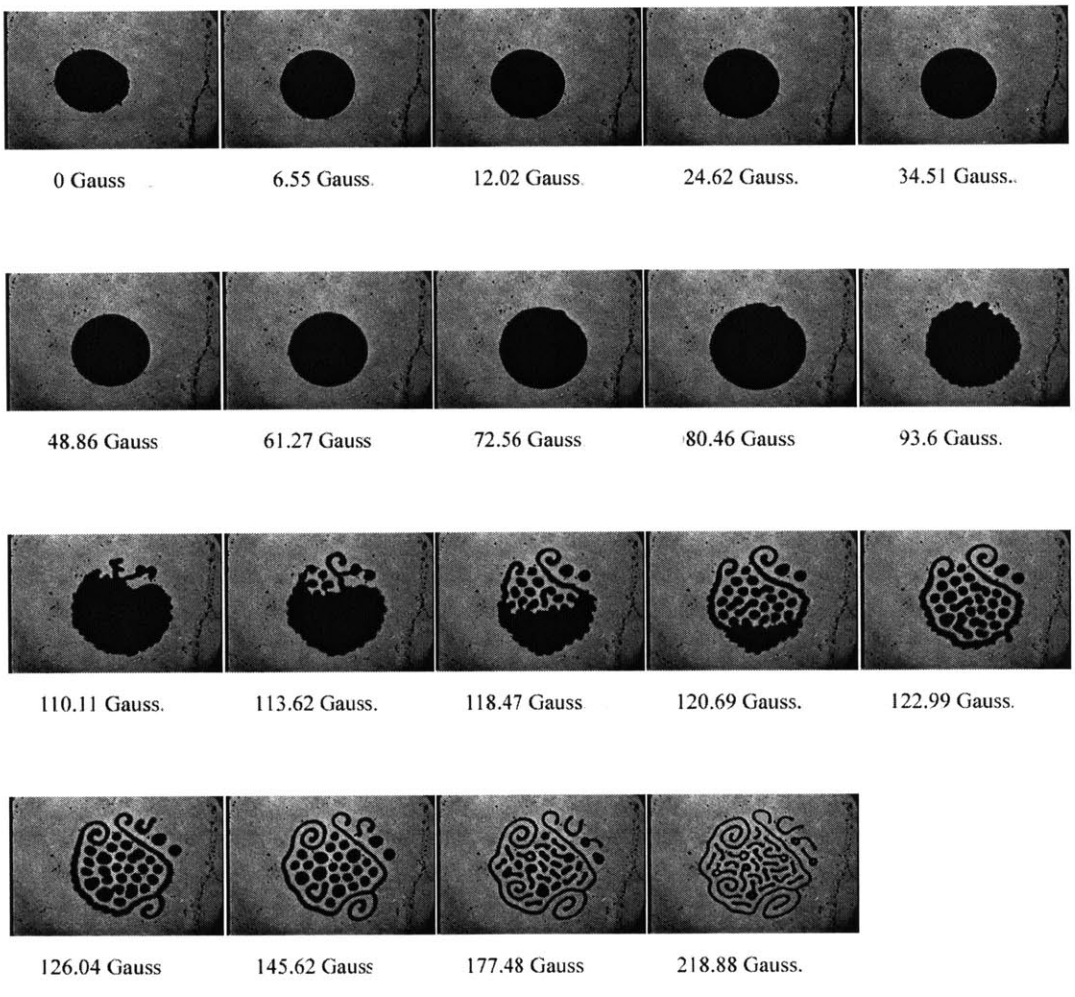

Figure D-151: Sequence 2: 200 μl, 1.4 mm, 25 Hz, 28.5 Gauss (rms)

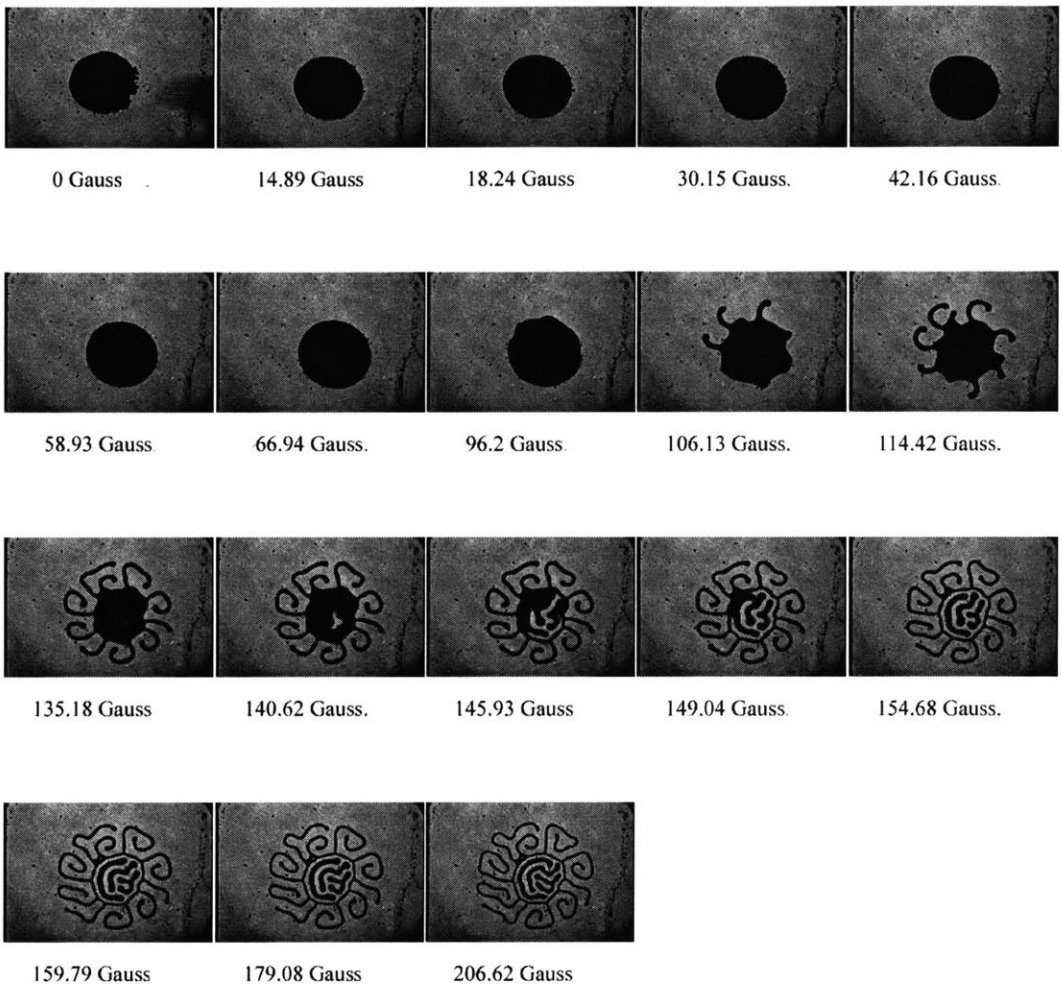

Figure D-152: Sequence 1: 200 μl, 1.4 mm, 30 Hz, 17.1 Gauss (rms)

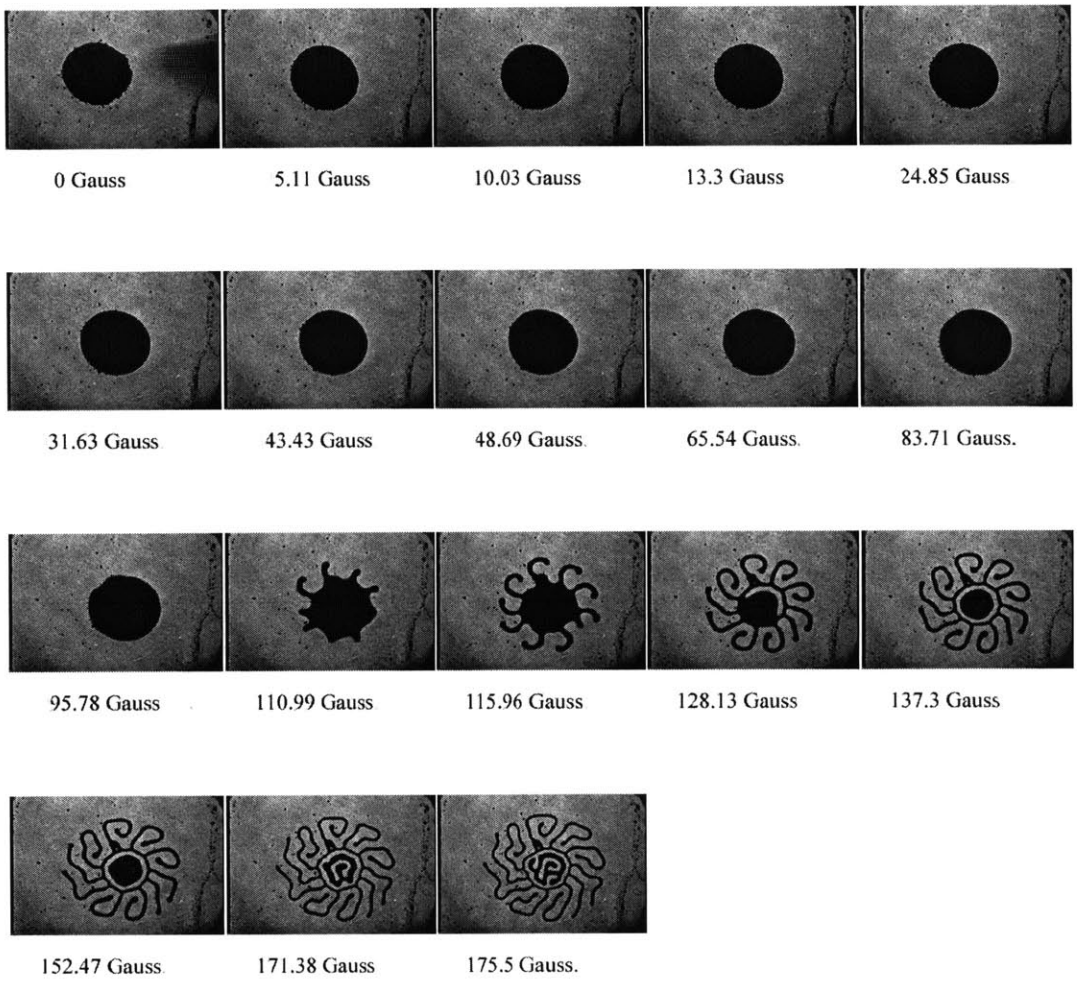

Figure D-153: Sequence 2: 200 μl, 1.4 mm, 30 Hz, 17.1 Gauss (rms)

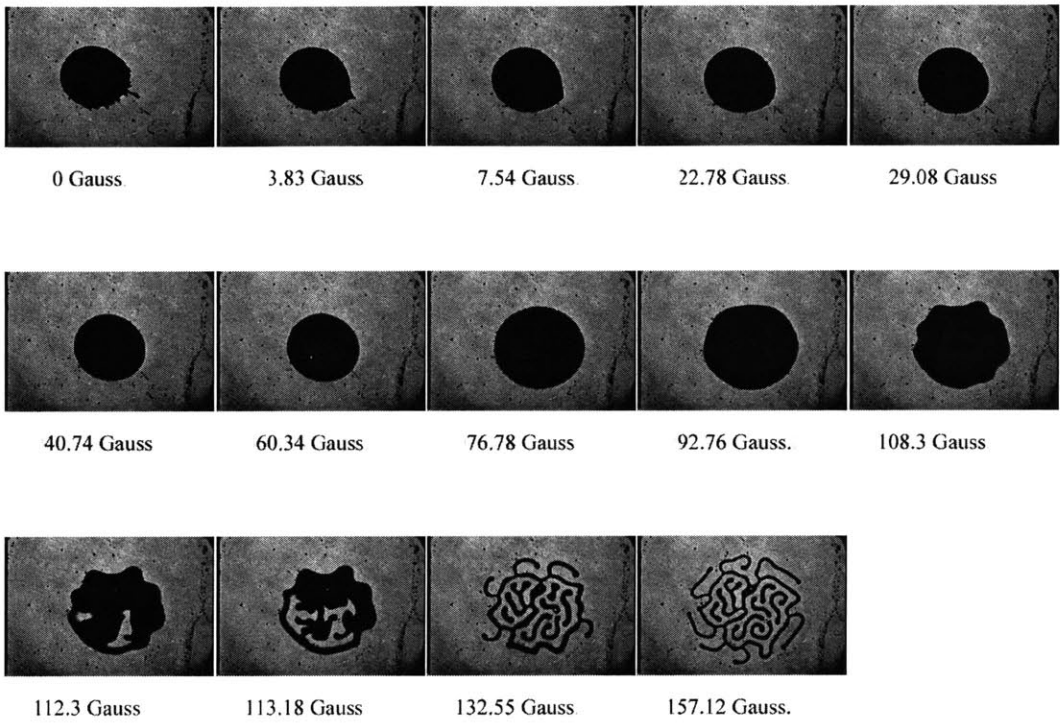

Figure D-154: Sequence 1: 200 μl, 1.4 mm, 30 Hz, 20.9 Gauss (rms)

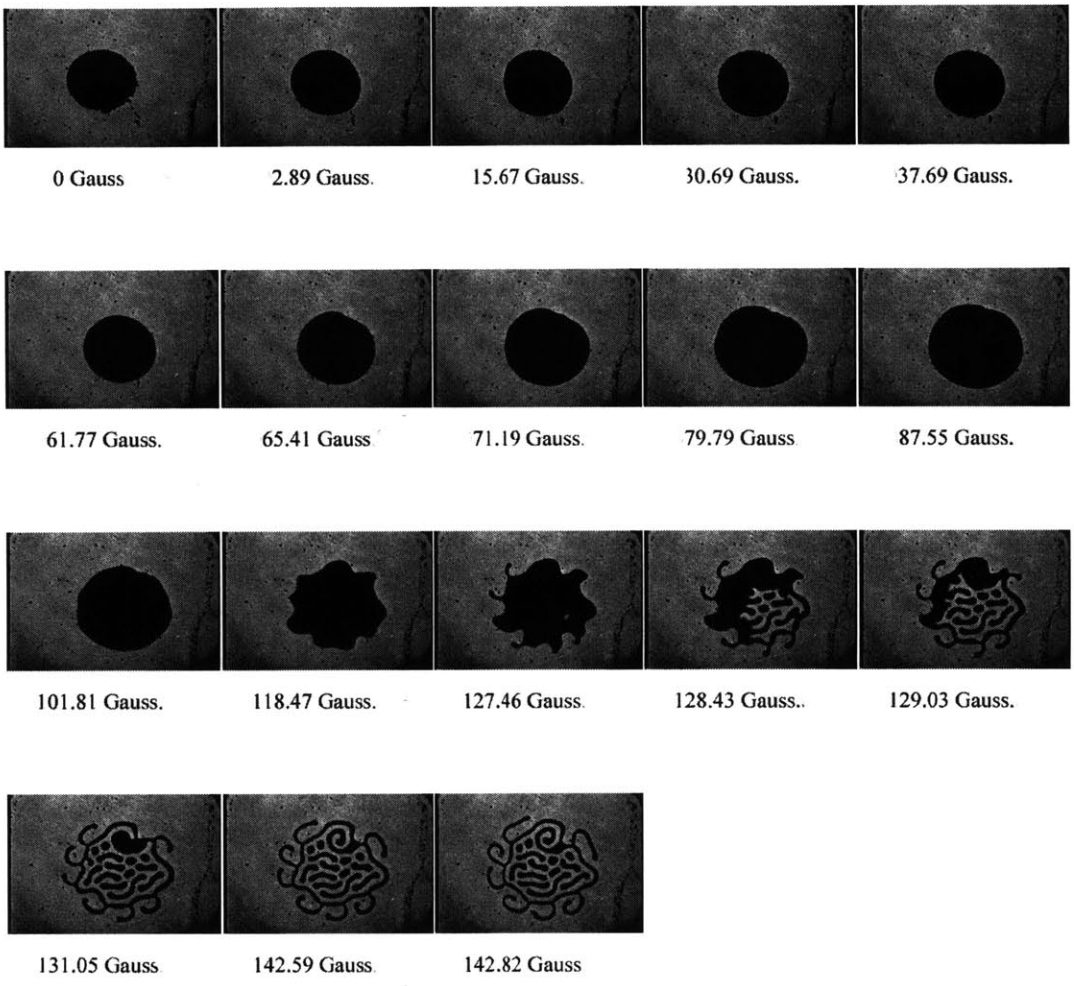

Figure D-155: Sequence 2: 200 μl, 1.4 mm, 30 Hz, 20.9 Gauss (rms)

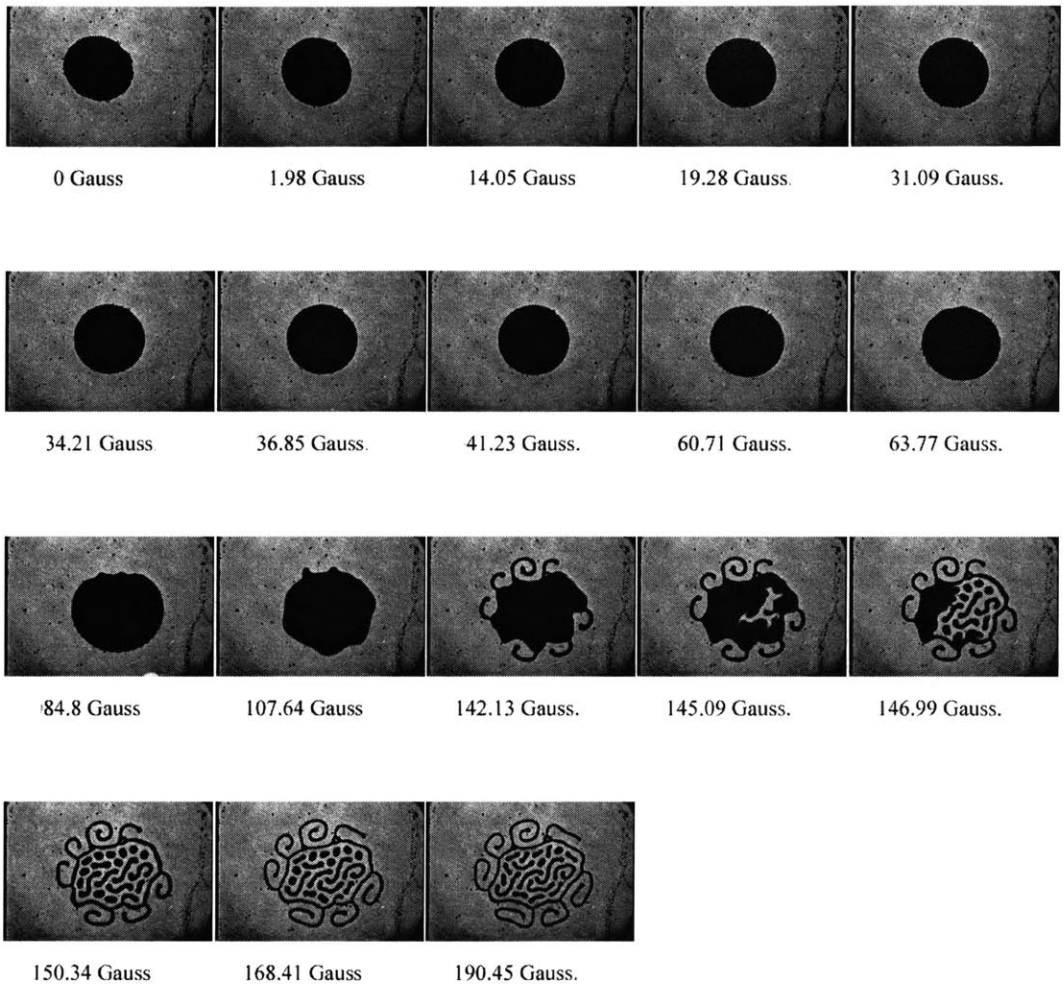

Figure D-156: Sequence 1: 200 μl, 1.4 mm, 30 Hz, 24.7 Gauss (rms)

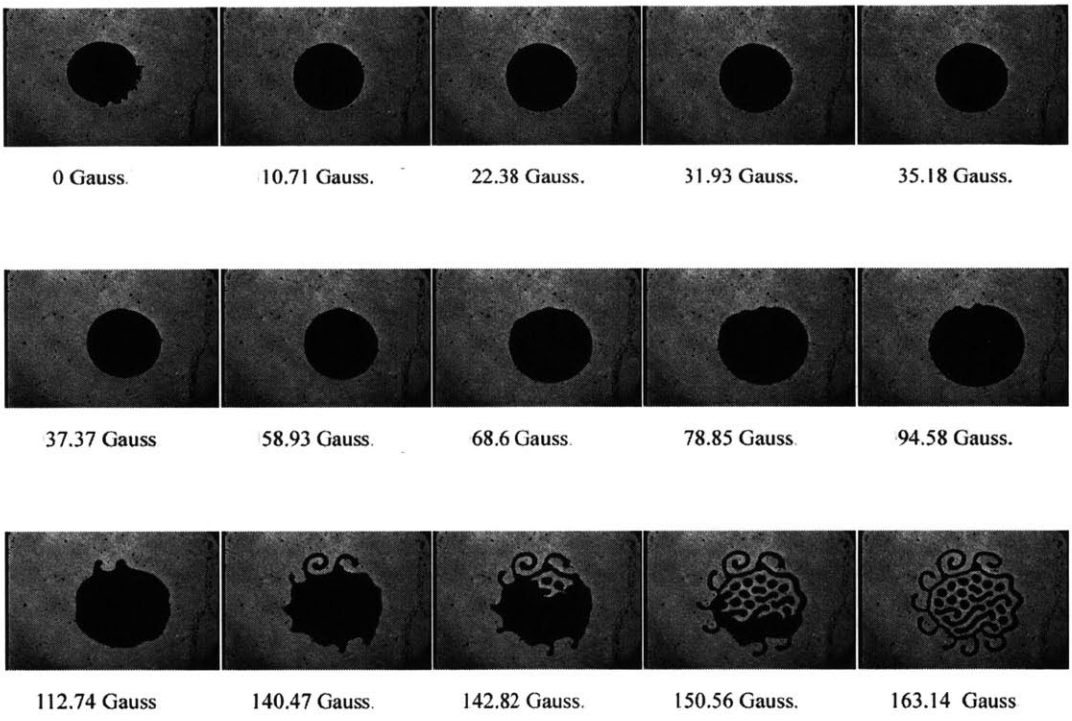

Figure D-157: Sequence 2: 200 μl, 1.4 mm, 30 Hz, 24.7 Gauss (rms)

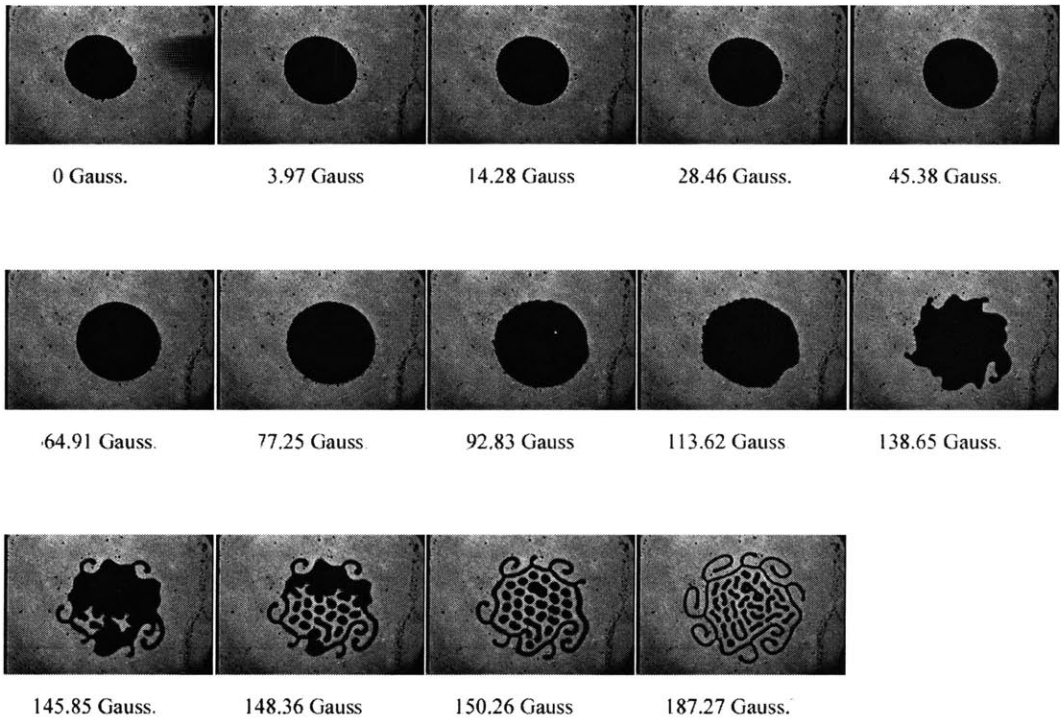

Figure D-158: Sequence 1: 200 μl, 1.4 mm, 30 Hz, 28.5 Gauss (rms)

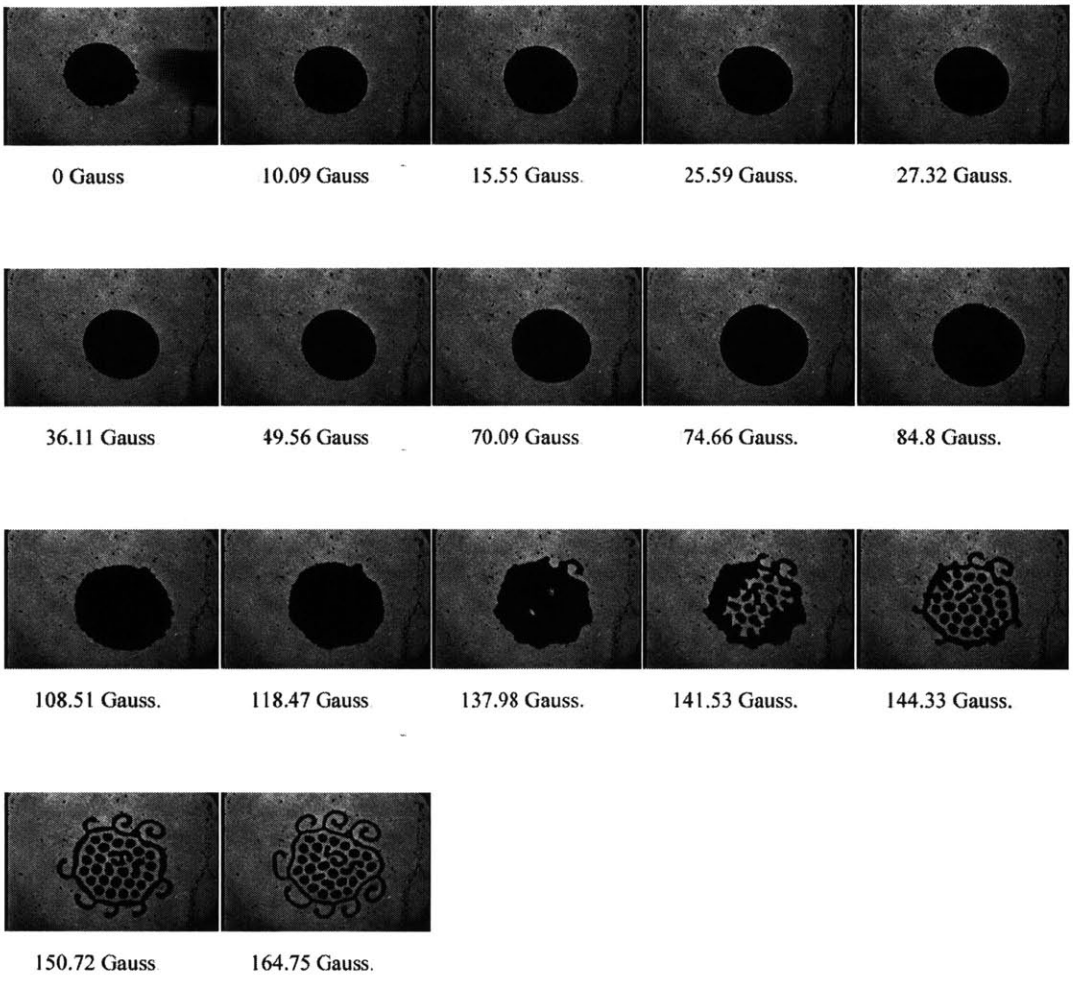

Figure D-159: Sequence 2: 200 μl, 1.4 mm, 30 Hz, 28.5 Gauss (rms)

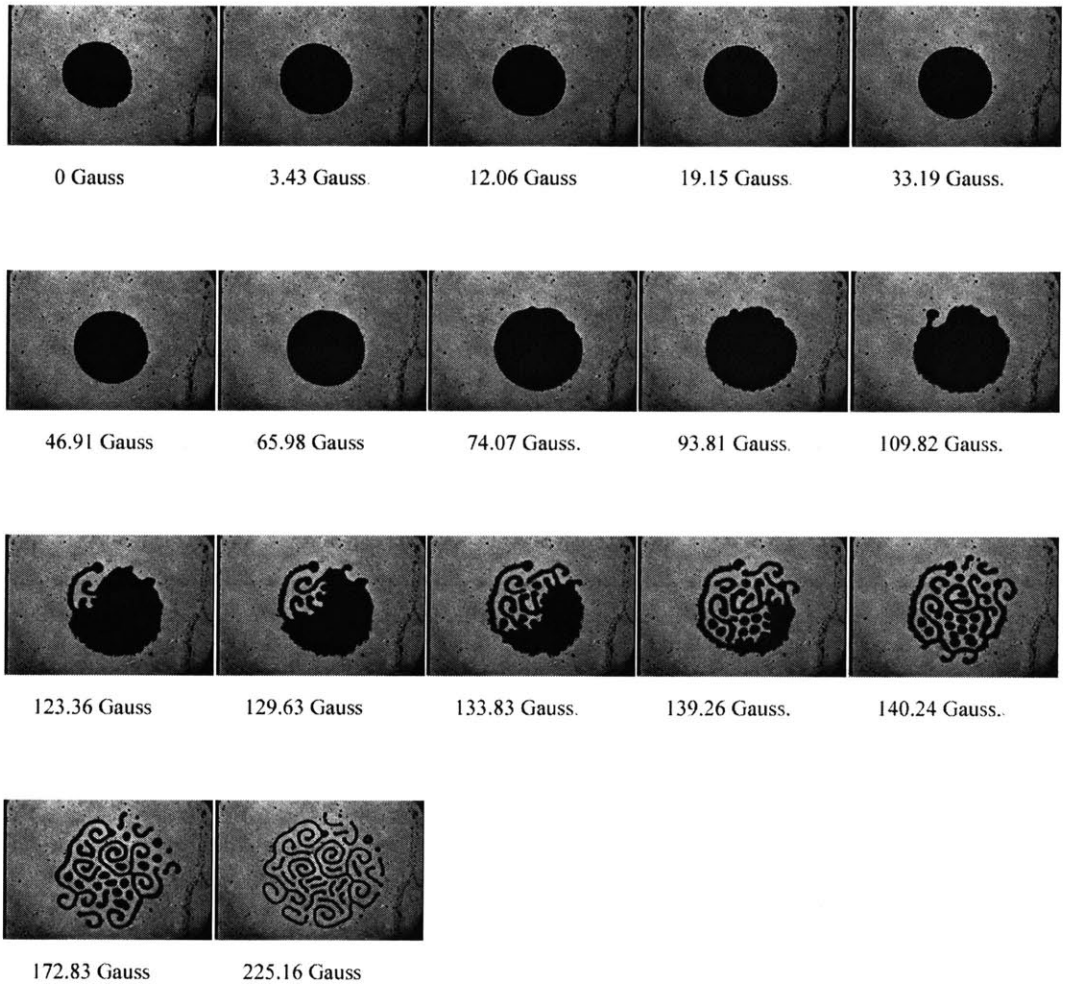

Figure D-160: Sequence 1: 200 μl, 1.4 mm, 30 Hz, 32.3 Gauss (rms)

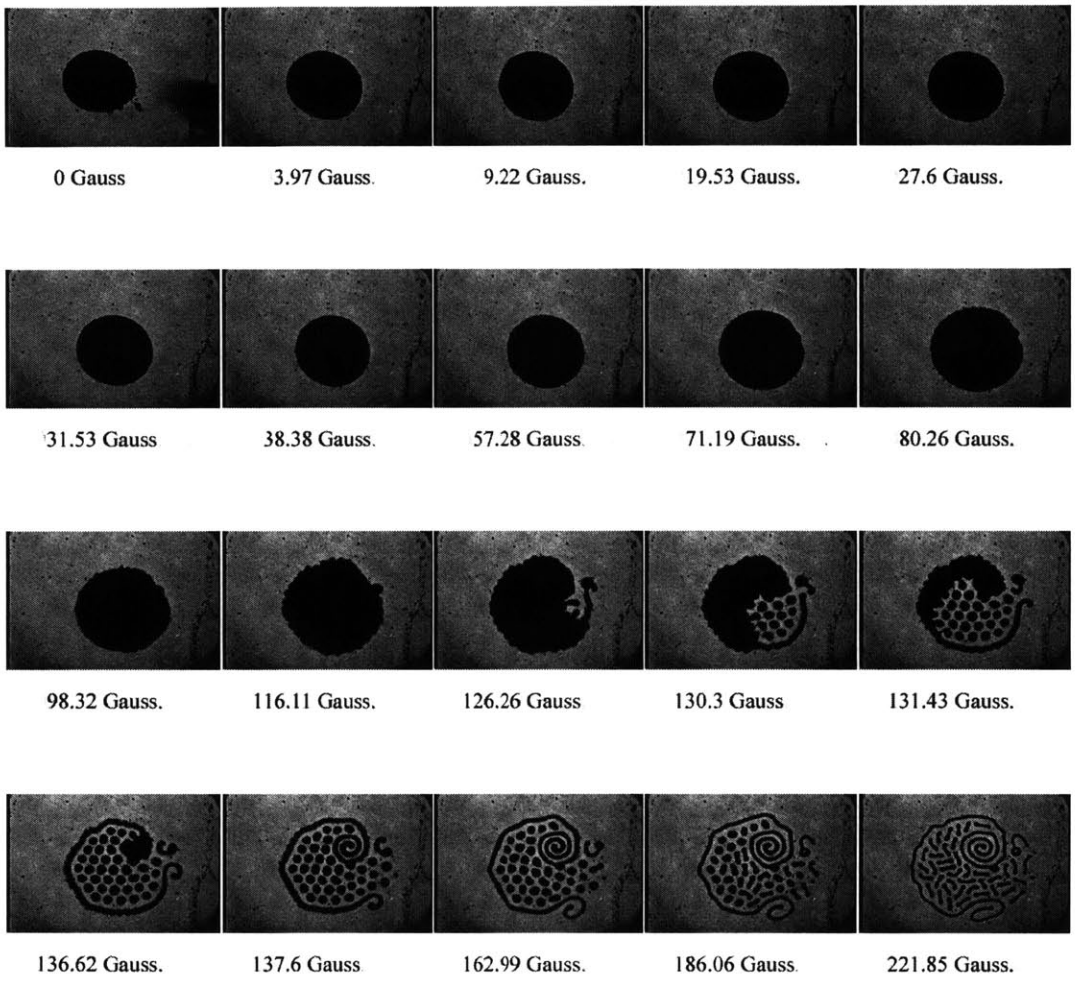

Figure D-161: Sequence 2: 200 μl, 1.4 mm, 30 Hz, 32.3 Gauss (rms)

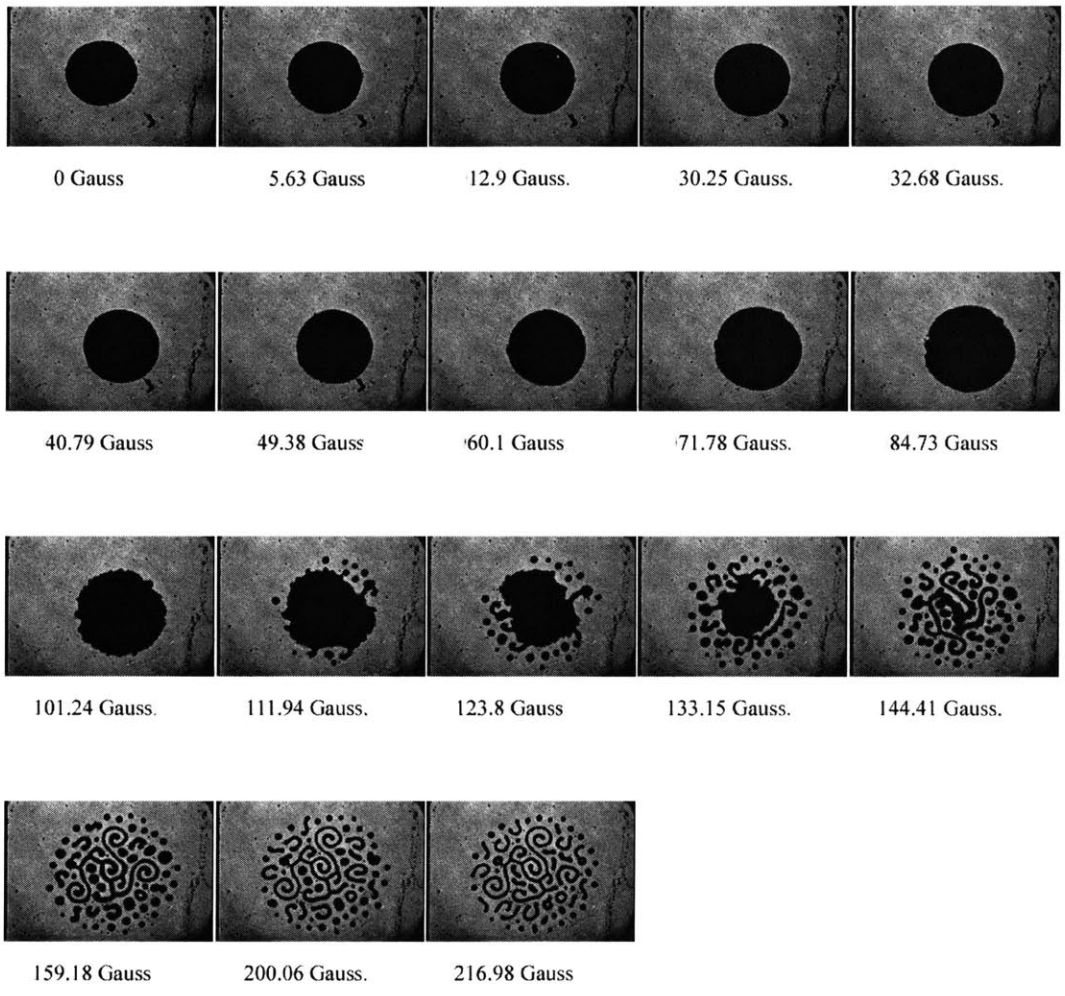

Figure D-162: Sequence 1: 200 μl, 1.4 mm, 30 Hz, 36.1 Gauss (rms)

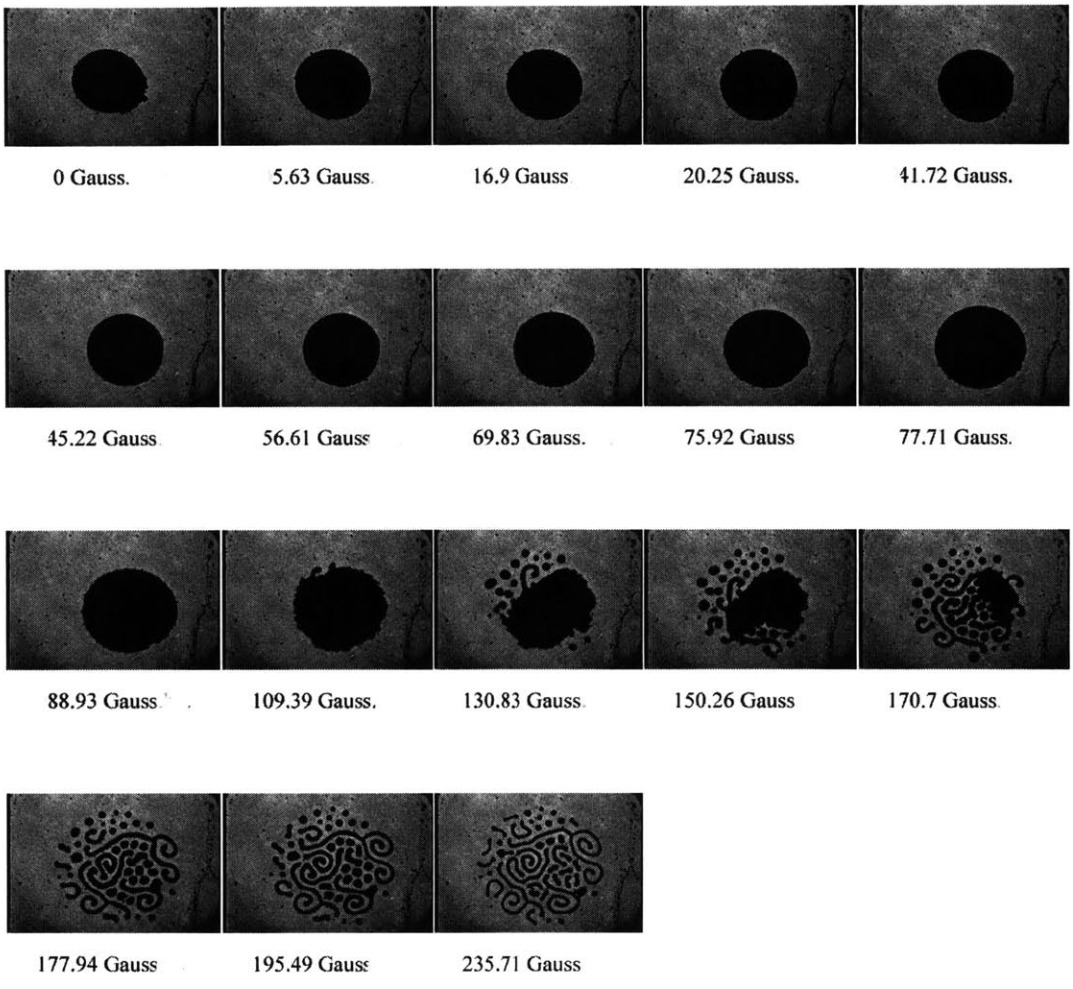

Figure D-163: Sequence 2: 200 μl, 1.4 mm, 30 Hz, 36.1 Gauss (rms)

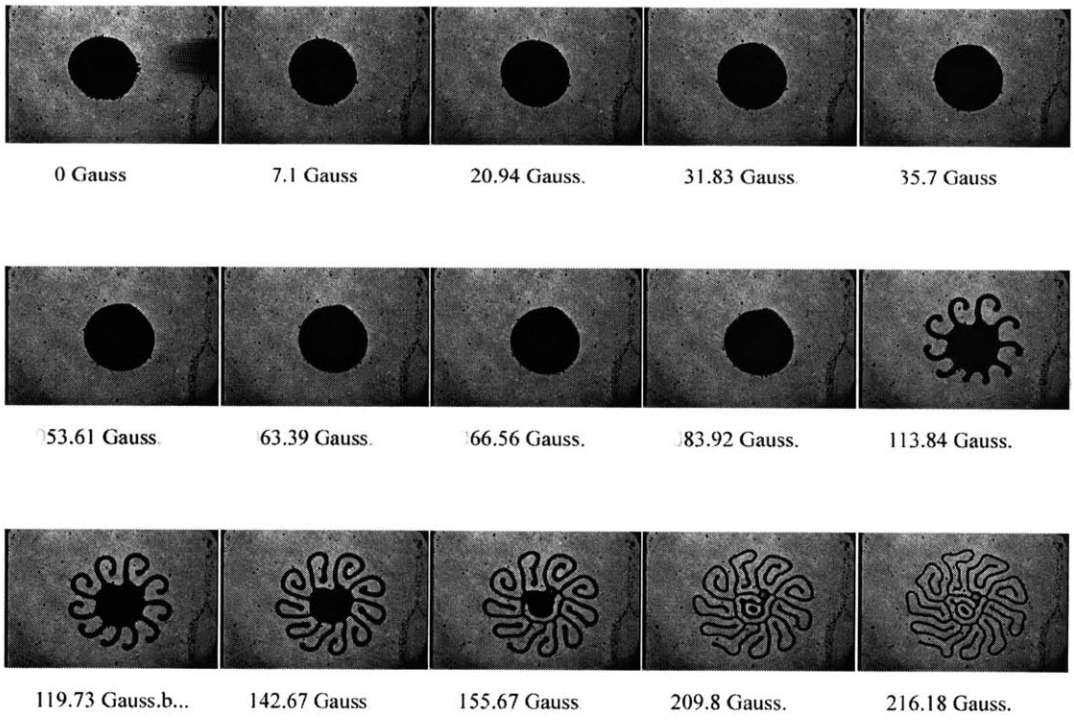

Figure D-164: Sequence 1: 200 μl, 1.4 mm, 35 Hz, 20.9 Gauss (rms)

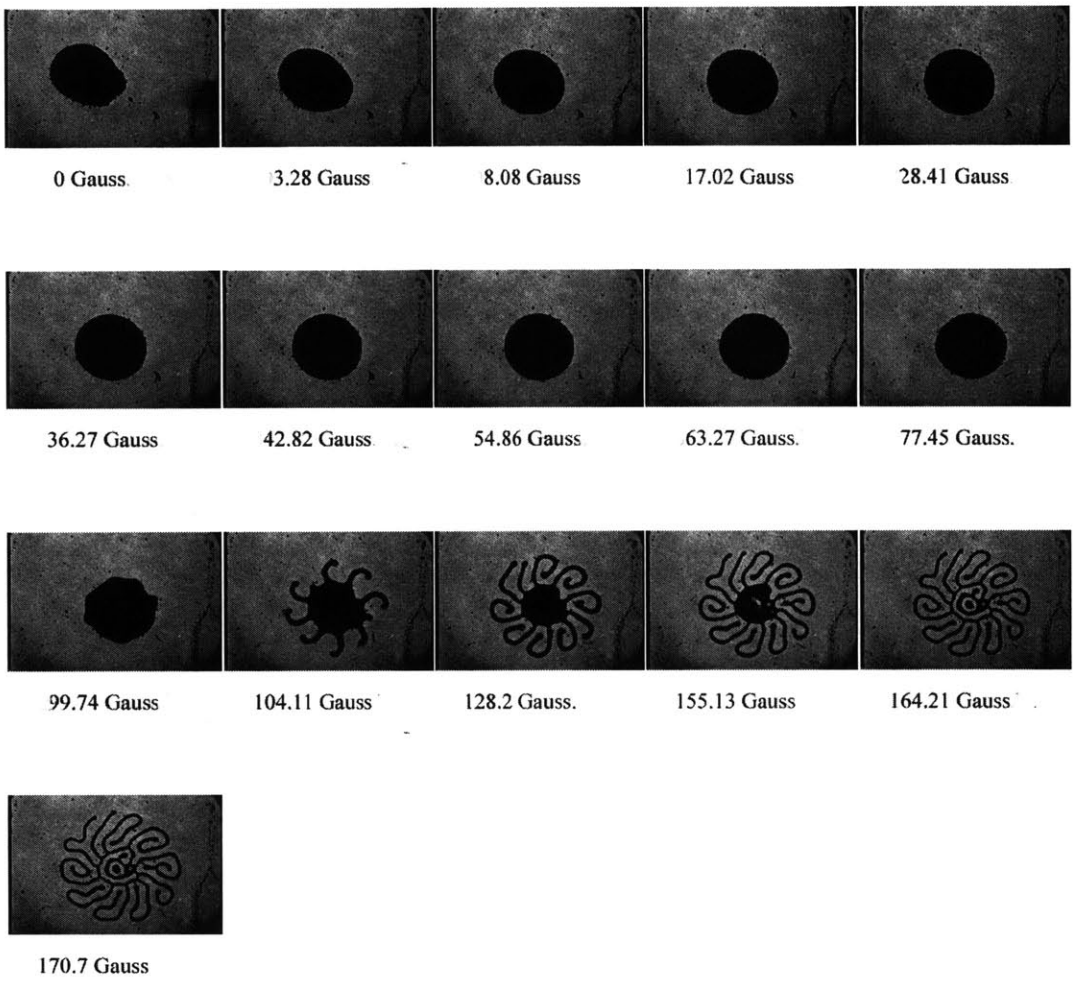

Figure D-165: Sequence 2: 200 μl, 1.4 mm, 35 Hz, 20.9 Gauss (rms)

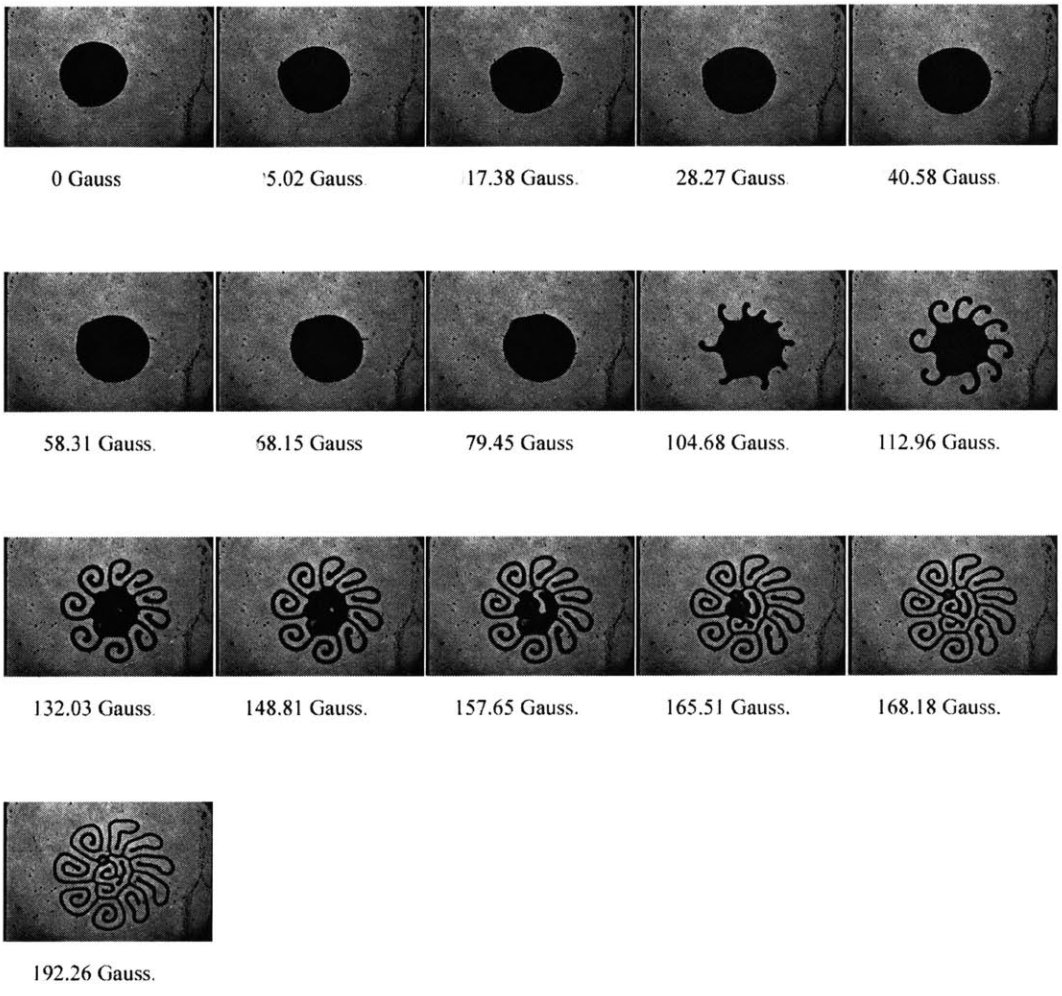

Figure D-166: Sequence 1: 200 μl, 1.4 mm, 35 Hz, 24.7 Gauss (rms)

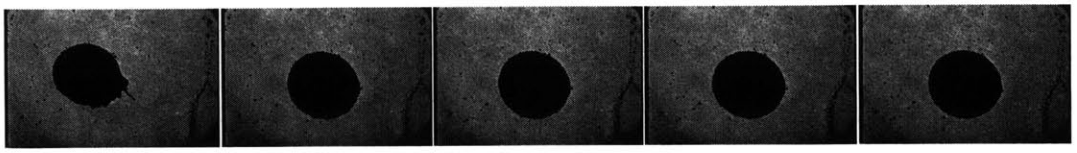

0 Gauss 13.41 Gauss 23.58 Gauss. 32.89 Gauss. 40.09 Gauss.

48.17 Gauss 50.37 Gauss 65.6 Gauss. 73.48 Gauss. 93.95 Gauss.

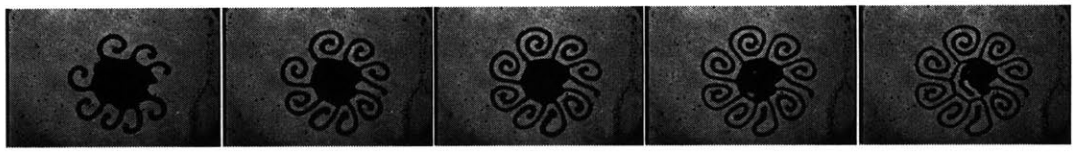

122.76 Gauss 135.64 Gauss. 151.02 Gauss. 167.8 Gauss. 175.8 Gauss.

189.92 Gauss

Figure D-167: Sequence 2: 200 μl, 1.4 mm, 35 Hz, 24.7 Gauss (rms)

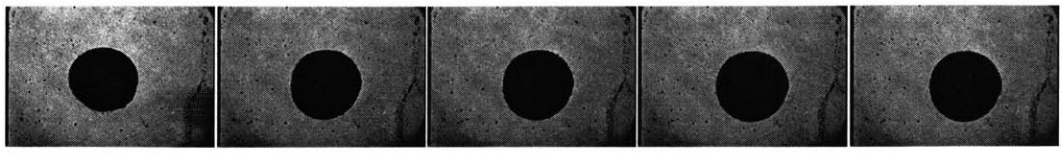

0 Gauss. 7.57 Gauss. 23.67 Gauss 35.23 Gauss. 45.38 Gauss.

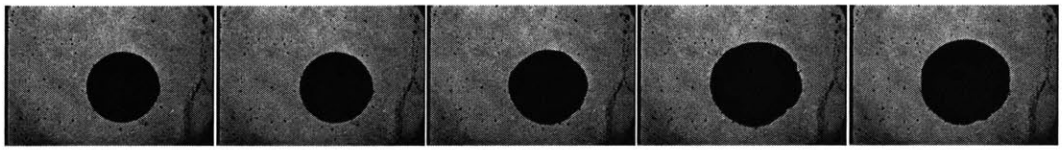

63.77 Gauss 64.91 Gauss 84.94 Gauss 102.89 Gauss. 123.88 Gauss.

145.85 Gauss 154.75 Gauss 158.72 Gauss 182.57 Gauss. 197.22 Gauss

221.05 Gauss

Figure D-168: Sequence 1: 200 μl, 1.4 mm, 35 Hz, 28.5 Gauss (rms)

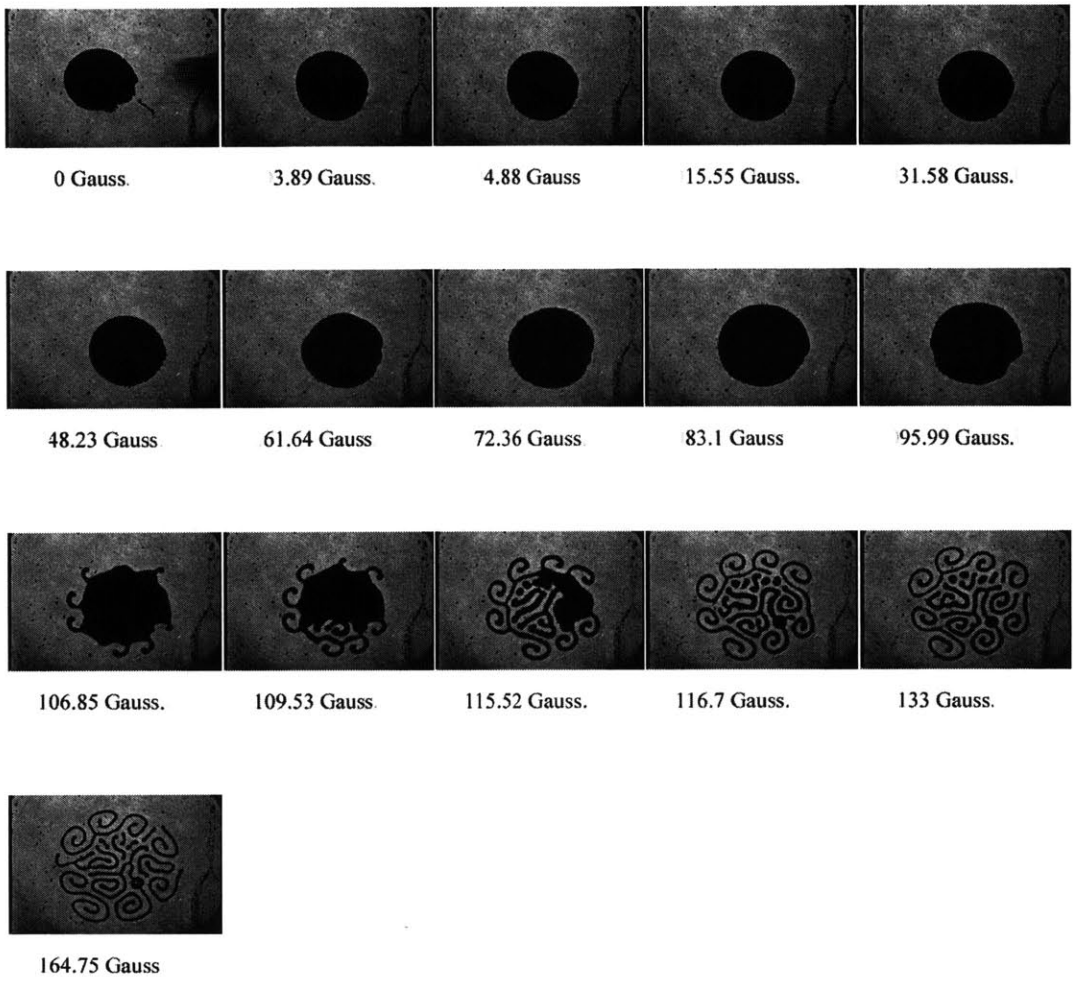

Figure D-169: Sequence 2: 200 μl, 1.4 mm, 35 Hz, 28.5 Gauss (rms)

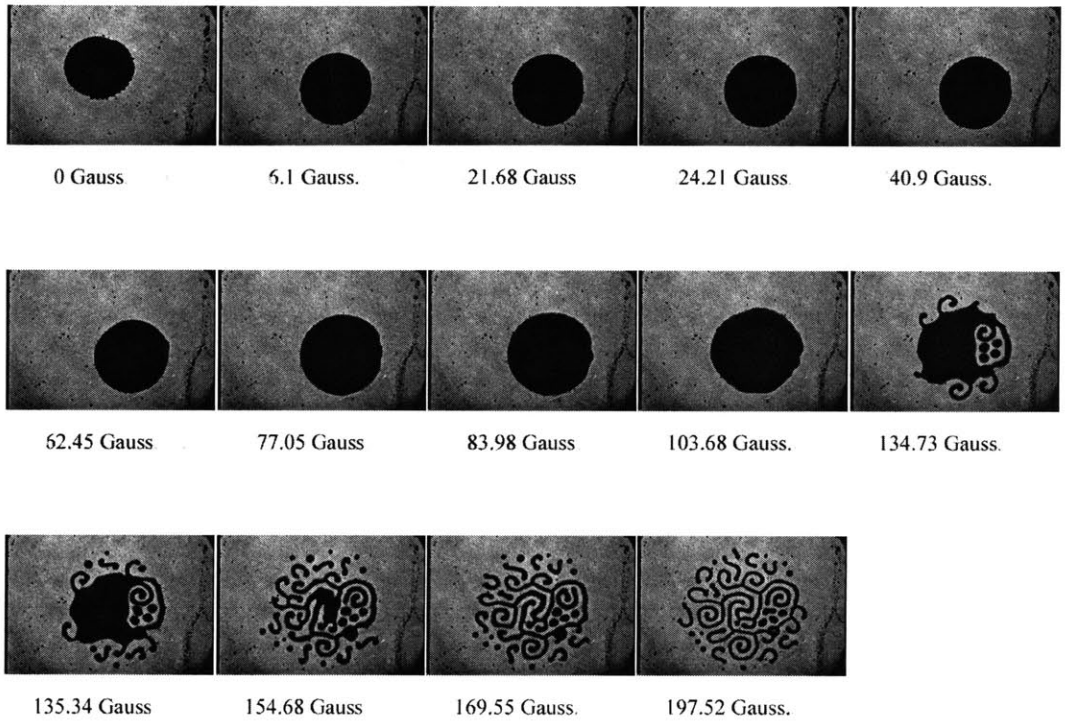

Figure D-170: Sequence 1: 200 μl, 1.4 mm, 35 Hz, 32.3 Gauss (rms)

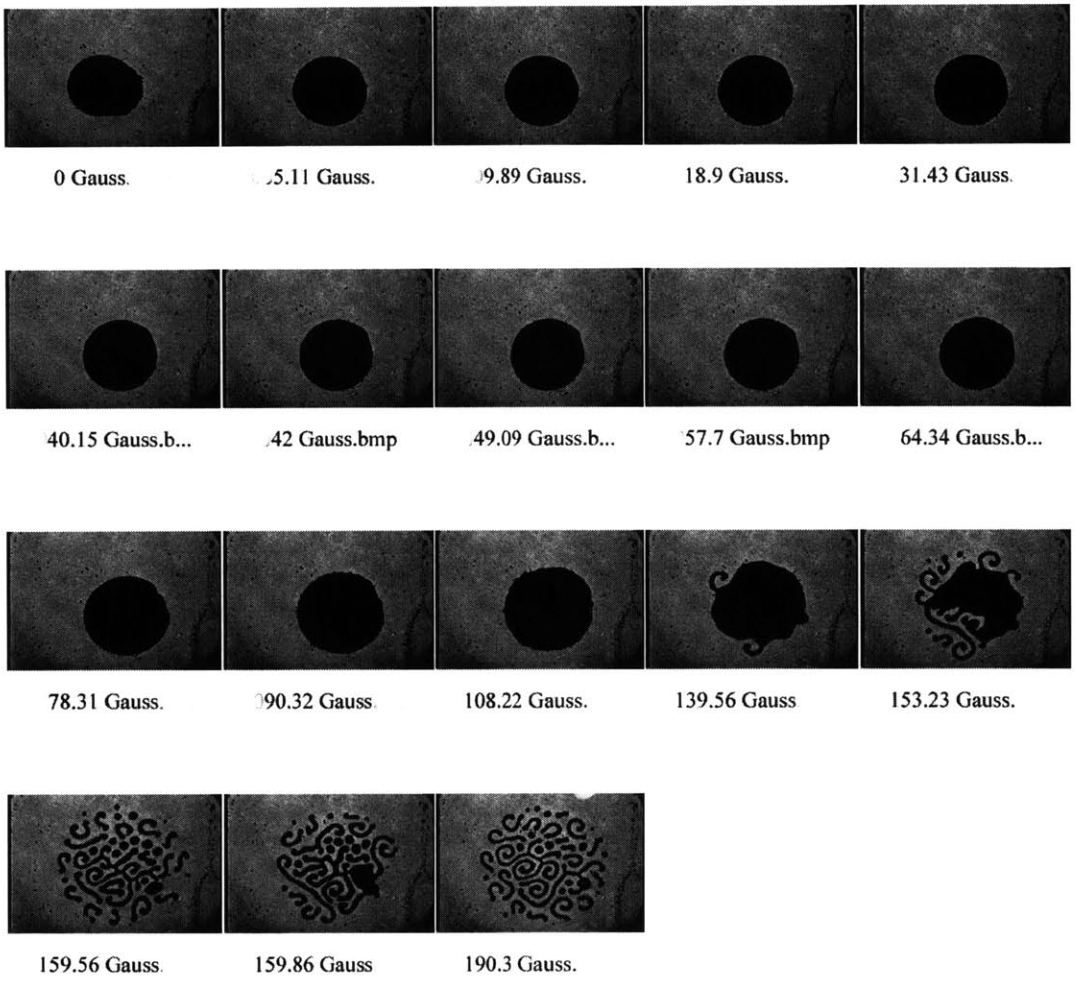

Figure D-171: Sequence 2: 200 μl, 1.4 mm, 35 Hz, 32.3 Gauss (rms)

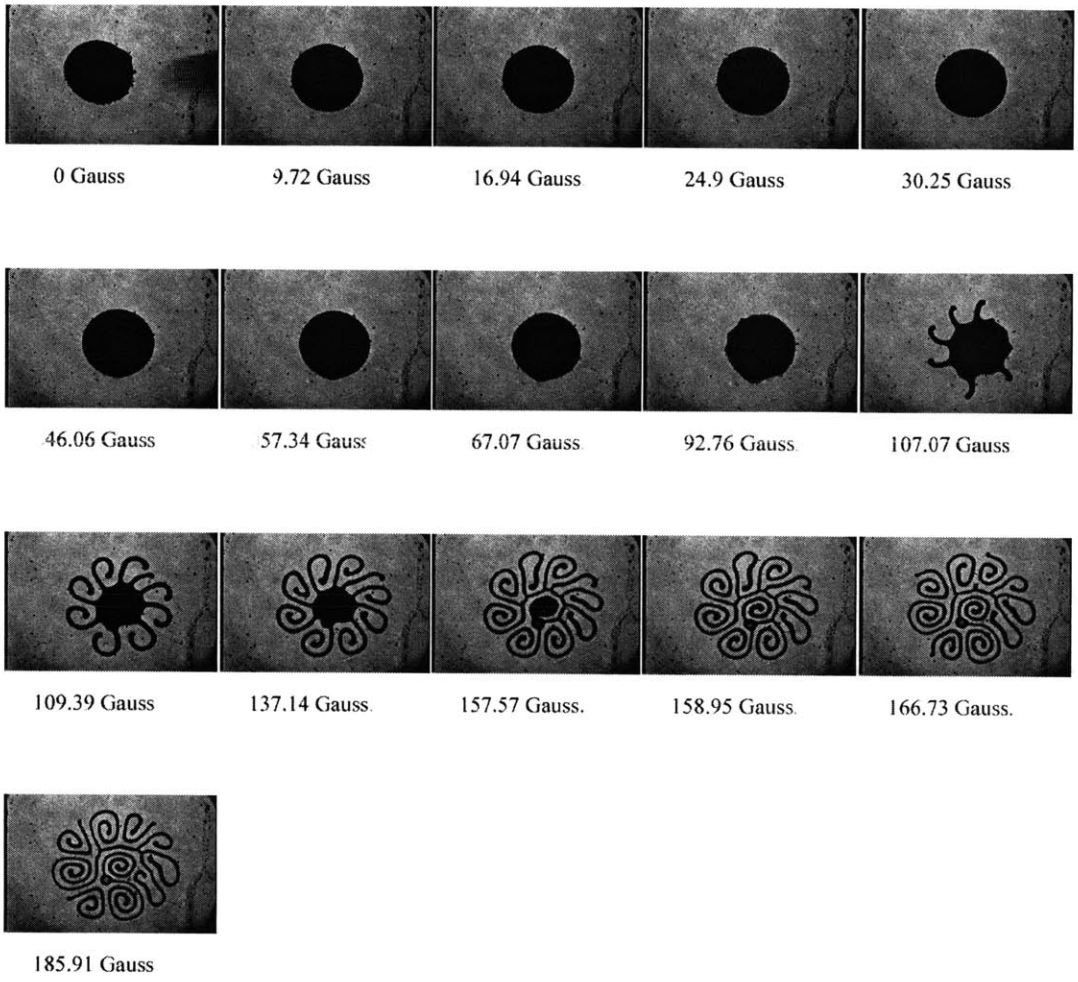

Figure D-172: Sequence 1: 200 μl, 1.4 mm, 40 Hz, 24.7 Gauss (rms)

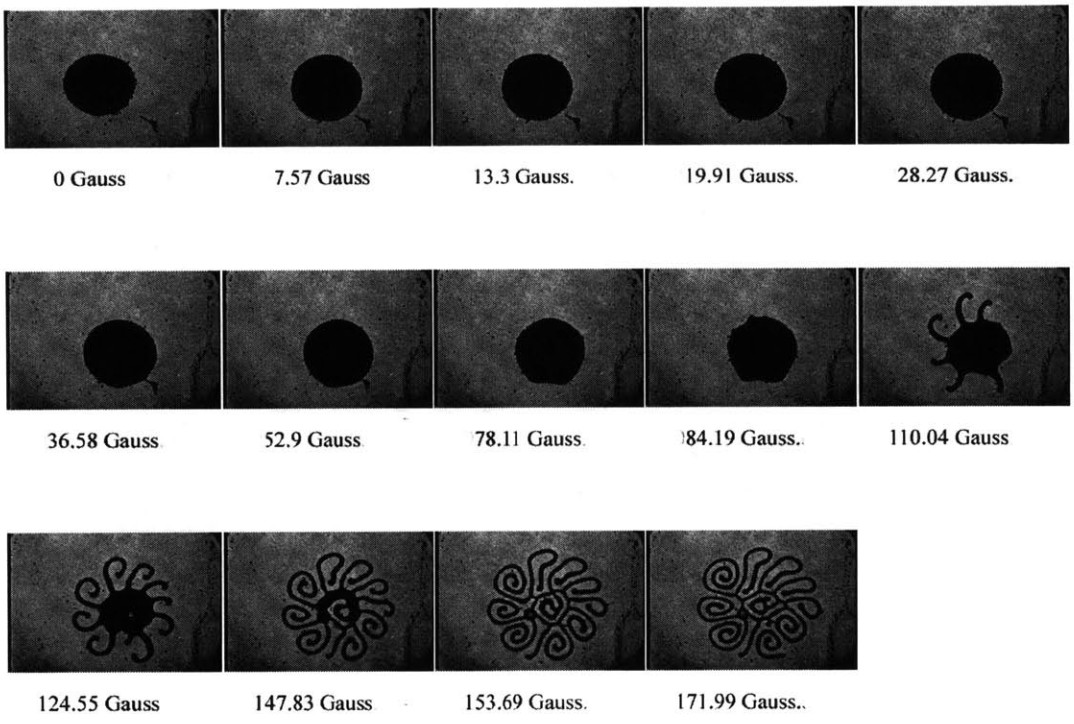

Figure D-173: Sequence 2: 200 μl, 1.4 mm, 40 Hz, 24.7 Gauss (rms)

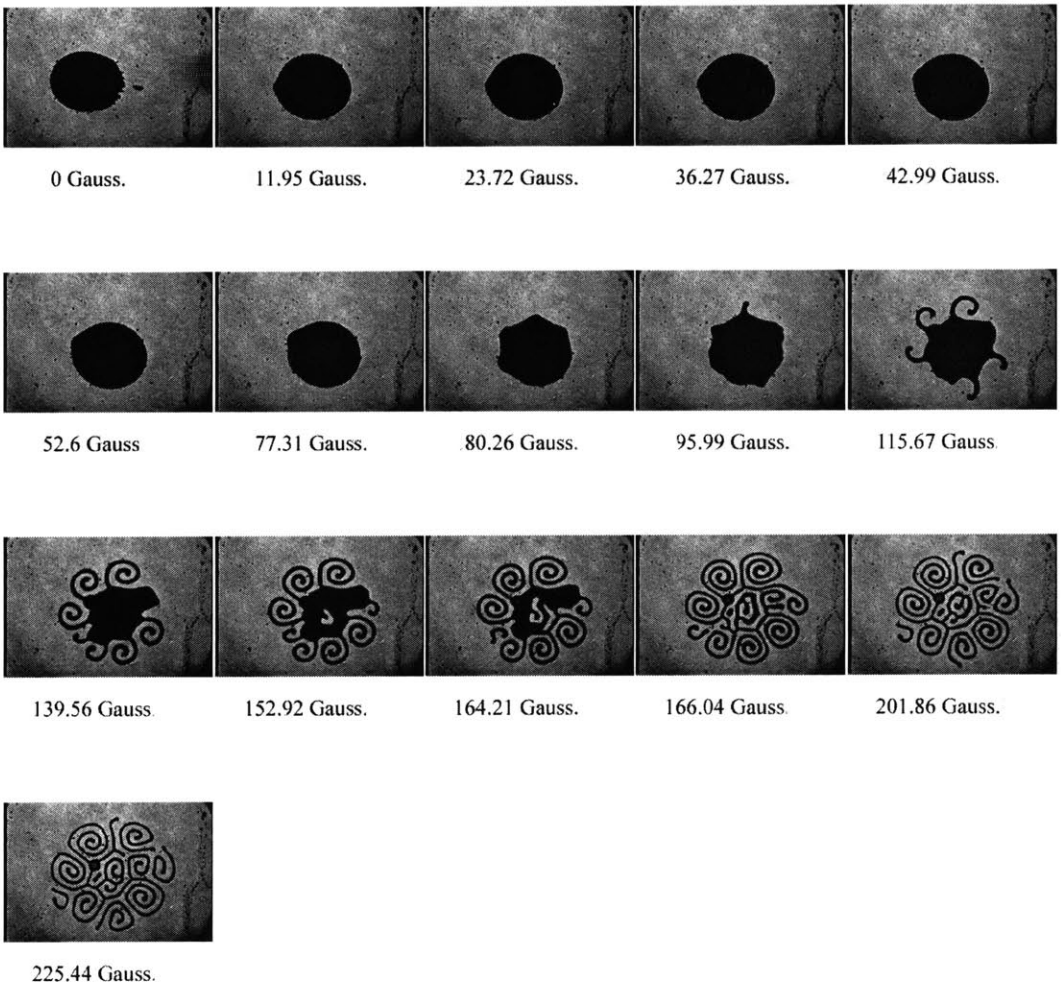

Figure D-174: Sequence 1: 200 μl, 1.4 mm, 40 Hz, 28.5 Gauss (rms)

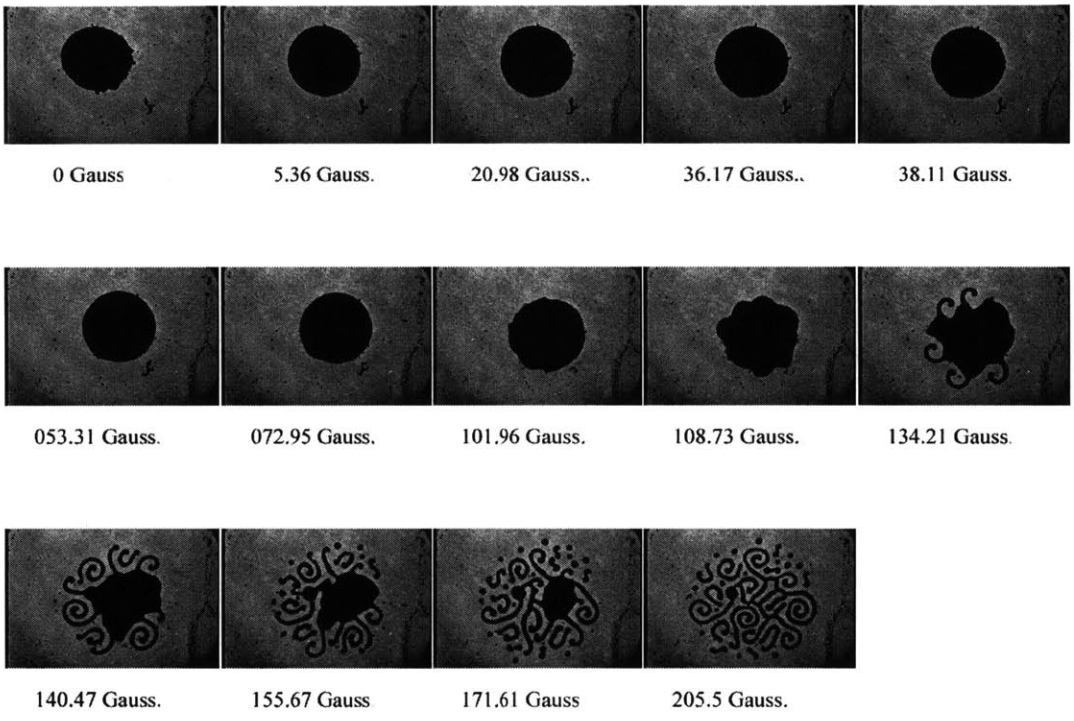

Figure D-175: Sequence 1: 200 μl, 1.4 mm, 40 Hz, 32.3 Gauss (rms)

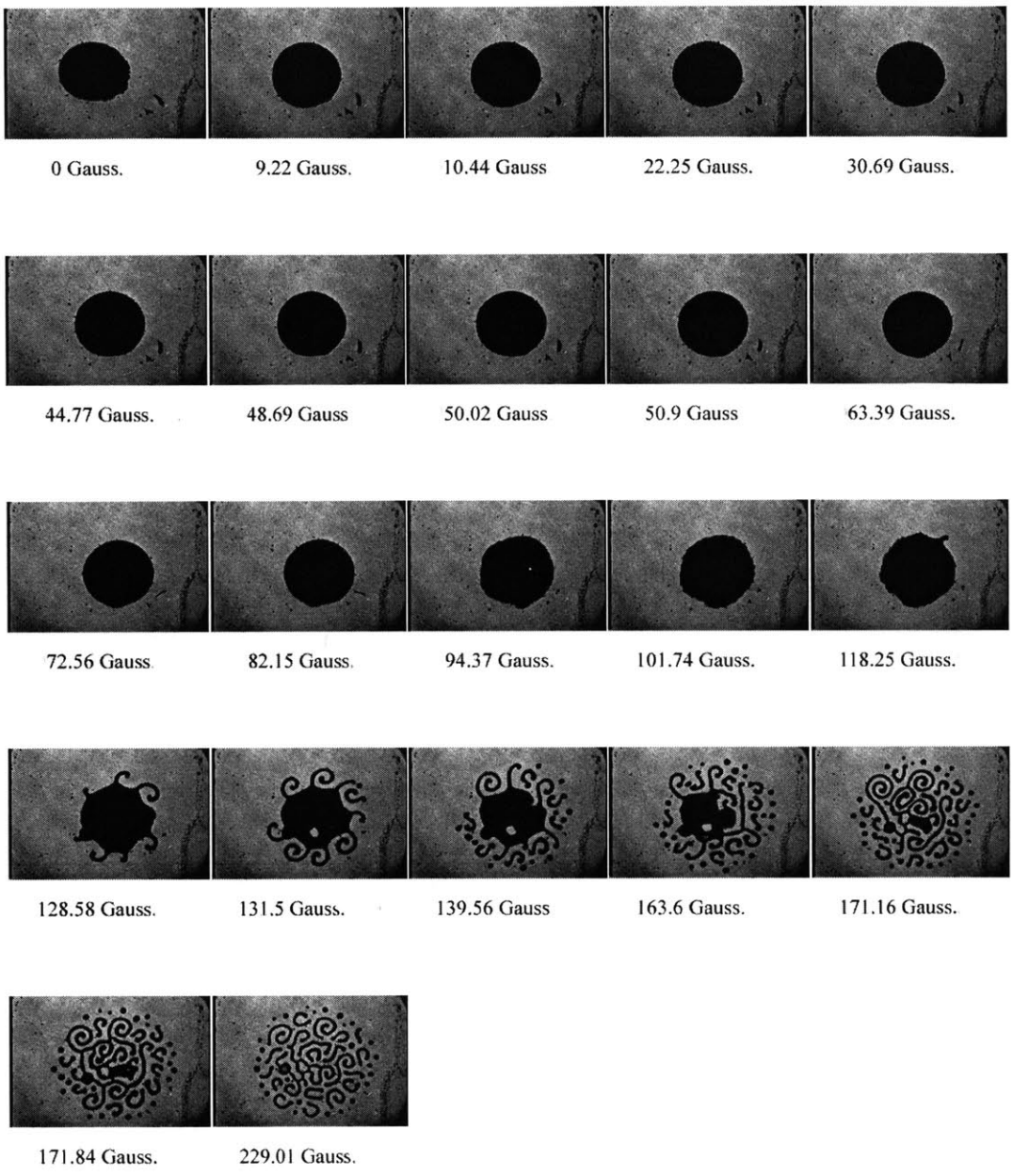

Figure D-176: Sequence 2: 200 μl, 1.4 mm, 40 Hz, 32.3 Gauss (rms)

Bibliography

[1] Ch. Alexiou, A. Schmidt, R. Klein, P. Hulin, Ch. Bergemann, and W. Arnold. Magnetic drug targeting: biodistribution and dependency on magnetic field strength. *Journal of Magnetism and Magnetic Materials.*, 252:363–366, Nov. 2002.

[2] N. Brusentsov, B. Gogosov, T. Brusentsova, A. Sergeev, N. Jurchenko, A. Kuznetsov, O. Kuznetsov, and L. Sumakov. Evaluation of ferromagnetic fluids and suspensions for the site-specific radiofrequency-induced hyperthermia of mx11 sarcoma cells in vitro. *Journal of Magnetism and Magnetic Materials.*, 225:113–117, 2001.

[3] Lord Corporation. Website visited: 12/03. http://lord.com.

[4] GH. Călugăru, C. Cotae, R. Bădesch, V. Bădecsu, and E. Luca. A new aspect of the movement of ferrofluids in a rotating magnetic field. *Rev. Roum. Phys.*, 21(4):439–440, 1976.

[5] T. Franklin. Ferrofluid flow phenomena. Master's thesis, Massachusetts Institute of Technology, 2003.

[6] R. Hergt, R. Hiergeist, I. Hilger, W. Kaiser, Y. Lapatnikov, S. Margel, and U. Richter. Maghemite nanoparticles with very high ac-losses for application in rf-magnetic hyperthermia. *Journal of Magnetism and Magnetic Materials.*, In Press, May 8, 2003.

[7] S. Lee, J. Jeong, S. Shin, J.C. Kim, Y.H. Chang, Y.M. Chang, and J.D. Kim. Nanoparticles of magnetic ferric oxides encapsulated with poly(d,l latide-co-glycolide) and their applications to magnetic resonance imaging contrast agent. *Journal of Magnetism and Magnetic Materials.*, In Press, Jan. 7, 2004.

[8] C. Lorenz and M. Zahn. Hele-shaw ferrohydrodynamics for rotating and dc magnetic fields. *Physics of Fluids Gallery of Fluid Motion.*, 15(9), Sept. 2003.

[9] R. Muller, H. Steinmetz, R. Hiergeist, and W. Gawalek. Magnetic particles for medical applications by glass crystallisation. *Journal of Magnetism and Magnetic Materials.*, In Press, Jan. 17, 2004.

[10] S. Odenbach. *Ferrofluids, Magnetically Controllable Fluids and Their Applications.* Springer, New York, USA, 2002.

[11] D. Paris and F. Hurd. *Basic Electromagnetic Theory.* McGraw Hill, NY, USA, 1969.

[12] S. Rhodes, J. Perez, S. Elborai, S. Lee, and M. Zahn. Ferrohydrodynamic hele-shaw cell flows and instabilities with simultaneous dc axial and in-plane rotating magnetic fields. *Abstract Submitted to International Congress of Theoretical and Applied Mechanics (ICTAM), Warsaw, Poland*, August 15-21, 2004.

[13] S. Rhodes, J. Perez, S. Elborai, S. Lee, and M. Zahn. Ferrofluid spiral formations and continuous-to-discrete phase transitions under simultaneously applied dc axial and ac in-plane rotating magnetic fields. *Abstract Submitted to International Conference of Magnetic Fluids (ICMF10), São Paulo, Brazil*, August 2-6, 2004.

[14] R. Rosensweig. *Ferrohydrodynamics.* Cambridge University Press, New York, USA, 1985.

[15] R. Rosensweig, J. Popplewell, and R. Johnston. Magnetic fluid motion in rotating field. *Journal of Magnetism and Magnetic Materials.*, 85, 1990.

[16] R. Rosensweig, M. Zahn, and R. Shumovich. Labrinthine instability in magnetic and dielectric fluids. *Journal of Magnetism and Magnetic Materials.*, 39:127–132, 1983.

[17] A. Rosenthal. Ferrofluid flow and torque measurements in rotating magnetic fields. Master's thesis, Massachusetts Institute of Technology, 2002.

[18] A. Rosenthal, C. Rinaldi, and M. Zahn. Torque measurements in spin-up flow of ferrofluids. *Submitted to ASME Journal of Fluids Engineering.*, 2002.

[19] M. Zahn. Magnetic fluid and nanoparticle applications to nanotechnology. *Journal of Nanoparticle Research.*, 3:73–78, Nov. 2000.

[20] M. Zahn and D. Greer. Ferrohydrodynamic pumping in spatially uniform sinusoidally time-varying magnetic fields. *Journal of Magnetism and Magnetic Materials.*, 149:165–173, 1995.

[21] M. Zahn and L.L. Pioch. Magnetizable fluid behavior with effective positive, zero, or negative dynamic viscosity. *Indian Journal of Engineering and Material Sciences.*, 5:400–410, 1998.

[22] M. Zahn and L.L. Pioch. Ferrofluid flows in ac and traveling wave magnetic fields with effective positive, zero, or negative viscosity. *Journal of Magnetism and Magnetic Materials.*, 201:144–148, 1999.

[23] M. Zahn and P.N. Wainman. Effects of fluid convection and particle spin on ferrohydrodynamic pumping in traveling wave magnetic fields. *Journal of Magnetism and Magnetic Materials.*, 122:323–328, 1993.